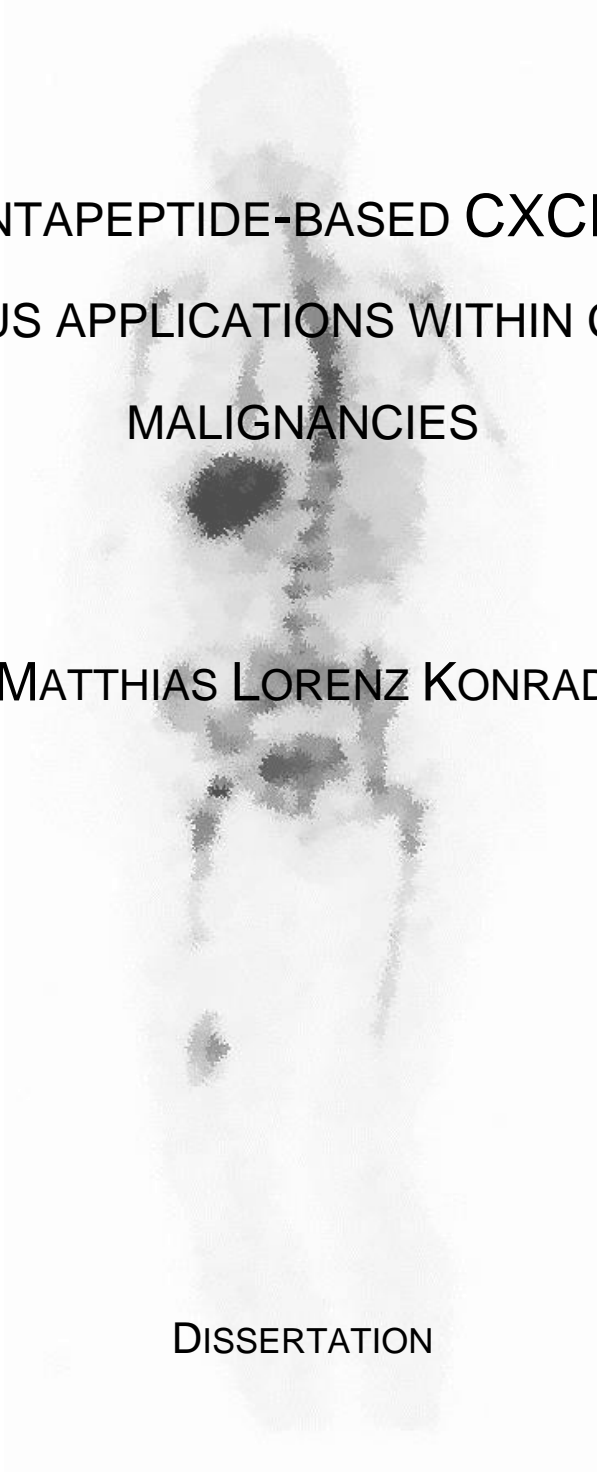




Technische Universität München

Fakultät für Chemie

Lehrstuhl für Pharmazeutische Radiochemie



**CYCLIC PENTAPEPTIDE-BASED CXCR4 LIGANDS
FOR VARIOUS APPLICATIONS WITHIN CANCEROUS
MALIGNANCIES**

MATTHIAS LORENZ KONRAD

DISSERTATION



Technische Universität München

Fakultät für Chemie

Cyclic pentapeptide-based CXCR4 ligands for various applications within cancerous malignancies

Matthias Lorenz Konrad

Vollständiger Abdruck der von der Fakultät für Chemie der Technischen Universität München zur Erlangung des akademischen Grades eines

Doktors der Naturwissenschaften (Dr. rer. nat.)

genehmigten Dissertation.

Vorsitzender:

Prof. Dr. Job Boekhoven

Prüfer der Dissertation:

1. Prof. Dr. Margret Schottelius
2. apl. Prof. Dr. Wolfgang Eisenreich

Die Dissertation wurde am 12.07.2021 bei der Technischen Universität München eingereicht und durch die Fakultät für Chemie am 29.09.2021 angenommen.

“Thunder only happens
when it’s raining”

– Fleetwood Mac –

Die vorliegende Arbeit wurde im Zeitraum zwischen August 2017 und November 2020 im Fachgebiet pharmazeutische Radiochemie der Technischen Universität München angefertigt.

ACKNOWLEDGEMENTS (IN GERMAN)

Bei Ihnen, Prof. Schottelius, möchte ich mich für 7 Jahre persönliche und fachliche Unterstützung bedanken. Danke für viele amüsante Stunden in Labor und Büro, unzählige Ideen und Ratschläge und die Betreuung dieser Doktorarbeit. Team SchoKo strikes again!

Ihnen, Herr Prof. Wester, danke ich für die Möglichkeit, an Ihrem Lehrstuhl forschen zu können und für die Bereitstellung aller Mittel und Werkzeuge, um im Labor erfolgreich zu sein.

Ich möchte mich besonders bei meinen Kooperationspartnern aus den Gruppen von Prof. Lapa, Prof. Keller und Prof. Quante für das mir entgegengebrachte Vertrauen und die Einblicke in die klinische Forschung, die Sie mir ermöglicht haben, bedanken.

Besonderer Dank gilt Dr. Beck und Dr. Urtz-Urban für das Management all meiner Tierversuchsantragsänderungen und die stets verlässliche Unterstützung bei meinen Experimenten.

Ebenfalls bedanken möchte ich mich bei Christine Winkler, den Herren Größlhuber und Matheis und dem Team des Strahlenschutzes, die gemeinsam Büro und Labor am Laufen gehalten haben.

Ein ganz spezieller Dank geht an dich, Mara. Mit Kokomo hat unser beider Promotionszeit fröhlich begonnen und mit viel Ernüchterung geht sie zu Ende. Ich würde sagen, wir haben das Beste draus gemacht, oder?! Ein Shoutout geht raus an die Autoradiographie!

Vielen herzlichen Dank, Markus, JPK, León, Basti, Jana, Vroni, Daniel, WU, Tanja und Thomas. Es war immer witzig mit euch, immer harmonisch und freundschaftlich. Ohne euch und eure Hilfe wäre das Ganze einfach nicht machbar gewesen. Danke!

Danke an Mama, Papa, Schorsch, Ruth, Hanni, Michi, danke an die gesamte Crew und alle meine Freunde! Ihr habt mich durch 10 Jahre Studium getragen, mich finanziert und meine Launen ertragen. Diese Arbeit widme ich euch und danke euch von ganzem Herzen.

CONTENT

ACKNOWLEDGEMENTS (IN GERMAN)	I
ABSTRACT	VII
KURZZUSAMMENFASSUNG	XI
I. INTRODUCTION	1
1. CANCER	1
2. MOLECULAR IMAGING OF CANCER	2
3. THERAPY OF CANCER	4
4. CHEMOKINES AND CHEMOKINE RECEPTORS	6
4.1. THE CHEMOKINE FAMILY	6
4.2. CXCL12 AND CXCR4	6
4.3. CXCL12 AND CXCR4 IN INFLAMMATION AND CANCER	8
5. MOLECULAR IMAGING AND THERAPY OF CXCR4-EXPRESSING CANCER	11
5.1. [⁶⁴ Cu]AMD3100	11
5.2. [⁶⁸ Ga]NOTA-NFB.....	11
5.3. [^{99m} Tc]CXCR4-L	12
5.4. CYCLIC PENTAPEPTIDES.....	12
6. OBJECTIVES	20
II. MATERIALS AND METHODS	23
1. GENERAL INFORMATION	23
1.1. REAGENTS, SOLVENTS AND BIOCHEMICALS	23
1.2. RADIOACTIVE ISOTOPES	24
1.3. INSTRUMENTS AND ANALYTICS	24
2. SYNTHESIS	26
2.1. GENERAL CONCEPTS	26
2.2. SYNTHESIS OF BUILDING BLOCKS.....	30
2.3. SYNTHESIZED PEPTIDES.....	40
3. RADIOLABELING	85
3.1. IODINE-125	85
3.2. TECHNETIUM-99M.....	85
3.3. LUTETIUM-177.....	89

3.4. FLUORINE-18	89
3.5. GALLIUM-68	90
3.6. GALLIUM-67	90
4. CELL CULTURE, <i>IN VITRO</i> EXPERIMENTS AND LIPOPHILICITY	92
4.1. CULTIVATION OF JURKAT LYMPHOMA CELLS	92
4.2. CULTIVATION OF CHEM-1 CELLS	92
4.3. IC ₅₀ DETERMINATION	92
4.4. INVIC ₅₀ DETERMINATION.....	93
4.5. INTERNALIZATION STUDIES	93
4.6. LOGD _{7.4} DETERMINATION.....	94
5. <i>IN VIVO</i> EXPERIMENTS AND IMAGING.....	95
5.1. CB17-SCID MICE AND JURKAT XENOGRFT MODEL.....	95
5.2. SMALL ANIMAL μ SPECT IMAGING	95
5.3. BIODISTRIBUTION STUDIES	96
5.4. FLUORESCENCE IMAGING	96
5.5. CLINICAL SPECT/CT IMAGING	96
5.6. CLINICAL PET/CT IMAGING	97
III. RESULTS AND DISCUSSION.....	99
1. OVERVIEW	99
2. TECHNETIUM-99M TRACERS.....	104
2.1. SYNTHESIS.....	105
2.2. RADIOSYNTHESIS.....	112
2.3. <i>IN VITRO</i> EVALUATION AND HYDROPHILICITY	114
2.4. <i>IN VIVO</i> BIODISTRIBUTION AND μ SPECT IMAGING	131
2.5. PROOF-OF-CONCEPT STUDY IN MEN.....	141
3. DOTA-CONJUGATED LIGANDS	146
3.1. SYNTHESIS.....	150
3.2. RADIOSYNTHESIS.....	150
3.3. <i>IN VITRO</i> EVALUATION AND HYDROPHILICITY.....	151
3.4. <i>IN VIVO</i> BIODISTRIBUTION.....	160
3.5. CONCLUSION.....	174
4. FLUORINE-18 TRACERS AND RADIOHYBRIDS	177
4.1. SYNTHESIS.....	180

4.2.	RADIOSYNTHESIS.....	181
4.3.	IN VITRO EVALUATION AND HYDROPHILICITY.....	184
4.4.	IN VIVO BIODISTRIBUTION.....	192
4.5.	CONCLUSION.....	195
5.	PEPTIDE-DRUG CONJUGATES.....	197
5.1.	SYNTHESIS.....	200
5.2.	RADIOSYNTHESIS.....	201
5.3.	IN VITRO EVALUATION AND HYDROPHILICITY.....	203
5.4.	CYTOTOXIC EFFECT.....	205
5.5.	IN VIVO BIODISTRIBUTION.....	208
5.6.	CONCLUSION.....	210
6.	OPTICAL IMAGING DEVICES.....	212
6.1.	SYNTHESIS.....	214
6.2.	RADIOSYNTHESIS.....	215
6.3.	IN VITRO EVALUATION AND HYDROPHILICITY.....	216
6.4.	IN VIVO BIODISTRIBUTION.....	218
6.5.	FLUORESCENCE IMAGING.....	221
6.6.	CONCLUSION.....	223
IV.	SUMMARY AND CONCLUSION.....	225
V.	REFERENCES.....	231
VI.	APPENDIX.....	249
1.	ADDITIONAL DATA.....	249
2.	LIST OF ABBREVIATIONS.....	254
3.	FIGURE INDEX.....	256
4.	TABLE INDEX.....	263
5.	SCHEME INDEX.....	265
6.	SUPPLEMENTARY INDEX.....	267

ABSTRACT

During the last decade, the G-protein coupled receptor CXCR4 has emerged as a valuable target for molecular imaging in cancer and in inflammatory conditions, and CXCR4-targeted peptide-receptor radionuclide therapy (PRRT) has shown first promising results in hematological cancers. Amongst the broad spectrum of CXCR4-targeted imaging agents that have been evaluated preclinically, only the PET ligand [⁶⁸Ga]Pentixafor (*cyclo*(-D-Tyr-D-MeOrn(Ambz-DOTA[⁶⁸Ga])-Arg-2-Nal-Gly-)) and its therapeutic analog [¹⁷⁷Lu]Pentixather (*cyclo*(-D-I-Tyr-D-MeOrn(Ambz-DOTA[¹⁷⁷Lu])-Arg-2-Nal-Gly-)) – both of which have been developed at the Technical University of Munich (TUM) – have entered clinical trials to date. By introducing an extended, tailor-made linker between the *CPCR4* (*cyclo*(-D-Tyr-D-MeOrn-Arg-2-Nal-Gly-)) peptide scaffold and the signaling unit at the *N*-terminus of the linker, Osl et al. obtained analogs of Pentixafor/Pentixather with improved receptor affinity that offered flexibility towards the *N*-terminal functionalization with more versatile labeling modalities. The objective of this work was to further exploit the initial approach of optimizing the linker unit such as to provide even greater flexibility of the *CPCR4*-linker construct towards modification with a broad spectrum of functionalities. These efforts were aimed at providing improved next-generation ligands based on the original [⁶⁸Ga]Pentixafor and [¹⁷⁷Lu]Pentixather design (CXCR4-DOTA series), ligands amenable for fluorine-18 labeling (CXCR4-SiFA series) as well as technetium-99m labeling (CXCR4-Tc series), ligands suitable for fluorescence imaging (CXCR4-OI series) and peptide-drug conjugates (PDCs) (CXCR4-MMAE series) carrying a cytotoxic payload.

CXCR4-targeted ligands were prepared *via* solid-phase and in-solution synthesis alongside with RP-HPLC-assisted purification and quality control. The ligands consist of the cyclic pentapeptide *CPCR4*, extended at its D-MeOrn side chain with a peptide linker and a terminal signaling unit such as a chelator. Determination of the ligands CXCR4 affinities (IC₅₀) was undertaken using Jurkat lymphoma cells in competitive binding assays with the radioligand ¹²⁵I-FC-131 (*cyclo*(-[¹²⁵I]D-Tyr-Arg-Arg-2-Nal-Gly-)). The internalization rates of the respective radiolabeled ligands into CXCR4 expressing Chem-1 cells were assessed in dual-tracer experiments using ¹²⁵I-FC-131 as an internal standard and the lipophilicity (logD_{7.4}) was examined using the shake-flask method. The investigation of pharmacokinetic profiles was performed by *in vivo*

μ SPECT imaging and *in vivo* biodistribution and fluorescence imaging studies using Jurkat tumor-bearing CB-17 SCID mice.

Initial peptide screening experiments provided CXCR4-Tc-06, bearing an IC₅₀ of 4.97 ± 1.34 nM and with that, a 5-fold higher CXCR4 affinity compared to [⁶⁸Ga]Pentixafor. This ligand, more precisely its optimized tracer backbone *CPCR4-Abz-a-r-dap* (*cyclo*(-D-Tyr-D-MeOrn(-Abz-D-Ala-D-Arg-D-Dap-NH₂)-Arg-2-Nal-Gly-)) was then used as the structural basis for the development of further ligands and was found to offer the desired flexibility towards the attachment of functional moieties.

In the first project within this work, a technetium-99m-labeled CXCR4 ligand was prepared, [^{99m}Tc]CXCR4-Tc-13, revealing almost quantitative labeling yields and a reliable labeling procedure, a more than 5-fold increased CXCR4 affinity compared to [⁶⁸Ga]Pentixafor and high tumor uptake *in vivo*. This compound was chosen as the candidate for a first application in men as part of an ongoing cooperation with the *Universitätsklinikum Augsburg*.

In the second part of this work, [^{nat}Ga/^{nat}Lu]CXCR4-DOTA-03 was prepared, exhibiting 15-fold and 12-fold higher CXCR4 affinities compared to [⁶⁸Ga]Pentixafor and [¹⁷⁷Lu]Pentixather, respectively, alongside with enhanced hydrophilicity. *In vivo*, [¹⁷⁷Lu]CXCR4-DOTA-03 displayed favorable tumor/organ ratios compared to [¹⁷⁷Lu]Pentixather and comparable ratios to [⁶⁸Ga]Pentixafor at 1h after injection. The ligand was further tested at 6 and 48 hours after injection and showed substantially higher amounts of tumor deposited activity compared to [¹⁷⁷Lu]Pentixather.

In the third part of this work, a radiohybrid ligand, CXCR4-SiFA-07, bearing both a silicon-fluoride acceptor (SiFA) moiety that enables efficient labeling with fluorine-18 *via* isotopic exchange reaction and a DOTA chelator to enable radiometal complexation was synthesized. [¹⁸F,^{nat}Ga]CXCR4-SiFA-07 exhibited exceptional CXCR4 affinity and suitable hydrophilicity (IC₅₀: 6.23 ± 1.57 nM; logD_{7.4}: -1.95 ± 0.05). *In vivo*, however, [¹⁸F,^{nat}Ga]CXCR4-SiFA-07 displayed elevated ligand uptake in mCXCR4 expressing organs such as lung, liver and spleen, thus prohibiting efficient tumor targeting.

The pronounced internalization of the compounds developed within this work triggered the design of PDCs. Targeted ligands were conjugated with a monomethyl auristatin-E (MMAE) derivative, bearing an additional linker that is specifically cleaved by

intracellular Cathepsin B. Our collaborators from the group of Prof. Dr. med. Keller examined CXCR4-MMAE-02 regarding its *in vitro* potential as a targeted chemotherapeutic drug. They revealed considerably elevated fractions of dead cancer cells upon incubation with the PDC due to arrest of the cells in the G2/M-phase prior to cell division. However, in a biodistribution experiment employing [¹²⁵I]CXCR4-MMAE-02, high off-target binding of the lipophilic radioligand prohibited efficient tumor targeting. A bimodal ligand, [¹⁷⁷Lu]CXCR4-MMAE-04, bearing both toxin and a chelator, provided enhanced hydrophilicity.

In the last project within this work, the Cy5.5 dye was utilized to obtain CXCR4-targeted fluorescent probes. CXCR4 affinities in the low nanomolar range and logD_{7.4} values below -1.5 were obtained for CXCR4-OI-01 and [¹²⁵I]CXCR4-OI-02. *In vivo* fluorescence imaging of organ slices and biodistribution studies revealed CXCR4 specific uptake in spleen and liver tissue. The bimodal ligand CXCR4-OI-03, additionally carrying a DOTA chelator, may provide a suitable basis for a fluorescence- and radio-guided surgery approach.

In summary, the iterative step-by-step optimization of the linker unit in Pentixafor/Pentixather-based tracers has yielded a novel scaffold that provides unprecedented flexibility towards functionalization of the targeting vector with a variety of even sterically demanding functionalities. Most of the compounds presented within this work displayed improved *in vitro* characteristics, and first *in vivo* biodistribution and imaging experiments demonstrate the great potential of the novel tracer design as a structural basis for the development of CXCR4-targeted imaging probes for diverse applications. However, the mechanism responsible for uptake in mCXCR4 expressing organs must be further elucidated to ensure the validity and translatability of mouse biodistribution data to the human situation. As demonstrated in a first-in-man study and in clear contrast to the mouse data obtained during the preclinical evaluation, the technetium tracer [^{99m}Tc]CXCR4-Tc-13 did not show elevated uptake in human liver or lung. This finding strongly encourages future clinical translation of other promising compounds obtained within the framework of this work.

KURZZUSAMMENFASSUNG

Während des letzten Jahrzehnts hat sich der G-Protein gekoppelte Rezeptor CXCR4 als wertvolles Target für die molekulare Bildgebung von Krebs und entzündlichen Erkrankungen hervorgetan und erste vielversprechende Ergebnisse in der CXCR4-gerichteten Peptid-Rezeptor Radionuklid Therapie (PRRT) hämatologischer Krebsarten wurden erhalten. Von dem breiten Spektrum CXCR4-gerichteter Bildgebungsagentien, die präklinisch evaluiert wurden, haben bisher nur der PET Ligand [⁶⁸Ga]Pentixafor (*cyclo*(-D-Tyr-D-MeOrn(Ambz-DOTA[⁶⁸Ga])-Arg-2-Nal-Gly-)) und sein therapeutisches Analogon [¹⁷⁷Lu]Pentixather (*cyclo*(-D-I-Tyr-D-MeOrn(Ambz-DOTA[¹⁷⁷Lu])-Arg-2-Nal-Gly-)) – welche beide an der Technischen Universität München (TUM) entwickelt wurden – klinische Studien erreicht. Durch die Verwendung eines verlängerten, maßgeschneiderten Linkers zwischen dem *CPCR4* ((*cyclo*(-D-Tyr-D-MeOrn-Arg-2-Nal-Gly-)) Peptidgerüst und der Signaleinheit am *N*-Terminus des Linkers, haben Osl et al. Analoga von Pentixafor/Pentixather mit verbesserter CXCR4 Affinität erhalten, die Flexibilität gegenüber der *N*-terminalen Funktionalisierung mit unterschiedlichen Markierungsmodalitäten aufweisen. Das Ziel der vorliegenden Arbeit war es, die Linker Einheit weiter zu optimieren, um noch größere Flexibilität des *CPCR4*-Linker Konstrukts gegenüber Modifikation mit einem breiten Spektrum an Funktionalitäten zu erreichen. Ein weiteres Ziel war die Herstellung einer neuen Generation von Liganden basierend auf dem Design von [⁶⁸Ga]Pentixafor und [¹⁷⁷Lu]Pentixather (CXCR4-DOTA Serie), Liganden, die mit Fluor-18 (CXCR4-SiFA Serie) oder Technetium-99m (CXCR4-Tc Serie) markiert werden können, Fluoreszenzliganden (CXCR4-OI Serie) und Peptid-Wirkstoff Konjugaten (CXCR4-MMAE Serie), die ein Zytotoxin tragen.

CXCR4-gerichtete Peptide wurden durch eine Kombination von Festphasen- und Lösungssynthese hergestellt, RP-HPLC-unterstützt aufgereinigt und qualifiziert. Die Liganden beinhalten das zyklische Pentapeptid *CPCR4*, erweitert an seiner D-MeOrn Seitenkette mit einem peptidischen Linker und einer terminalen Signaleinheit, beispielsweise einem Chelator. Jurkat Lymphomzellen und der Radioligand ¹²⁵I-FC-131 (*cyclo*(-[¹²⁵I]D-Tyr-Arg-Arg-2-Nal-Gly-)) wurden in kompetitiven Bindungsstudien eingesetzt, um die CXCR4 Affinität (IC₅₀) der neuen Liganden zu bestimmen. Die Internalisierungsraten der entsprechenden radiomarkierten

Verbindungen in Chem-1 Zellen wurden in Dual-Tracer Experimenten mit ^{125}I -FC-131 als internem Standard durchgeführt und die Lipophilie ($\log D_{7.4}$) durch die Shake Flask Methode bestimmt. Die Pharmakokinetik neuer Verbindungen wurde durch *in vivo* μSPECT Bildgebung, sowie *in vivo* Biodistributionen und Fluoreszenzimagining von Jurkat Tumor-tragenden CB-17 SCID Mäusen, untersucht.

Peptid Screening-Experimente zu Beginn der Arbeit brachten CXCR4-Tc-06 hervor, das mit einem IC_{50} von 4.97 ± 1.34 nm eine 5-fache höhere CXCR4 Affinität als ^{68}Ga]Pentixafor aufweist. Diese Verbindung, speziell ihr optimiertes Peptidgerüst *CPCR4-Abz-a-r-dap* (*cyclo*(-D-Tyr-D-MeOrn(-Abz-D-Ala-D-Arg-D-Dap-NH₂)-Arg-2-Nal-Gly-)) wurde als Startpunkt für die Entwicklung weiterer Liganden benutzt, da es die gewünschte Flexibilität gegenüber der Modifikation mit funktionellen Einheiten besitzt.

Im ersten Projekt innerhalb der vorliegenden Arbeit wurde ein Technetium-99m markierter CXCR4 Ligand, $^{99\text{m}}\text{Tc}$]CXCR4-Tc-13 hergestellt, der in einem verlässlichen Radiomarkierungsprozess nahezu quantitative Ausbeuten aufweist, eine mehr als 5-fach erhöhte Rezeptor Affinität im Vergleich zu ^{68}Ga]Pentixafor und hohen Tumor Uptake *in vivo* zeigt. Diese Verbindung wurde als Kandidat für eine erste Anwendung im Patienten ausgewählt als Teil einer Kooperation mit dem *Universitätsklinikum Augsburg*.

Im zweiten Teil dieser Arbeit wurde der Ligand $^{nat}\text{Ga}/^{nat}\text{Lu}$]CXCR4-DOTA-03 hergestellt, der 15-fache beziehungsweise 12-fache CXCR4 Affinität im Vergleich zu ^{68}Ga]Pentixafor und ^{177}Lu]Pentixather und gesteigerte Hydrophilie besitzt. Eine Stunde nach Injektion zeigte ^{177}Lu]CXCR4-DOTA-03 bessere Tumor/Organ Verhältnisse als ^{177}Lu]Pentixather und vergleichbare Werte mit ^{68}Ga]Pentixafor. Der Ligand wurde zudem 6 und 48 Stunden nach Injektion untersucht und konnte eine gesteigerte Tumor-deponierte Aktivität im Vergleich zu ^{177}Lu]Pentixather aufweisen.

Im dritten Teil dieser Arbeit wurde der Radiohybridligand CXCR4-SiFA-07 entwickelt, der sowohl eine Silizium-Fluorid Akzeptor (SiFA) Einheit zur effizienten Radiomarkierung mit Fluor-18 *via* Isotopenaustausch trägt, als auch einen DOTA Chelator zur Komplexierung mit Radiometallen. $^{18}\text{F},^{nat}\text{Ga}$]CXCR4-SiFA-07 besitzt herausragende CXCR4 Affinität und eine geeignete Hydrophilie (IC_{50} : 6.23 ± 1.57 nm; $\log D_{7.4}$: -1.95 ± 0.05). *In vivo* zeigte $^{18}\text{F},^{nat}\text{Ga}$]CXCR4-SiFA-07 erhöhten Ligand

Uptake in mCXCR4 exprimierende Organe Lunge, Leber und Milz, was eine effizientes Tumor Targeting verhinderte.

Die ausgeprägte Internalisierung der Verbindungen, die in dieser Arbeit entwickelt wurden, ermöglichte das Design von Peptid-Wirkstoff Konjugaten. Zielgerichtete Liganden wurden mit einem Monomethyl Auristatin-E (MMAE) Derivat verknüpft, das einen zusätzlichen Linker trägt, der spezifisch von intrazellulärem Cathepsin B gespalten wird. Unsere Kooperationspartner aus der Gruppe von Prof. Dr. Keller untersuchten CXCR4-MMAE-02 hinsichtlich seines *in vitro* Potentials als Chemotherapeutikum. Sie entdeckten eine erhöhte Anzahl toter Krebszellen nach Inkubation mit dem Konjugat aufgrund des Arrests der Krebszellen in der G2/M Phase vor deren Replikation. In einem Biodistributionsexperiment zeigte [¹²⁵I]CXCR4-MMAE-02 geringe Tumoraufnahme aufgrund seiner hohen Lipophilie. Der bimodale Ligand [¹⁷⁷Lu]CXCR4-MMAE-04, der sowohl Toxin als auch einen Chelator trägt, zeigte deutlich erhöhte Hydrophilie.

In einem letzten Projekt wurde das Farbstoffmolekül Cy5.5 dafür benutzt, CXCR4-spezifische Fluoreszenzliganden herzustellen. Affinitäten im niedrigen nanomolaren Bereich und logD_{7.4}-Werte unterhalb von -1.5 wurden so für die beiden Verbindungen CXCR4-OI-01 und [¹²⁵I]CXCR4-OI-02 erreicht. *In vivo* Fluoreszenzbildgebung von Organschnitten und Biodistributionsstudien zeigten CXCR4-spezifischen Uptake in Milz- und Lebergewebe. Der bimodale Ligand CXCR4-OI-03, der zusätzlich einen Chelator trägt, könnte für die Anwendung in der Fluoreszenz- und Radiologie-gestützten operativen Behandlung eine vielversprechende Verbindung darstellen.

Die iterative Schritt-für-Schritt Optimierung des Linkers in Pentixafor/Pentixather-basierten Tracern hat ein neues Peptidgerüst ergeben, das die Funktionalisierung des Targeting-Vektors mit einer Reihe selbst sterisch anspruchsvoller Funktionalitäten erlaubt. Die meisten Verbindungen, die in dieser Arbeit entwickelt wurden, zeigten verbesserte *in vitro* Eigenschaften und erste *in vivo* Biodistributions- und Bildgebungsexperimente belegten großes Potential des neuen Tracer Designs als strukturelle Basis für die Entwicklung vielfältiger, CXCR4-gerichteter Bildgebungsagentien. Der Mechanismus, der für den Uptake in mCXCR4 exprimierende Organe verantwortlich ist, muss weiter aufgedeckt werden, um die Validität von Biodistributionen in der Maus und die Übertragbarkeit auf den Menschen gewährleisten zu können. Wie jedoch in einer ersten Patientenstudie bestätigt, zeigt

der Technetium Tracer [^{99m}Tc]CXCR4-Tc-13 keinen erhöhten Uptake in menschliche Leber oder Lunge. Dieser Umstand bekräftigt die mögliche klinische Translation anderer, vielversprechender Verbindungen, die in dieser Arbeit entwickelt wurden.

I. INTRODUCTION

1. Cancer

In 2020, about 19.3 million new cases of cancer were registered worldwide and circa 10 million people died from cancer, making it the most prominent cause of premature deaths in the so-called “developed” countries (Figure 1) (1).

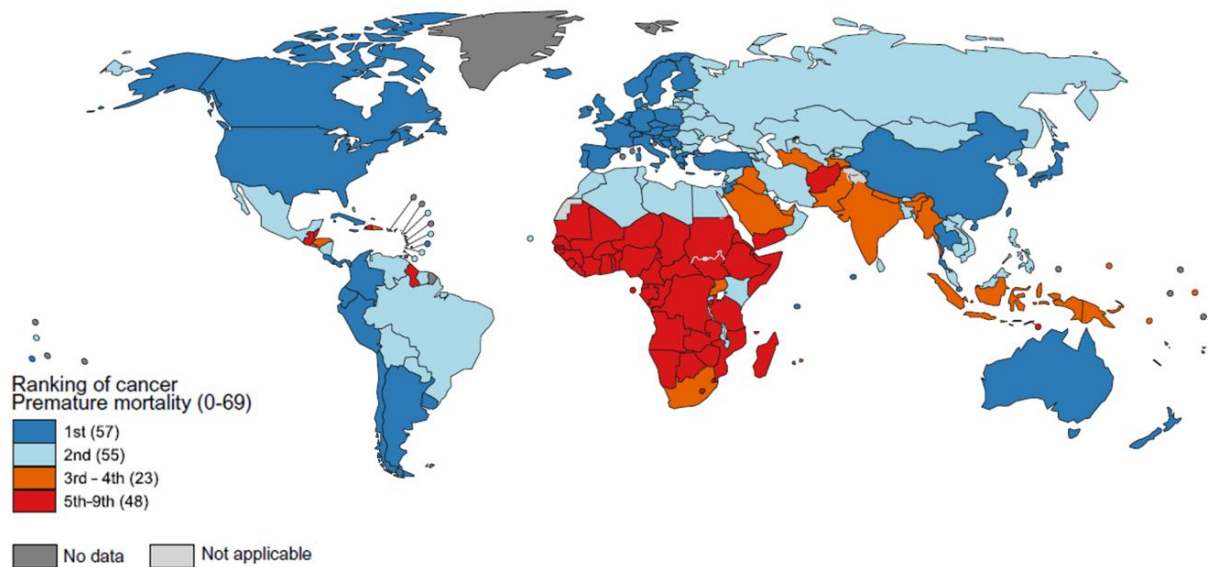


Figure 1: Ranking of cancer-associated premature mortality worldwide; figure adapted from literature (1).

Most cancer associated deaths arise from malignant tissue of the lung and colorectum, the prostate in men and the breast in women. Even though the cancer survival rate has increased since the 1970s, the overall five-year survival rate does not exceed 67% in the USA. Lowest survival rates are found for pancreas (10%), liver (20%), esophagus (20%) and lung (21%) cancer (2). Most of the cancer patients die due to metastasis of the primary lesion or cardiovascular intricacies resulting from the disease itself or the treatment (3). This circumstance calls for an early detection of the tumor prior to metastasis and furthermore a more targeted approach concerning the treatment.

2. Molecular Imaging of Cancer

An early diagnosis of cancer is pivotal for a positive patient treatment perspective. However, if not randomly detected during a routine visit at a doctor's office and screening experiments such as mammography or PSA testing, cancer is usually attested after first symptoms are perceived or, coming along with drastically decreased chances of survival, even later (4–6). In a multitude of cases, changes in the subjects blood samples indicate an underlying cancerous disease that, in the case of solid tumors, is usually confirmed by resonance imaging with computed tomography (CT), magnetic resonance imaging (MRI) or ultrasound (US) and typified by means of biopsy (7–10). CT or MRI, capable of delineating the tumors morphology, are complemented by molecular imaging methods positron emission tomography (PET) and single-photon emission tomography (SPECT), providing information about the tumor on a cellular level, tumor entity, nutrient uptake or the microenvironment (11–13).

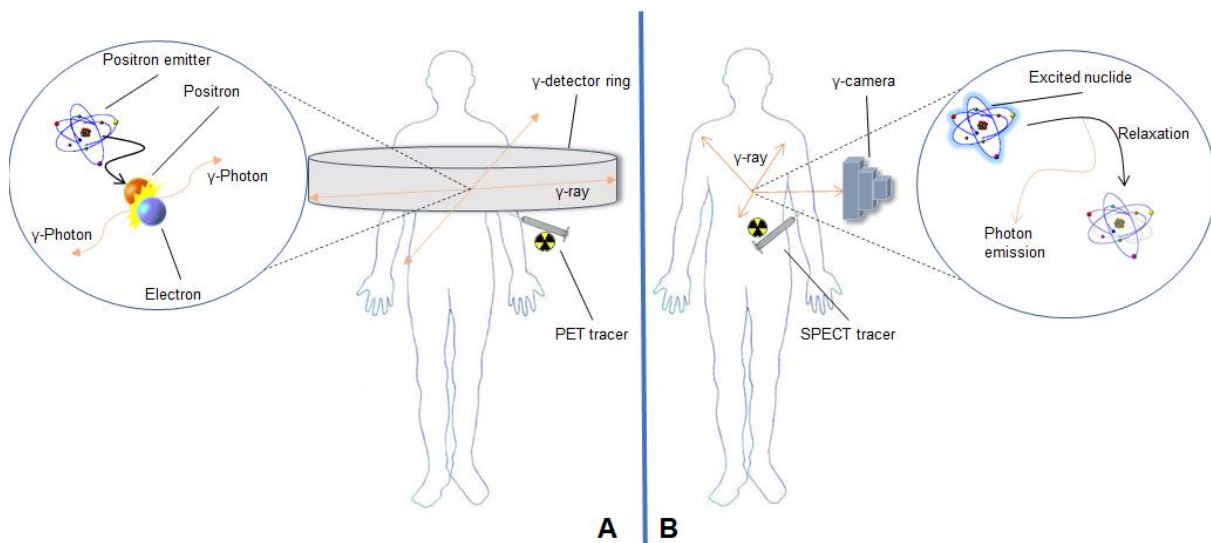


Figure 2: The principles of PET and SPECT imaging: **A**: schematic representation of i.v. PET tracer application and γ -photon coincidence detection by a γ -detector ring; positron emission and annihilation by collision with an electron under emission of two γ -photons in opposite direction (encircled), **B**: schematic representation of i.v. SPECT tracer application and γ -photon detection by a rotating γ -camera; relaxation of an excited radionuclide under emission of a γ -photon (encircled).

Figure 2 visualizes the principles of PET and SPECT imaging using γ -detectors (14). SPECT scanners are substantially cheaper compared to PET and display more widespread availability, independent from university centers. Furthermore, typical SPECT isotopes such as Tc-99m or Ga-67 generally exhibit longer half-lives, making them more suitable for the examination of lengthy biological processes and qualifying

them for a larger distribution range (15). Since their introduction to the market in 2000, SPECT/CT hybrid scanners have further unfolded the potential of SPECT imaging in clinical facilities and private practices all around the globe (16,17).

When a PET nuclide such as F-18 or Ga-68 decays, it emits a positron that migrates through tissue and loses its kinetic energy upon collisions with particles until it has lost its entire kinetic energy (thermalization). Subsequently, the positron is annihilated by collision with an electron, which leads to the emission of two gamma rays of 511 keV in an 180° angle. The average migration pathway of a positron in tissue is dependent on the particles energy and specifying the maximum resolution of PET images that is obtainable using this isotope. Upon annihilation with an electron, two identical photons bearing 511 keV energy each are sent out in a near 180° angle along the so-called line of response (18). The first PET/CT hybrid scanner was introduced into the market in 2001. More recently, PET/MRI hybrid systems were introduced that provide high spatial resolution anatomic images with high contrast in soft tissues without additional radiation dosage to the patient. Despite the technical challenges of simultaneous PET and MRI image acquisition, great clinical impact is provided by these systems (19,20). Apart from nuclear imaging techniques PET/SPECT and anatomical imaging by CT/MRI, fluorescence imaging represents another molecular imaging approach. This technique relies on the systemic application of a targeted fluorophore, its subsequent excitation in the body and detection of relaxation photons. Fluorescence imaging provides images with high sensitivity, excellent spatial and temporal resolution. However, *in vivo*, light scattering, autofluorescence and attenuation of light by hemoglobin absorption leads to exponential light decay in tissue and therefore limited penetration depths (21,22). The application of fluorophores that are excited by light with a wavelength between 750 and 900 nm, so-called near-infrared (NIR) fluorophores bears high potential, as tissue absorption of NIR light is significantly lower and thus, penetration depths of a few centimeters can be reached (22,23). Most of the applications of *in vivo* fluorescence imaging so far are limited to pre-clinical small animal imaging or surgical guidance. Hybrid approaches utilizing MRI/CT or PET/SPECT together with NIR imaging are discussed as promising development of *in vivo* fluorescence imaging, potentially providing detailed information by synergy of molecular imaging techniques (24–28).

3. Therapy of Cancer

The treatment of cancer is traditionally built on measures that aim towards the removal or elimination of cancer cells from the body (Figure 3):

- Surgery,
- local radiation exposure and
- systemic treatment with drugs.

The first line of cancer treatment for any solid tumor remains surgery (29,30). Local radiation therapy is widely used to either destroy remaining cancer cells after surgery or to shrink the tumor and cause better differentiation from the surrounding benign

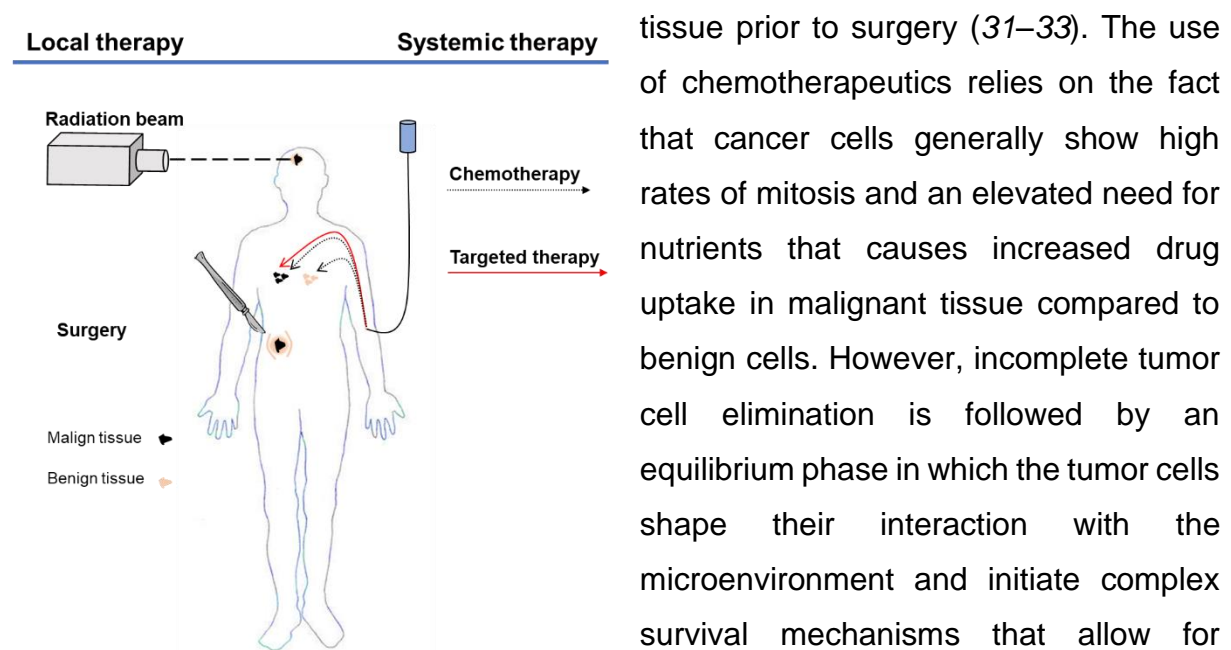


Figure 3: Schematic representation of local cancer therapy by radiation beam exposure and surgery (left side); systemic chemotherapy using an unselective approach (dotted arrow) damaging both malign and benign tissue and targeted therapy (red arrow) that ideally damages only malign tissue (right side).

tissue prior to surgery (31–33). The use of chemotherapeutics relies on the fact that cancer cells generally show high rates of mitosis and an elevated need for nutrients that causes increased drug uptake in malignant tissue compared to benign cells. However, incomplete tumor cell elimination is followed by an equilibrium phase in which the tumor cells shape their interaction with the microenvironment and initiate complex survival mechanisms that allow for immune evasion and drug resistance (30,34). Side effects of the treatment are prevalent and sometimes outweighing the therapeutic benefit for the patients (35).

Deeper understanding of tumor phenotypes has led to the discovery of cancer associated molecular targets and to the development of therapeutics specifically designed to interact with these targets. This approach provides substantially increased specificity for tumor cells and is therefore termed highly promising concerning increased treatment efficacy and less pronounced adverse effects (36). Small molecules, peptides, antibodies, or antibody fragments are biochemically engineered to provide efficient targeting and suitable pharmacokinetic

profiles. Numerous molecular targets were identified throughout the years and today, a large number of targeted probes is available for the specific treatment of various tumor phenotypes (37–39).

One particular aspect of targeted therapy, PRRT, has been an emerging market throughout the last decade. Radioisotope-labeled peptides such as PSMA-targeted [¹⁷⁷Lu]PSMA-617 or sstr2-targeted [¹⁷⁷Lu]-octreotate were licensed by companies such as Novartis in billion-dollar contracts (40). Hence, significant efforts are made to develop novel targeted peptides, antibodies and antibody fragments, all based on the same principle: delivery of a therapeutic radioisotope such as Lu-177 or Y-90 *via* a target-specific vector. This type of therapy has proven to provide therapeutic efficacy with low off-target toxicity (41–43). Therapeutic effects are prevalently observed after a minimum number of injections whereas prevalent chemotherapy usually requires recurrent application. Moreover, the detection of the radioactivity allows for mathematical estimation of organ dose prior and during therapy (44).

Apart from the choice of radiometal, the suitability of the vector and the respective molecular target are pivotal aspects to be considered. The first radiolabeled therapeutic peptide to gain market approval was the aforementioned sstr2-targeted [¹⁷⁷Lu]-octreotate (45). The somatostatin receptors (sstr1–sstr5) belong to the family of G-protein coupled receptors, and of these, sstr2 is known to be highly overexpressed on a number of cancer cells and it is therefore an appropriate target for nuclear imaging and PRRT (46,47).

4. Chemokines and Chemokine Receptors

4.1. The Chemokine Family

Chemokines are chemotactic cytokines, small messenger proteins that control the migration and venue of cells, especially immune cells (48). According to the position of *N*-terminal cysteine (C) residues in their structures, chemokines and their receptors (R) are subdivided into four families:

- CXC(R), bearing one amino acid between the cysteines,
- CX3C(R), bearing three amino acids between the cysteines,
- CC(R), bearing two neighboring cysteines and
- C(R), bearing one cysteine (49).

Until today, 47 chemokines and 20 chemokine receptors were identified in humans (50). Receptors that are capable of binding chemokines belong to the class of G-protein-coupled receptors (GPCR). They are the largest family of membrane proteins and mediate the majority of cellular responses to hormones and neurotransmitters (51). A shared structural feature of all GPCR are their seven transmembrane α -helices. Upon ligand binding from the extracellular side, structural transformation in the helices is induced, leading to the release of intracellularly attached heterotrimeric G-proteins and activation of downstream signaling (52). A multitude of cellular signaling pathways is directly influenced by the interplay between chemokines and their receptors and pivotal biological processes are being regulated (53,54).

4.2. CXCL12 and CXCR4

The stromal cell-derived factor-1 (SDF-1 or CXCL12) is an 89-amino acid (in its major occurring α -form) chemokine whose activity is tightly regulated by a number of determining factors. A variety of organs are known to express CXCL12, namely lung, lymph nodes, heart, thymus and liver. Moreover, CXCL12 is the most abundant chemokine in the bone marrow (55). Early knock-out experiments in mice revealed not only the substantial influence of CXCL12 on processes like embryonic hematopoiesis and neurogenesis, but further revealed its endogenous receptor CXCR4 (56–59).

Under physiological conditions, the interplay between CXCR4 and CXCL12 regulates a great number of cellular processes such as hematopoiesis, vascular development, lymphoid organ morphogenesis, cardiogenesis, neural differentiation and cell trafficking from bone marrow to blood circulation and lymph to lymphoid (55). All of these processes, pivotal for the viability of an animal, are controlled by signaling pathways initiated by the release of the G-proteins upon CXCL12 binding as depicted in Figure 4.

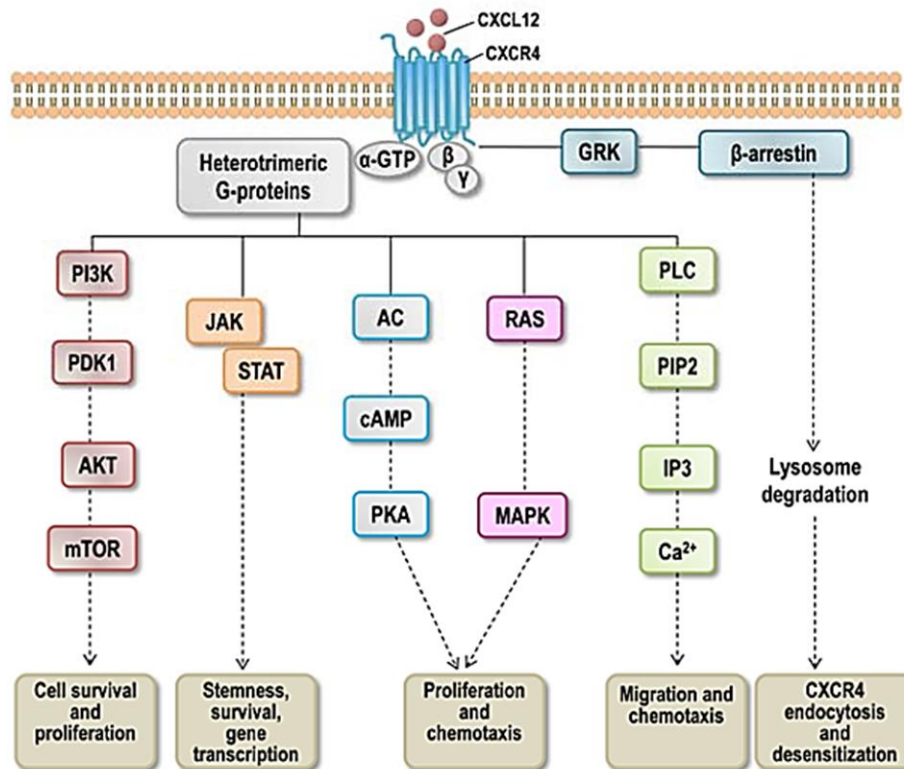


Figure 4: Downstream signaling pathways initiated by CXCL12 binding onto CXCR4 and the subsequent release of intracellularly attached heterotrimeric G-proteins; The activity of the receptor is then regulated by recruitment of β-arrestin and the concomitant internalization of the CXCL12/CXCR4 complex; figure adapted from literature (55).

When CXCR4 is activated, β-arrestin is recruited, managing the endocytosis and lysosomal degradation of the receptor in order to desensitize and regulate cellular signaling (60). The relationship between CXCR4 and CXCL12 was long believed to be monogamous, however more proteins were detected which can interact with CXCR4. Among others, the atypical chemokine macrophage migration inhibitory factor (MIF) and extracellular Ubiquitin, an 8.6 kDa regulatory protein, were identified as ligands for the CXCR4 receptor and potentially modulate the response of the receptor to CXCL12 activation (61–63). Noteworthy, another G-protein coupled receptor capable of binding CXCL12 was found: CXCR7, which was later renamed to ACKR3 (atypical chemokine receptor 3) because it acts as a scavenger for the ligand without activation of

downstream signaling (64). The crosstalk of both receptors, CXCR4 and ACKR3, has been shown to have significant impact on signaling under both, physiological and pathological circumstances (60,65).

4.3. CXCL12 and CXCR4 in Inflammation and Cancer

Feng et al. reported on the role of CXCR4 as a co-receptor for the HI-virus entry into T-cells (66). Since then, CXCR4 and its endogenous ligand CXCL12 have gained attention as pathological markers in autoimmune diseases like multiple sclerosis, rheumatoid arthritis and lupus, and cardiovascular diseases (67–70). The CXCR4/CXCL12 axis plays a pivotal role in maintaining tissue homeostasis. Cancer, described by Dvorak as a “wound that refuses to heal”, represents a chronic damage of tissue (71). CXCR4 overexpression was confirmed in more than 20 different cancer types, particularly cancers arising from the hematological system such as leukemia and multiple myeloma but also solid cancers arising from breast, prostate, the ovaries, lung, the gastrointestinal system, kidneys, skin and soft tissues (Table 1) (55,72–80).

Table 1: Cancer types arising from cells of the hematopoietic system, brain, gastrointestinal system and miscellaneous tissues that reportedly overexpress the CXCR4 receptor; table was adapted from literature (81) and modified.

Hematopoietic system	
Multiple myeloma	Acute lymphoblastic leukemia
B-cell, T-cell and non-Hodgkin lymphoma	Acute myelogenous leukemia Chronic lymphocytic leukemia
Brain	
Glioma	Neuroblastoma
Glioblastoma	Medullablastoma
Gastrointestinal system	
Pancreatic cancer	Gastric and stomach cancer
Colorectal cancer	Esophageal cancer
Hepatocellular cancer	
Miscellaneous tissues	
Melanoma	Prostate cancer
Soft tissue sarcoma	Ovarian cancer
Chondrosarcoma	Breast cancer
Small-cell lung cancer	Renal cell cancer
Non-small-cell lung cancer	Thyroid cancer
Nasopharyngeal cancer	

Various tumors produce and distribute CXCL12 to attract CXCR4 expressing immune cells (82). These immune cells and other cells in the microenvironment such as fibroblasts and endothelial cells respond to elevated concentrations of chemokine by induction of proliferation processes like angiogenesis, structural support and growth (73,83,84). The cancer cells themselves are overexpressing the CXCR4 receptor as an answer to high amounts of stimulating proteins such as Vascular Endothelial Growth Factor (VEGF) and Epidermal Growth Factor (EGF), the hypoxia inducible factor-1 α and transcription factors such as the nuclear respiratory factor-1 that are secreted by cells in the tumor microenvironment (73). The CXCR4/CXCL12 axis is influencing the microenvironment of tumor lesions and establishes a crosstalk of cells (and stem cells) that is overall beneficial for tumor cell survival, invasion and resistance to therapy.

Different studies based on cancer patient screenings indicate a negative correlation of survival prognosis with high CXCR4 expression (70,82,84,85). This circumstance is mainly based on the strong metastatic potential of highly CXCR4 overexpressing tumors. When a mismatch between CXCL12 concentration and CXCR4 expression in the tumor lesions occurs, tumor cells are prone to migrate towards organs, known to bear elevated concentrations of CXCL12, such as lung, liver, bone marrow or lymph nodes (83). In the case of hematological cancers like leukemia, multiple myeloma and lymphoma, migration of CXCR4 overexpressing cancer cells to niches of high CXCL12 expression mimics the homing of normal stem cells to the bone marrow, however in this case, with detrimental consequences (Figure 5) (84).

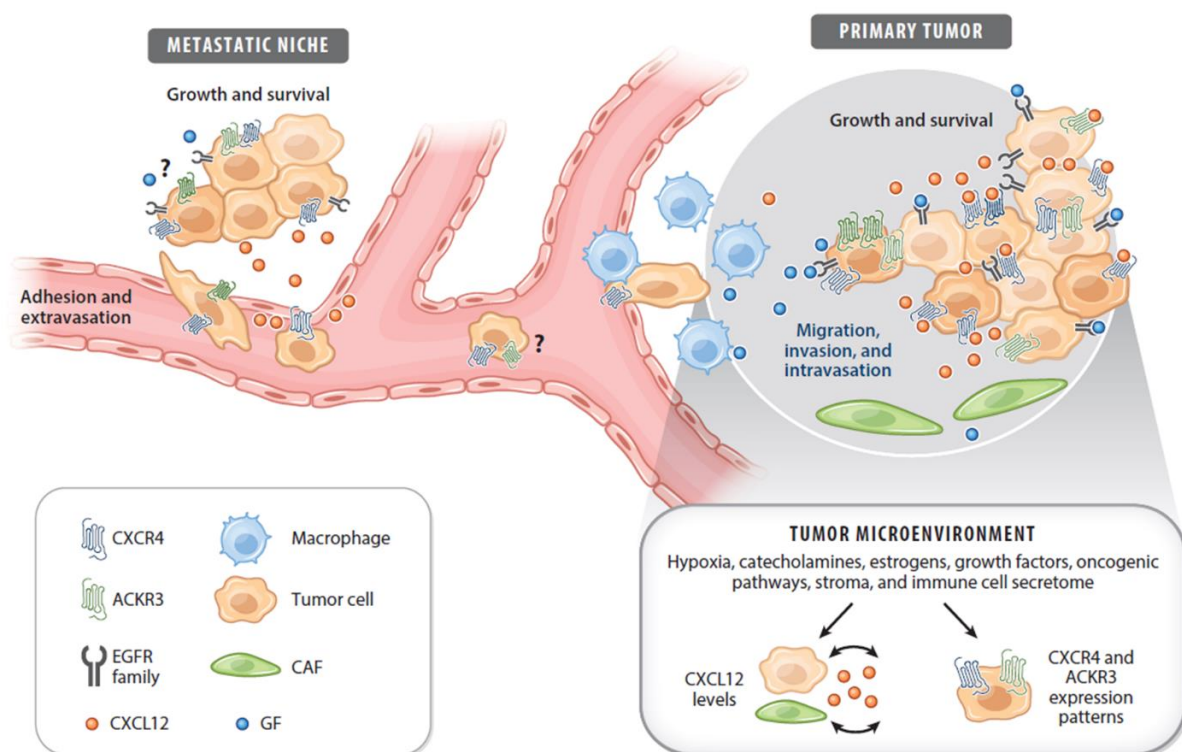


Figure 5: The role of the CXCR4/CXCL12/ACKR3 axis in tumor proliferation and metastasis: crosstalk of CXCR4 expressing cancer cells in the primary lesion with the microenvironment such as cancer-associated fibroblasts (CAF) regulates tumor growth and survival until a mismatch occurs that drives the targeted metastasis into CXCL12 expressing niches such as lung, liver, lymph nodes and bone marrow; the role of ACKR3 during tumor metastasis remains uncertain; figure adapted from literature (60).

The role of ACKR3 in CXCR4 mediated tumor metastasis remains, in large parts, uncertain. However, as described earlier, its co-expression together with CXCR4 is a crucial mediating factor for cell signaling and its involvement in tumor progression and metastasis is therefore more than speculative.

5. Molecular Imaging and Therapy of CXCR4-expressing Cancer

Based on the above-described importance of the CXCR4/CXCL12 axis in the development and progression of cancer, several groups engaged in the development of CXCR4 targeted compounds suitable for an application in molecular imaging and therapy. The following chapter will provide an overview of the strategies employed so far. Ligand development started out in the early 1990s when a screening experiment for substances capable of blocking HIV cell entry, provided a potent inhibitor molecule. Only later it was discovered that this inhibitor binds CXCR4 and the role of CXCR4 as a co-receptor for the virus entry was then identified in 1996 (66). Since then, a multitude of ligands for the CXCR4 receptor were developed that can be classified into four groups:

- Modified CXCL12 and fragments thereof,
- small-molecule ligands,
- antibodies against CXCR4 and
- peptide ligands based on horseshoe crab toxins (86).

Even though large numbers of CXCR4-targeted radioligands have been developed, only a few examples for a clinical application are reported thus far.

5.1. [⁶⁴Cu]AMD3100

The bi-cyclam AMD3100 proved to inhibit HIV-1 and HIV-2 strains by blocking of the CXCR4 receptor. Gerlach and coworkers utilized the affinity of the cyclam moieties for metal ions and discovered that the CXCR4 affinity of AMD3100 increases 7-fold upon complexation with Cu²⁺ (87). In preclinical studies, [⁶⁴Cu]AMD3100 exhibited slow background clearance and high off-target binding (88–90). A clinical imaging study in cancer patients was terminated after treatment of two participants (NCT02069080).

5.2. [⁶⁸Ga]NOTA-NFB

In 1991, Morimoto and coworkers discovered the anti-HIV potential of a family of toxins derived from the Japanese horseshoe crab in a screening experiment (91). Size reduction, gradual elimination of their cytotoxic properties and stabilization by chemical

modification ultimately resulted in two lead compounds (92–95). An optimized ligand, [⁶⁸Ga]NOTA-NFB (H₂NOC-Arg-*cyclo*(Cys(S-)-Cit-Arg-Tyr-Pro-D-Lys-Lys-Cit-Tyr-Cys(S-))-Nal-Arg-Arg-NOTA[⁶⁸Ga]) was prepared and displayed decent tumoral uptake alongside rapid background clearance in xenograft-bearing mice (96). In 2015, the first clinical data employing [⁶⁸Ga]NOTA-NFB was published. The tracer was well tolerated in healthy volunteers and was able to display lesions in glioma and breast cancer patients (NCT02327442). However, substantial tracer uptake in the liver was noted (97). In 2019, the results of the proof-of-concept study in breast cancer patients were published. The tracer facilitated PET/CT detection of a high percentage of lesions, however showed relatively low SUV_{max} values compared to [¹⁸F]FDG alongside a lack in correlation between tracer uptake in CXCR4-positive tissue and CXCR4 expression levels (98).

5.3. [^{99m}Tc]CXCR4-L

Further downsizing and chemical modification of horseshoe crab toxin-derived ligands resulted in a small cyclic peptide, amenable to labeling with technetium-99m *via* the HYNIC method. In healthy volunteers, [^{99m}Tc]CXCR4-L ((*cyclo*(-D-Tyr-D-MeOrn(HYNIC/EDDA[^{99m}Tc])-Arg-Nal-Gly-))) exhibited radiation doses comparable to other imaging studies with technetium-99m tracers. The ligand was eliminated *via* the renal and the hepatobiliary pathway. In patients with suspected glioma, the ligand was able to display tumor lesions with appropriate tumor/background ratios (99).

5.4. Cyclic Pentapeptides

5.4.1. FC-131 and CPCR4

Identification of amino acids in the structures of toxin-derived ligands Ac-TN14003 (Ac-Arg¹-Arg²-Nal³-*cyclo*(Cys⁴(S-)-Tyr⁵-Cit⁶-Lys⁷-D-Lys⁸-Pro⁹-Tyr¹⁰-Arg¹¹-Cit¹²-Cys¹³(S-))-Arg¹⁴-COOH) and Ac-TZ14011 (Ac-Arg¹-Arg²-Nal³-*cyclo*(Cys⁴(S-)-Tyr⁵-Cit⁶-Arg⁷-D-Lys⁸-Pro⁹-Tyr¹⁰-Arg¹¹-Cit¹²-Cys¹³(S-))-Arg¹⁴-CONH₂) that are indispensable for CXCR4 binding, revealed Arg², Nal³, Tyr⁵ and Arg¹⁴ which are located in close proximity to each other due to the conformation of such peptides (94). Fuji and coworkers created cyclic pentapeptides carrying only these amino acids, connected by

a bridging glycine residue. A cyclic peptide, namely FC-131 (*cyclo*(-D-Tyr-Arg-Arg-Nal-Gly-), Figure 6) was found to be equipotent to its parent ligands Ac-TN14003 and Ac-TZ14011 concerning the affinity towards CXCR4 and the HIV inhibitory effect (100–103).

Elucidation of the binding mode of this small peptide ligand to CXCR4 was the aim of detailed mutagenesis and computational docking experiments. Concordant data revealed that the basic side chains of Arg² and Arg³ are tightly interacting with CXCR4's Asp¹⁸⁷ and Asp¹⁷¹, respectively while Tyr¹ forms a hydrogen bond with Tyr⁴⁵. Asp⁹⁷, His¹¹³, Thr¹¹⁷ as well as Glu²⁸⁸ of the receptor are further involved in the binding of the cyclic peptide, quite similar to what was observed for small-molecule inhibitors such as AMD3100 and LY2510924 (*cyclo*[Phe-Tyr-Lys(*i*Pr)-D-Arg-2-Nal-Gly-D-Glu]-Lys(*i*Pr)-NH₂) (104–108). FC-131 and similar pentapeptides are therefore located between the transmembrane domains TM-3 and TM-5, while Arg¹ interacts with the extracellular loop ECL-2 (Figure 6). Both residues, Arg¹ and D-Tyr⁵ are hence pointing towards the extracellular region (ECR) of CXCR4 and might therefore be amenable for functionalization (109).

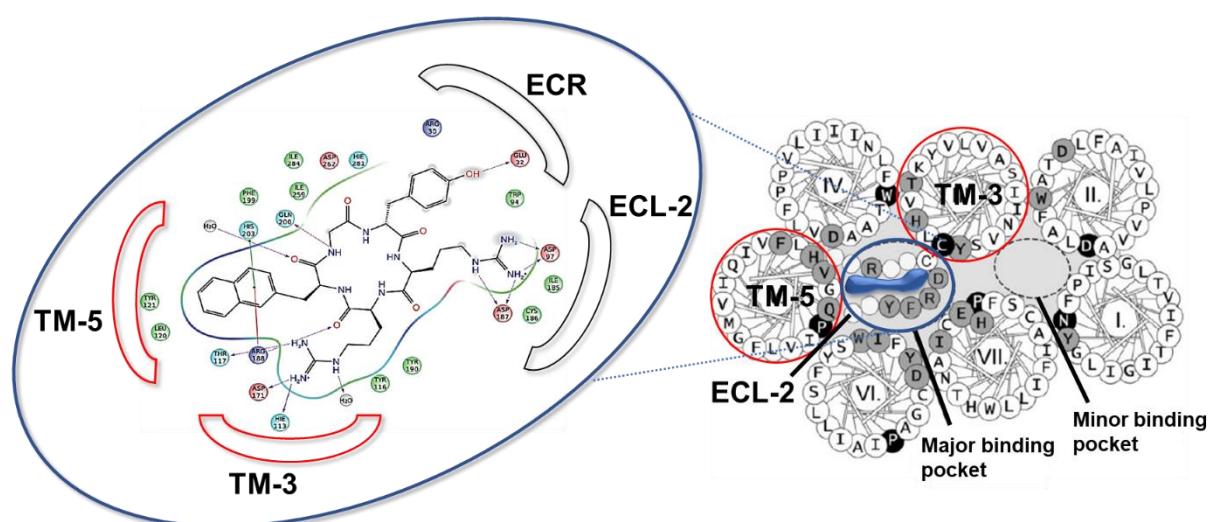


Figure 6: Binding mode of FC-131 in complex with the CXCR4 receptor; cyclic pentapeptides are located within the major binding pocket, sandwiched between transmembrane (TM) regions 3 and 5 and extracellular loop (ECL) 2; Tyrosine is pointing towards the extracellular region (ECR). Figures were adapted from (109) and modified.

In 2007, Ueda et al. conducted the amide-methylation and stereo-inversion of one arginine residue to yield a peptide (*cyclo*(-D-Tyr-D-MeArg-Arg-Nal-Gly-)) with even higher affinity than FC-131 (110). Tamamura and coworkers then reported the insertion of an ornithine residue in exchange for Arg¹ was tolerated without significant loss in affinity due to the orientation of this amino acid towards the extracellular side of the

receptor (111). This free ornithine δ -amine of the newly developed scaffold *CPCR4* (*cyclo(-D-Tyr-D-MeOrn-Arg-Nal-Gly-)*) constituted the basis for the subsequent development of a first CXCR4-targeted tracer, based on the exploitation of the ornithine side chain for chemical modification and introduction of a radiolabel.

5.4.2. Pentixafor and Pentixather

Demmer et al. were able to show that aromatic substituents at the *CPCR4* ornithine side chain are well tolerated (112). The *CPCR4* binding scaffold was extended by an aminomethylbenzoic acid (*Ambz*) spacer and the chelator DOTA was coupled to the free amino terminus (Figure 7). The un-complexed ligand displayed low CXCR4 affinity with an IC_{50} of 150 nM in a competitive binding assay employing Jurkat lymphoma cells (^{125}I -FC-131 as radioligand). When the chelate with indium or gallium was formed, though, considerably increased affinities were found. In the case of gallium, an IC_{50} in the low nanomolar range was observed. The ^{68}Ga -labeled compound exhibited extraordinarily fast clearance from background tissue and high uptake into OH-1 small-cell lung cancer tumors in a biodistribution study in mice (113). A follow-up study confirmed the outstanding affinity of the novel ligand alongside with high hydrophilicity and stability *in vivo*. The following biodistribution and PET imaging experiments in mice showed no enhanced uptake in mCXCR4 expressing organs such as lung, liver, spleen and bone marrow due to the lack of mCXCR4 affinity and rapid tracer clearance from the kidneys (114). The ligand was first termed *CPCR4.2* and is now known under the name Pentixafor (Figure 7).

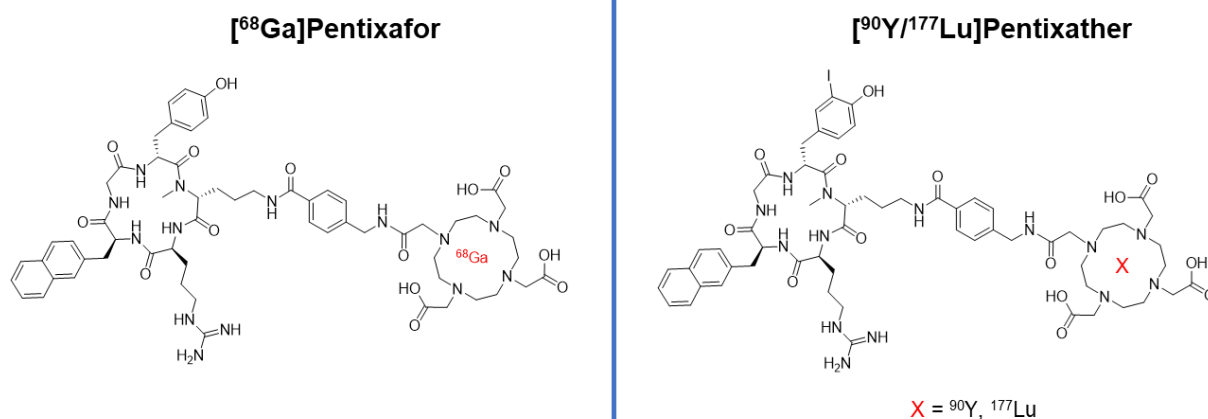


Figure 7: Structures of PET imaging agent [⁶⁸Ga]Pentixafor and its therapeutic analog [⁹⁰Y/¹⁷⁷Lu]Pentixather.

[⁶⁸Ga]Pentixafor has been employed as a CXCR4 specific PET imaging agent in hematologic cancers such as multiple myeloma and leukemia (Figure 8) as well as in solid cancers such as small-cell lung cancer, glioblastoma and esophageal cancer, however in the case of solid cancers, with less promising results (115–120). Moreover, [⁶⁸Ga]Pentixafor has been used for PET imaging of inflammatory diseases such as myocardial infarction, ischemic stroke and atherosclerosis (121–131). The compound is currently investigated in four separate clinical trials assessing its potential for PET imaging of neuroendocrine tumors (NCT03335670), multiple myeloma (NCT04561492), lymphoma (NCT03436342) and leukemia (NCT04504526) (132–135).

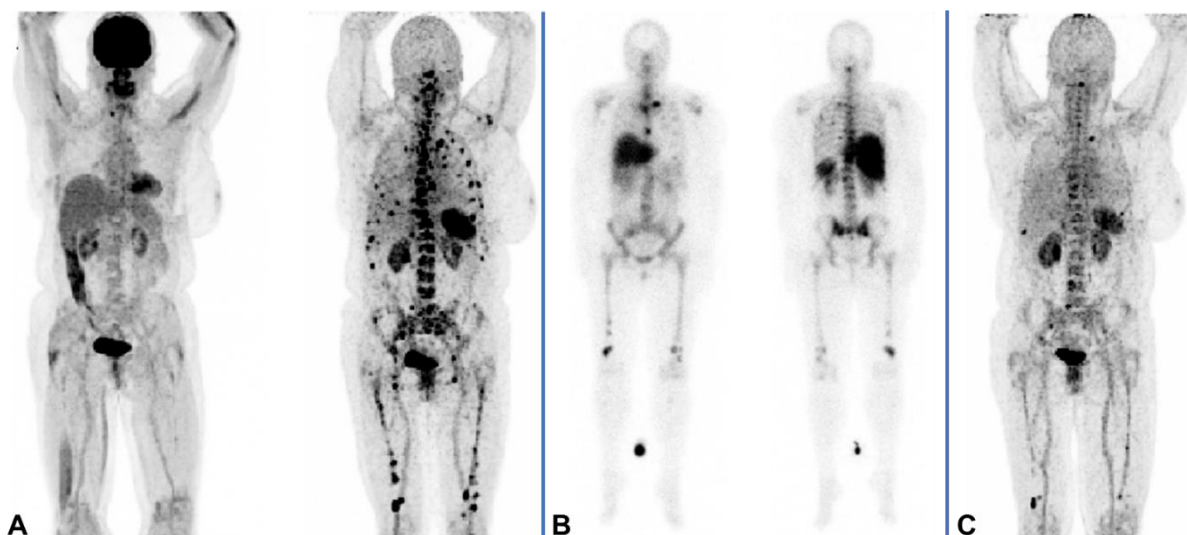


Figure 8: PET imaging of a patient suffering from multiple myeloma pre and post [^{177}Lu]Pentixather treatment: **A:** Pre-treatment maximum-intensity projections (MIP) of [^{18}F]FDG (left) and [^{68}Ga]Pentixafor (right) PET images; **B:** Scintigraphy images of the same patient 7 days after injection of 7.8 GBq [^{177}Lu]Pentixather; **C:** Post-treatment MIP of [^{68}Ga]Pentixafor PET images of the same patient; figure adapted from (136).

In patients suffering from multiple myeloma, high uptake of [^{68}Ga]Pentixafor was observed in the majority of tumor lesions (121). Hence, a theranostic approach was tested, employing the Pentixafor peptide precursor complexed with therapeutic isotopes such as lutetium-177 or yttrium-90. Unfortunately, upon exchange of gallium-68, affinity towards CXCR4 was diminished by a factor of nearly two (137). However, when the CXCR4 peptide scaffold was iodinated at its D-tyrosine residue, even higher affinity of the lutetium and yttrium complexes compared to [Ga]Pentixafor were observed (Figure 7). In preclinical studies, [^{177}Lu]Pentixather displayed rapid clearance from excretion organs in Daudi lymphoma-bearing mice and high and persistent tumor uptake up to one week after injection. As opposed to its diagnostic analog [^{68}Ga]Pentixafor, affinity towards the murine CXCR4 receptor was determined, leading to slightly enhanced ligand uptake in mCXCR4 expressing organs such as lung, spleen and liver (138). In 2016, the University Hospital Würzburg conducted a first in-human endo-radiotherapy study in patients suffering from advanced multiple myeloma (Figure 8). Both, the lutetium-177 and yttrium-90 labeled derivatives were well tolerated without any acute non-hematological adverse effects, however, a high dose was deposited in the bone marrow making stem-cell support mandatory. Pentixather was retained in tumor lesions up to two weeks after injection leading to metabolic responses of the cancer tissues as confirmed by [^{18}F]FDG PET scanning (139). Low toxicity was further

confirmed in patients suffering from lymphoma and acute lymphoblastic leukemia (140–142).

5.4.3. Second Generation Ligands

In preclinical studies following the introduction of [¹⁷⁷Lu]Pentixather, the DOTA chelator of the highly affine peptide scaffold was exchanged with NOTA. The copper-64 and [¹⁸F]AIF complexes retained high affinity towards CXCR4 and displayed promising tumor uptakes in biodistribution experiments. Due to their higher lipophilicity compared to [⁶⁸Ga]Pentixafor, however, slower blood clearance and higher unspecific tracer retention in non-target tissues such as liver and intestines was observed (143,144). When the DOTA chelator of the [⁶⁸Ga]Pentixafor labeling precursor was replaced by NOTA, the gallium-68 labeled substance displayed 9.5-fold decreased tumor uptake in Daudi xenograft-bearing mice even though 1.4-fold higher affinity compared to [⁶⁸Ga]Pentixafor was determined (145). The outcome of this study showed that exchange of DOTA in the structures of Pentixafor and Pentixather does accompany complications. Due to the compact size of the peptides (Figure 9), minimal changes in the chelator geometry oftentimes resulted in significant loss of affinity or *in vivo* targeting potential, thus prohibiting the exchange of DOTA with different functionalities (137,143,144). The expansion of the portfolio beyond [⁶⁸Ga]Pentixafor PET imaging and [¹⁷⁷Lu/⁹⁰Y]Pentixather PRRT was therefore aggravated and demanded further optimization of the ligand-receptor interaction.

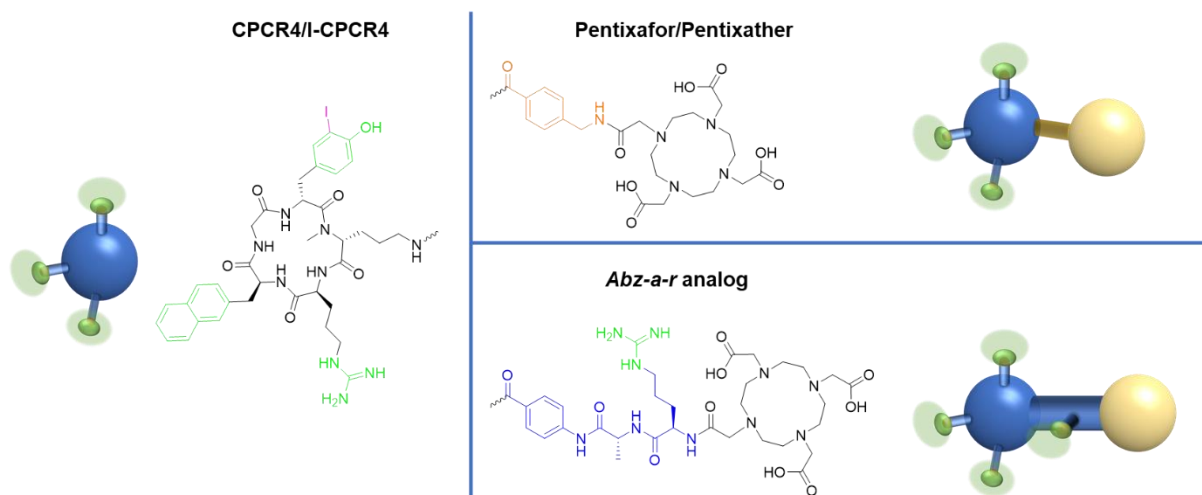


Figure 9: Structures (and corresponding artistic 3D models) of the CPCR4 binding scaffold (blue sphere) and its iodine carrying analog I-CPCR4, Pentixafor and Pentixather with their Ambz linker highlighted in orange (orange cylinder) and the Abz-a-r analog with its improved linker highlighted in blue (blue cylinder); interaction sites with the CXCR4 binding cavity are highlighted in green (green spheres) and DOTA chelators represented by yellow spheres.

In a Ph.D. thesis, on which this work is based, groundbreaking improvements of ligand flexibility towards chemical modification without loss of affinity were made by the introduction of an alternative linker structure. Among a variety of sequences, a linear peptide fragment, consisting of an aminobenzoic acid (*Abz*) instead of *Ambz*, an adjacent D-alanine residue and an N-terminal D-arginine (*Abz-a-r*, Figure 9) emerged as the most potent linker. Compared to [^{nat}Ga]Pentixafor, the [^{nat}Ga]-complexed novel ligand (*cyclo*(-D-Tyr-D-MeOrn(**Abz-D-Ala-D-Arg**-DOTA)-Arg-Nal-Gly-) = CPCR4-Abz-a-r-DOTA, Figure 9) exhibited a 60-fold higher affinity and 4-fold increased internalization into CXCR4 expressing cells. Furthermore, when complexed with lutetium or yttrium, affinity remained in the low nanomolar range, in contrast to what was observed for [^{nat}Lu/^{nat}Y]Pentixafor. *In vivo*, however, those beneficial characteristics were not reflected in improved tumor uptake. Moreover, linker-induced affinity towards the murine CXCR4 receptor resulted in elevated tracer uptake in lung, liver and spleen and the additional positive charge led to higher retention of the tracer in the kidneys (Figure 10).

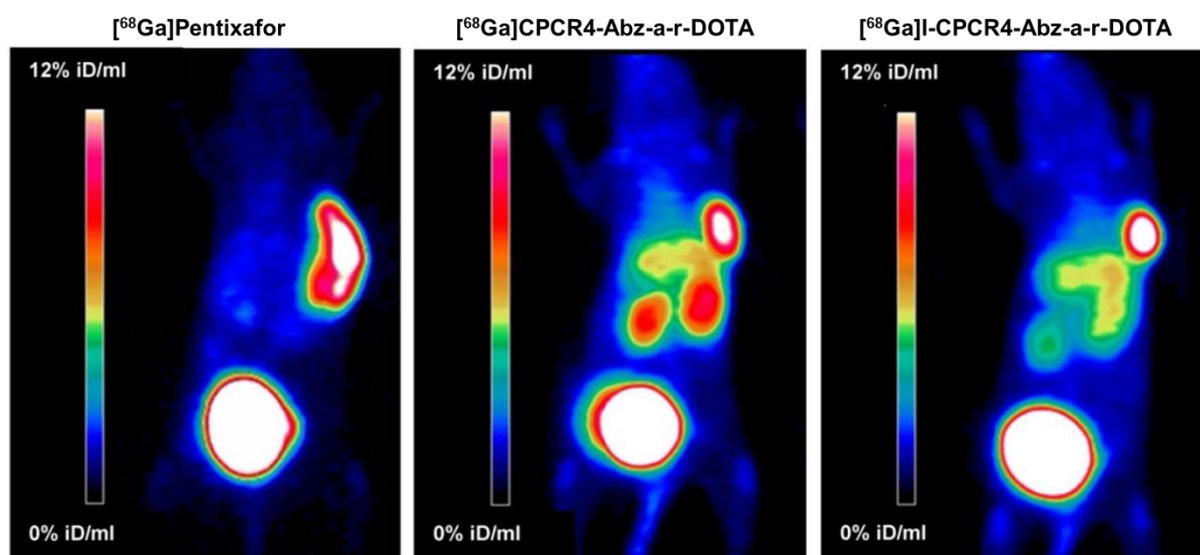


Figure 10: Maximum-intensity-projection (MIP) images of Daudi xenograft-bearing CB-17 SCID mice injected with $[^{68}\text{Ga}]$ Pentixafor (left), $[^{68}\text{Ga}]$ CPCR4-Abz-a-r-DOTA (middle) and $[^{68}\text{Ga}]$ I-CPCR4-Abz-a-r-DOTA (right); static PET images were acquired one hour after injection of the respective tracer; figures adapted from (146).

Backbone iodination of Pentixafor to yield Pentixather was chosen to sustain high CXCR4 affinity upon complexation with therapeutic nuclides. In the case of the novel ligand CPCR4-Abz-a-r-DOTA (*cyclo*(-D-Tyr-D-MeOrn(**Abz-D-Ala-D-Arg**-DOTA)-Arg-Nal-Gly-), Figure 9), backbone iodination led to unchanged or slightly lower affinities of the corresponding metal complexes and partial agonism of I-CPCR4-Abz-a-r-DOTA (*cyclo*(-D-I-Tyr-D-MeOrn(**Abz-D-Ala-D-Arg**-DOTA)-Arg-Nal-Gly-), Figure 9). Both lutetium labeled ligands were evaluated in a biodistribution study in comparison to their parent compound $[^{177}\text{Lu}]$ Pentixather. $[^{177}\text{Lu}]$ CPCR4-Abz-a-r-DOTA and $[^{177}\text{Lu}]$ I-CPCR4-Abz-a-r-DOTA exhibited higher tumor uptake and overall high tumor retention up to 48 hours after injection, potentially due to their enhanced affinity and internalization (146).

In a subsequent patent application, Osl et al. described the derivatization of the newly developed peptide scaffold with different functional moieties. An AMBF₃-based precursor for F-18 labeling displayed high affinity in the low nanomolar range but unfortunately, radiochemical yields below 5% prohibited further assessment of the compound. Other ligands from this series bearing more sterically demanding functionalities, however, suffered substantial loss of affinity compared to CPCR4-Abz-a-r-DOTA (147,148). Even though significantly improved target interaction and flexibility towards chemical modification was gained by introduction of an *Abz-a-r* linker, the development of ligands carrying more versatile functionalities was not feasible.

6. Objectives

The overarching goal of this study was to build upon the work of Osl et al. by further modification/expansion of the *Abz-a-r* linker to obtain a novel tracer backbone that offers even higher flexibility towards the replacement of DOTA by diverse functionalities (Figure 11).

In a first generation of ligands, different moieties were added to the pre-existing scaffold to test which structural optimizations are required. Based on these insights, a novel tracer backbone was developed, carrying an elongated and optimized linker scaffold that ensures high affinity, internalization and hydrophilicity (Figure 11). This scaffold was then derivatized with different functionalities. A third generation of ligands was subsequently prepared, bearing the attachment site for sterically demanding functionalities even further removed from the CPCR4 binding motif. The optimizations ultimately allowed derivatization with DOTA, technetium chelators, SiFA moieties, the fluorophore Cy5.5 and the toxin MMAE.

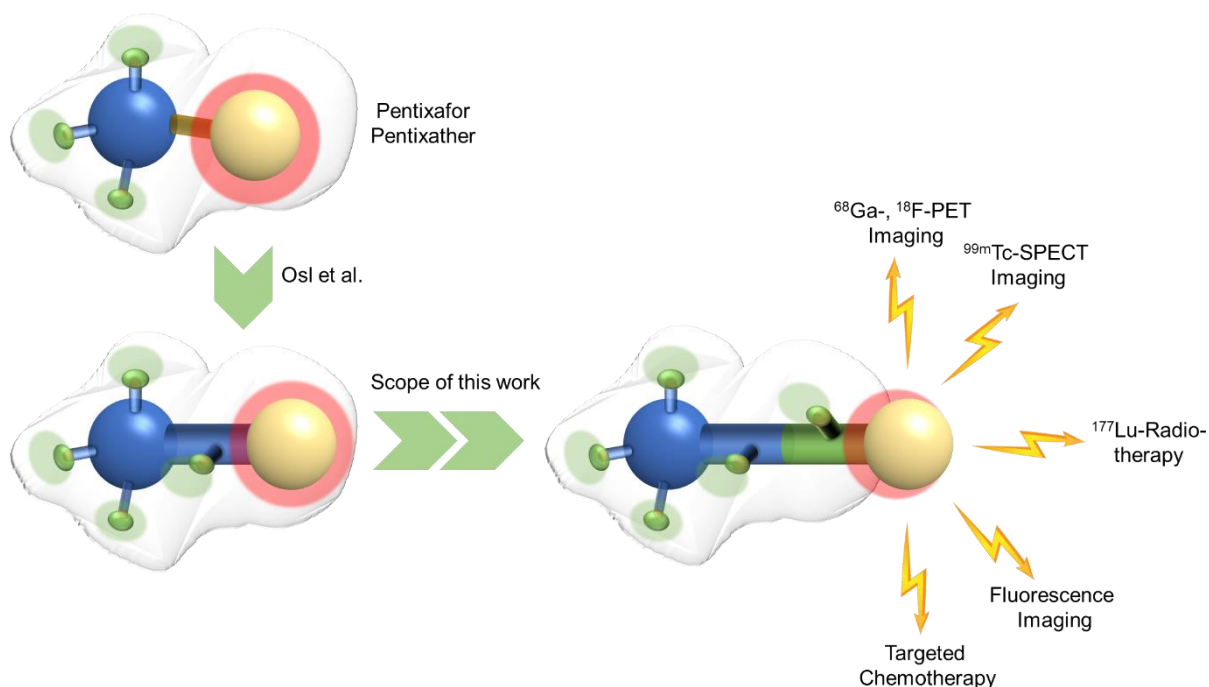


Figure 11: The scope of this work: Development of a novel tracer backbone based on CXCR4 ligands carrying the CPCR4 peptide scaffold (blue sphere) and an optimized linker (blue cylinder) as reported by Osl et al.: enhancement of the linker-binding pocket interaction (green spheres) by elongation with an additional optimized linker (green cylinder) which facilitates the removal of the functional moiety (yellow sphere) from the binding cavity to minimize repulsion (red sphere). This modification enables the application of this tracer backbone in PET, SPECT and fluorescence imaging, PRRT and targeted chemotherapy.

Second-generation compounds initially retained the DOTA chelator while only the linker moiety was changed. Evaluation of the novel ligands in comparison with their

parent molecules Pentixafor and Pentixather gave insight into the effect of linker modification on the physicochemical properties of the optimized compounds.

Peptides suitable for the efficient and stable incorporation of technetium-99m were planned, employing a selection of hydrophilic open-chain chelators, 6-hydrazinonicotinic acid (HYNIC), and the tetraamine chelator N4. Furthermore, their radiolabeling characteristics and *in vitro* and *in vivo* properties were comparatively studied. Concerning the open-chain chelators, a library of glycosylated functional groups was prepared, bearing different hydrophilicities.

Another goal was the preparation of fluorine-18 labeling precursors based on the silicon-fluoride acceptor (SiFA) strategy. The establishment of the labeling procedure and the structural optimization of these ligands with special focus on hydrophilicity and affinity was conducted.

Ligands, bearing high affinity and internalization rates while carrying a cytotoxic payload were planned. The compounds were further selected with regards to their drug-induced cancer cell cytotoxicity, proving the feasibility of such a targeted chemotherapy concept. A monomethyl auristatin-E (MMAE) derivative carrying a cleavable linker was employed for this purpose facilitating the release of the active toxin within the cancer cells.

The connection of the fluorescent dye Cy5.5 with the newly developed tracer backbone was planned to yield novel compounds suitable for *in vitro* and *in vivo* fluorescence imaging of CXCR4. Moreover, a bimodal tracer, enabling both optical as well as nuclear imaging was developed.

Ligands bearing a suitable CXCR4 affinity, determined by an IC_{50} value, a high internalization rate, determined in reference to ^{125}I -FC-131, as well as appropriate hydrophilicity, expressed by a $\log D_{7.4}$ value, were further evaluated in *in vivo* experiments such as small animal imaging or biodistribution. The aim of this study was the preparation of a novel tracer backbone enabling the modification with different functionalities for PET imaging (with e.g. ^{68}Ga , ^{18}F), SPECT imaging (with e.g. ^{99m}Tc , ^{67}Ga), optical imaging (with Cy5.5), PRRT (with e.g. ^{177}Lu , ^{90}Y) and targeted therapy (with MMAE).

II. MATERIALS AND METHODS

1. General Information

1.1. Reagents, Solvents and Biochemicals

Purchased reagents were used without further purification. The entirety of protected amino acids and analogs thereof were purchased from *Bachem* (Bubendorf, Switzerland), *Iris Biotech GmbH* (Marktredwitz, Germany), *Carbolution Chemicals GmbH* (St. Ingbert, Germany) and *Merck Millipore* (Darmstadt, Germany). The 2-Chlorotrityl chloride (2-CTC) resin was obtained from *Iris Biotech GmbH* (Marktredwitz, Germany) or *CEM* (Matthews, USA). Reagents for peptide synthesis were purchased from *Iris Biotech GmbH* (Marktredwitz, Germany), *Sigma-Aldrich* (Munich, Germany) and *Molekula GmbH* (Garching, Germany). Solvents and reagents for organic synthesis were purchased from either *Alfa Aesar* (Karlsruhe, Germany), *Sigma-Aldrich* (Munich, Germany) or *VWR* (Darmstadt, Germany).

Chematech (Dijon, France) provided the DOTA-GA derivatives and DOTA derivatives were provided by *Macrocyclics* (Plano, USA). The Cy5.5 dye was obtained from *Lumiprobe* (Hunt Valley, USA). The vc-PAB-MMAE derivative was purchased from *Creative Biolabs* (Shirley, USA).

Biochemicals, such as DMEM (Ham's F-12, with stable Gln) and RPMI 1640 (with Gln) medium, fetal bovine serum (FBS superior), phosphate-buffered saline (PBS Dulbecco, w/o Ca²⁺, Mg²⁺), trypsin/EDTA (0.05%/0.02% in PBS, w/o Ca²⁺, Mg²⁺) and Hank's buffered salt solution (HBSS, with 0.35 g/L NaHCO₃ and Ca²⁺, Mg²⁺) were obtained from *Biochrom GmbH* (Berlin, Germany) or *Sigma-Aldrich* (Munich, Germany).

Water for RP-HPLC solvents was obtained from the in-house Millipore system from *Thermo Fischer Scientific Inc.* (Waltham MA, USA). Tracepure[®] water for labeling experiments was received from *Merck Millipore* (Darmstadt, Germany).

1.2. Radioactive Isotopes

Labeling with Iodine-125 was carried out using a [¹²⁵I]NaI solution in NaOH (40 mM, S_A = 74 TBq/mmol) from *Hartmann Analytik GmbH* (Braunschweig, Deutschland).

[^{99m}Tc]-Pertechnetate was obtained by elution of a Drytech™ Technetium Generator from *GE Healthcare* (Munich, Germany) with physiological NaCl solution (0.9%; v/v). The generator was provided by the *Klinikum Rechts der Isar* (Technical University Munich, Munich, Germany).

A solution of [¹⁷⁷Lu]LuCl₃ (HCl (0.04 M); S_A > 3 TBq/mg, 740 MBq/mL) was provided by *ITM GmbH* (Garching, Germany) and used directly for labeling experiments.

[¹⁸F]-Fluoride in target water was provided by the *Klinikum Rechts der Isar* (Technical University Munich, Munich, Germany).

[⁶⁸Ga]GaCl₃ for radiosynthesis was obtained by elution of a ⁶⁸Ge/⁶⁸Ga-generator from *iThemba LABS* (Cape Town, South Afrika) with aqueous HCl (1.0 M). Synthesis was carried out on an automated Gallelut⁺ system from *Scintomics GmbH* (Fürstfeldbruck, Germany).

[⁶⁷Ga]Ga-citrate (NaCl_{aq}; S_A = 74 MBq/mL) was provided by *Mallinckrodt Pharmaceuticals* (Dublin, Ireland) and converted to [⁶⁷]GaCl₃ prior to radiosynthesis.

1.3. Instruments and Analytics

Solid-phase peptide synthesis (SPPS) was carried out by manual operation using 24 mL polypropylene syringes equipped with an in-built filter as synthesis reactor. The syringes were shaken during reaction time by an Intelli-Mixer syringe shaker from *Neolab* (Heidelberg, Germany).

Eluents for all RP-HPLC operations were water (solvent A) and acetonitrile (solvent B), both containing 0.1 vol% TFA. For *semi*-preparative RP-HPLC runs, solvent B was used with 5 vol% H₂O. Analytical and *semi*-preparative RP-HPLC runs were performed using Shimadzu gradient systems from *Shimadzu Deutschland GmbH* (Neufahrn, Germany), each equipped with a SPD-20A UV/Vis detector (λ = 220 nm, 254 nm). A Multokrom 100 C18 (125 × 4.6 mm, 5 μm particle size) column provided by *CS GmbH* (Langerwehe, Germany) was used for analytical RP-HPLC runs and operated at a flow rate of 1 mL/min. Both specific gradients and the corresponding retention times *t_R* are cited in the text. *Semi*-preparative RP-HPLC purification was performed with a

Multokrom 100 RP 18 (250 × 10 mm, 5 µm particle size) column from *CS GmbH* (Langerwehe, Germany) operated at a constant flow rate of 5 mL/min.

Analytical and *semi*-preparative radio-RP-HPLC runs were performed using a Multokrom 100 C18 (125 × 4.0 mm, 5 µm particle size) column from *CS GmbH* (Langerwehe, Germany). Radioactivity was detected by connection of the outlet of the UV-photometer to a NaI(Tl) well-type scintillation counter from *EG&G Ortec* (Munich, Germany).

Radioactive probes such as mouse organs or cell-test vials were measured on a WIZARD^{2®} 2480 automatic γ-Counter from *Perkin Elmer* (Waltham MA, USA).

Radio-TLC measurements were conducted on a Scan-RAM[™] from *LabLogic Systems Ltd.* (Broomhill, UK). Chromatograms thereof were analyzed using the Laura[™] software from *LabLogic Systems Ltd.* (Broomhill, UK).

RP-HPLC (radio-)chromatograms were evaluated using the LabSolution software from *Shimadzu Corp.* (Kyoto, Japan)

Mass spectra for characterization of organic substances were acquired on an expression⁺ CMS quadrupole mass spectrometer from *Advion Ltd.* (Harlow, UK).

NMR spectra were recorded at 300 K on an AVHD-300 or an AVHD-400 spectrometer, both devices from *Bruker Corporation* (Billerica, USA).

pH values were measured with a SevenEasy pH-meter from *Mettler Toledo* (Gießen, Germany).

Purification via flash-chromatography was carried out on an Isolera[™] Prime System from *Biotage* (Uppsala, Sweden), running a Biotage 09474 Rev. E Bio pump. A *Biotage™* SNAP KP-C₁₈ cartridge (12 g, 93 Å pore diameter, 382 m²/g surface) was used applying a linear gradient of solvent B (ACN, 0.1 vol% TFA, 2 vol% H₂O) in solvent A (H₂O, 0.1 vol% TFA).

Lyophilization of peptides was carried out using an Alpha 1-2 LDplus lyophilization instrument from *Christ* (Osterode am Harz, Germany), employing a RZ-2 vacuum pump from *Vacuubrand GmbH* (Wertheim, Germany).

IC₅₀ values were calculated using GraphPad Prism 6 from *GraphPad Software Inc.* (San Diego, USA).

2. Synthesis

2.1. General Concepts

2.1.1. SPPS – General Procedures

GP1: 2-CTC-resin loading

Loading of the 2-CTC resin with a Fmoc-protected amino acid (AA) was carried out by stirring a suspension of the 2-CTC-resin (1.0 eq.; max. loading capacity: 1.6 mmol/g) and a Fmoc-AA-OH (1.5 eq.) in DMF with DIPEA (3.0 eq.) at room temperature for 2–5h. Remaining chlorotriyl-residues were capped by the addition of methanol (5 mL/g resin) and incubation for 15 min. Subsequently, the resin was filtered off and washed with DMF (5 × 5 mL/g resin) and methanol (3 × 5 mL/g resin) before drying *in vacuo*. Final loading *l* of the dry resin with the Fmoc-AA-OH was determined by the following equation:

$$l \left[\frac{\text{mmol}}{\text{g}} \right] = \frac{(m_2 - m_1) \times 1000}{(M_W - M_{HCl}) m_2}$$

GP2: On-resin peptide coupling

GP2a): Standard peptide coupling

The respective side-chain protected Fmoc-AA-OH (1.5 eq.) was dissolved in DMF (8 mL/g resin) and pre-activated by addition of TBTU (1.5 eq.), HOBt/HOAt (1.5 eq.) and DIPEA (3 eq.). After pre-activation for 15 minutes, the solution was added to the resin-bound free amine peptide 2-CTC-AA-NH₂ and shaken for 2h at r.t. The resin was then washed with DMF (6 × 5 mL/g resin) and after Fmoc de-protection, the next amino acid was coupled analogously.

GP2b): Low reactivity and fragment condensation

For amino acids with low reactivity (such as Fmoc-Abz-OH) or peptide fragment condensation, HATU (1.5 eq.) and HOAt (1.5 eq.) instead of TBTU and HOBt were used. Prolonged reaction times of up to 48h were oftentimes needed to achieve satisfactory conversion.

GP2c): Amino acids susceptible to racemization

For Fmoc-dap(Boc)-OH, Fmoc-dap(Dde)-OH and Fmoc-cys(Trt)-OH as well as fragments bearing these amino acids as their C-terminus, pre-activation was shortened to 2–5 min and 2,4,6-Collidine was used as base to minimize racemization.

GP3: On-resin/In-solution Fmoc de-protection

The resin-bound Fmoc-AA-peptide was treated with 20% piperidine in DMF (v/v, 8 mL/g resin) for 5 min and subsequently for 15 min. Afterwards, the resin was washed thoroughly with DMF (8 × 5 mL/g resin).

Resin-cleaved Fmoc-bearing peptides were dissolved in DMF and piperidine was added (20 vol%). The mixture was allowed to stand at r.t. for 15 minutes before removal of the solvents under reduced pressure.

GP4: On-resin Dde de-protection

GP4a): Harsh conditions

The Dde-protected peptide (1.0 eq.) was treated with a solution of 2% hydrazine monohydrate in DMF (v/v, 5 mL/g resin) for 15 min. If a Fmoc-protecting group was used alongside with Dde, harsh conditions also removed Fmoc. After de-protection, the resin was washed with DMF (6 × 5 mL/g resin).

GP4b): Mild conditions

In the case of present Fmoc-groups that are not supposed to be simultaneously removed, Dde de-protection was performed by adding a solution of imidazole (0.46 g) and hydroxylamine hydrochloride (0.63 g) in NMP (2.5 mL) and DMF (0.5 mL) for 3h at r.t. Dde was specifically removed in the presence of Fmoc. After de-protection, the resin was washed with DMF (6 × 5 mL/g resin).

GP5: *t*Bu/Boc/Pbf/Trt de-protection

Removal of *t*Bu/Boc/Pbf-protecting groups was carried out by dissolving the crude product in TFA and stirring for 90 min at r.t. For removal of Trt protecting groups, TIPS was added to the mixture. After removing TFA under a stream of nitrogen, the residue was dissolved in a mixture of *t*-butanol and water. After lyophilization, the crude de-protected peptide was obtained.

GP6: N-Acetylation

Acetylation of an amine functionality was achieved by reacting the respective resin-bound peptide with a mixture of DIPEA (5.0 eq.) and Ac₂O (5.0 eq.) in DMF (5 mL/g resin) for 2h.

GP7: Peptide cleavage off the resin**GP7a): Preservation of acid-labile protecting groups**

The resin-bound peptide was treated with a mixture of DCM/HFIP (4/1 (v/v), 8 mL/g resin) for 60 min. The solution containing the fully protected peptide was separated and the resin was treated with another portion of the cleavage solution for 60 min. Both fractions were combined, and the solvents removed under reduced pressure. After lyophilization, the crude fully protected peptide was obtained.

GP7b): Cleavage of acid-labile protecting groups

The fully protected resin-bound peptide was treated with a mixture of TFA/TIPS/H₂O (95/2.5/2.5 (v/v/v)) and the syringe shaken for 30 min. The solution was separated from the resin and the resin was treated in the same way for another 30 min. Both filtrates were combined and concentrated under a stream of nitrogen. After addition of a mixture of *t*-butanol and water and subsequent lyophilization, the crude peptide was obtained.

GP8: Condensation of peptide fragments in solution

Connection of peptidic fragments such as the *CPCR4* peptide scaffold, linker units or peptide-based functional moieties was carried out in DMF, employing small molar excess of the synthesized C-terminus bearing fragment (1.1–1.3 eq.) and HOAt/HATU as coupling reagents. If the activated amino acid was dap or cys, 2,4,6-Collidine was used as base, in every other case DIPEA. Reactions were conducted at r.t. and monitored via RP-HPLC until satisfactory conversion. Reactions were stopped by removing the solvent under reduced pressure.

2.1.2. ^{nat}Ga-/^{nat}Lu-Complexation

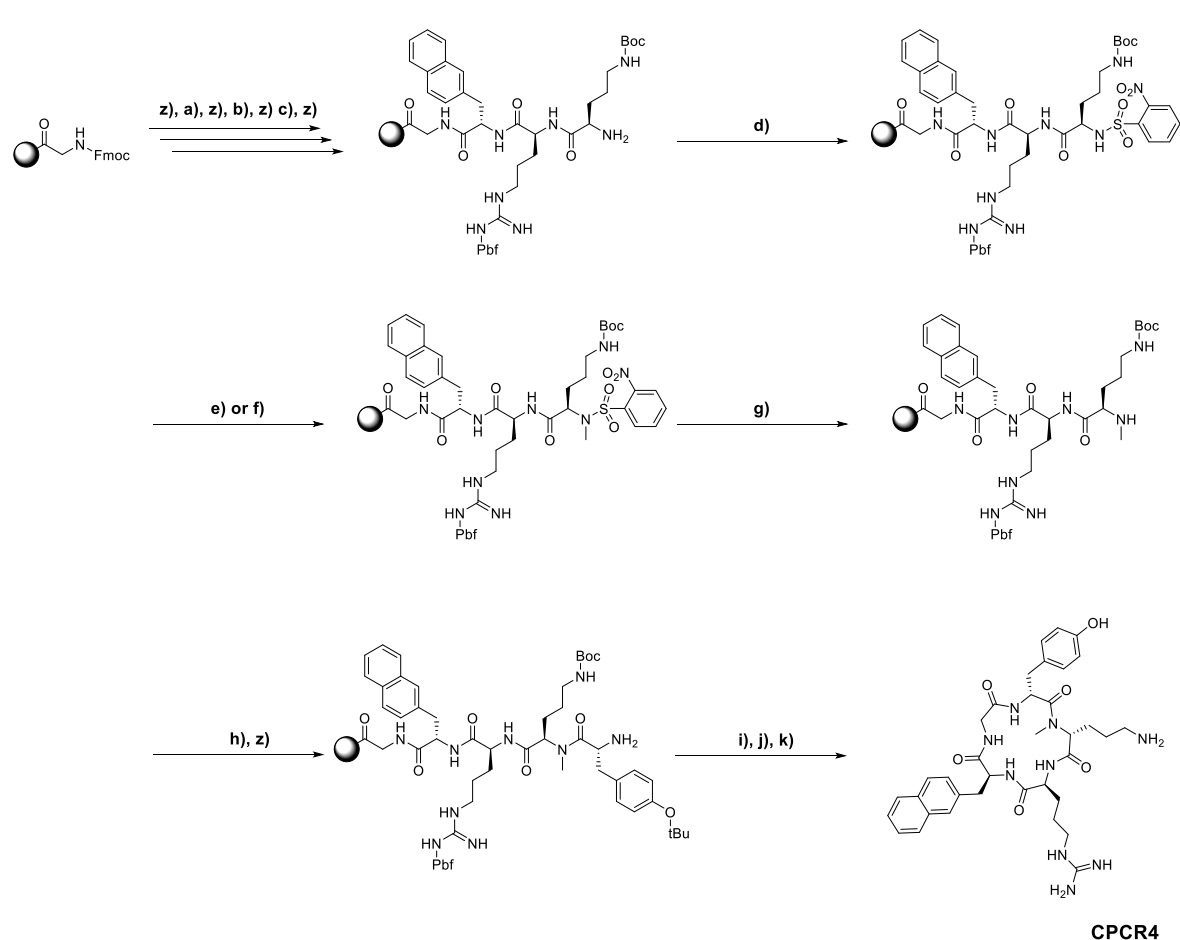
For the complexation of DOTA- and DOTA-GA-conjugated peptides with ^{nat}Ga and ^{nat}Lu, the fully de-protected and purified peptides were used. Peptides were dissolved in DMSO, DMSO/H₂O mixtures or H₂O, ideally to a concentration of 1.0 mM. The required amounts of peptide (30–500 nmol) were given into an Eppendorf tube and ^{nat}Ga(NO₃)₃ or ^{nat}LuCl₃ (3.0 eq. each, typically 20 mM in H₂O or DMSO) were added. The vial was heated to 95°C for 30 min and the quantitative conversion checked by RP-HPLC and ESI-MS. The reaction mixture was used without further purification if no educt was traceable.

2.1.3. [^{nat}I]Iodination of *CPCR4*

Iodination of the tyr-bearing peptide scaffold *CPCR4* was achieved according to a procedure described in literature. Briefly, the fully de-protected and purified *CPCR4*-bearing peptide was dissolved in MeCN/H₂O (1/1 (v/v)) to a concentration of 1.0 mM and NIS (0.3–0.5 eq./ 10 mM in MeCN) was added. After 5 min at r.t., the reaction mixture was subjected to RP-HPLC purification.

2.2. Synthesis of Building Blocks

2.2.1. The *CPCR4* Peptide Scaffold



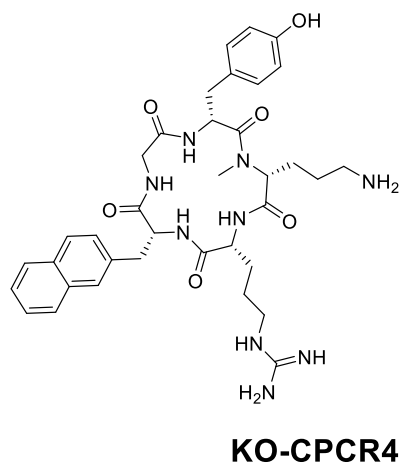
Scheme 1: Synthesis of *CPCR4*: z) 20% Piperidine in DMF (v/v); a) Fmoc-L-2-Nal-OH (1.5 eq.), HOAt (1.5 eq.), TBTU (1.5 eq.), DIPEA (3.0 eq.); b) Fmoc-L-Arg(Pbf)-OH (1.5 eq.), HOAt (1.5 eq.), TBTU (1.5 eq.), DIPEA (3.0 eq.); c) Fmoc-D-Orn(Boc)-OH (1.5 eq.), HOAt (1.5 eq.), TBTU (1.5 eq.), DIPEA (3.0 eq.); d) Collidine (10 eq.), *o*-NBS-Cl (4.0 eq.); e) Ph₃P (5.0 eq.), MeOH (10 eq.), DIAD (5.0 eq.); f) Me₂SO₄ (10 eq.), DBU (3.0 eq.); g) DBU (5.0 eq.), mercaptoethanol (10 eq.), h) Fmoc-D-Tyr(*t*Bu)-OH (3.0 eq.), HOAt (3.0 eq.), HATU (3.0 eq.), DIPEA (5.0 eq.); i) 20% HFIP in DCM (v/v); j) DPPA (3.0 eq.), NaHCO₃ (5.0 eq.); k) TFA.

The synthesis of the *CPCR4* peptide scaffold (*cyclo*(D-Tyr-D-[NMe]Orn-Arg-2-Nal-Gly)) was realized in analogy to a previously described procedure and as depicted in Scheme 1 (149). In short, Fmoc-Gly-OH was immobilized on 2-CTC resin (GP1) and Fmoc-2-Nal-OH, Fmoc-Arg(Pbf)-OH and Fmoc-D-Orn(Boc)-OH were coupled according with GP2a) and 3. After coupling of Fmoc-D-Orn(Boc)-OH, the *N*-terminus was Fmoc de-protected (GP3) and newly protected by reaction with *o*-NBS-Cl (4.0 eq.) and 2,4,6-Collidine (10 eq.) in NMP for 15 min (*step d*). Methylation of the *N*-terminus was achieved by either employing *Mitsunobu* conditions: (*step e*); Ph₃P (5.0 eq.),

MeOH (10 eq.), DIAD (5.0 eq.) in THF, 10 min) or using Dimethylsulfate: (step *f*); Me₂SO₄ (10 eq.), DBU (3.0 eq.) in NMP, 2x2 min) (150). De-protection of the methylated terminus was attained by incubation of the resin-bound peptide with DBU (5.0 eq.) for 5 min before addition of 2-mercaptoethanol (10 eq.). After 30 min, the resin was washed thoroughly with DMF. The following coupling of Fmoc-D-Tyr(*t*Bu)-OH (step *h*) was achieved by using HOAt and HATU as coupling reagents (GP2b)). After final Fmoc de-protection (GP3), the peptide was cleaved off the resin under retention of acid-labile protecting groups according with GP7a). Cyclization was carried out using DPPA (3.0 eq.) and NaHCO₃ (5.0 eq.) in a 1.0 mM solution of peptide in DMF. After completion of the reaction monitored by RP-HPLC, the product solution was concentrated under reduced pressure. The resulting crude product was fully deprotected by treatment with TFA (GP5) before precipitation in Et₂O. Purification of the peptide by flash-chromatography yielded an off-white solid.

CPCR4: RP-HPLC (10 to 95% B in 15 min): $t_R = 6.49$ min, $\kappa' = 4.01$. Calculated monoisotopic mass (C₃₆H₄₇N₉O₆): 701.36, found: 701.8 [M+H]⁺, 351.4 [M+2H]²⁺.

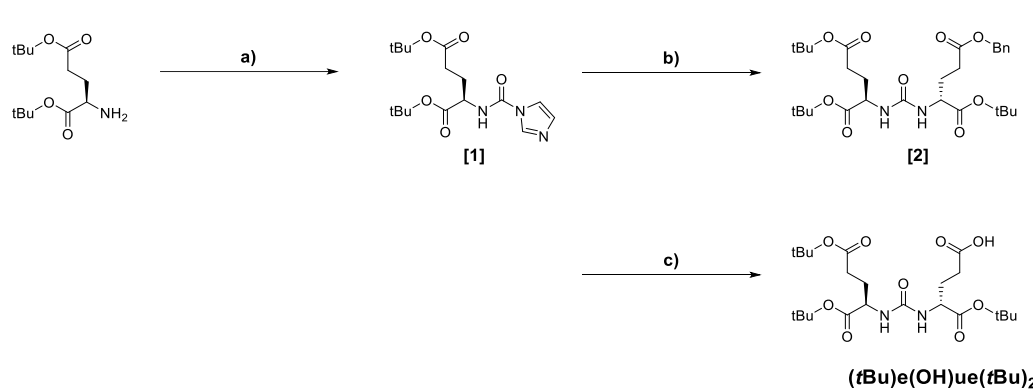
2.2.2. The KO-*CPCR4* Peptide Scaffold



KO-CPCR4 (cyclo(D-Tyr-D-[NMe]Orn-D-Arg-D-2-Nal-Gly) was synthesized according with the described procedure for *CPCR4*, with the difference being that Fmoc-D-2-Nal-OH and Fmoc-D-Arg(Pbf)-OH were used instead of the respective L-configured amino acids.

KO-CPCR4: RP-HPLC (10 to 60% B in 15 min): $t_R = 9.26$ min, $\kappa' = 6.12$. Calculated monoisotopic mass (C₃₆H₄₇N₉O₆): 701.36, found: 701.4 [M+H]⁺, 351.3 [M+2H]²⁺.

2.2.3. The (tBu)e(OH)ue(tBu)₂ Motif



Scheme 2: Synthesis of (tBu)e(OH)ue(tBu)₂: a) TEA (2.5 eq.), DMAP (0.04 eq.), CDI (1.1 eq.); 0°C–r.t., o.n.; b) TEA (2.0 eq.), D-glu(OBn)-OtBu (1.0 eq.); 0°C–r.t., 40°C, o.n.; c) Pd/C (10%); r.t., o.n.

The synthesis of the (tBu)e(OH)ue(tBu)₂ motif was accomplished according to recent literature (151) via 2 intermediate synthons.

Di-tert-butyl-(1H-imidazole-1-carbonyl)-D-glutamate [1]

In short, D-glu(OtBu)-OtBu (1.0 eq.) was dissolved in DCM and treated with TEA (2.5 eq.) and DMAP (0.04 eq.) on ice. CDI (1.1 eq.) was added and the mixture was stirred over night without further cooling. The reaction was stopped by addition of NaHCO₃ (sat.) and the organic layer washed with H₂O and brine twice each. The solvent was evaporated and the crude product [1] was obtained as a colorless oil (91% yield). The product was used in subsequent reactions without further purification.

Di-tert-butyl-(1H-imidazole-1-carbonyl)-D-glutamate [1]: RP-HPLC: (10 to 90% B in 15 min): $t_R = 14.50$ min, $\kappa' = 8.48$. Calculated monoisotopic mass (C₁₇H₂₇N₃O₅): 353.2, found: 376.3 [M+Na]⁺.

5-benzyl-1-(tert-butyl)-(((R)-1,5-di-tert-butoxy-1,5-dioxopentan-2-yl)carbamoyl)-D-glutamate [2]

The educt [1] (1.0 eq.) was dissolved in DCE and cooled on ice before addition of TEA (2.0 eq.) and D-glu(OBn)-OtBu (1.0 eq.). The mixture was heated to 40°C over night. The solvent was then concentrated *in vacuo* and the crude product underwent silica flash-chromatography employing EtOAc/*n*-hexane/TEA (500/500/0.8 (v/v/v)). After removal of the solvents under reduced pressure, the desired product [2] was obtained as a colorless oil (84% yield).

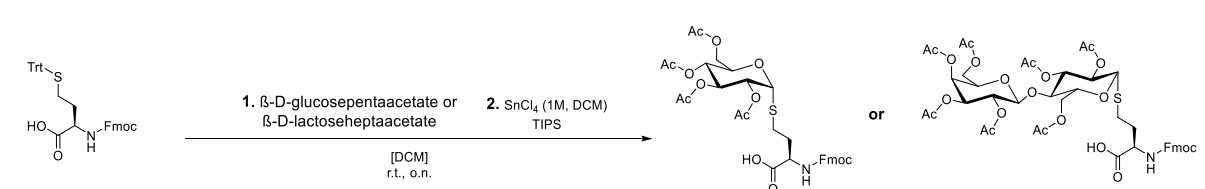
5-Benzyl-1-(*tert*-butyl)-(((*R*)-1,5-di-*tert*-butoxy-1,5-dioxopentan-2-yl)carbamoyl)-D-glutamate [2]: RP-HPLC: (10 to 90% B in 20 min): $t_R = 17.43$ min, $\kappa' = 10.94$. Calculated monoisotopic mass ($C_{30}H_{46}N_2O_9$): 578.3, found: 601.5 $[M+Na]^+$, 523.3 $[M-tBu+H]^+$, 467.3 $[M-2tBu+H]^+$, 411.3 $[M-3tBu+H]^+$.

(*t*Bu)e(OH)u(*t*Bu)₂

The benzyl-protected educt [2] (1.0 eq.) was dissolved in EtOH and palladium (10% on activated charcoal, 0.1 eq.) was added. A H₂-atmosphere was maintained over night to facilitate the de-protection reaction. The catalyst was filtered off by passing the mixture through a celite[®] pad. The solvent of the resulting clear solution was evaporated under reduced pressure to yield the desired product as a colorless oil that solidifies (82% yield).

e(*t*Bu)u(*t*Bu)₂ [3]: RP-HPLC (10 to 90% B in 15 min): $t_R = 12.00$ min, $\kappa' = 6.14$. Calculated monoisotopic mass ($C_{23}H_{49}N_2O_9$): 488.3, found: 489.4 $[M+H]^+$, 516.4 $[M+Na]^+$.

2.2.4. Glycosylated Homocysteine



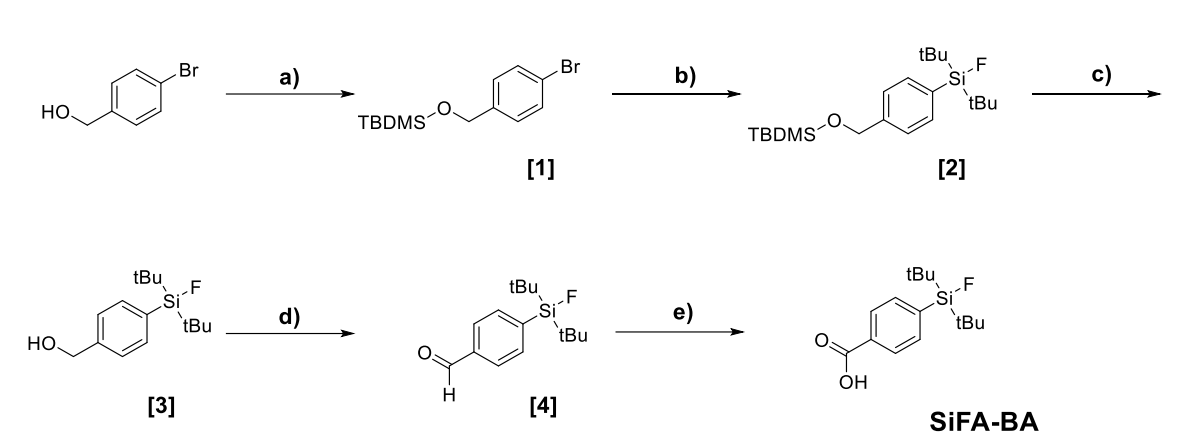
Scheme 3: Reaction of Fmoc-D-HCy(Trt)-OH with peracetylated β-D-glucose or β-D-lactose employing SnCl₄ and TIPS in a one-pot reaction.

For the glycosylation of Fmoc-D-HCy(Trt)-OH, the respective per-acetylated precursor (β-D-glucose pentaacetate/β-D-lactose heptaacetate) was used. The sugar (1.0 eq.) and the protected amino acid (1.2 eq.) were added in argon stream to a round bottom flask and dissolved in DCM. TIPS (1.3 eq.) was added as a scavenger for Trt⁺ and SnCl₄ (2.4 eq., 1.0 M in DCM) was given dropwise to the reaction mixture. After initial yellow coloring, the mixture became colorless, and a precipitate formed after stirring over night at r.t. The mixture was diluted with DCM and acidified with HCl (1.0 M). The organic layer was extracted with HCl and H₂O twice each and dried over Na₂SO₄. The solvent was evaporated *in vacuo* and the crude product purified *via* flash chromatography.

Fmoc-D-HCy-(β -D-Gluc(OAc)₄)-OH: HPLC (30 to 80% B in 15 min): t_R = 9.90 min, κ' = 4.92. Calculated monoisotopic mass (C₃₃H₃₇NO₁₃S): 687.20, found: 688.2 [M+H]⁺.

Fmoc-D-HCy-(β -D-Lac(OAc)₇)-OH: HPLC (30 to 80% B in 15 min): t_R = 10.70 min, κ' = 5.80. Calculated monoisotopic mass (C₄₅H₅₃NO₂₁S): 975.28, found: 976.0 [M+H]⁺.

2.2.5. SiFA-Benzoic Acid (SiFA-BA)



Scheme 4: Synthesis of SiFA-BA: a) TBDMOSiCl₂, imidazole (DMF); r.t., o.n.; b) tBuLi, di-tert-butyl difluorosilane (THF); -78°C–r.t., o.n.; c) HCl (MeOH); r.t., o.n.; d) pyridinium chlorochromate (DCM); 0°C, 2.5h; e) KMnO₄ (DCM, tBuOH, NaH₂PO₄ buffer); r.t.–5°C.

The synthesis of the silicon fluoride acceptor moiety SiFA-BA was achieved leaning on the published procedure with some modifications (152). Reactions were carried out in dried flasks under argon atmosphere. The desired product was obtained after five reaction steps starting with 4-bromobenzyl alcohol.

((4-bromobenzyl)oxy)(tert-butyl)dimethylsilane [1]

4-Bromobenzyl alcohol (1.0 eq.) was dissolved in DMF_{abs.} (15 mL/g educt) and imidazole (1.2 eq.) and TBDMOSiCl₂ (1.2 eq.) were added under vigorous stirring. The reaction mixture was stirred over night at r.t., poured into cold H₂O and the aqueous phase extracted five times with Et₂O. The organic phases were combined, washed twice with sat. NaHCO₃ solution and brine, dried over MgSO₄ and concentrated *in vacuo*. The crude product was purified *via* silica flash chromatography employing 5% EtOAc in petrol ether (v/v). After removal of the solvents under reduced pressure, the protected alcohol [1] was obtained as a colorless oil (95% yield).

((4-Bromobenzyl)oxy)(*tert*-butyl)dimethylsilane [1]: RP-HPLC: (50 to 100% B in 15 min): $t_R = 15.0$ min, $\kappa' = 3.61$.

$^1\text{H-NMR}$ (400 MHz, CDCl_3 , 300 K): $\delta = 0.10$ (6H, s, SiMe_2tBu), 0.95 (9H, s, SiMe_2tBu), 4.69 (2H, s, CH_2OSi), 7.21 (2H, d), 7.46 (2H, d) ppm.

Di-*tert*-butyl(4-((*tert*-butyldimethylsilyloxy)methyl)phenyl)fluorosilane [2]

Compound [2] (1.0 eq.) was dissolved in $\text{THF}_{\text{abs.}}$ (10 mL/g educt) and cooled to -78°C before addition of tBuLi (2.4 eq.) in pentane ($c = 1.7$ mol/L). After stirring for 30 min at -78°C , the reaction mixture was added dropwise to a solution of di-*tert*-butyldifluorosilane (1.2 eq.) in $\text{THF}_{\text{abs.}}$ (10 mL/g) at -78°C . The solution was stirred overnight and allowed to warm to r.t. before addition of brine. The crude product was extracted three times with Et_2O , the combined organic phases dried over MgSO_4 and the solvents evaporated *in vacuo* to afford a yellowish oil (95% yield). The crude product [2] was used without further purification.

Di-*tert*-butyl(4-((*tert*-butyldimethylsilyloxy)methyl)phenyl)fluorosilane [2]: RP-HPLC: (50 to 100% B in 20 min): $t_R = 19.0$ min, $\kappa' = 5.80$.

4-(Di-*tert*-butylfluorosilanyl)benzyl alcohol [3]

De-protection of [2] was achieved by suspension in MeOH (25 mL/g educt) and using catalytic amounts of concentrated HCl (0.25 mL/g). After stirring the mixture overnight at r.t., the solvent was removed under reduced pressure. The remainder was dissolved in Et_2O (20 mL/g educt) and washed with sat. NaHCO_3 solution. The aqueous layer was then three times extracted with Et_2O , the combined organic phases dried over MgSO_4 , and the solvent evaporated *in vacuo* to afford a yellowish oil (98% yield). The crude product [3] was used without further purification.

4-(Di-*tert*-butylfluorosilanyl)benzyl alcohol [3]: RP-HPLC: (50 to 100% B in 15 min): $t_R = 8.2$ min, $\kappa' = 3.32$.

4-(Di-*tert*-butylfluorosilyl)benzaldehyde [4]

Oxidation to the aldehyde was attained employing *Corey-Suggs* conditions. The educt [3] (1.0 eq.) was dissolved in $\text{DCM}_{\text{abs.}}$ (15 mL/g educt) and added dropwise to an ice-cooled suspension of PCC (2.5 eq.) in $\text{DCM}_{\text{abs.}}$ (20 mL/g PCC). After stirring for 30 min at 0°C and subsequently 2.5h at r.t., Et_2O was added, and the supernatant decanted from the solid. The black remainder was washed with Et_2O , and the combined organic

phases filtered through a pad of silica gel (10 cm/g product). The solvent was evaporated *in vacuo* and [4] obtained as a yellowish oil (96% yield).

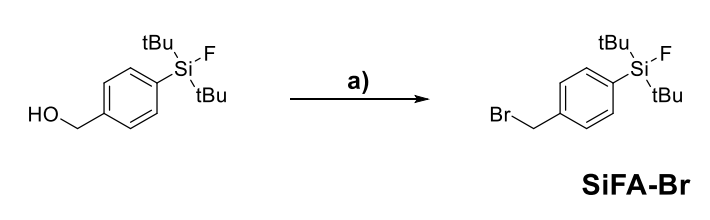
4-(Di-*tert*-butylfluorosilyl)benzaldehyde [4]: RP-HPLC: (50 to 100% B in 15 min): $t_R = 10.5$ min, $\kappa' = 3.27$.

4-(Di-*tert*-butylfluorosilyl)benzoic acid (= SiFA-BA)

The aldehyde [4] (1.0 eq.) was dissolved in *t*BuOH (23 mL/g educt), DCM (2.5 mL/g educt) and $\text{NaH}_2\text{PO}_4 \cdot \text{H}_2\text{O}$ (1.25 M, pH = 4.0–4.5, 15 mL/g educt) and $\text{KMnO}_{4,\text{aq}}$ (1.0 M, 23 mL/g educt) was added. After stirring for 25 min, the mixture was cooled to 5°C. KMnO_4 (1.0 eq.) was added, and the reaction quenched shortly afterwards by addition of sat. NaHCO_3 solution. The mixture was dried over MgSO_4 , and the solvent evaporated under reduced pressure. The crude product was purified by recrystallization from $\text{Et}_2\text{O}/n$ -hexane (1/3, v/v) and afforded a colorless solid (60% yield).

4-(Di-*tert*-butylfluorosilyl)benzoic acid (= SiFA-BA): RP-HPLC: (50 to 100% B in 15 min): $t_R = 8.5$ min, $\kappa' = 3.47$. Calculated monoisotopic mass ($\text{C}_{15}\text{H}_{23}\text{FO}_2\text{Si}$): 282.4; found: $m/z = 281.1$ [$\text{M}-\text{H}$] $^-$, 235.1 [$\text{M}-\text{COOH}$] $^-$.

2.2.6. SiFA-Bromide (SiFA-Br)



Scheme 5: Synthesis of SiFA-Br: a) CBr_4 , PPh_3 ; 0°C–r.t.

The Synthesis of SiFA-Br was performed according to a procedure described in literature (153). In short, the SiFA benzylalcohol was dissolved in DCM and the solution cooled to 0°C. CBr_4 (1.1 eq.) was added before PPh_3 was added over a period of 30 min in small portions. The mixture was then stirred for 2h at r.t., the solvent removed *in vacuo* and the remainder washed with *n*-hexane. The precipitate was filtered off and the liquid concentrated *in vacuo*. Subsequent silica flash chromatography employing *n*-pentane as mobile phase, afforded the desired product as a colorless oil (32–39% yield).

(4-Bromomethylphenyl)-di-*tert*-butyl-fluorosilane (SiFA-Br): RP-HPLC: (50 to 100% B in 15 min): $t_R = 15.10$ min, $\kappa' = 6.95$. Calculated monoisotopic mass ($C_{15}H_{24}BrFSi$): 330.08; found: $m/z = 331.3$ [M-H]⁻.

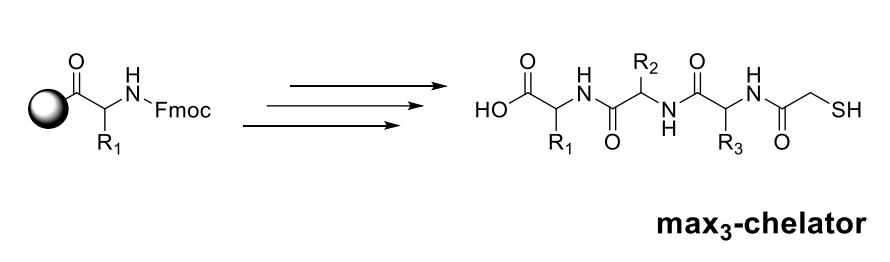
¹H NMR (300 MHz, CDCl₃, 293 K) δ 7.63–7.54 (m, 2H, 2x-CH-), 7.40 (d, $J = 8.0$ Hz, 2H, 2x-CH-), 4.50 (s, 2H, -CH₂-), 1.06 (d, $J = 1.2$ Hz, 18H, 2xtBu).

¹³C NMR (75 MHz, CDCl₃, 293 K) δ 139.50 (-CH-), 135.00 (-CH-), 134.95 (-CH-), 134.84 (-CH-), 134.66 (-CH-), 128.72 (-CH-), 33.88 (-CH₂-), 27.88 (6xtBu C), 20.92 (tert. C), 20.75 (tert. C).

2.2.7. Chelators

2.2.7.1. *max*₃-based Chelators

Independent of their respective amino acid identity (R_{1-3}), technetium chelators based on the combination of any 3 amino acids (= “x₃”) and a terminal 2-mercaptoacetic acid (= “ma”), were synthesized *via* standard Fmoc-peptide synthesis strategy according to general procedures 1, 2, 3 and 7.

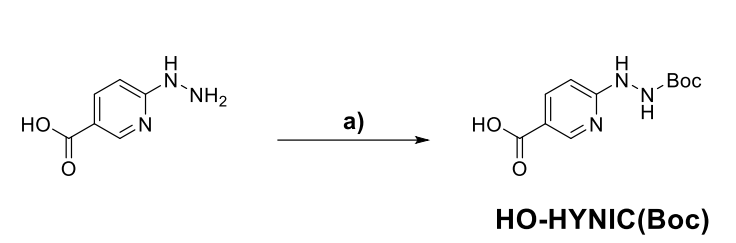


Scheme 6: Synthesis of *max*₃-based chelators according to Fmoc-peptide synthesis strategy.

Resulting protected chelators were either used in fragment condensation with a linker unit or in the case of glycosylated chelators, de-acetylated before coupling.

De-acetylation of β -D-glucose(OAc)₄- and β -D-lactose(OAc)₇-modified chelators was achieved by dissolving the crude chelators in MeOH (2 mL/50 mg) and adjusting the pH to 10–11 with KCN. After at least 4h at ambient temperature, de-acetylated chelators were precipitated in Et₂O.

2.2.7.2. HO-HYNIC(Boc)

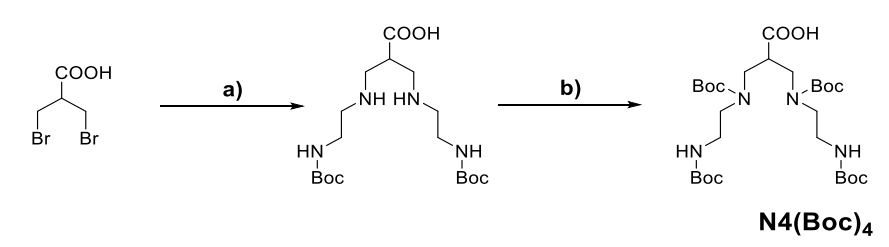


Scheme 7: Boc protection of 6-hydrazinonicotinic acid: a) Boc_2O (1.0 eq.), NEt_3 (1.3 eq.).

The Synthesis of HO-HYNIC(Boc) was realized following the published procedures (154,155). In short, 6-hydrazinonicotinic acid was reacted with Boc_2O (1.0 eq.) and triethylamine (1.3 eq.) in DMF overnight. The solvent was evaporated under reduced pressure and the crude product was subjected to silica flash-chromatography employing EtOAc followed by EtOAc + 1.0 vol% AcOH. The desired product was obtained as a white powder after removal of the solvent.

ESI-MS: Calculated monoisotopic mass ($\text{C}_{11}\text{H}_{15}\text{N}_3\text{O}_4$): 253.11, found: 254.4 $[\text{M}+\text{H}]^+$.

2.2.7.3. The N4 Chelator



Scheme 8: Synthesis of the protected N4 chelator: a) *Tert*-butyl-(2-aminoethyl)-carbamate (4.0 eq.); b) NEt_3 (3.0 eq.), Boc_2O (4.0 eq.).

3-((*tert*-butoxycarbonyl)(2-((*tert*-butoxycarbonyl)amino)ethyl)amino)-2-(((*tert*-butoxycarbonyl)(2-((*tert*-butoxycarbonyl)amino)ethyl)amino)methyl)Propanoic acid (N4 chelator) was synthesized on the basis of the published literature (156). In short, *tert*-butyl-(2-aminoethyl)-carbamate (4.0 eq.) was slowly added to 3-bromo-2-(bromomethyl)propanoic acid (1.0 eq.) in THF (25 mL/mmol) under vigorous stirring. The mixture was stirred for 4h at ambient temperature before removing the solvent under reduced pressure at ambient temperature. The crude product was dissolved in acetone/ H_2O (1/1 (v/v), 25 mL/mmol), cooled to 0 °C and NEt_3 (3.0 eq.) was added. After 5 min pre-activation, Boc_2O (4.0 eq.) was added. The

mixture was stirred for 15h (0°C to r.t.), the solvent removed under reduced pressure and the raw product purified via flash chromatography (35 to 95% MeCN in H₂O, 15 min).

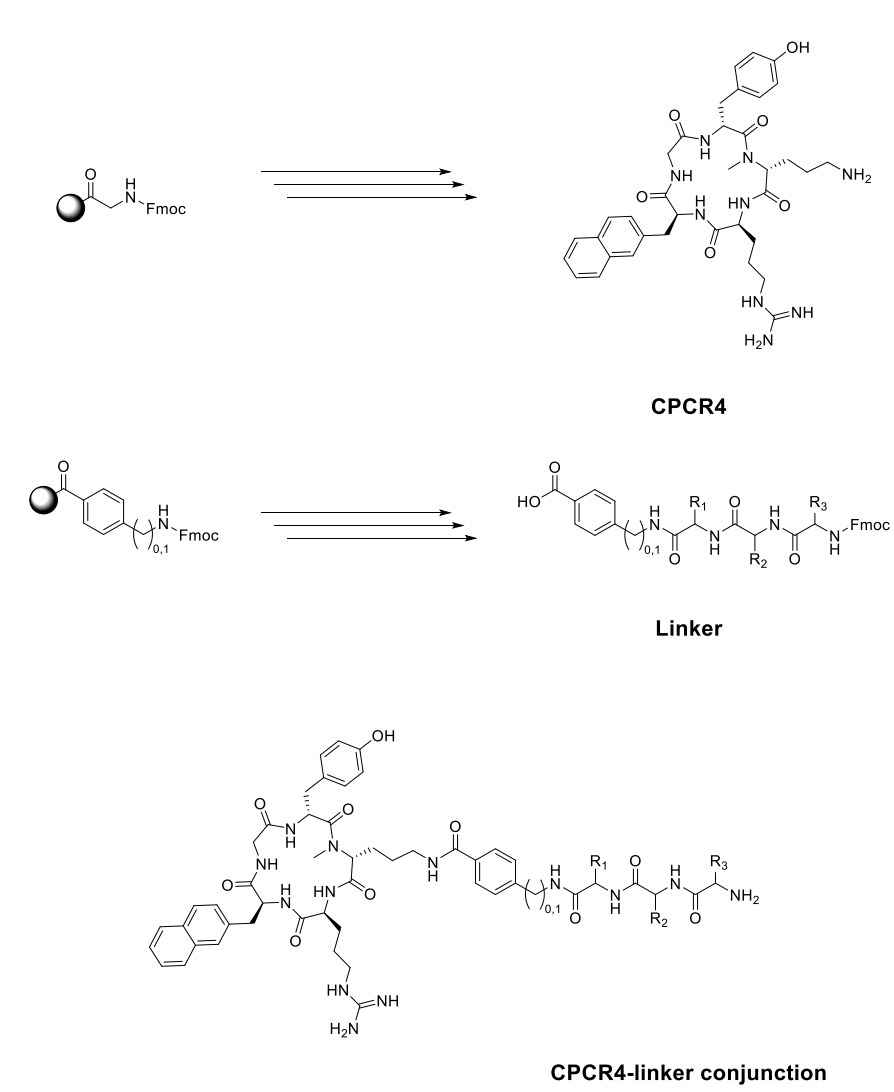
R_f (EtOAc+0.5 vol% AcOH) = 0.65.

MS (ESI, positive): calculated monoisotopic mass for C₂₈H₅₂N₄O₁₀: 604.37; found by ESI-MS: m/z = 605.0 [M+H]⁺.

¹H-NMR (400 MHz, DMSO-*d*₆) δ = 7.17-6.19 (m, 2H, NH), 3.28-3.17 (m, 6H, CH₂), 3.10-2.95 (m, 6H, CH₂), 2.94- 2.90 (m, 1H, CH), 1.38 (s, 18H, CH₃), 1.36 (s, 18H, CH₃).

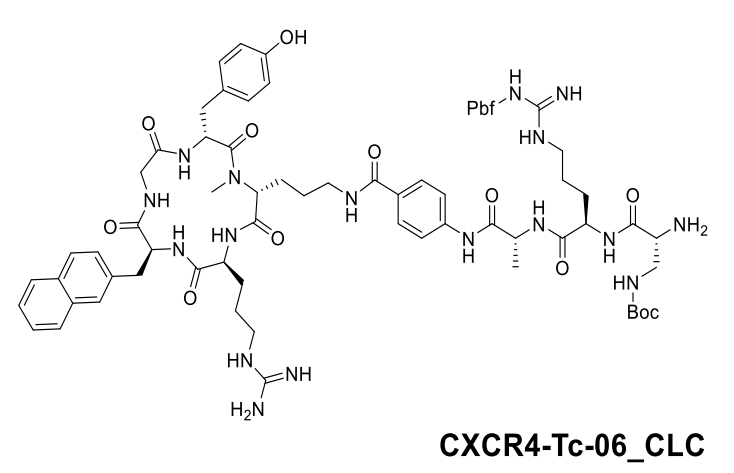
2.3. Synthesized Peptides

With the exception of only seven ligands within this study (namely CXCR4-Tc-01, -03–05 and CXCR4-MMAE-01–03), peptides were prepared by coupling of 2 fragments, the *CPCR4* peptide scaffold and a specific linker unit (L), prior to the addition of the functional moiety at the *N*-terminal site of the *CPCR4*-linker conjunction (CLC). This principle is visualized in the following scheme 9.



Scheme 9: Principle of CPCR4-linker conjunction synthesis; SPPS of the CPCR4 peptide scaffold, a universal linker unit CXCR4-X_L and the final product of a condensation between both fragments CXCR4-X_{CLC}.

Special focus is set on the *CPCR4*-linker conjunction of compound CXCR4-Tc-06, namely CXCR4-Tc-06_{CLC}. This sequence of amino acids was found relatively early within this study and was used as a basis for most of the labeling precursors and active compounds. In the presentation of results and the discussion of data, this peptide was paraphrased as optimized tracer backbone *CPCR4-Abz-a-r-dap* (Scheme 10).



Scheme 10: Structure of the *CPCR4*-linker conjunction *CXCR4-Tc-06_CLC*, paraphrased as optimized tracer backbone *CPCR4-Abz-a-r-dap*.

This synthon was produced multiple times in large amounts of up to 200 mg. Synthesis was carried out as depicted in the description for *CXCR4-Tc-06* below.

To obtain respective *CPCR4*-linker-conjunctions (CLC), the *CPCR4* peptide scaffold was elongated at the D-[NMe]Orn side chain with a fully protected linker unit according to GP8. These linker units (L) were synthesized *via* SPPS and are all based on HO-*Abz*- or HO-*Ambz*-, followed by two or three amino acids. A length of four chain links in the linker unit was not exceeded in most cases, as conversion with the peptide scaffold dropped drastically beyond the length of four. The linker units were cleaved off the resin under retention of all protecting groups (GP7a)), purified and coupled to the *CPCR4* peptide scaffold. After subsequent Fmoc de-protection, the *CPCR4*-linker conjunctions (CLC) were purified and reacted with the respective functional moiety (F), carrying a labeling moiety, a fluorescent dye or a toxin.

To classify the peptide fragments in the following part of the work, a letter-number code will be introduced:

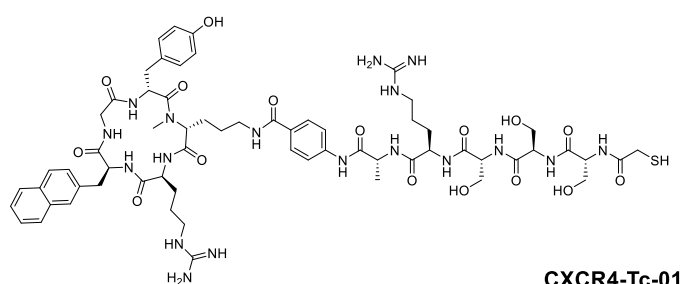
	CXCR4-	Project	-	Ligand-Nr.	_L/CLC/F
Project 1:	CXCR4-	Tc	-	01 - 15	_L/CLC/F
Project 2:	CXCR4-	DOTA	-	01 - 05	_L/CLC/F
Project 3:	CXCR4-	SiFA	-	01 - 07	_L/CLC/F
Project 4:	CXCR4-	MMAE	-	01 - 04	_L/CLC/F
Project 5:	CXCR4-	OI	-	01 - 03	_L/CLC/F
L	=	Peptide linker			
CLC	=	<i>CPCR4</i> -Linker conjunction			
F	=	Functional moiety			

Five different projects were pursued within this work: precursors for the labeling with technetium-99m (CXCR4-Tc series), DOTA-conjugated precursors for the labeling with lutetium-177 or gallium-68 (CXCR4-DOTA series), SiFA-conjugated precursors for the labeling with fluorine-18 (CXCR4-SiFA series), PDCs (CXCR4-MMAE series) and optical imaging devices (CXCR4-OI series). The following passage contains the description of fragment synthesis and the analytical data obtained for these fragments.

2.3.1. CXCR4-Tc-01 – 15

Two different types of technetium-99m labeling precursors were synthesized, all based on open-chain chelators. The first type includes the peptidic mas₃-conjugated (CXCR4-Tc-01 – 07) and the glycosylated chelators (CXCR4-Tc-08 – 11), whereas the second type of precursors is carrying the chelators HYNIC (CXCR4-Tc-12) or N4 (CXCR4-Tc-13 – 15). The synthesis of these types of chelators was depicted earlier.

CXCR4-Tc-01

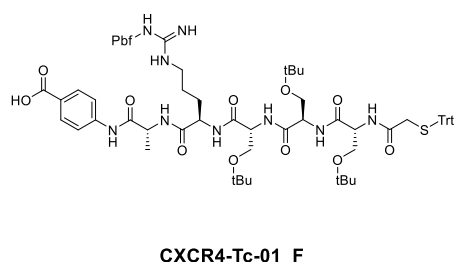


Synthesis of CXCR4-Tc-01 was achieved by fragment condensation (GP8) employing the fully deprotected and purified *CPCR4* peptide scaffold and the fully protected chelator-conjugated fragment

CXCR4-Tc-01_F. Final removal of all acid-labile protecting groups according to GP5 and purification *via semi-preparative* RP-HPLC yielded the desired product.

CXCR4-Tc-01: RP-HPLC (10 to 90% B in 15 min): $t_R = 9.82$ min, $\kappa' = 5.10$. Calculated monoisotopic mass (C₆₃H₈₆N₁₈O₁₆S): 1382.62, found: 692.2 [M+2H]²⁺.

Fragments used in the synthesis of CXCR4-Tc-01

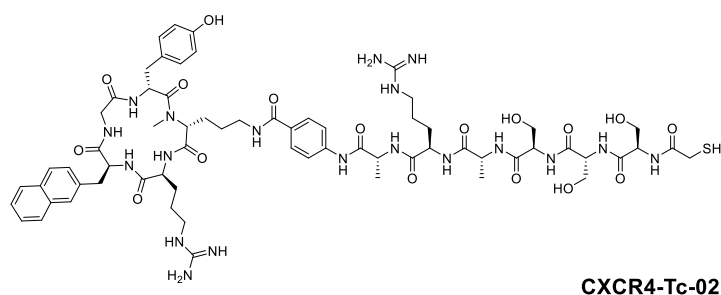


Fragment CXCR4-Tc-01_F was prepared by SPPS. Resin was loaded with Fmoc-Abz-OH (GP1) and Fmoc-D-Ala-OH coupled according with GP2b) and 3. Elongation of the peptide employing Fmoc-D-Arg(Pbf)-OH, Fmoc-D-Ser(tBu)-OH and Trityl-mercaptoacetic acid (GP2a), 3), cleavage off

the resin under retention of acid-labile protecting groups (GP7a)) and lastly *semi*-preparative RP-HPLC purification yielded the respective fragment.

CXCR4-Tc-01_F: RP-HPLC (40 to 95% B in 15 min): $t_R = 17.99$ min, $\kappa' = 11.32$. Calculated monoisotopic mass ($C_{71}H_{95}N_9O_{14}S_2$): 1361.64, found: 1363.1 $[M+H]^+$.

CXCR4-Tc-02

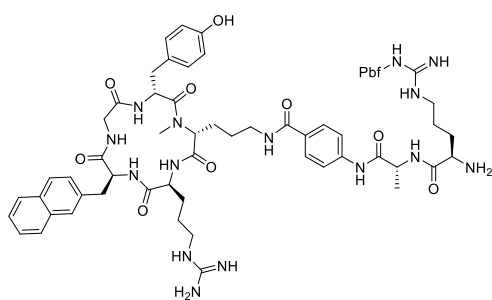


CXCR4-Tc-02 was synthesized by condensation of fragments CXCR4-02_CLC and CXCR4-Tc-02_F according with GP8. The resulting peptide was de-protected (GP5) and purified

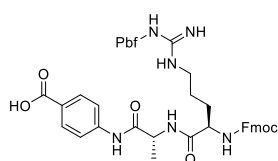
by *semi*-preparative RP-HPLC to yield the desired product.

CXCR4-Tc-02: RP-HPLC (15 to 45% B in 15 min): $t_R = 9.10$ min, $\kappa' = 3.55$. Calculated monoisotopic mass ($C_{66}H_{91}N_{19}O_{17}S$): 1453.66, found: 728.6 $[M+2H]^{2+}$.

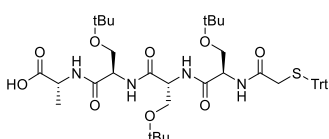
Fragments used in the synthesis of CXCR4-Tc-02



CXCR4-Tc-02_CLC



CXCR4-Tc-02_L



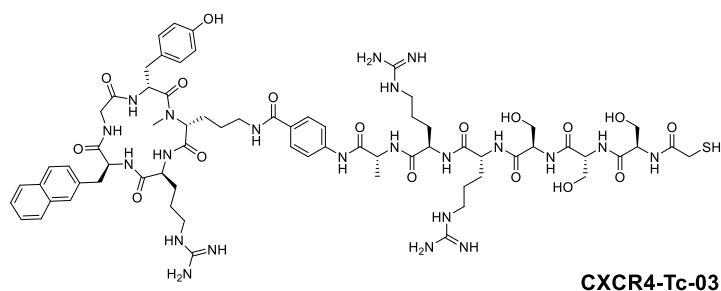
CXCR4-Tc-02_F

CXCR4-Tc-02_L was prepared starting out with resin-bound Fmoc-Abz-OH (GP1). Elongation with Fmoc-D-Ala-OH (GP2b, 3) and Fmoc-D-Arg(Pbf)-OH (GP2a, 3), followed by cleavage off the resin according with GP7a), yielded the respective product.

Condensation of the purified linker with the *CPCR4* peptide scaffold (GP8), subsequent Fmoc de-protection (GP3) and

purification by *semi*-preparative RP-HPLC afforded the synthon CXCR4-Tc-02_CLC. CXCR4-Tc-02_F was synthesized *via* SPPS on the basis of resin-bound Fmoc-D-Ala-OH (GP1). Coupling of Fmoc-D-Ser(*t*Bu)-OH and Tritylmercaptoacetic acid according with GP2a) and GP3, followed by resin cleavage (GP7a)) and purification *via semi*-preparative RP-HPLC afforded the desired synthon. CXCR4-Tc-02_L: RP-HPLC (10 to 90% B in 15 min): $t_R = 15.33$ min, $\kappa' = 8.48$. Calculated monoisotopic mass ($C_{44}H_{50}N_6O_9S$): 838.34, found: 839.1 $[M+H]^+$. CXCR4-Tc-02_CLC: RP-HPLC (10 to 90% B in 15 min): $t_R = 10.46$ min, $\kappa' = 6.07$. Calculated monoisotopic mass ($C_{65}H_{85}N_{15}O_{12}S$): 1299.62, found: 525.3 $[M-Pbf+2H]^{2+}$. CXCR4-Tc-02_F: RP-HPLC (40 to 100% B in 15 min): $t_R = 16.54$ min, $\kappa' = 8.68$. Calculated monoisotopic mass ($C_{45}H_{62}N_4O_9S$): 834.42, found: 835.2 $[M+H]^+$.

CXCR4-Tc-03

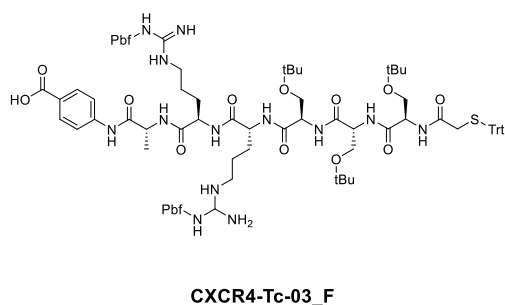


CXCR4-Tc-03 was synthesized as depicted for CXCR4-Tc-01. Condensation of the *CPCR4* peptide scaffold and the chelator-carrying fragment Tc-CXCR4-03_F was achieved applying GP8.

Final de-protection (GP5) and purification *via semi*-preparative RP-HPLC afforded the respective ligand.

CXCR4-Tc-03: RP-HPLC (10 to 90% B in 15 min): $t_R = 9.00$ min, $\kappa' = 4.63$. Calculated monoisotopic mass ($C_{69}H_{98}N_{22}O_{17}S$): 1538.72, found: 770.4 $[M+2H]^{2+}$.

Fragments used in the synthesis of CXCR4-Tc-03

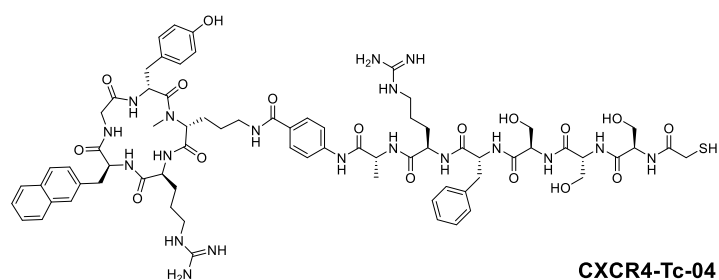


Fragment CXCR4-Tc-03_F was prepared by SPPS. Fmoc-Abz-OH was loaded onto 2-CTC resin (GP1) and elongated by linear synthesis with Fmoc-D-Ala-OH (GP3, 2b), Fmoc-D-Arg(Pbf)-OH, Fmoc-D-Ser(*t*Bu)-OH and Tritylmercaptoacetic acid (GP2a, 3). Cleavage off the resin under retention of

protecting groups (GP7a)) and subsequent purification by *semi*-preparative RP-HPLC provided the desired fragment.

CXCR4-Tc-03_F: RP-HPLC (10 to 90% B in 15 min): $t_R = 18.41$ min, $\kappa' = 11.50$. Calculated monoisotopic mass ($C_{90}H_{123}N_{13}O_{18}S_3$): 1769.83, found: 1771.2 $[M+H]^+$.

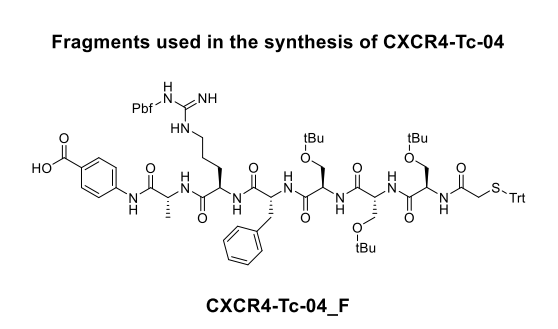
CXCR4-Tc-04



Compound CXCR4-Tc-04 was synthesized in analogy to CXCR4-Tc-01 and -03. The fragment CXCR4-Tc-04_F was condensed with *CPCR4* by means of GP8. Subsequent acidic de-protection according

with GP5 and purification by *semi*-preparative RP-HPLC afforded the respective ligand.

CXCR4-Tc-04: RP-HPLC (10 to 90% B in 15 min): $t_R = 10.20$ min, $\kappa' = 5.47$.
Calculated monoisotopic mass (C₇₂H₉₅N₁₉O₁₇S): 1529.69, found: 766.1 [M+2H]²⁺.

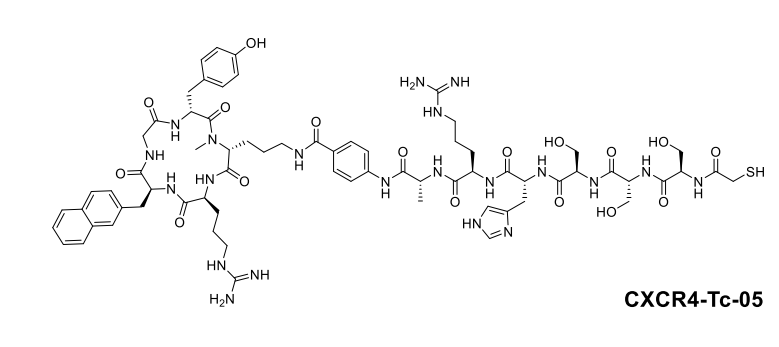


Fragment CXCR4-Tc-04_F was prepared by SPPS on the basis of resin-bound Fmoc-Abz-OH (GP1). Coupling of Fmoc-D-Ala-OH (GP2b), 3), Fmoc-D-Arg(Pbf)-OH, Fmoc-D-Phe-OH, Fmoc-D-Ser(*t*Bu)-OH and Tritylmercaptoacetic acid (GP2a), 3),

followed by cleavage off the resin (GP7a)) and *semi*-preparative RP-HPLC purification yielded the protected fragment.

CXCR4-Tc-04_F: RP-HPLC (10 to 90% B in 15 min): $t_R = 17.44$ min, $\kappa' = 10.49$.
Calculated monoisotopic mass (C₈₀H₁₀₄N₁₀O₁₅S₂): 1508.71, found: 1509.8 [M+H]⁺.

CXCR4-Tc-05

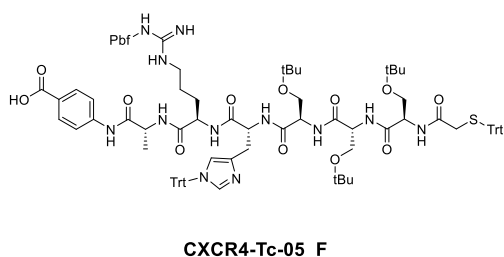


CXCR4-Tc-05 was synthesized in equivalence to CXCR4-Tc-01, -03 and -04. Briefly, fragment Tc-CXCR4-05_F was condensed with the CPCR4 peptide scaffold applying

GP8. Subsequent deprotection (GP5) and purification *via semi*-preparative RP-HPLC afforded the desired product.

CXCR4-Tc-05: RP-HPLC (10 to 90% B in 15 min): $t_R = 9.53$ min, $\kappa' = 4.74$. Calculated monoisotopic mass (C₆₉H₉₃N₂₁O₁₇S): 1519.68, found: 761.2 [M+2H]²⁺.

Fragments used in the synthesis of CXCR4-Tc-05



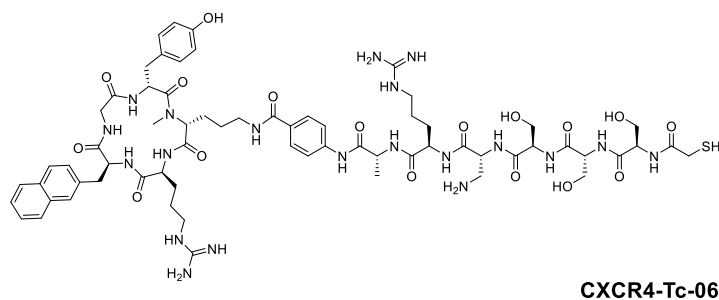
Fragment CXCR4-Tc-05_F was produced *via* SPPS. Fmoc-Abz-OH was immobilized on 2-CTC resin (GP1), Fmoc de-protected (GP3) and elongated with Fmoc-D-Ala-OH (GP2b)), Fmoc-D-Arg(Pbf)-OH, Fmoc-D-His(Trt)-OH, Fmoc-D-Ser(*t*Bu)-OH and Tritylmercaptoacetic acid (GP2a), 3).

Cleavage off the resin according with GP7a) yielded the fully protected synthon.

CXCR4-Tc-05_F: RP-HPLC (10 to 90% B in 15 min): $t_R = 17.84$ min, $\kappa' = 10.25$.

Calculated monoisotopic mass (C₉₆H₁₁₆N₁₂O₁₅S₂): 1740.81, found: 1742.3 [M+H]⁺.

CXCR4-Tc-06

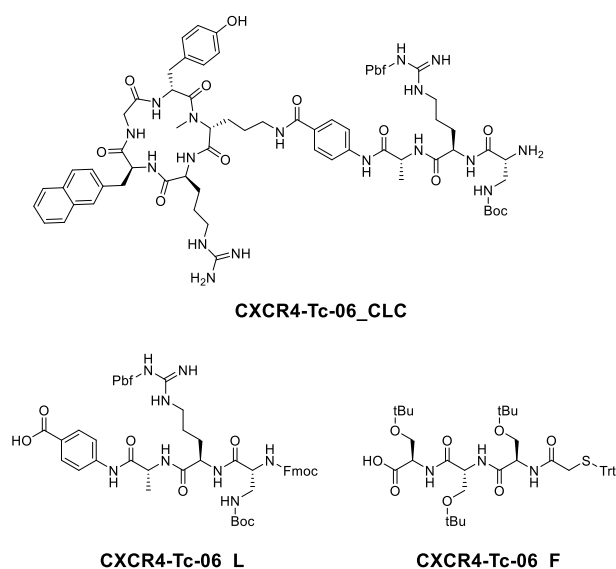


The synthesis of CXCR4-Tc-06 was based on the synthesis protocol for CXCR4-Tc-02. Fragments CXCR4-Tc-06_CLC and CXCR4-Tc-06_F were coupled following GP8.

Subsequent removal of all acid-labile protecting groups according with GP5 and purification *via semi-preparative* RP-HPLC afforded the desired product.

CXCR4-Tc-06: RP-HPLC (35 to 65% B in 15 min): $t_R = 8.85$ min, $\kappa' = 3.43$. Calculated monoisotopic mass (C₆₆H₉₂N₂₀O₁₇S): 1468.67, found: 735.1 [M+2H]²⁺.

Fragments used in the synthesis of CXCR4-Tc-06



CPCR4-linker conjunction CXCR4-Tc-06_CLC was prepared by condensation of fragments CPCR4 and CXCR4-Tc-06_L by means of GP8. Fmoc de-protection of the crude product (GP3) and purification by *semi*-preparative RP-HPLC yielded the respective synthon.

Linker structure CXCR4-Tc-06_L was synthesized using Fmoc-Abz-OH-loaded 2-CTC resin (GP1). Coupling of Fmoc-D-Ala-OH

(GP2b), 3), Fmoc-D-Arg(Pbf)-OH (GP2a), 3) and Fmoc-D-dap(Boc)-OH (GP2c), 3), followed by resin-cleavage according with GP7a), provided the respective fragment.

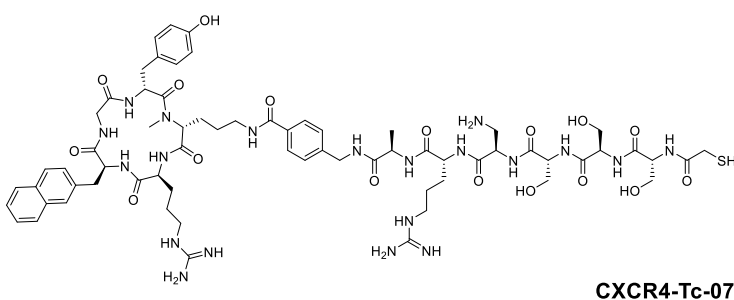
CXCR4-Tc-06_F was synthesized analogously *via* SPPS. Elongation of resin-bound Fmoc-D-Ser(*t*Bu)-OH (GP1) with the same amino acid and Tritylmercaptoacetic acid (GP2a), 3), followed by resin cleavage (GP7a)) yielded the fully protected functional fragment.

CXCR4-Tc-06_L: RP-HPLC (50 to 95% B in 15 min): $t_R = 13.52$ min, $\kappa' = 5.76$. Calculated monoisotopic mass (C₅₂H₆₄N₈O₁₂S): 1024.44, found: 1025.2 [M+H]⁺.

CXCR4-Tc-06_CLC: RP-HPLC (10 to 95% B in 15 min): $t_R = 8.83$ min, $\kappa' = 3.42$. Calculated monoisotopic mass (C₇₃H₉₉N₁₇O₁₅S): 1485.72, found: 744.6 [M+2H]²⁺.

CXCR4-Tc-06_F: HPLC (10 to 90% B in 15 min): $t_R = 14.85$ min, $\kappa' = 5.39$. Calculated monoisotopic mass (C₄₂H₅₇N₃O₈S): 763.39, found: 764.7 [M+H]⁺.

CXCR4-Tc-07

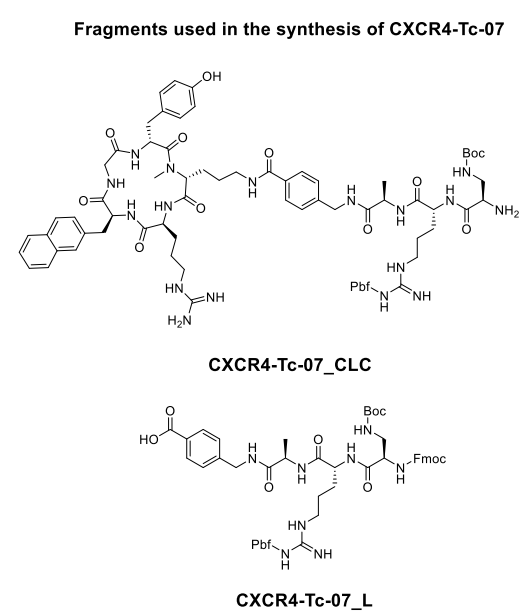


CXCR4-Tc-07 was prepared in accordance with the synthesis of CXCR4-Tc-06. Connection of the functional fragment Tc-CXCR4-06_F with synthon

CXCR4-Tc-07_CLC was facilitated by means of GP8. Subsequent de-protection of the

crude product according with GP5 and *semi*-preparative RP-HPLC purification yielded the desired product.

CXCR4-Tc-07: RP-HPLC (20 to 60% B in 15 min): $t_R = 7.26$ min, $\kappa' = 2.63$. Calculated monoisotopic mass ($C_{67}H_{94}N_{20}O_{17}S$): 1482.68, found: 742.4 $[M+2H]^{2+}$.

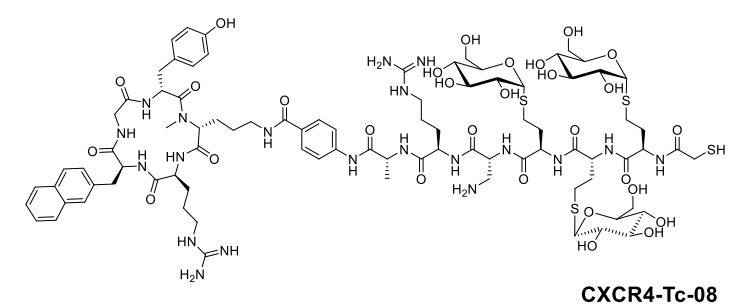


The linker CXCR4-Tc-07_L was produced in linear SPPS. Fmoc-Ambz-OH was immobilized on 2-CTC resin (GP1), Fmoc deprotected (GP3) and elongated with Fmoc-D-Ala-OH, Fmoc-D-Arg(Pbf)-OH (GP2a), 3) and Fmoc-D-dap(Boc)-OH (GP2c). Resin cleavage following GP7a) and purification *via semi*-preparative RP-HPLC afforded the respective linker.

CXCR4-Tc-07_L: RP-HPLC (30 to 90% B in 15 min): $t_R = 13.70$ min, $\kappa' = 5.85$. Calculated monoisotopic mass ($C_{53}H_{66}N_8O_{12}S$): 1038.45, found: 1039.6 $[M+H]^+$.

CXCR4-Tc-07_CLC: RP-HPLC (10 to 90% B in 15 min): $t_R = 8.97$ min, $\kappa' = 3.49$. Calculated monoisotopic mass ($C_{74}H_{101}N_{17}O_{15}S$): 1499.74, found: 750.2 $[M+2H]^{2+}$.

CXCR4-Tc-08

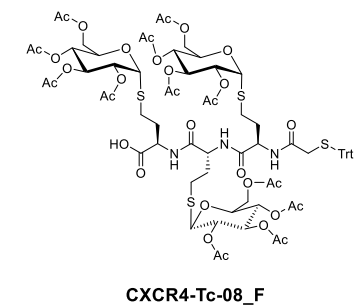


Synthesis of CXCR4-Tc-08 was based on the previously described synthesis of CXCR4-Tc-06. Fragments CXCR4-Tc-06_CLC and CXCR4-Tc-08_F were

condensed according with GP8. Deacetylation of the crude product was facilitated by incubation with KCN as depicted above. Subsequent removal of acid-labile protecting groups (GP5) and purification by *semi*-preparative RP-HPLC yielded the desired product.

CXCR4-Tc-08: RP-HPLC (5 to 55% B in 15 min): $t_R = 9.51$ min, $\kappa' = 3.76$. Calculated monoisotopic mass ($C_{87}H_{128}N_{20}O_{29}S_4$): 2044.80, found: 1023.7 $[M+2H]^{2+}$.

Fragments used in the synthesis of CXCR4-Tc-08

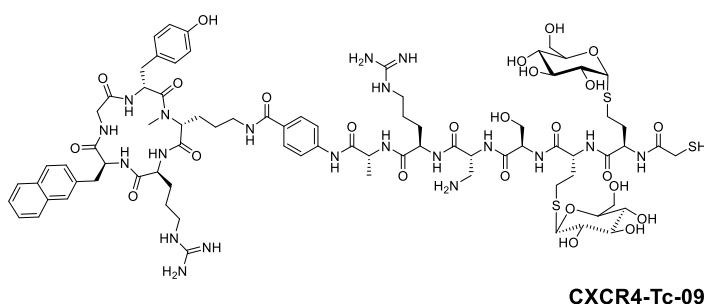


The β -D-glucosetetraacetate-modified chelator CXCR4-Tc-08_F was fabricated by SPPS using HO-D-HCy(β -D-glucosyl(OAc)₄)-Fmoc as starting material on 2-CTC resin (GP1). Coupling of the same amino acid and Tritylmercaptoacetic acid according with GP2a) and GP3, followed by cleavage off the resin under retention of acid-labile

protecting groups (GP7a)) and *semi*-preparative RP-HPLC purification, afforded the respective functional fragment.

CXCR4-Tc-08_F: RP-HPLC (10 to 95% B in 15 min): $t_R = 12.97$ min, $\kappa' = 6.59$. Calculated monoisotopic mass ($C_{75}H_{93}N_3O_{32}S_4$): 1675.46, found: 1677.2 $[M+H]^+$.

CXCR4-Tc-09

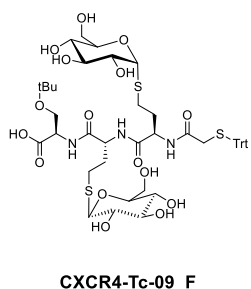


CXCR4-Tc-09 was synthesized as described for CXCR4-Tc-08. Fragment CXCR4-Tc-06_CLC was prepared as described above and condensed with the

deacetylated functional fragment CXCR4-Tc-09_F under use of GP8. De-protection according with GP5 and purification by *semi*-preparative RP-HPLC afforded the desired product.

CXCR4-Tc-09: RP-HPLC (10 to 60% B in 15 min): $t_R = 9.00$ min, $\kappa' = 3.00$. Calculated monoisotopic mass ($C_{80}H_{116}N_{20}O_{25}S_3$): 1852.76, found: 927.4 $[M+2H]^{2+}$, 618.7 $[M+3H]^{3+}$.

Fragments used in the synthesis of CXCR4-Tc-09

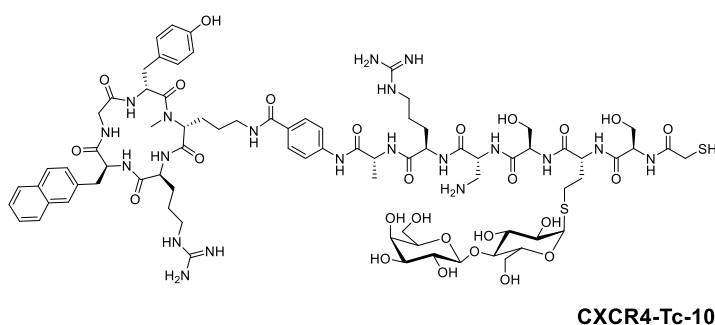


For the synthesis of fragment CXCR4-Tc-09_F, Fmoc-D-Ser(*t*Bu)-OH was immobilized on 2-CTC resin (GP1). Coupling of HO-D-HCy(β -D-glucosyl(OAc)₄)-Fmoc and Tritylmercaptoacetic acid (GP2a), 3), followed by resin cleavage (GP7a)) provided the crude fragment. Acetyl protecting groups were removed

by incubation with KCN as outlined above and the resulting fragment was by *semi*-preparative RP-HPLC before further reaction.

CXCR4-Tc-09_F: HPLC (10 to 95% B in 15 min): t_R = 8.70 min, κ' = 2.87. Calculated monoisotopic mass (C₄₈H₆₅N₃O₁₆S₃): 1035.35, found: 1036.3 [M+H]⁺.

CXCR4-Tc-10

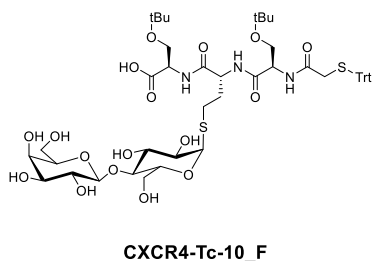


Compound CXCR4-Tc-10 was synthesized *via* fragment condensation in analogy with CXCR4-Tc-08 and -09. The de-acetylated chelator CXCR4-Tc-10_F was activated and coupled to the

CXCR4-Tc-06_CLC synthon according with GP8. De-protection (GP5) and *semi*-preparative RP-HPLC purification yielded the respective labeling precursor.

CXCR4-Tc-10: RP-HPLC (10 to 60% B in 15 min): t_R = 7.90 min, κ' = 2.38. Calculated monoisotopic mass (C₇₉H₁₁₄N₂₀O₂₆S₂): 1822.77, found: 920.4 [M+H₂O+2H]²⁺, 614.1 [M+H₂O+3H]³⁺.

Fragments used in the synthesis of CXCR4-Tc-10

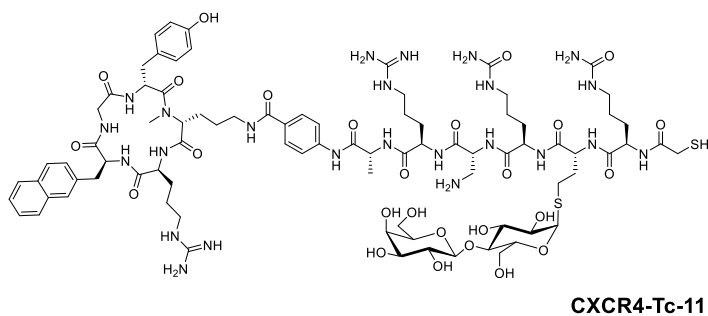


Functional fragment CXCR4-Tc-10_F was obtained by SPPS. Fmoc-D-Ser(*t*Bu)-OH was immobilized on 2-CTC resin (GP1) and elongated with Fmoc-D-HCy(β -D-lactosyl(OAc)₇)-OH, Fmoc-D-Ser(*t*Bu)-OH and Tritylmercaptoacetic acid (GP2a), 3). The chelator was cleaved off the

resin (GP7a)), de-acetylated as depicted above and purified by *semi*-preparative RP-HPLC.

CXCR4-Tc-10_F: RP-HPLC (10 to 95% B in 15 min): $t_R = 11.59$ min, $\kappa' = 4.68$. Calculated monoisotopic mass ($C_{51}H_{71}N_3O_{17}S_2$): 1061.42, found: 1061.8 $[M+H]^+$.

CXCR4-Tc-11

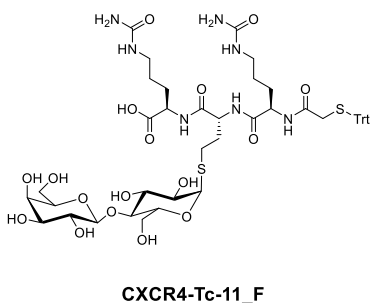


CXCR4-Tc-11 was obtained after fragment condensation (GP8) of synthon CXCR4-Tc-06_CLC and the chelator fragment CXCR4-Tc-11_F in analogy with CXCR4-Tc-08, -09

and -10. Removal of all acid-labile protecting groups (GP5) and purification *via semi*-preparative RP-HPLC afforded the desired product.

CXCR4-Tc-11: RP-HPLC (10 to 60% B in 15 min): $t_R = 8.00$ min, $\kappa' = 3.05$. Calculated monoisotopic mass ($C_{85}H_{126}N_{24}O_{26}S_2$): 1962.87, found: 982.6 $[M+2H]^{2+}$, 655.5 $[M+3H]^{3+}$.

Fragments used in the synthesis of CXCR4-Tc-11

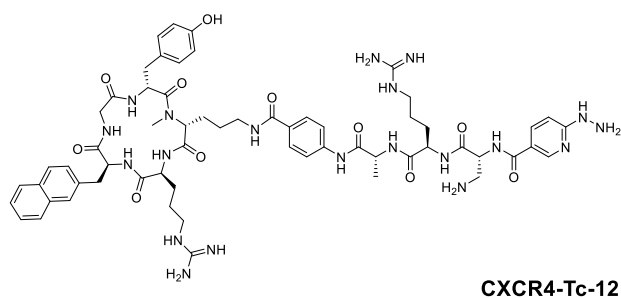


Fragment CXCR4-Tc-11_F was prepared by linear SPPS. Fmoc-D-Cit-OH was immobilized on 2-CTC resin (GP1), Fmoc de-protected (GP3) and elongated with Fmoc-D-HCy(β -D-lactosyl(OAc)₇)-OH, Fmoc-D-Cit-OH and Tritylmercaptoacetic acid (GP2a, 3). Cleavage off the resin (GP7a)) and de-acetylation as depicted above, followed by

purification by *semi*-preparative RP-HPLC yielded the respective synthon.

CXCR4-Tc-11_F: RP-HPLC (10 to 95% B in 15 min): $t_R = 7.90$ min, $\kappa' = 3.89$. Calculated monoisotopic mass ($C_{49}H_{67}N_7O_{17}S_2$): 1089.40, found: 1089.9 $[M+H]^+$.

CXCR4-Tc-12

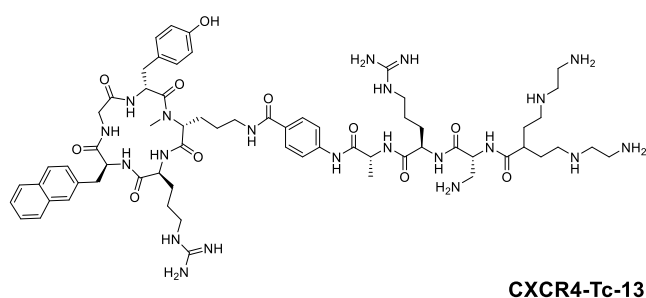


CXCR4-Tc-12 was obtained by coupling of the chelator HO-HYNIC(Boc) to the *CPCR4*-linker conjunction CXCR4-Tc-06_CLC according to GP8. Following de-protection of acid-labile protecting

groups (GP5) and purification *via semi*-preparative RP-HPLC yielded the respective compound.

CXCR4-Tc-12: RP-HPLC (5 to 55% B in 15 min): $t_R = 7.88$ min, $\kappa' = 2.36$. Calculated monoisotopic mass ($C_{61}H_{80}N_{20}O_{11}$): 1268.63, found: 635.6 $[M+2H]^{2+}$.

CXCR4-Tc-13

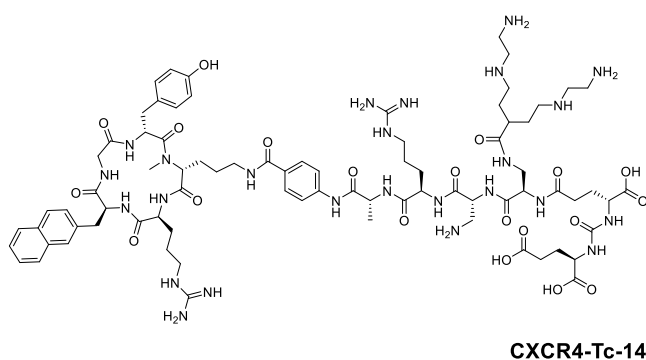


CXCR4-Tc-13 was synthesized as depicted for CXCR4-Tc-12. The fully protected N4 chelator was coupled to the synthon CXCR4-Tc-06_CLC (GP8). The resulting peptide was de-protected

according with GP5 and purified by *semi*-preparative RP-HPLC to afford the desired product.

CXCR4-Tc-13: RP-HPLC (10 to 60% B in 15 min): $t_R = 8.03$ min, $\kappa' = 3.94$. Calculated monoisotopic mass ($C_{63}H_{93}N_{21}O_{11}$): 1319.74, found: 660.7 $[M+2H]^{2+}$, 441.0 $[M+3H]^{3+}$.

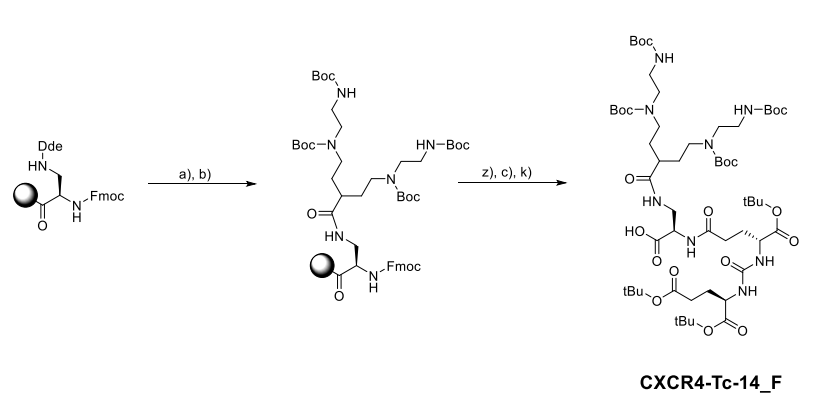
CXCR4-Tc-14



CXCR4-Tc-14 was synthesized in analogy to CXCR4-Tc-10. Fragment CXCR4-Tc-14_F was activated by means of GP8 and coupled to the fragment CXCR4-Tc-06_CLC. Global de-protection as outlined in GP5 and subsequent purification *via semi*-

preparative RP-HPLC afforded the desired product.

CXCR4-Tc-14: RP-HPLC (10 to 60% B in 15 min): $t_R = 8.03$ min, $\kappa' = 5.08$. Calculated monoisotopic mass ($C_{77}H_{113}N_{25}O_{20}$): 1707.86, found: 855.5 $[M+2H]^{2+}$, 570.6 $[M+3H]^{3+}$, 427.1 $[M+4H]^{4+}$.

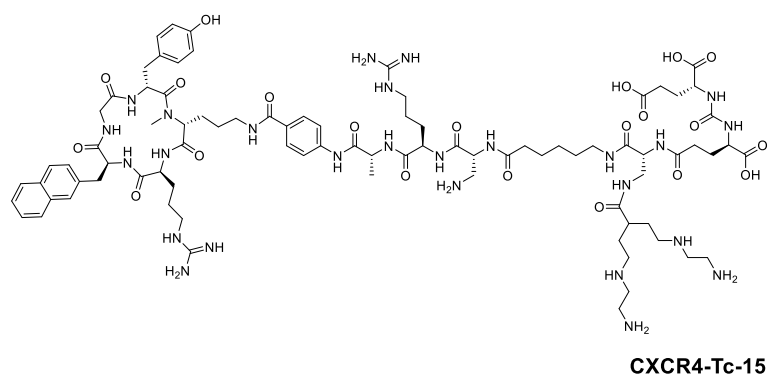


Scheme 11: Synthesis of the N4-chelator-conjugated moiety CXCR4-Tc-14_F: a) Imidazole (0.46 g), $[NH_3OH]Cl$ (0.63 g); b) HO-N4(Boc)₄ (1.5 eq.), HOAt (1.5 eq.), TBTU (1.5 eq.), 2,4,6-Collidine (3.0 eq.); z) 20% Piperidine in DMF (v/v); c) $(tBu)e(OH)ue(tBu)_2$ (1.5 eq.), HOAT (1.5 eq.), TBTU (1.5 eq.), DIPEA (3.0 eq.); k) 20% HFIP in DCM (v/v).

Fragment CXCR4-Tc-14_F was obtained by SPPS, starting out with immobilized Fmoc-D-dap(Dde)-OH (GP1). Specific Dde de-protection according to GP4b) provided the free side chain amine to couple the fully protected N4(Boc)₄ chelator (GP2). Fmoc de-protection (GP3) and coupling of the $(tBu)e(OH)ue(tBu)_2$ synthon (GP2), followed by cleavage off the resin (GP7a)) and purification by *semi*-preparative RP-HPLC resulted in the respective fragment.

CXCR4-Tc-14_F: RP-HPLC (10 to 95% B in 15 min): $t_R = 16.75$ min, $\kappa' = 10.10$. Calculated monoisotopic mass ($C_{54}H_{96}N_8O_{19}$): 1160.68, found: 1162.2 $[M+H]^+$, 531 $[M-Boc+2H]^{2+}$.

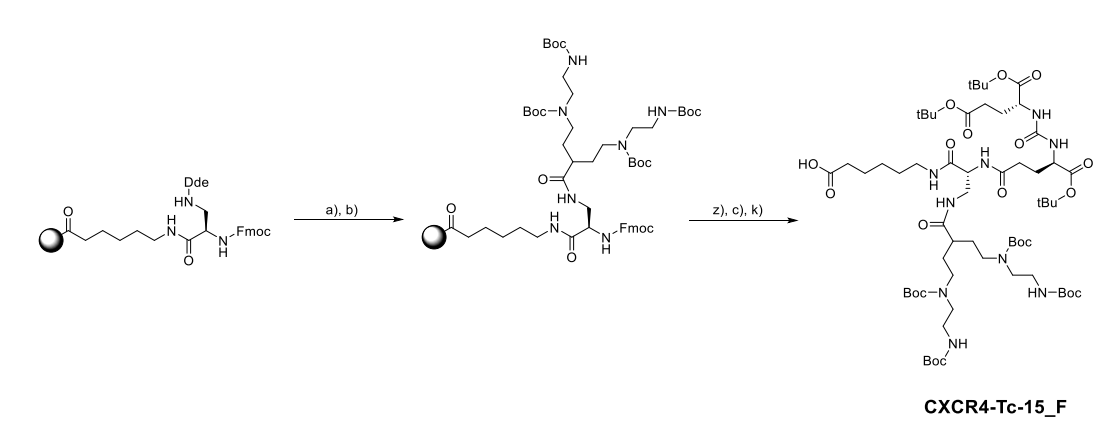
CXCR4-Tc-15



CXCR4-Tc-15 was obtained by condensation of fragments CXCR4-Tc-06_CLC and CXCR4-Tc-15_F by means of GP8. The resulting peptide was de-protected according with GP5 and

subjected to *semi*-preparative RP-HPLC purification to afford the desired product.

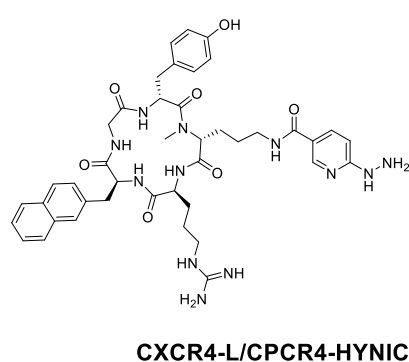
CXCR4-Tc-15: RP-HPLC (10 to 60% B in 15 min): $t_R = 7.83$ min, $\kappa' = 4.76$. Calculated monoisotopic mass ($C_{83}H_{124}N_{26}O_{21}$): 1820.94, found: 1821.5 $[M+H]^+$, 910.8 $[M+2H]^{2+}$, 607.4 $[M+3H]^{3+}$.



Scheme 12: Synthesis of the N4-chelator-conjugated moiety CXCR4-Tc-15_F: a) Imidazole (0.46 g), $[NH_3OH]Cl$ (0.63 g); b) HO-N4(Boc)₄ (1.5 eq.), HOAt (1.5 eq.), TBTU (1.5 eq.), 2,4,6-Collidine (3.0 eq.); z) 20% Piperidine in DMF (v/v); c) $(tBu)e(OH)ue(tBu)_2$ (1.5 eq.), HOAT (1.5 eq.), TBTU (1.5 eq.), DIPEA (3.0 eq.); k) 20% HFIP in DCM (v/v).

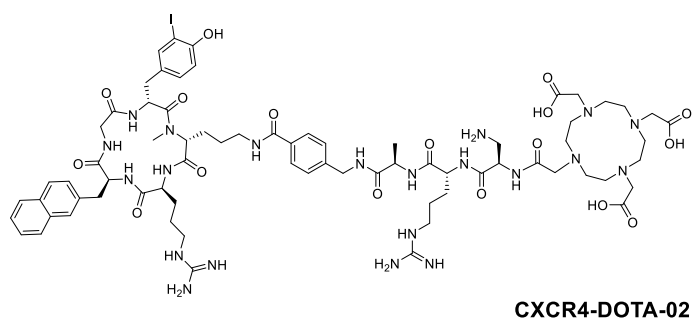
The fragment CXCR4-Tc-15_F was synthesized as described for CXCR4-14_F. Shortly, Fmoc-6-Ahx-OH was immobilized on 2-CTC resin (GP1). Fmoc de-protection (GP3) and coupling of Fmoc-D-dap(Dde)-OH (GP2c), followed by selective Dde de-protection (GP4b)), afforded a free side chain amine functionality. The fully protected N4(Boc)₄ chelator was coupled (GP2a)), the peptide Fmoc deprotected (GP3), elongated with the $(tBu)e(OH)ue(tBu)_2$ synthon (GP2a)), cleaved off the resin (GP7a)) and purified by *semi-preparative* RP-HPLC to yield the respective functional fragment. CXCR4-Tc-15_F: RP-HPLC (10 to 95% B in 15 min): $t_R = 16.57$ min, $\kappa' = 6.52$. Calculated monoisotopic mass ($C_{60}H_{107}N_9O_{20}$): 1273.76, found: 1274.6 $[M+H]^+$.

2.3.2. CXCR4-L/CPCR4-HYNIC



Compound CPCR4-HYNIC (*cyclo*(D-Tyr-D-[MMe]Orn(HYNIC)-Arg-2-Nal-Gly), literature-known as CXCR4-L, was synthesized by fragment condensation of CPCR4 and the synthon HO-HYNIC(Boc) following GP8. Subsequent de-protection according with GP5 and purification by

CXCR4-DOTA-02



CXCR4-DOTA-02 was obtained by iodination of the purified compound CXCR4-DOTA-01 with NIS as described above. Separation of the di-iodinated byproduct and unreacted educt by subjection to *semi-*

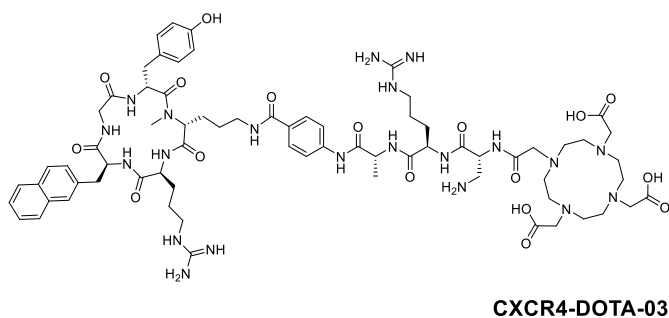
preparative RP-HPLC, yielded the respective product. Formation of ^{nat}Ga or ^{nat}Lu complexes was achieved by incubation of the final product with the respective salt as depicted above.

CXCR4-DOTA-02: RP-HPLC (10 to 60% B in 15 min): $t_R = 8.85$ min, $\kappa' = 3.02$. Calculated monoisotopic mass ($C_{72}H_{102}IN_{21}O_{17}$): 1659.68, found: 1660.6 $[M+H]^+$, 830.7 $[M+2H]^{2+}$, 553.9 $[M+3H]^{3+}$.

$[^{nat}Ga]CXCR4-DOTA-02$: RP-HPLC (10 to 60% B in 15 min): $t_R = 8.73$ min, $\kappa' = 5.98$. Calculated monoisotopic mass ($C_{72}H_{100}GaIN_{21}O_{17}$): 1726.59, found: 863.9 $[M+2H]^{2+}$, 576.6 $[M+3H]^{3+}$.

$[^{nat}Lu]CXCR4-DOTA-02$: RP-HPLC (10 to 60% B in 15 min): $t_R = 8.80$ min, $\kappa' = 6.04$. Calculated monoisotopic mass ($C_{72}H_{99}LuN_{21}O_{17}$): 1831.60, found: 916.8 $[M+2H]^{2+}$, 611.6 $[M+3H]^{3+}$.

CXCR4-DOTA-03



CXCR4-DOTA-03 was synthesized by coupling of DOTA to the CXCR4-Tc-06_CLC synthon according with the described procedure above. Subsequent deprotection (GP5) and purification by *semi-*preparative RP-HPLC

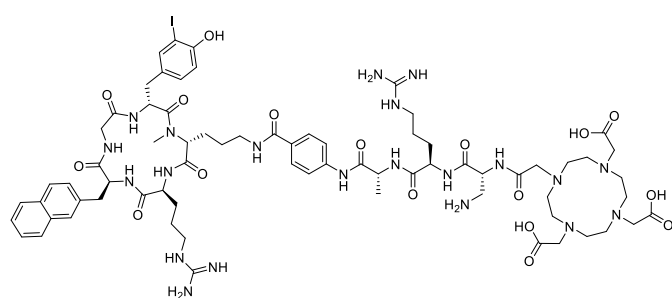
yielded the desired product. Complexes with ^{nat}Ga and ^{nat}Lu were obtained by incubation with the respective salt as depicted above.

CXCR4-DOTA-03: RP-HPLC (20 to 75% B in 15 min): $t_R = 5.36$ min, $\kappa' = 1.33$. Calculated monoisotopic mass ($C_{71}H_{101}N_{21}O_{17}$): 1519.77, found: 1521.0 $[M+H]^+$, 760.8 $[M+2H]^{2+}$, 507.9 $[M+3H]^{3+}$.

[^{nat}Ga]CXCR4-DOTA-03: RP-HPLC (20 to 75% B in 15 min): $t_R = 6.65$ min, $\kappa' = 1.89$.
Calculated monoisotopic mass (C₇₁H₉₉GaN₂₁O₁₇): 1586.68, found: 1569.5 [M+H]⁺,
795.0 [M+2H]²⁺, 529.6 [M+3H]³⁺.

[^{nat}Lu]CXCR4-DOTA-03: RP-HPLC (20 to 75% B in 15 min): $t_R = 6.62$ min, $\kappa' = 1.76$.
Calculated monoisotopic mass (C₇₁H₉₈LuN₂₁O₁₇): 1691.69, found: 1691.9 [M+H]⁺,
846.8 [M+2H]²⁺, 565.1 [M+3H]³⁺.

CXCR4-DOTA-04



CXCR4-DOTA-04

Ligand CXCR4-DOTA-04 was obtained by iodination of compound CXCR4-DOTA-03 with NIS as described above. The resulting reaction mixture was subjected to *semi-preparative* RP-HPLC purification to afford the

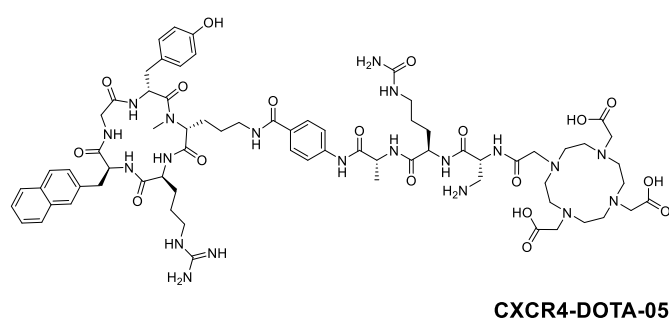
desired product. Complexes with metals ^{nat}Ga and ^{nat}Lu were formed by incubation with the respective salt as depicted above.

CXCR4-DOTA-04: RP-HPLC (20 to 80% B in 15 min): $t_R = 5.72$ min, $\kappa' = 1.54$.
Calculated monoisotopic mass (C₇₁H₁₀₀IN₂₁O₁₇): 1645.67, found: 1647.2 [M+H]⁺,
824.4 [M+2H]²⁺, 550.0 [M+3H]³⁺.

[^{nat}Ga]CXCR4-DOTA-04: RP-HPLC (20 to 80% B in 15 min): $t_R = 5.52$ min, $\kappa' = 1.40$.
Calculated monoisotopic mass (C₇₁H₉₈GaN₂₁O₁₇): 1712.58, found: 857.1 [M+2H]²⁺,
572.2 [M+3H]³⁺.

[^{nat}Lu]CXCR4-DOTA-04: RP-HPLC (20 to 80% B in 15 min): $t_R = 5.55$ min, $\kappa' = 1.44$.
Calculated monoisotopic mass (C₇₁H₉₇LuN₂₁O₁₇): 1817.58, found: 910.2 [M+2H]²⁺,
607.1 [M+3H]³⁺.

CXCR4-DOTA-05



CXCR4-DOTA-05 was synthesized by fragment condensation of the CPCR4 peptide scaffold with the linker unit CXCR4-DOTA-05_L following GP8. Subsequent de-protection according with GP5 and

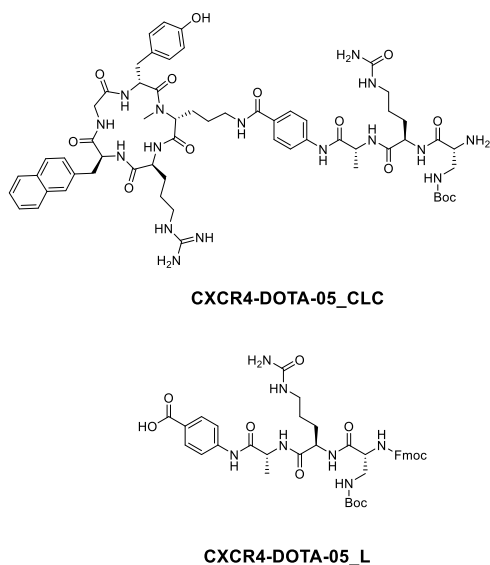
purification *via semi-preparative* RP-HPLC yielded the desired product. Complexes with ^{nat}Ga and ^{nat}Lu were formed as depicted.

CXCR4-DOTA-05: RP-HPLC (10 to 60% B in 15 min): $t_R = 8.40$ min, $\kappa' = 5.46$. Calculated monoisotopic mass ($\text{C}_{71}\text{H}_{100}\text{N}_{20}\text{O}_{18}$): 1520.75, found: 1522.0 $[\text{M}+\text{H}]^+$, 761.6 $[\text{M}+2\text{H}]^{2+}$.

$[\text{nat}\text{Ga}]$ CXCR4-DOTA-05: RP-HPLC (10 to 60% B in 15 min): $t_R = 8.33$ min, $\kappa' = 5.41$. Calculated monoisotopic mass ($\text{C}_{71}\text{H}_{98}\text{N}_{20}\text{GaO}_{18}$): 1587.66, found: 794.6 $[\text{M}+2\text{H}]^{2+}$, 529.8 $[\text{M}+3\text{H}]^{3+}$.

$[\text{nat}\text{Lu}]$ CXCR4-DOTA-05: RP-HPLC (10 to 60% B in 15 min): $t_R = 8.42$ min, $\kappa' = 5.48$. Calculated monoisotopic mass ($\text{C}_{71}\text{H}_{97}\text{LuN}_{20}\text{O}_{18}$): 1692.67, found: 847.2 $[\text{M}+2\text{H}]^{2+}$, 565.1 $[\text{M}+3\text{H}]^{3+}$.

Fragments used in the synthesis of CXCR4-DOTA-05



The linker synthon CXCR4-DOTA-05_L was prepared by SPPS employing resin-bound Fmoc-Abz-OH (GP1) as starting material. Elongation with Fmoc-D-Ala-OH (GP2b), 3), Fmoc-D-Cit-OH (GP2a), 3) and Fmoc-D-dap(Boc)-OH (GP2c), 3), followed by cleavage off the resin under retention of acid-labile protecting groups (GP7a)), provided the crude linker.

After *semi-preparative* RP-HPLC purification of the linking moiety, CPCR4 was functionalized on its free amine side chain

with the respective linker, applying GP8. Fmoc de-protection (GP3) and purification by *semi-preparative* RP-HPLC afforded the respective CPCR4-linker conjunction.

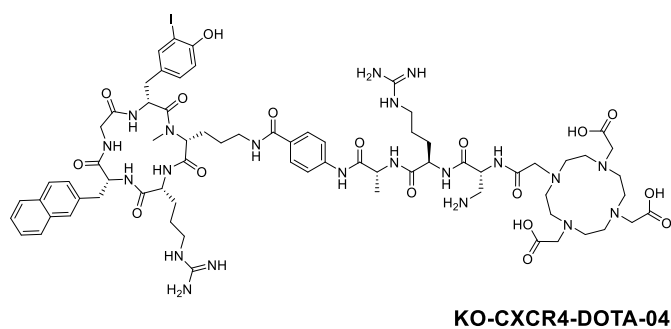
CXCR4-DOTA-05_L: RP-HPLC (10 to 95% B in 15 min): $t_R = 10.86$ min, $\kappa' = 3.98$.

Calculated monoisotopic mass ($C_{39}H_{47}N_7O_{10}$): 773.34, found: 774.5 $[M+H]^+$.

CXCR4-DOTA-05_CLC: RP-HPLC (10 to 95% B in 15 min): $t_R = 7.03$ min, $\kappa' = 3.39$.

Calculated monoisotopic mass ($C_{60}H_{82}N_{16}O_{13}$): 1234.62, found: 618.2 $[M+2H]^{2+}$.

KO-CXCR4-DOTA-04



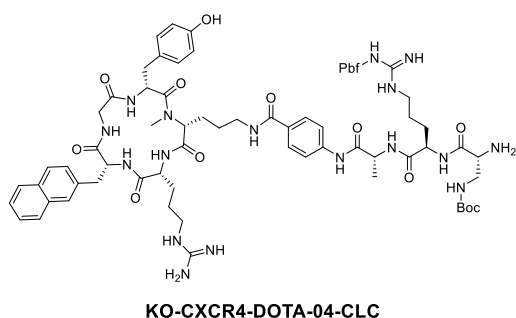
The knock-out ligand KO-CXCR4-DOTA-04 was prepared in analogy with CXCR4-DOTA-03. DOTA was connected to the free amine-bearing synthon KO-CXCR4-DOTA-04_CLC as

depicted above. Removal of acid-labile protecting groups (GP5) and *semi*-preparative RP-HPLC purification yielded the respective crude product. Iodination of the purified compound as depicted above and subsequent removal of byproducts by *semi*-preparative RP-HPLC purification afforded the desired product. Stable complexes were formed by incubation with the respective ^{nat}Ga or ^{nat}Lu salts as described above. KO-CXCR4-DOTA-04: RP-HPLC (10 to 60% B in 15 min): $t_R = 10.17$ min, $\kappa' = 3.62$. Calculated monoisotopic mass ($C_{71}H_{100}IN_{21}O_{17}$): 1645.67, found: 824.5 $[M+2H]^{2+}$, 550.2 $[M+3H]^{3+}$.

$[^{nat}Ga]KO-CXCR4-DOTA-04$: RP-HPLC (10 to 60% B in 15 min): $t_R = 10.05$ min, $\kappa' = 3.57$. Calculated monoisotopic mass ($C_{71}H_{98}GaIN_{21}O_{17}$): 1712.58, found: 857.7 $[M+2H]^{2+}$, 572.5 $[M+3H]^{3+}$.

$[^{nat}Lu]KO-CXCR4-DOTA-04$: RP-HPLC (10 to 60% B in 15 min): $t_R = 10.13$ min, $\kappa' = 3.60$. Calculated monoisotopic mass ($C_{71}H_{97}ILuN_{21}O_{17}$): 1817.58, found: 910.9 $[M+2H]^{2+}$, 607.5 $[M+3H]^{3+}$.

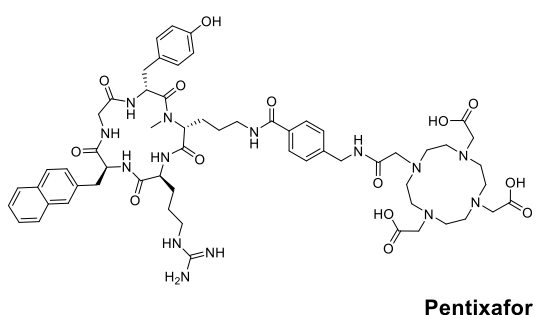
Fragments used in the synthesis of KO-CXCR4-DOTA-04



Coupling of the linker unit CXCR4-Tc-06_L to the KO-CPCR4 peptide scaffold was facilitated applying GP8. Subsequent Fmoc de-protection (GP3) and purification by *semi*-preparative RP-HPLC, yielded the KO-CXCR4-DOTA-04_CLC synthon.

KO-CXCR4-DOTA-04_CLC: RP-HPLC (10 to 95% B in 15 min): $t_R = 8.95$ min, $\kappa' = 3.48$. Calculated monoisotopic mass ($C_{73}H_{99}N_{17}O_{15}S$): 1485.72, found: 744.8 $[M+2H]^{2+}$.

2.3.4. Pentixafor



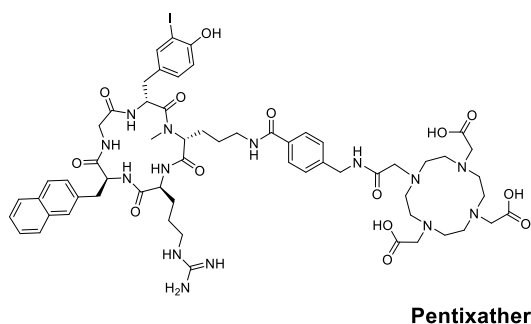
Synthesis of Pentixafor (*cyclo*(D-Tyr-D-[MMe]Orn(Ambz-DOTA)-Arg-2-Nal-Gly) was carried out according with the published literature (138). In short, HO-Ambz-Fmoc was coupled to CPCR4 (GP8) and the product Fmoc de-protected (GP3). After purification *via semi*-

preparative RP-HPLC, DOTA was coupled as described. The resulting peptide was purified by *semi*-preparative RP-HPLC to afford the desired product. Complexation was achieved by incubation with $[^{nat}Ga]Ga(NO_3)_3$ as depicted above.

Pentixafor: RP-HPLC (15 to 45% B in 15 min): $t_R = 14.96$ min, $\kappa' = 9.19$. Calculated monoisotopic mass ($C_{60}H_{80}N_{14}O_{14}$): 1220.60, found: 1220.8 $[M+H]^+$.

$[^{nat}Ga]$ Pentixafor: RP-HPLC (10 to 60% B in 15 min): $t_R = 8.73$ min, $\kappa' = 3.37$. Calculated monoisotopic mass ($C_{60}H_{78}GaN_{14}O_{14}$): 1287.51, found: 863.9 $[M+2H]^{2+}$, 576.6 $[M+3H]^{3+}$.

2.3.5. Pentixather



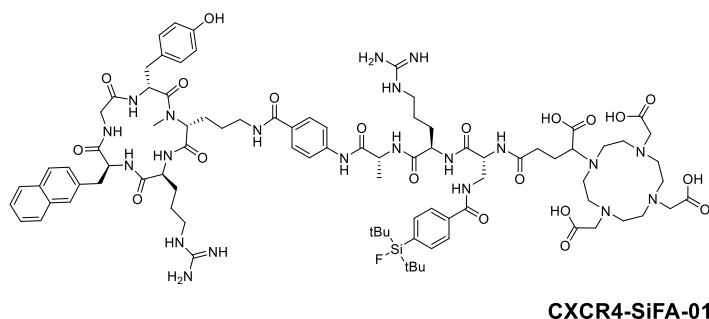
Pentixather was obtained by iodination of the purified Pentixafor scaffold using NIS as described. Removal of the byproduct and recovery of the educt *via semi-preparative* RP-HPLC provided the desired ligand. Incubation with [^{nat}Lu]LuCl₃ as outlined above, afforded the respective complex.

Pentixather: RP-HPLC (15 to 45% B in 15 min): $t_R = 10.60$ min, $\kappa' = 4.30$. Calculated monoisotopic mass (C₆₀H₇₉I₁₄O₁₄): 1346.59, found: 1347.7 [M+H]⁺, 676.2[M+2H]²⁺.
[^{nat}Lu]Pentixather: RP-HPLC (10 to 60% B in 15 min): $t_R = 9.34$ min, $\kappa' = 4.19$. Calculated monoisotopic mass (C₆₀H₇₉LuN₁₄O₁₄): 1518.41, found: 1519.2 [M+H]⁺, 760.4 [M+2H]²⁺.

2.3.6. CXCR4-SiFA-01 – 07

Moieties bearing a silicon-fluoride accepting functionality (SiFA) were produced using the synthon SiFA-benzoic acid (SiFA-BA) or SiFA-benzyl bromide (SiFA-Br). The synthesis of these building blocks was outlined above. The respective functional fragments, carrying a SiFA moiety were purified and used in standard peptide synthesis.

CXCR4-SiFA-01



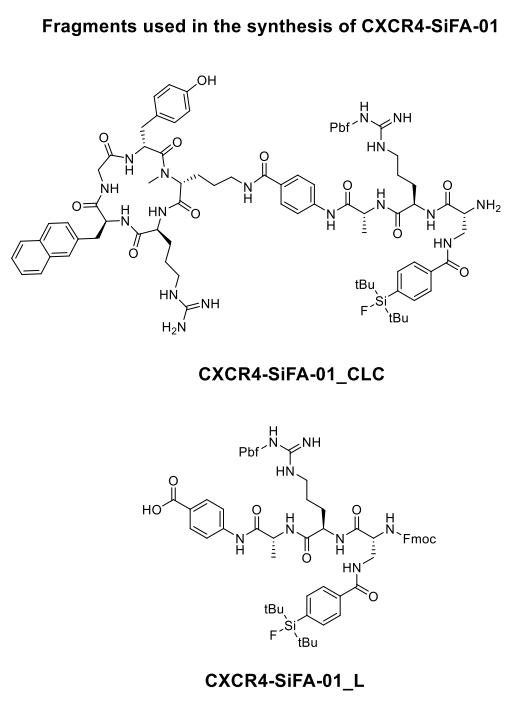
CXCR4-SiFA-01 was synthesized by fragment condensation of the *CPCR4*-linker conjunction CXCR4-SiFA-01_CLC (1.0 eq.) with DOTA-GA anhydride (1.1 eq.) in DMF

and DIPEA (3.0 eq.). After 3h at ambient temperature, the solvent was evaporated under reduced pressure and the crude product was de-protected according with GP5.

Purification *via semi-preparative RP-HPLC* afforded the desired product. Complexes with ^{nat}Ga and ^{nat}Lu were formed as described above.

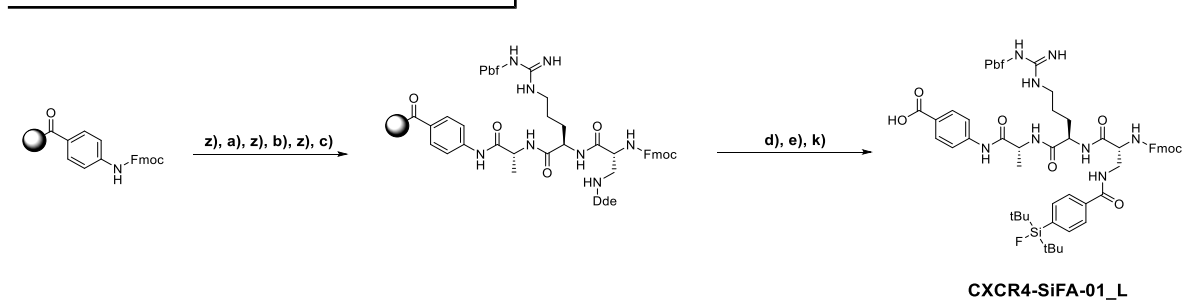
$^{[nat}\text{Ga}]$ CXCR4-SiFA-01: RP-HPLC (10 to 90% B in 15 min): $t_R = 8.98$ min, $\kappa' = 3.48$.
Calculated monoisotopic mass ($\text{C}_{89}\text{H}_{124}\text{FGaN}_{21}\text{O}_{20}\text{Si}$): 1922.83, found: 1924.0
 $[\text{M}+\text{H}]^+$, 962.9 $[\text{M}+2\text{H}]^{2+}$.

$^{[nat}\text{Lu}]$ CXCR4-SiFA-01: RP-HPLC (10 to 90% B in 15 min): $t_R = 9.77$ min, $\kappa' = 3.94$.
Calculated monoisotopic mass ($\text{C}_{89}\text{H}_{124}\text{FLuN}_{21}\text{O}_{20}\text{Si}$): 2028.85, found: 1015.1
 $[\text{M}+2\text{H}]^{2+}$.



CXCR4-SiFA-01_CLC was prepared by coupling of the CXCR4-SiFA-01_L linker unit to the *CPCR4* peptide scaffold by means of GP8. Fmoc de-protection (GP3) and purification by *semi-preparative RP-HPLC* yielded the respective synthon.

The synthesis of CXCR4-SiFA-01_L was performed as depicted in Scheme 13.



Scheme 13: Synthesis of CXCR4-SiFA-01_L via SPPS: z) 20% Piperidine in DMF (v/v); a) Fmoc-D-Ala-OH (2.0 eq.), HOAt (2.0 eq.), HATU (2.0 eq.), DIPEA (5.0 eq.); b) Fmoc-D-Arg(Pbf)-OH (1.5 eq.), HOAt (1.5 eq.), TBTU (1.5 eq.), DIPEA (3.0 eq.); c) Fmoc-D-dap(Dde)-OH (1.5 eq.), HOAt (1.5 eq.), TBTU (1.5 eq.), 2,4,6-Collidine (3.0 eq.); d) Imidazole (0.46 g), $[\text{NH}_2\text{OH}]\text{Cl}$ (0.63 g); e) SiFA-BA-OH (1.5 eq.), HOAt (1.5 eq.), TBTU (1.5 eq.), DIPEA (3.0 eq.); k) 20% HFIP in DCM (v/v).

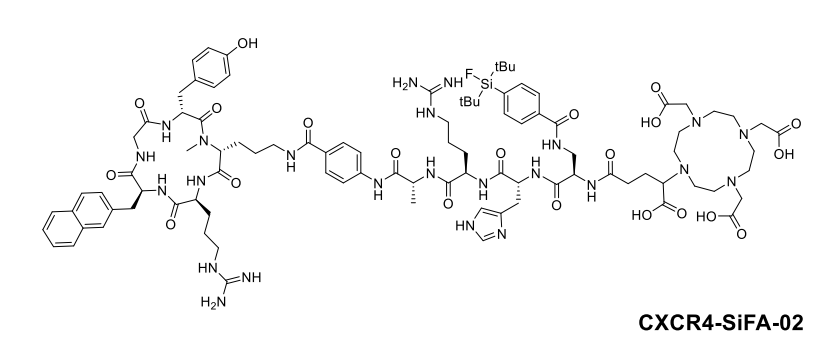
CXCR4-SiFA-01_L was synthesized by immobilization of Fmoc-Abz-OH on 2-CTC resin (GP1). Elongation with Fmoc-D-Ala-OH (GP2b), 3), Fmoc-D-Arg(Pbf)-OH (GP2a),

3) and Fmoc-D-dap(Dde)-OH (GP2c), 3) was followed by selective Dde side chain de-protection (GP4b)) and coupling of SiFA-BA (GP2a)). The peptide fragment was cleaved off the resin under retention of acid-labile protecting groups (GP7a)) and purified by *semi*-preparative RP-HPLC to yield the desired linker unit.

CXCR4-SiFA-01_L: RP-HPLC (50 to 95% B in 15 min): $t_R = 17.70$ min, $\kappa' = 10.00$.
Calculated monoisotopic mass ($C_{62}H_{77}FN_8O_{11}SSi$): 1188.52, found: 1189.3 $[M+H]^+$.

CXCR4-SiFA-01_CLC: RP-HPLC (20 to 100% B in 15 min): $t_R = 12.49$ min, $\kappa' = 8.99$.
Calculated monoisotopic mass ($C_{83}H_{112}FN_{17}O_{14}SSi$): 1649.80, found: 1651.3 $[M+H]^+$.

CXCR4-SiFA-02



Ligand CXCR4-SiFA-02 was prepared in analogy with CXCR4-SiFA-01. In short, synthon CXCR4-SiFA-02_CLC (1.0 eq.) was coupled with DOTA-GA anhydride

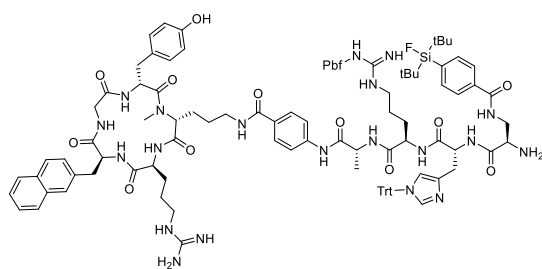
(1.1 eq.) under usage of DIPEA (3.0 eq.) in DMF (3h, r.t.). The solvent was evaporated under reduced pressure, the crude product de-protected according with GP5 and purified *via semi*-preparative RP-HPLC to afford the desired product. Cold complexes with ^{nat}Ga and ^{nat}Lu were formed as depicted above.

CXCR4-SiFA-02: RP-HPLC (10 to 90% B in 15 min): $t_R = 8.43$ min, $\kappa' = 3.22$.
Calculated monoisotopic mass ($C_{95}H_{133}FN_{24}O_{21}Si$): 1992.98, found: 997.2 $[M+2H]^{2+}$, 665.7 $[M+3H]^{3+}$.

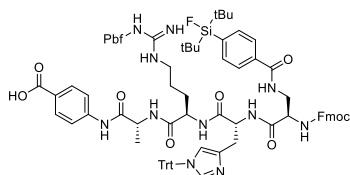
$[^{nat}Ga]CXCR4-SiFA-02$: RP-HPLC (10 to 90% B in 15 min): $t_R = 5.40$ min, $\kappa' = 1.84$.
Calculated monoisotopic mass ($C_{95}H_{131}FGaN_{24}O_{21}Si$): 2059.89, found: 1031.2 $[M+2H]^{2+}$, 688.8 $[M+3H]^{3+}$.

$[^{nat}Lu]CXCR4-SiFA-02$: RP-HPLC (10 to 90% B in 15 min): $t_R = 5.89$ min, $\kappa' = 2.13$.
Calculated monoisotopic mass ($C_{95}H_{130}FLuN_{24}O_{21}Si$): 2164.90, found: 1084.8 $[M+2H]^{2+}$, 723.1 $[M+3H]^{3+}$.

Fragments used in the synthesis of CXCR4-SiFA-02



CXCR4-SiFA-02_CLC



CXCR4-SiFA-02_L

CPCR4-linker conjunction CXCR4-SiFA-02_CLC was obtained by coupling of the respective linker CXCR4-SiFA-02_L with the *CPCR4* peptide scaffold, applying GP8. *Semi*-preparative RP-HPLC purification yielded the respective synthon.

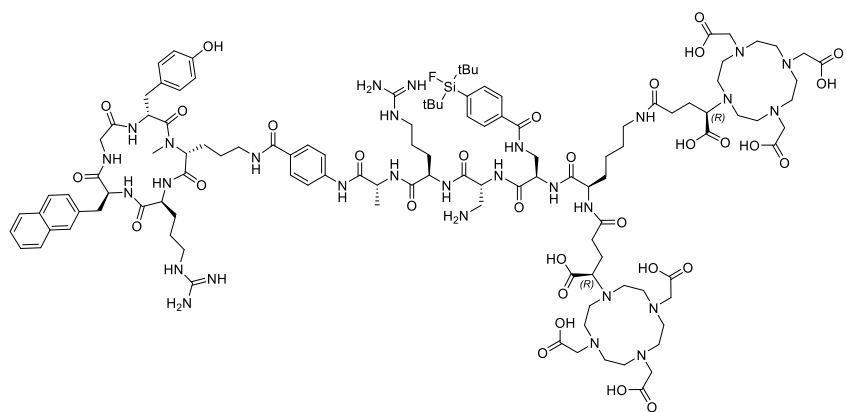
The linker unit CXCR4-SiFA-02_L was obtained through SPPS in analogy to CXCR4-SiFA-01_L. In short, resin-bound Fmoc-Abz-OH (GP1) was coupled with Fmoc-D-Ala-OH (GP2b), 3),

Fmoc-D-Arg(Pbf)-OH (GP2a), 3), Fmoc-D-His(Trt)-OH (GP2a), 3) and Fmoc-D-dap(Dde)-OH (GP2c), 3). Selective Dde de-protection (GP4b)), coupling of SiFA-BA (GP2a)) and cleavage off the resin (GP7a)) yielded the crude product. The peptide was purified *via semi*-preparative RP-HPLC prior to further reaction.

CXCR4-SiFA-02_L: RP-HPLC (70 to 95% B in 15 min): $t_R = 19.04$ min, $\kappa' = 11.90$. Calculated monoisotopic mass (C₈₇H₉₈FN₁₁O₁₂SSi): 1567.69, found: 1568.9 [M+H]⁺.

CXCR4-SiFA-02_CLC: RP-HPLC (10 to 90% B in 15 min): $t_R = 13.28$ min, $\kappa' = 5.25$. Calculated monoisotopic mass (C₁₀₈H₁₃₃FN₂₀O₁₅SSi): 2028.97, found: 1788.2 [M-Trt+H]⁺, 1016.6 [M+2H]²⁺.

CXCR4-SiFA-03



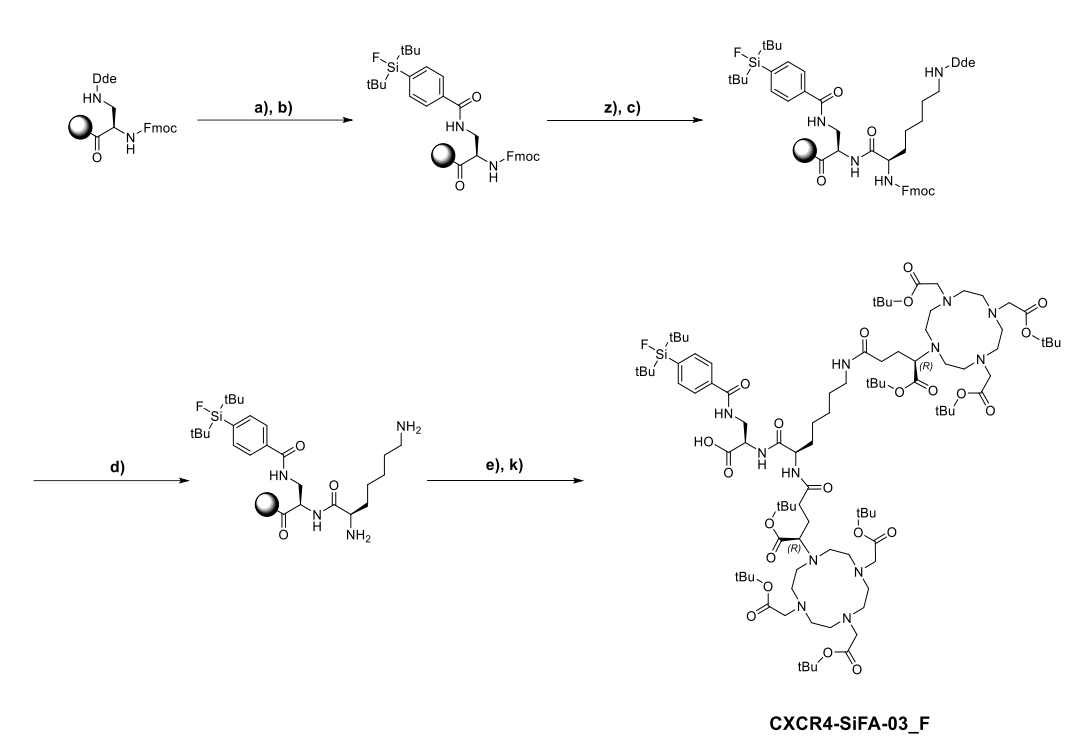
CXCR4-SiFA-03

Synthesis of ligand CXCR4-SiFA-03 was achieved using *CPCR4*-linker conjunction CXCR4-Tc-06_CLC and synthon CXCR4-SiFA-03_F. Connection of both fragments in accordance with GP8, subsequent de-protection (GP5) and purification by *semi*-preparative RP-HPLC yielded the respective final product. Complexes of CXCR4-SiFA-03 with ^{nat}Ga and ^{nat}Lu were formed by applying conditions as depicted above. As two (*R*)-DOTA-GA chelators are present, twice the amount of respective salt were used to achieve complete conversion.

CXCR4-SiFA-03: RP-HPLC (20 to 60% B in 15 min): $t_R = 8.77$ min, $\kappa' = 2.95$.
Calculated monoisotopic mass ($\text{C}_{117}\text{H}_{174}\text{FN}_{29}\text{O}_{31}\text{Si}$): 2528.27, found: 844.5 $[\text{M}+3\text{H}]^{3+}$, 633.4 $[\text{M}+4\text{H}]^{4+}$.

$[\text{nat}\text{Ga}]$ CXCR4-SiFA-03: RP-HPLC (20 to 60% B in 15 min): $t_R = 8.82$ min, $\kappa' = 3.04$.
Calculated monoisotopic mass ($\text{C}_{117}\text{H}_{170}\text{FGa}_2\text{N}_{29}\text{O}_{31}\text{Si}$): 2662.09, found: 1333.1 $[\text{M}+2\text{H}]^{2+}$, 889.5 $[\text{M}+3\text{H}]^{3+}$.

$[\text{nat}\text{Lu}]$ CXCR4-SiFA-03: RP-HPLC (20 to 60% B in 15 min): $t_R = 9.71$ min, $\kappa' = 3.34$.
Calculated monoisotopic mass ($\text{C}_{117}\text{H}_{168}\text{FLuN}_{29}\text{O}_{31}\text{Si}$): 2872.10, found: 1438.5 $[\text{M}+2\text{H}]^{2+}$, 958.7 $[\text{M}+3\text{H}]^{3+}$.

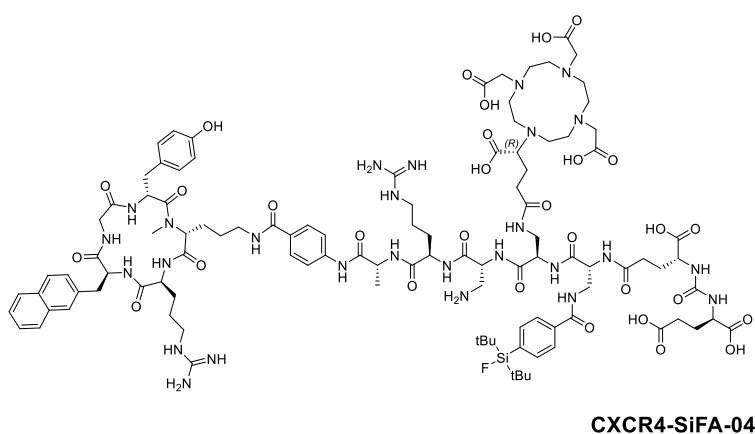


Scheme 14: Synthesis of the SiFA-conjugated fragment CXCR4-SiFA-03_F: a) imidazole (0.43 g), $[\text{NH}_2\text{OH}]\text{Cl}$ (0.63 g); b) SiFA-BA-OH (1.5 eq.), HOAt (1.5 eq.), TBTU (1.5 eq.), DIPEA (3.0 eq.); z) 20% Piperidine in DMF (v/v); c) Fmoc-k(Dde)-OH (1.5 eq.), HOAt (1.5 eq.), TBTU (1.5 eq.), DIPEA (3.0 eq.); d) 2% hydrazine in DMF (v/v); e) (R)-DOTA-GA(*t*Bu)₄-OH (3.0 eq.), HOAt (3.0 eq.), HATU (3.0 eq.), DIPEA (6.0 eq.); k) 20% HFIP in DCM (v/v).

Fragment CXCR4-SiFA-03_F was obtained by SPPS. Fmoc-D-dap(Dde)-OH was immobilized on 2-CTC resin (GP1) and Dde de-protected according with GP4b). Coupling of SiFA-BA (GP2a)), Fmoc de-protection (GP3) and coupling of Fmoc-D-Lys(Dde)-OH (GP2a)) was followed by removal of both Dde and Fmoc protecting groups as described in GP4a). Addition of (R)-DOTA-GA(*t*Bu)₄ (GP2b)) and cleavage off the resin (GP7a)) yielded the fully protected fragment.

CXCR4-SiFA-03_F: RP-HPLC (25 to 95% B in 15 min): $t_R = 12.32$ min, $\kappa' = 4.36$. Calculated monoisotopic mass ($\text{C}_{94}\text{H}_{165}\text{FN}_{12}\text{O}_{22}\text{Si}$): 1861.19, found: $931.2 [\text{M}+2\text{H}]^{2+}$.

CXCR4-SiFA-04



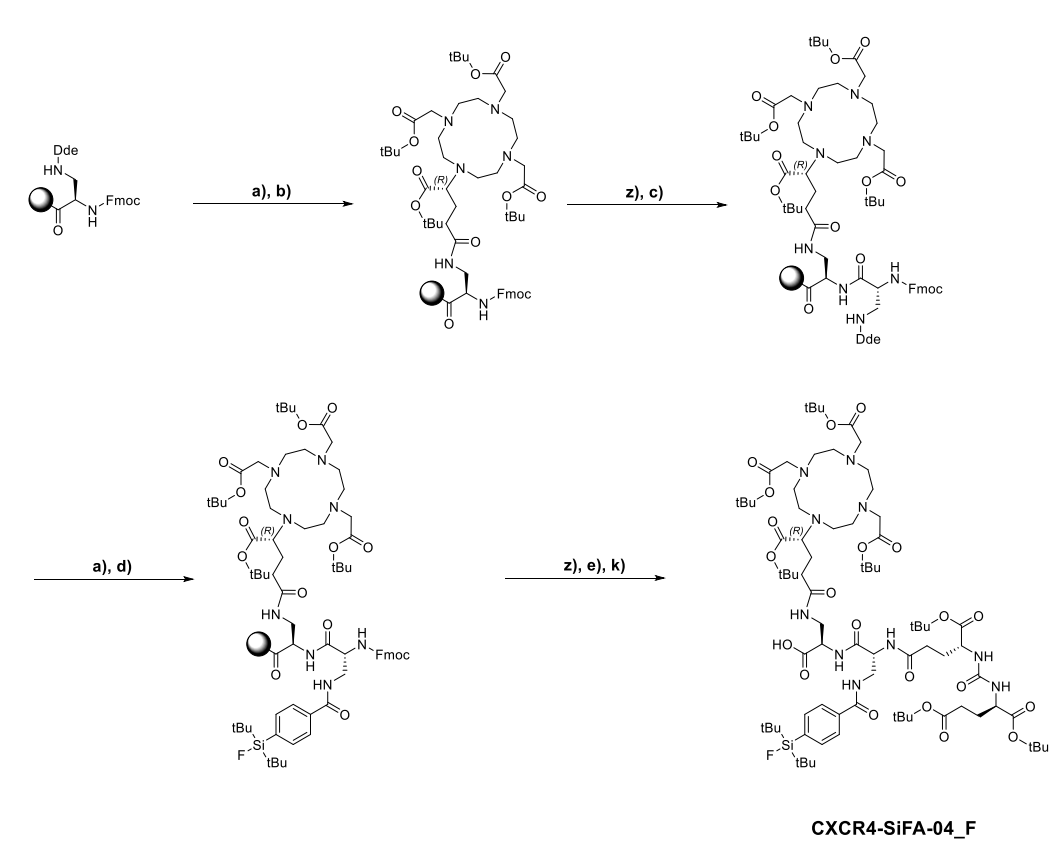
CXCR4-SiFA-04 was synthesized according with CXCR4-SiFA-03. Briefly, synthon CXCR4-Tc-06_CLC was coupled with CXCR4-SiFA-04_F (GP8). The resulting peptide was de-protected applying GP5 and purified by *semi-*

preparative RP-HPLC to afford the respective labeling precursor. Complexation with ^{nat}Ga or ^{nat}Lu was undertaken as described above.

CXCR4-SiFA-04: RP-HPLC (10 to 60% B in 15 min): $t_R = 11.70$ min, $\kappa' = 6.80$.
Calculated monoisotopic mass ($\text{C}_{106}\text{H}_{152}\text{FN}_{27}\text{O}_{30}\text{Si}$): 2330.10, found: 1167.2
[M+2H] $^{2+}$, 778.6 [M+3H] $^{3+}$, 584.3 [M+4H] $^{4+}$.

[^{nat}Ga]CXCR4-SiFA-04: RP-HPLC (10 to 60% B in 15 min): $t_R = 12.32$ min, $\kappa' = 7.21$.
Calculated monoisotopic mass ($\text{C}_{106}\text{H}_{150}\text{FGa}_{27}\text{O}_{30}\text{Si}$): 2397.01, found: 1200.7
[M+2H] $^{2+}$, 801.0 [M+3H] $^{3+}$.

[^{nat}Lu]CXCR4-SiFA-04: RP-HPLC (20 to 60% B in 15 min): $t_R = 11.72$ min, $\kappa' = 6.69$.
Calculated monoisotopic mass ($\text{C}_{106}\text{H}_{149}\text{FLu}_{27}\text{O}_{30}\text{Si}$): 2502.01, found: 835.7
[M+3H] $^{3+}$.

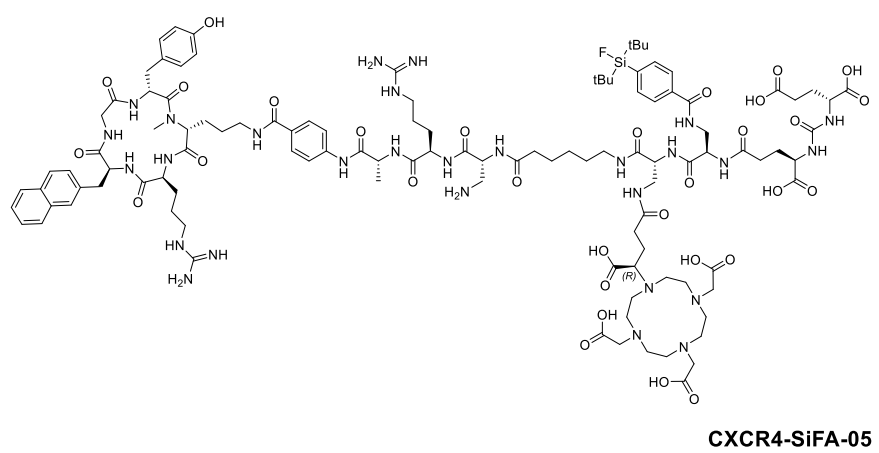


Scheme 15: Synthesis of the SiFA-conjugated fragment CXCR4-SiFA-04_F: a) imidazole (0.43 g), $[\text{NH}_2\text{OH}]\text{Cl}$ (0.63 g); b) (R)-DOTA-GA(*t*Bu)₄-OH (1.5 eq.), HOAt (1.5 eq.), TBTU (1.5 eq.), DIPEA (3.0 eq.); z) 20% Piperidine in DMF (v/v); c) Fmoc-D-dap(Dde)-OH (1.5 eq.), HOAt (1.5 eq.), TBTU (1.5 eq.), 2,4,6-Collidine (3.0 eq.); d) SiFA-BA-OH (1.5 eq.), HOAt (1.5 eq.), TBTU (1.5 eq.), DIPEA (3.0 eq.); e) (*t*Bu)_e(OH)ue(*t*Bu)₂, HOAt (1.5 eq.), TBTU (1.5 eq.), DIPEA (3.0 eq.); k) 20% HFIP in DCM (v/v).

The SiFA-conjugated synthon CXCR4-SiFA-04_F was prepared by SPPS on the basis of resin-bound Fmoc-D-dap(Dde)-OH (GP1). Selective side-chain de-protection according with GP4b) provided a free amine functionality to couple (R)-DOTA-GA(*t*Bu)₄ (GP2b)). Fmoc de-protection (GP3), coupling of Fmoc-D-dap(Dde)-OH (GP2c)) and selective Dde de-protection (GP4b)) resulted in a branching position for the addition of SiFA-BA (GP2b)). The fragment (*t*Bu)_e(OH)ue(*t*Bu)₂ was coupled (GP2b)) after removal of the remaining Fmoc protecting group (GP3). The peptide was ultimately cleaved off the resin support (GP7a)) and purified by *semi*-preparative RP-HPLC prior to further reaction steps.

CXCR4-SiFA-04_F: RP-HPLC (10 to 95% B in 15 min): $t_R = 15.97$ min, $\kappa' = 6.61$. Calculated monoisotopic mass (C₇₉H₁₃₅FN₁₀O₂₁Si): 1606.96, found: 1609.1 $[\text{M}+\text{H}]^+$, 805.4 $[\text{M}+2\text{H}]^{2+}$.

CXCR4-SiFA-05

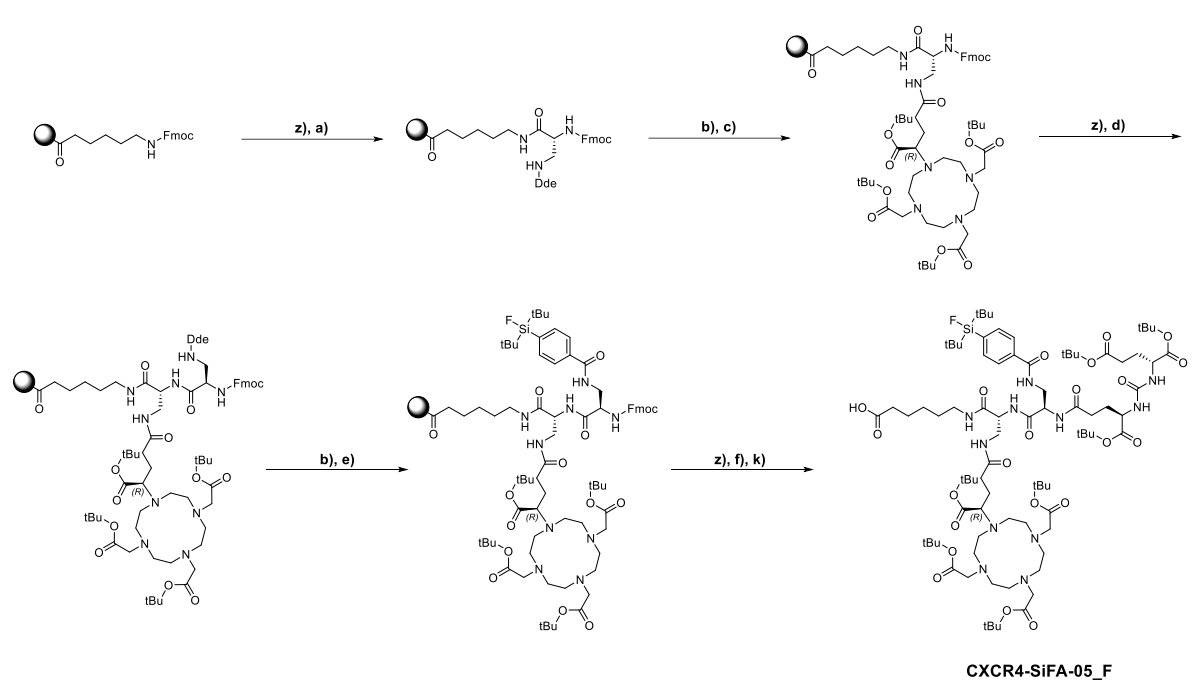


Synthesis of CXCR4-SiFA-05 was achieved by condensation of fragments CXCR4-Tc-06_CLC and the SiFA-conjugated fragment CXCR4-SiFA-05_F according with GP8. Final de-protection (GP5) and purification of the resulting peptide by *semi*-preparative RP-HPLC provided the desired product. Complex formation with the stable isotopes of Gallium and Lutetium was achieved as described above.

CXCR4-SiFA-05: RP-HPLC (10 to 60% B in 15 min): $t_R = 11.70$ min, $\kappa' = 8.36$.
Calculated monoisotopic mass ($C_{112}H_{163}FN_{28}O_{31}Si$): 2443.18, found: 1221.9
 $[M+2H]^{2+}$, 814.8 $[M+3H]^{3+}$, 611.3 $[M+4H]^{4+}$.

$[^{nat}Ga]$ CXCR4-SiFA-05: RP-HPLC (10 to 60% B in 15 min): $t_R = 11.82$ min, $\kappa' = 8.46$.
Calculated monoisotopic mass ($C_{112}H_{160}FGaN_{28}O_{31}Si$): 2509.08, found: 1255.3
 $[M+2H]^{2+}$, 837.0 $[M+3H]^{3+}$.

$[^{nat}Lu]$ CXCR4-SiFA-05 RP-HPLC (10 to 60% B in 15 min): $t_R = 12.72$ min, $\kappa' = 9.18$.
Calculated monoisotopic mass ($C_{112}H_{159}FLuN_{28}O_{31}Si$): 2614.09, found: 1307.8
 $[M+2H]^{2+}$, 872.1 $[M+3H]^{3+}$.

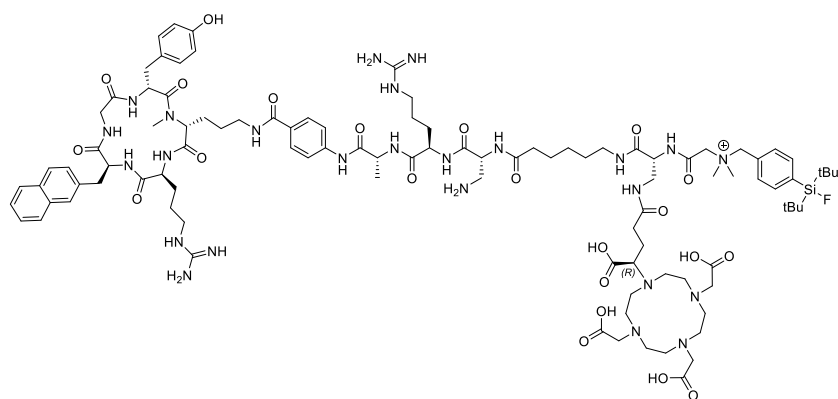


Scheme 16: Synthesis of the SiFA-conjugated fragment CXCR4-SiFA-05_F: z) 20% Piperidine in DMF (v/v); a) Fmoc-D-dap(Dde)-OH (1.5 eq.), HOAt (1.5 eq.), TBTU (1.5 eq.), 2,4,6-Collidine (3.0 eq.); b) imidazole (0.43 g), $[NH_2OH]Cl$ (0.63 g); c) (R)-DOTA-GA(*t*Bu)₄-OH (1.5 eq.), HOAt (1.5 eq.), TBTU (1.5 eq.), DIPEA (3.0 eq.); d) Fmoc-D-dap(Dde)-OH (1.5 eq.), HOAt (1.5 eq.), TBTU (1.5 eq.), 2,4,6-Collidine (3.0 eq.); e) SiFA-BA-OH (1.5 eq.), HOAt (1.5 eq.), TBTU (1.5 eq.), DIPEA (3.0 eq.); f) (*t*Bu)*e*(OH)*ue*(*t*Bu)₂, HOAt (1.5 eq.), TBTU (1.5 eq.), DIPEA (3.0 eq.); k) 20% HFIP in DCM (v/v).

CXCR4-SiFA-05_F was prepared in analogy with CXCR4-SiFA-04_F, with the difference being the resin-bound amino acid. Briefly, Fmoc-Ahx-OH was immobilized on 2-CTC resin (GP1), Fmoc de-protected (GP3) and coupled with Fmoc-D-dap(Dde)-OH (GP2c). Selective side-chain de-protection (GP4b)) and (R)-DOTA-GA(*t*Bu)₄ coupling was followed by Fmoc de-protection (GP3) and addition of Fmoc-D-dap(Dde)-OH according with GP2c). Again, Dde was selectively removed (GP4b)) and SiFA-BA was coupled with the side chain amine (GP2b)). Fmoc de-protection (GP3), condensation with the (*t*Bu)*e*(OH)*ue*(*t*Bu)₂ synthon (GP2a)) and cleavage off the resin under retention of acid-labile protecting groups (GP7a)) afforded the respective fragment. Purification *via semi-preparative* RP-HPLC was conducted before further reaction.

CXCR4-SiFA-05_F: RP-HPLC (10 to 95% B in 15 min): $t_R = 15.62$ min, $\kappa' = 6.26$. Calculated monoisotopic mass (C₈₅H₁₄₆FN₁₁O₂₂Si): 1720.04, found: 1721.3 [M+H]⁺, 861.6 [M+2H]²⁺.

CXCR4-SiFA-06



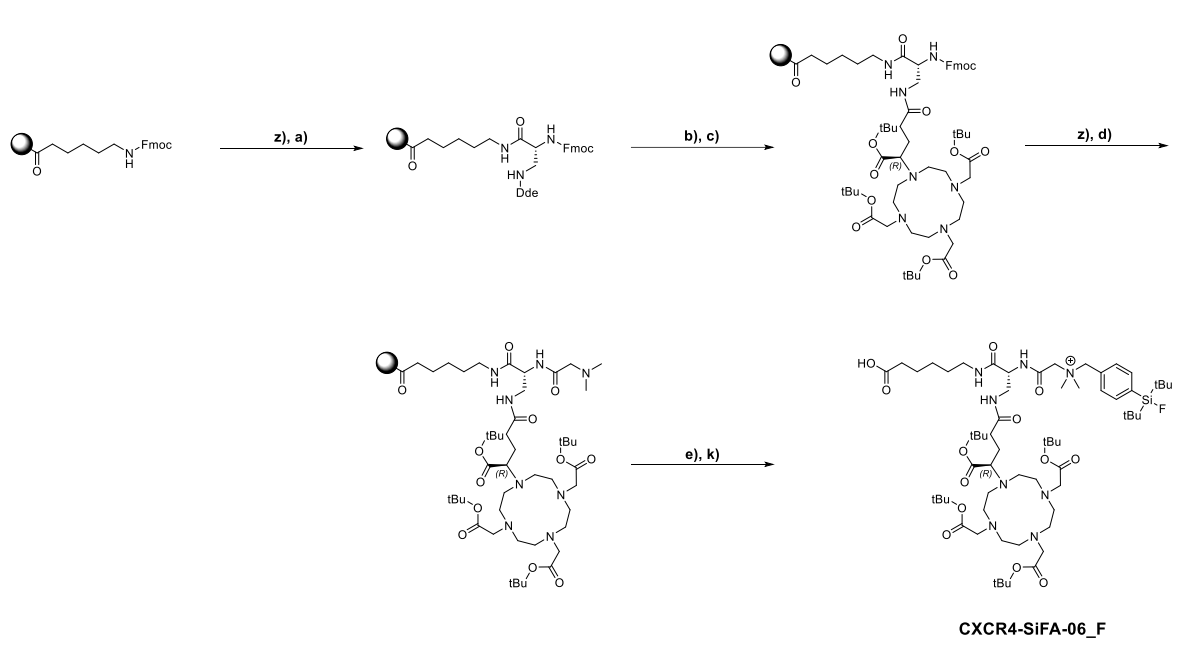
CXCR4-SiFA-06

CXCR4-SiFA-06 was prepared following the synthesis of CXCR4-SiFA-05. The synthon CXCR4-SiFA-06_F was condensed with the *CPCR4*-linker conjunction CXCR4-Tc-06_CLC according with GP8. Subsequent treatment with TFA (GP5) and purification *via semi-preparative* RP-HPLC afforded the desired peptide. Stable complexes with ^{nat}Ga or ^{nat}Lu were prepared by incubation with the respective salt.

CXCR4-SiFA-06: RP-HPLC (10 to 60% B in 15 min): $t_R = 11.70$ min, $\kappa' = 8.00$.
Calculated monoisotopic mass ($C_{102}H_{153}FN_{25}O_{22}Si^+$): 2127.14, found: 1063.4
[M+2H]²⁺, 709.2 [M+3H]³⁺.

[^{nat}Ga]CXCR4-SiFA-06: RP-HPLC (10 to 60% B in 15 min): $t_R = 11.73$ min, $\kappa' = 8.02$.
Calculated monoisotopic mass ($C_{102}H_{150}FGaN_{25}O_{22}Si^+$): 2193.04, found: 1096.7
[M+2H]²⁺, 731.3 [M+3H]³⁺, 548.7 [M+4H]⁴⁺.

[^{nat}Lu]CXCR4-SiFA-06: RP-HPLC (10 to 60% B in 15 min): $t_R = 12.71$ min, $\kappa' = 8.78$.
Calculated monoisotopic mass ($C_{102}H_{149}FLuN_{25}O_{22}Si^+$): 2298.05, found: 1149.3
[M+2H]²⁺, 766.4 [M+3H]³⁺.

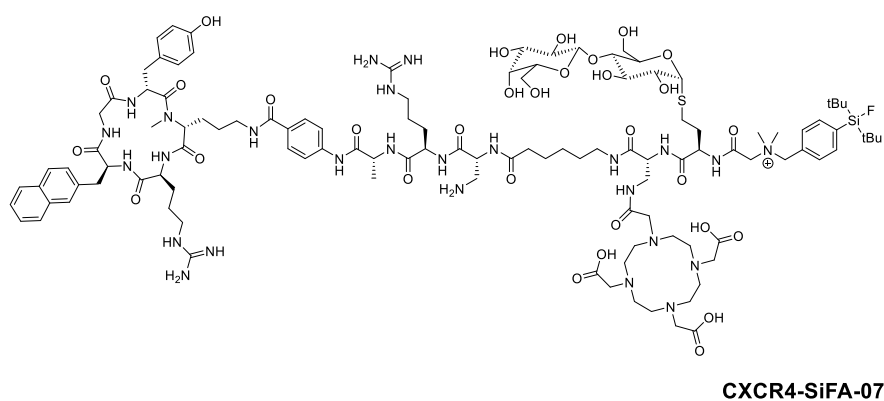


Scheme 17: Synthesis of the SiFA-conjugated fragment CXCR4-SiFA-06_F: z) 20% Piperidine in DMF (v/v); a) Fmoc-D-dap(Dde)-OH (1.5 eq.), HOAt (1.5 eq.), TBTU (1.5 eq.), 2,4,6-Collidine (3.0 eq.); b) imidazole (0.43 g), [NH₂OH]Cl (0.63 g); c) (R)-DOTA-GA(tBu)₄-OH (1.5 eq.), HOAt (1.5 eq.), TBTU (1.5 eq.), DIPEA (3.0 eq.); d) DMG-OH (1.5 eq.), HOAt (1.5 eq.), TBTU (1.5 eq.), 2,4,6-Collidine (3.0 eq.); e) SiFA-Br (3.0 eq.), DIPEA (3.0 eq.); k) 20% HFIP in DCM (v/v).

SiFA-conjugated fragment CXCR4-SiFA-06_F was prepared as shown. Fmoc-Ahx-OH was immobilized on solid support (GP1), Fmoc de-protected (GP3) and elongated with Fmoc-D-dap(Dde)-OH (GP2c). Selective side-chain de-protection applying GP4b) facilitated the addition of (R)-DOTA-GA(tBu)₄ by means of GP2a). Dimethylglycine was coupled (GP2a), 3) and reacted with SiFA-Br (3.0 eq.) in DMF and DIPEA (3.0 eq.) over night at ambient temperature. The peptide was eventually cleaved off the solid support (GP7a)) and purified *via semi-preparative* RP-HPLC.

CXCR4-SiFA-06_F: RP-HPLC (10 to 95% B in 15 min): $t_R = 11.64$ min, $\kappa' = 4.36$. Calculated monoisotopic mass (C₆₃H₁₁₂FN₈O₁₃Si⁺): 1235.81, found: 1235.9 [M+H]⁺.

CXCR4-SiFA-07

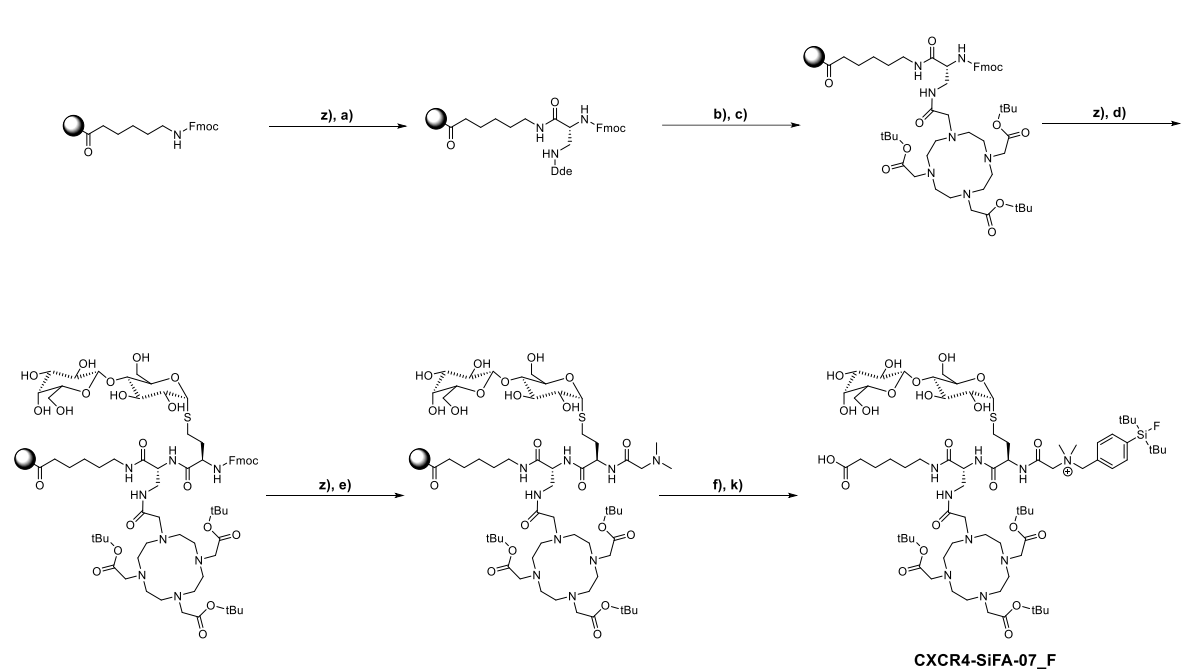


CXCR4-SiFA-07 was synthesized according with CXCR4-SiFA-06. Briefly, CXCR4-Tc-06_CLC was condensed with CXCR4-SiFA-07_F applying GP8. Final removal of acid-labile protecting groups (GP5) and purification of the crude product by *semi*-preparative RP-HPLC yielded the desired fluorine-18 labeling precursor. Complexes with ^{nat}Ga or ^{nat}Lu were prepared as characterized above.

CXCR4-SiFA-07: RP-HPLC (10 to 95% B in 15 min): $t_R = 7.61$ min, $\kappa' = 5.09$.
Calculated monoisotopic mass ($C_{102}H_{153}FN_{25}O_{22}Si^+$): 2496.25, found: 838.8
 $[M+H_2O+3H]^{3+}$.

$[^{nat}Ga]CXCR4-SiFA-07$: RP-HPLC (10 to 60% B in 15 min): $t_R = 11.23$ min, $\kappa' = 4.62$.
Calculated monoisotopic mass ($C_{115}H_{174}FGaN_{26}O_{31}SSi^+$): 2563.16, found: 861.5
 $[M+H_2O+3H]^{3+}$.

$[^{nat}Lu]CXCR4-SiFA-07$: RP-HPLC (10 to 60% B in 15 min): $t_R = 11.47$ min, $\kappa' = 3.99$.
Calculated monoisotopic mass ($C_{115}H_{173}FLuN_{26}O_{31}SSi^+$): 2668.16, found: 896.3
 $[M+H_2O+3H]^{3+}$.



Scheme 18: Synthesis of the SiFA-conjugated fragment CXCR4-SiFA-07_F: z) 20% Piperidine in DMF (v/v); a) Fmoc-D-dap(Dde)-OH (1.5 eq.), HOAt (1.5 eq.), TBTU (1.5 eq.), 2,4,6-Collidine (3.0 eq.); b) imidazole (0.43 g), $[NH_2OH]Cl$ (0.63 g); c) DOTA(*t*Bu)₃-OH (1.5 eq.), HOAt (1.5 eq.), TBTU (1.5 eq.), DIPEA (3.0 eq.); d) Fmoc-D-HCy(β -D-lactosyl)-OH (1.5 eq.), HOAt (1.5 eq.), HATU (1.5 eq.), DIPEA (3.0 eq.); e) DMG-OH (1.5 eq.), HOAt (1.5 eq.), TBTU (1.5 eq.), 2,4,6-Collidine (3.0 eq.); f) SiFA-Br (3.0 eq.), DIPEA (3.0 eq.); k) 20% HFIP in DCM (v/v).

Fmoc-Ahx-OH was immobilized on 2-CTC resin (GP1), Fmoc de-protected (GP3) and coupled with Fmoc-D-dap(Dde)-OH according with GP2c). Selective side-chain de-protection (GP4b)) afforded a free amine functionality to couple DOTA(*t*Bu)₃ (GP2a)). Subsequent removal of Fmoc (GP3) and coupling of Fmoc-D-HCy(β -D-lactosyl)-OH as depicted in GP2b), followed by addition of Dimethylglycine (GP2a), 3) and SiFA-Br (3.0 eq. in DMF, DIPEA 3.0 eq., r.t., o.n.) resulted in the final amino acid sequence. Cleavage off the resin under retention of acid-labile protecting groups (GP7a)) and purification by *semi*-preparative RP-HPLC yielded the respective fragment.

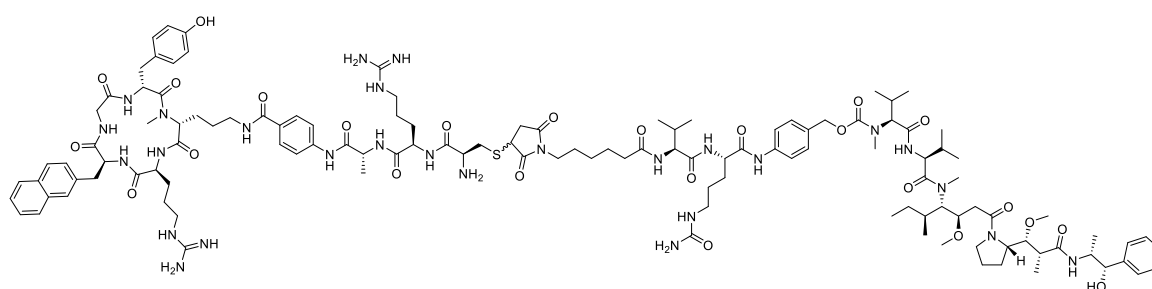
CXCR4-SiFA-07_F: RP-HPLC (10 to 95% B in 15 min): t_R = 9.55 min, κ' = 5.23. Calculated monoisotopic mass (C₇₂H₁₂₇FN₉O₂₂SSi⁺): 1548.86, found: 1550.3 [M+H]⁺, 775.3 [M+2H]²⁺.

2.3.7. CXCR4-MMAE-01 – 04

Michael addition of the “HS”-bearing peptides onto the maleimide-carrying vc-PAB-MMAE toxin derivative was conducted as follows. The fully unprotected

peptide was dissolved in DMF (1.0 mg/mL) and added to the toxin in DMF (1.1 mg/mL). DIPEA (0.5 μ L/mg peptide) was added, and the reaction mixture stirred at r.t. for 2h. Completion of the sulfhydryl-maleimido reaction was confirmed by RP-HPLC and purification was carried out by *semi*-preparative RP-HPLC.

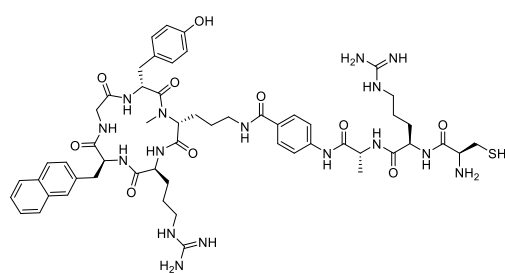
CXCR4-MMAE-01



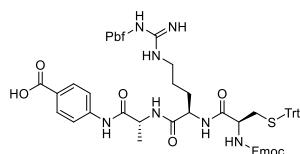
CXCR4-MMAE-01

CXCR4-MMAE-01 was prepared by sulfhydryl-maleimido coupling as depicted above. Subsequent purification *via semi*-preparative RP-HPLC afforded the desired product. CXCR4-MMAE-01: RP-HPLC: (25 to 70% B in 15 min): t_R = 9.31 min, κ' = 3.23. Calculated monoisotopic mass (C₁₂₃H₁₇₉N₂₇O₂₅S): 2466.33, found: 1234.0 [M+2H]²⁺, 823.2 [M+3H]³⁺.

Fragments used in the synthesis of CXCR4-MMAE-01



CXCR4-MMAE-01_CLC



CXCR4-MMAE-01_L

CXCR4-MMAE-01_L was prepared by SPPS on the basis of resin-bound Fmoc-Abz-OH (GP1). Elongation with Fmoc-D-Ala-OH (GP2b), 3), Fmoc-D-Arg(Pbf)-OH (GP2a), 3) and Fmoc-D-Cys(Trt)-OH (GP2c), 3) was followed by resin-cleavage under retention of all protecting groups (GP7a)).

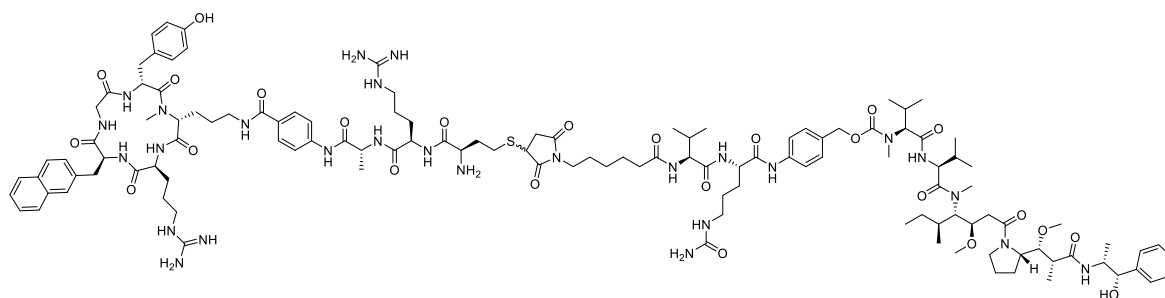
The purified linker was condensed with the *CPCR4* peptide scaffold according with GP8, Fmoc de-protected (GP3) and purified by *semi*-preparative RP-HPLC to yield the

fragment CXCR4-MMAE-01_CLC.

CXCR4-MMAE-01_L: RP-HPLC (10 to 90% B in 15 min): t_R = 17.77 min, κ' = 10.98. Calculated monoisotopic mass (C₆₆H₆₉N₇O₁₀S₂): 1183.45, found: 1184.4 [M+H]⁺.

CXCR4-MMAE-01_CLC: RP-HPLC: (10 to 90% B in 15 min): $t_R = 9.80$ min, $\kappa' = 4.43$.
Calculated monoisotopic mass ($C_{55}H_{74}N_{16}O_{10}S$): 1150.55, found: 1151.3 $[M+H]^+$,
576.4 $[M+2H]^{2+}$.

CXCR4-MMAE-02

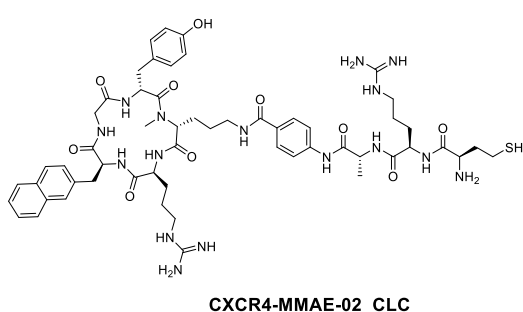


CXCR4-MMAE-02

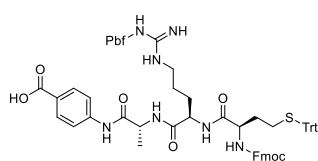
Synthesis of CXCR4-MMAE-02 was accomplished in analogy to CXCR4-MMAE-01. Coupling of the fragment CXCR4-MMAE-02_CLC with the toxin was carried out as depicted above by incubation in the presence of DIPEA. *Semi-preparative* RP-HPLC purification afforded the desired product.

CXCR4-MMAE-02: RP-HPLC: (25 to 70% B in 15 min): $t_R = 9.39$ min, $\kappa' = 3.87$.
Calculated monoisotopic mass ($C_{124}H_{181}N_{27}O_{25}S$): 2480.34, found: 1241.0 $[M+2H]^{2+}$,
827.8 $[M+3H]^{3+}$.

Fragments used in the synthesis of CXCR4-MMAE-02



CXCR4-MMAE-02_CLC



CXCR4-MMAE-02_L

CXCR4-MMAE_L was prepared by linear SPPS starting with the resin loading of Fmoc-Abz-OH (GP1). Subsequent coupling of Fmoc-D-Ala-OH (GP2b), 3), Fmoc-D-Arg(Pbf)-OH (GP2a), 3) and Fmoc-D-HCy(Trt)-OH (GP2a), 3), followed by resin cleavage according with GP7a) yielded the crude linker moiety.

After *semi-preparative* RP-HPLC purification of the linker unit, condensation with CPCR4 was achieved by means of GP8. Fmoc de-protection (GP3) and removal of acid-labile

protecting groups (GP5) was ensued by purification *via semi-preparative* RP-HPLC to yield the respective peptide CXCR4-MMAE-02_CLC.

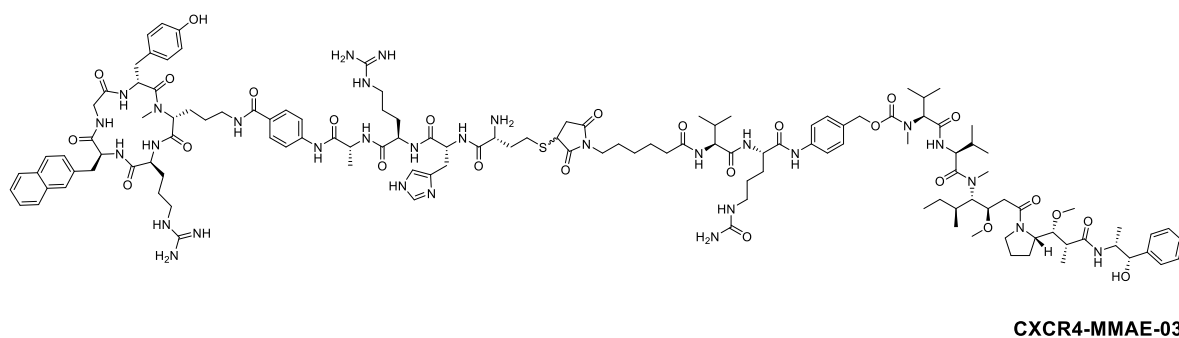
CXCR4-MMAE-02_L: RP-HPLC (10 to 90% B in 15 min): $t_R = 17.79$ min, $\kappa' = 10.35$.

Calculated monoisotopic mass ($C_{67}H_{71}N_7O_{10}S_2$): 1197.47, found: 1198.2 $[M+H]^+$.

CXCR4-MMAE-02_CLC: RP-HPLC (10 to 90% B in 15 min): $t_R = 9.84$ min, $\kappa' = 4.46$.

Calculated monoisotopic mass ($C_{56}H_{76}N_{16}O_{10}S$): 1164.57, found: 583.2 $[M+2H]^{2+}$.

CXCR4-MMAE-03



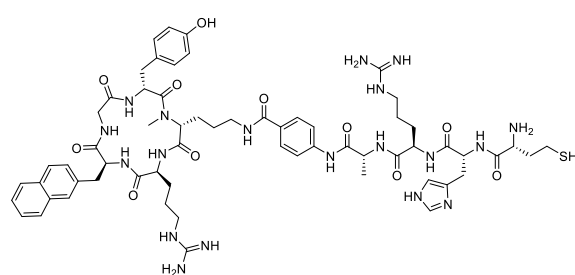
CXCR4-MMAE-03

CXCR4-MMAE-03 was prepared as depicted for CXCR4-MMAE-01 and -02. *CPCR4*-linker conjunction CXCR4-MMAE-03_CLC was coupled with the toxin by sulfhydryl-maleimido reaction as described above. Subjection of the reaction mixture to *semi*-preparative RP-HPLC purification afforded the desired PDC.

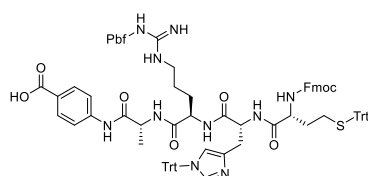
CXCR4-MMAE-03: RP-HPLC (30 to 70% B in 15 min): $t_R = 5.93$ min, $\kappa' = 2.49$.

Calculated monoisotopic mass ($C_{130}H_{188}N_{30}O_{26}S$): 2617.40, found: 1310.1 $[M+2H]^{2+}$, 873.8 $[M+3H]^{3+}$.

Fragments used in the synthesis of CXCR4-MMAE-03



CXCR4-MMAE-03_CLC



CXCR4-MMAE-03_L

Linear SPPS on the basis of resin-bound Fmoc-Abz-OH (GP1) provided the linker CXCR4-MMAE-03_L. Elongation with Fmoc-D-Ala-OH (GP2b), 3, Fmoc-D-Arg(Pbf)-OH (GP2a), 3, Fmoc-D-His(Trt)-OH (GP2a), 3 and Fmoc-D-HCy(Trt)-OH (GP2a), 3 and final resin cleavage (GP7a) alongside with *semi*-preparative RP-HPLC purification yielded the respective peptide fragment. Coupling with the *CPCR4* peptide scaffold (GP8), Fmoc de-protection

(GP3), removal of remaining protecting groups (GP5) and *semi*-preparative RP-HPLC purification afforded the fragment CXCR4-MMAE-03_CLC.

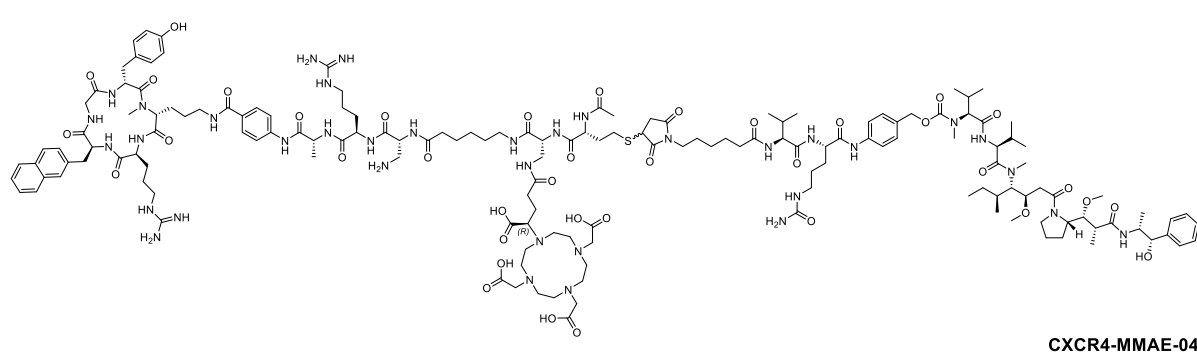
CXCR4-MMAE-03_L: RP-HPLC (10 to 90% B in 15 min): $t_R = 11.39$ min, $\kappa' = 3.95$.

Calculated monoisotopic mass ($C_{92}H_{92}N_{10}O_{11}S_2$): 1576.64, found: 789.4 $[M+2H]^{2+}$.

CXCR4-MMAE-03_CLC: RP-HPLC (10 to 90% B in 15 min): $t_R = 9.83$ min, $\kappa' = 3.92$.

Calculated monoisotopic mass ($C_{62}H_{83}N_{19}O_{11}S$): 1301.62, found: 652.1 $[M+2H]^{2+}$.

CXCR4-MMAE-04



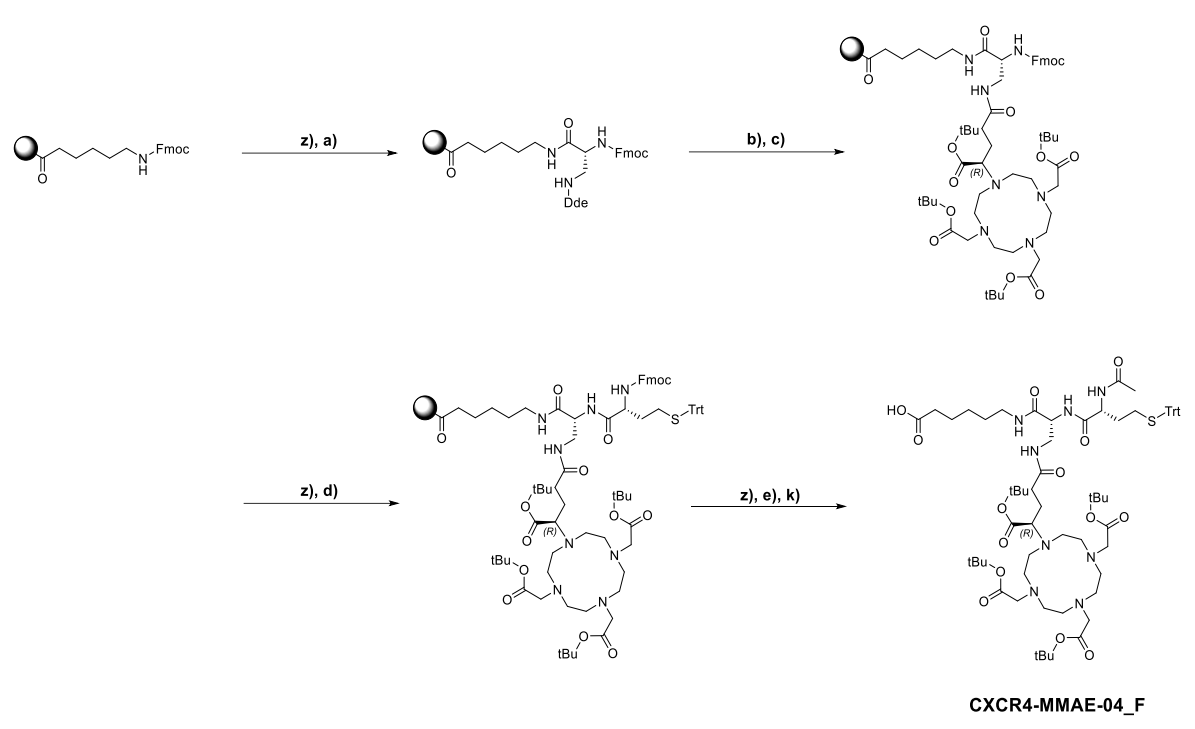
Sulfhydryl-maleimido coupling of fragments CXCR4-MMAE-04_CLC_F and the toxin was conducted as depicted above. After incubation of both peptides in the presence of DIPEA, the mixture was subjected to *semi*-preparative RP-HPLC purification to afford the desired product CXCR4-MMAE-04. Complexation with ^{nat}Lu was achieved as described.

CXCR4-MMAE-04: RP-HPLC (20 to 70% B in 15 min): $t_R = 9.63$ min, $\kappa' = 6.41$.

Calculated monoisotopic mass ($C_{157}H_{236}N_{36}O_{38}S$): 3265.74, found: 1634.4 $[M+2H]^{2+}$, 1089.8 $[M+3H]^{3+}$, 817.7 $[M+4H]^{4+}$.

$[^{nat}Lu]CXCR4-MMAE-04$: RP-HPLC (20 to 70% B in 15 min): $t_R = 10.46$ min, $\kappa' = 7.05$.

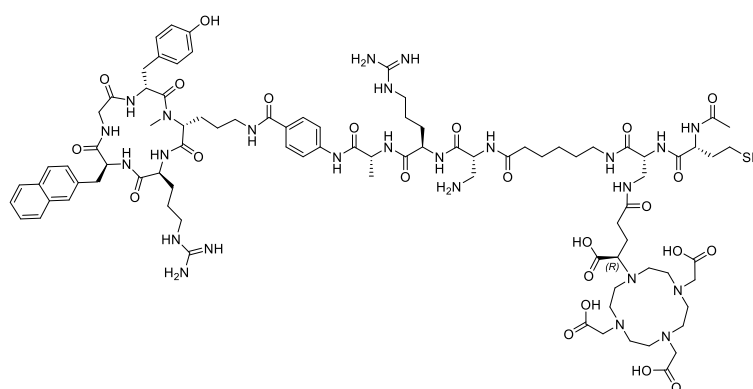
Calculated monoisotopic mass ($C_{157}H_{233}LuN_{36}O_{38}S$): 3437.65, found: 1720.1 $[M+2H]^{2+}$, 1146.9 $[M+3H]^{3+}$,



Scheme 19: Synthesis of the (R)-DOTA-GA(tBu)₄-conjugated fragment CXCR4-MMAE-04_F: z) 20% Piperidine in DMF (v/v); a) Fmoc-D-dap(Dde)-OH (1.5 eq.), HOAt (1.5 eq.), TBTU (1.5 eq.), 2,4,6-Collidine (3.0 eq.); b) imidazole (0.43 g), [NH₂OH]Cl (0.63 g); c) (R)-DOTA-GA(tBu)₄-OH (1.5 eq.), HOAt (1.5 eq.), TBTU (1.5 eq.), DIPEA (3.0 eq.); d) Fmoc-D-HCy(Trt)-OH (1.5 eq.), HOAt (1.5 eq.), HATU (1.5 eq.), DIPEA (3.0 eq.); e) DIPEA (5.0 eq.), Ac₂O (5.0 eq.) k) TFA/TIPS/H₂O (95/2.5/2.5; v/v/v).

CXCR4-MMAE-04_F was prepared as depicted in the reaction scheme above. Fmoc-Ahx-OH was immobilized on 2-CTC resin (GP1), Fmoc de-protected (GP3) and elongated with Fmoc-D-dap(Dde)-OH according with GP2c). Selective Dde removal (GP4b)) and coupling of (R)-DOTA-GA(tBu)₄-OH (GP2a)) were followed by Fmoc de-protection (GP3) and coupling of Fmoc-D-HCy(Trt)-OH. The N-terminus was de-protected (GP3) and acetylated (GP6) before the fragment was cleaved off the resin under retention of protecting groups (GP7a)).

Fragments used in the synthesis of CXCR4-MMAE-04



CXCR4-MMAE-04_CLC_F

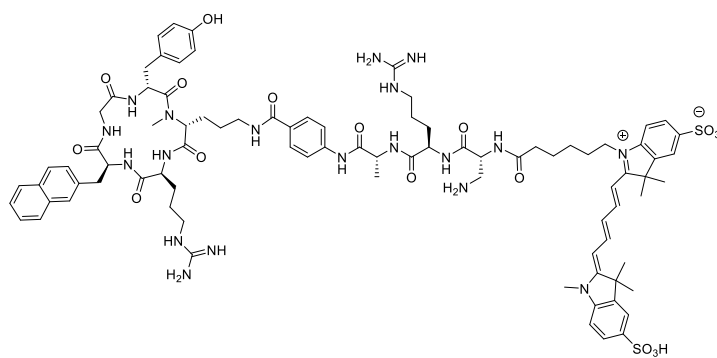
The synthesis of CXCR4-MMAE-04_CLC_F was carried out by condensation reaction between CXCR4-Tc-06_CLC and the fragment CXCR4-MMAE-04_F according with GP8. The resulting product was de-protected under acidic conditions (GP5) and purified *via semi-preparative* RP-HPLC to afford the desired compound.

CXCR4-MMAE-04_F: RP-HPLC (10 to 95% B in 15 min): $t_R = 12.64$ min, $\kappa' = 8.72$. Calculated monoisotopic mass ($C_{69}H_{104}N_8O_{14}S$): 1300.74, found: 1060.2 $[M-Trt+H]^+$, 651.6 $[M+2H]^{2+}$.

CXCR4-MMAE-04_CLC_F: RP-HPLC (10 to 95% B in 15 min): $t_R = 6.22$ min, $\kappa' = 1.85$. Calculated monoisotopic mass ($C_{89}H_{131}N_{25}O_{23}S$): 1949.96, found: 652.3 $[M+3H]^{3+}$.

2.3.8. CXCR4-OI-01 – 03

CXCR4-OI-01



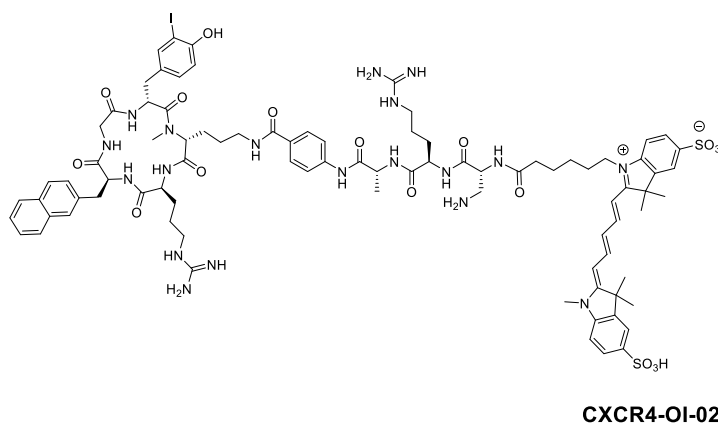
CXCR4-OI-01

CXCR4-OI-01 was prepared on the basis of *CPCR4*-linker conjugation CXCR4-Tc-06_CLC. The purified peptide underwent in-solution peptide coupling (GP8) with the Cy5.5 carboxylic acid. Subsequent

de-protection (GP5) and purification *via semi-preparative* RP-HPLC afforded the desired product.

CXCR4-OI-1: RP-HPLC (5 to 55% B in 15 min): $t_R = 8.73$ min, $\kappa' = 2.76$. Calculated monoisotopic mass ($C_{87}H_{111}N_{19}O_{17}S_2$): 1757.78, found: 880.5 $[M+2H]^{2+}$, 587.3 $[M+3H]^{3+}$.

CXCR4-OI-02

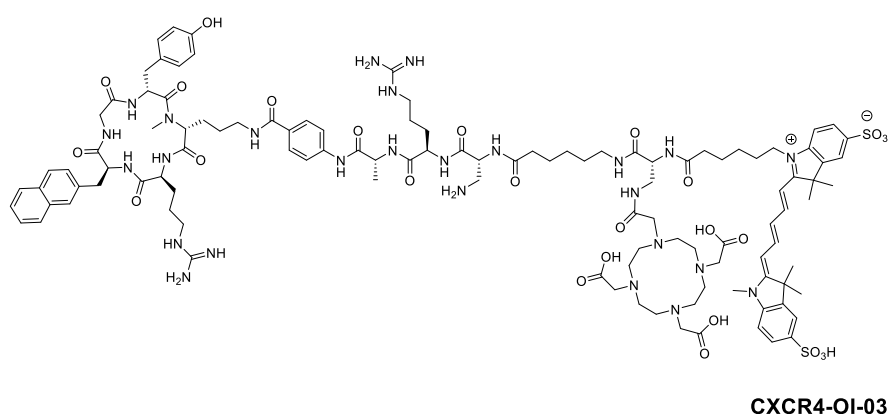


Ligand CXCR4-OI-02 was obtained by iodination of CXCR4-OI-01 according with the procedure depicted above. Briefly, CXCR4-OI-01 was dissolved in a MeCN/H₂O mixture (1/1 (v/v)) to a concentration of 1.0 mM and NIS (0.3–0.5 eq./ 10 mM in

MeCN) was added. Purification by *semi*-preparative RP-HPLC afforded the desired peptide.

CXCR4-OI-2: RP-HPLC (5 to 55% B in 15 min): $t_R = 11.00$ min, $\kappa' = 3.93$. Calculated monoisotopic mass ($C_{87}H_{110}N_{19}O_{17}S_2$): 1883.68, found: 942.7 $[M+2H]^{2+}$, 630.4 $[M+3H]^{3+}$.

CXCR4-OI-03

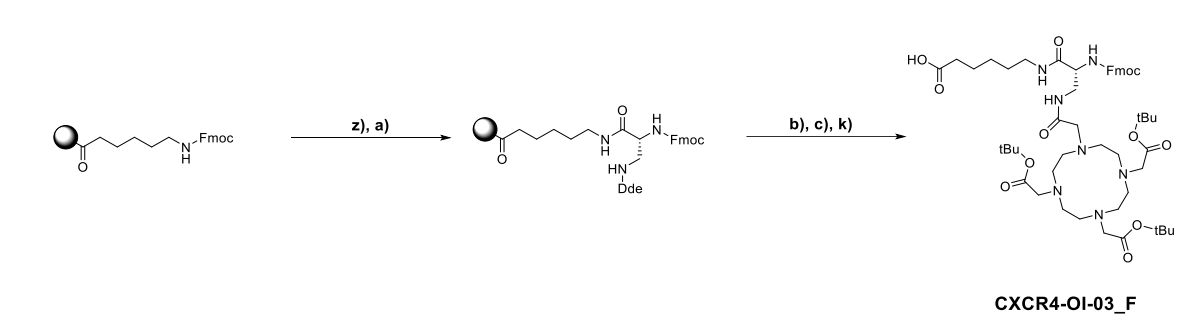


CXCR4-OI-3 was prepared in analogy with CXCR4-OI-1. The carboxylic acid-carrying Cy5.5 was condensed with CXCR4-OI-03_CLC_F under usage of GP8. Subsequent de-protection (GP5) and subjection to *semi*-preparative RP-HPLC purification yielded

the desired product. Complexation with ^{nat}Lu was achieved by incubation with the respective chloride salt as depicted above.

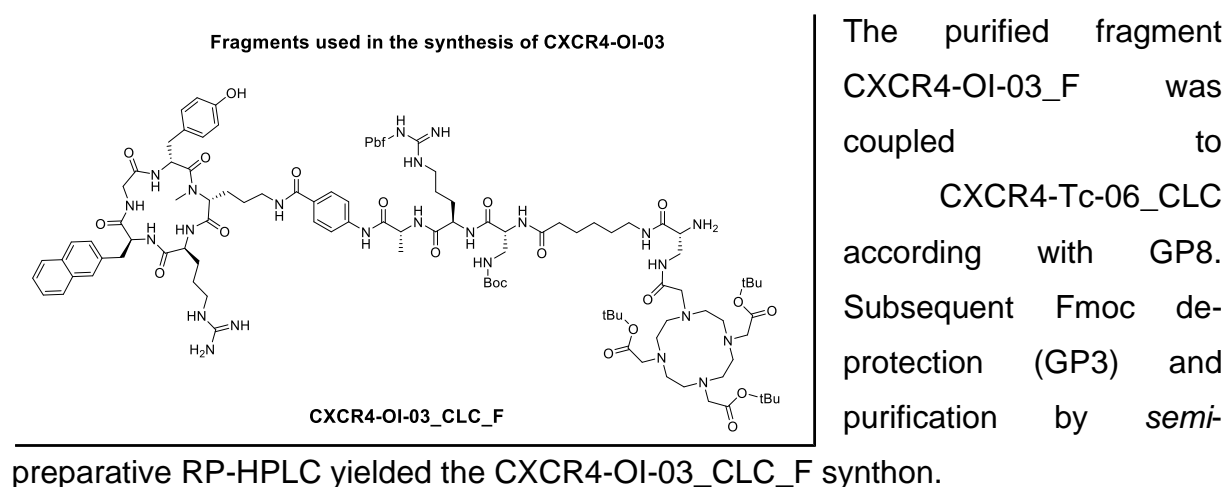
CXCR4-OI-03: RP-HPLC (10 to 60% B in 15 min): $t_R = 9.34$ min, $\kappa' = 6.19$. Calculated monoisotopic mass ($\text{C}_{112}\text{H}_{154}\text{N}_{26}\text{O}_{26}\text{S}_2$): 2343.10, found: 1173.4 $[\text{M}+2\text{H}]^{2+}$, 782.7 $[\text{M}+3\text{H}]^{3+}$.

^{nat}Lu CXCR4-OI-03: RP-HPLC (10 to 60% B in 15 min): $t_R = 8.78$ min, $\kappa' = 3.39$. Calculated monoisotopic mass ($\text{C}_{112}\text{H}_{151}\text{LuN}_{26}\text{O}_{26}\text{S}_2$): 2515.01, found: 1258.4 $[\text{M}+2\text{H}]^{2+}$, 839.3 $[\text{M}+3\text{H}]^{3+}$.



Scheme 20: Synthesis of the DOTA-conjugated fragment CXCR4-OI-03_F: z) 20% Piperidine in DMF (v/v); a) Fmoc-D-dap(Dde)-OH (1.5 eq.), HOAt (1.5 eq.), TBTU (1.5 eq.), 2,4,6-Collidine (3.0 eq.); b) imidazole (0.43 g), $[\text{NH}_2\text{OH}]\text{Cl}$ (0.63 g); c) DOTA(*t*Bu)₃-OH (1.5 eq.), HOAt (1.5 eq.), TBTU (1.5 eq.), DIPEA (3.0 eq.); k) 20% HFIP in DCM (v/v).

Fragment CXCR4-OI-03_F was synthesized *via* SPPS. Fmoc-Ahx-OH was immobilized on resin (GP1) and coupled with Fmoc-D-dap(Dde)-OH according with GP2c). Selective side-chain de-protection (GP4b)), coupling of DOTA(*t*Bu)₃ (GP2a)) and resin cleavage under retention of protecting groups (GP7a)) yielded the respective fragment.



CXCR4-OI-03_F: RP-HPLC (10 to 95% B in 15 min): $t_R = 16.66$ min, $\kappa' = 7.33$.

Calculated monoisotopic mass ($C_{52}H_{79}N_7O_{12}S$): 993.58, found: 938.7 $[M-tBu+H]^+$.

CXCR4-OI-03_CLC_F: RP-HPLC (10 to 95% B in 15 min): $t_R = 9.14$ min, $\kappa' = 3.33$.

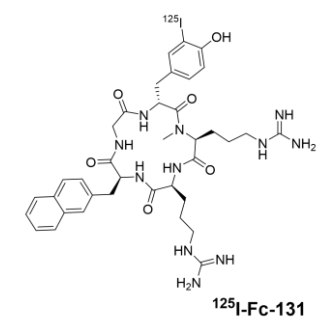
Calculated monoisotopic mass ($C_{110}H_{166}N_{24}O_{24}S$): 2239.22, found: 1120.3 $[M+2H]^{2+}$.

3. Radiolabeling

3.1. Iodine-125

Approximately 50–150 µg of unlabeled and purified precursor were dissolved in 20 µL DMSO and 280 µL TRIS buffer (25 mM TRIS-HCl, 0.4 mM NaCl, pH = 7.5) was added. After addition of 5 µL [¹²⁵I]NaI solution (15–20 MBq), the mixture was transferred into a reaction tube, coated with 150 µg Iodogen®. After incubation for 15 min at r.t., the supernatant was removed from the oxidant and subjected to RP-HPLC purification. Labeling of PDCs and optical imaging devices slightly deviated from this procedure. Detailed information can be found in the respective chapters within the presentation of results and discussion of data.

¹²⁵I-FC-131



The standard ligand for *in vitro* testing of CXCR4-directed ligands was prepared as depicted above. RP-HPLC purification was carried out applying the following conditions. The correct radio-peak was identified by comparison of the retention time with the respective UV-peak.

¹²⁵I-FC-131: RP-HPLC (20 to 55% B in 15 min): $t_R = 9.35$ min, $\kappa' = 5.23$.

3.2. Technetium-99m

Labeling of peptides with technetium-99m was carried out dependent on the chelator used. In general, the peptides and respective admixtures, either taken from aqueous solutions or used as freeze-dried formulations, were incubated with freshly eluted [^{99m}Tc]NaTcO₄-solution applying elevated temperature.

3.2.1. mas₃-conjugated and Glycosylated Ligands

Labeling of peptides carrying a mas₃ chelator or a glycosylated derivative thereof was conducted alike. The general concept was based on the preparation of PSMA I&S (158) and was implemented as follows.

An aqueous labeling mixture or freeze-dried formulation was prepared by mixing the stock solutions according to the following indication:

Stock 1: 6.76 μL

Stock 2: 10 μL

Stock 3: 5.0 μL

Stock 4: 8.0 μL

Stock 6: 2.0 μL

Stock 1: 1.78 g sodium-phosphate-dibasic dihydrate were dissolved in 50 mL H_2O (= solution 1). 1.38 g sodium-phosphate-monobasic monohydrate were dissolved in 50 mL H_2O (= solution 2). 47.35 mL of solution 1 and 2.65 mL of solution 2 were mixed to yield stock 1.

Stock 2: 5 mL of stock 1 were diluted with 5 mL of H_2O to yield stock 2.

Stock 3: The respective mas_3 - or glycosylated chelator-conjugated peptide was dissolved in DMSO or H_2O or a mixture thereof to a concentration of usually 1.0 mM.

Stock 4: 2.5 g disodiumtartrate dehydrate were dissolved in 10 mL of stock 1 to yield stock 4.

Stock 5: 30 mg ascorbic acid were mixed with 10 mL aqueous HCl (10 mM).

Stock 6: 4.0 mg tin(II)chloride dihydrate were dissolved in 1.0 mL of stock 5. This solution was freshly prepared for every aqueous labeling experiment or preparation of freeze-dried formulations.

For the labeling reaction, freshly eluted $^{99\text{m}}\text{Tc}[\text{NaTcO}_4]$ -solution (0.5–8.0 mL, 50–950 MBq) was added to the aqueous mixture or freeze-dried formulation and heated for 25–30 min at 90–95°C. The vial was removed from the heating bath and left to cool for 5 minutes.

Quality control was performed by radio-TLC and radio-RP-HPLC directly from the reaction mixture.

radio-RP-HPLC: $t_{\text{R}} (^{99\text{m}}\text{TcO}_4^-) = t_0 - 2 \text{ min}$, $t_{\text{R}} (^{99\text{m}}\text{Tc-colloid}) = t_0 - 2 \text{ min}$, $t_{\text{R}} (^{99\text{m}}\text{Tc-tartrate}) = 2 - 3 \text{ min}$, $t_{\text{R}} (^{99\text{m}}\text{Tc-peptide}) = > 3 \text{ min}$.

radio-TLC on silica-coated 60 RP-18 F254s strips employing different mobile phases:
 $\text{NH}_4\text{OAc}/\text{DMF}$ (1/1, v/v): $R_{\text{f}} (^{99\text{m}}\text{TcO}_4^-) = 0$, $R_{\text{f}} (^{99\text{m}}\text{Tc-colloid}) = 0$, $R_{\text{f}} (^{99\text{m}}\text{Tc-tartrate}) = 0.5 - 0.8$, $R_{\text{f}} (^{99\text{m}}\text{Tc-peptide}) = 0.8 - 1$.

NaCl (0.9 vol% in H_2O): $R_{\text{f}} (^{99\text{m}}\text{TcO}_4^-) = 1$, $R_{\text{f}} (^{99\text{m}}\text{Tc-colloid}) = 1$, $R_{\text{f}} (^{99\text{m}}\text{Tc-tartrate}) = 0$, $R_{\text{f}} (^{99\text{m}}\text{Tc-peptide}) = 0$.

The resulting technetium-99m-labeled compounds were used without further purification when the yields were determined to be $\geq 95\%$ by both radio-RP-HPLC and TLC methods. If additional purification was needed, following procedure was applied. A Sep-Pak C8 Plus Light Cartridge (145 mg sorbent, 37–55 μm) was preconditioned with 10 mL EtOH_{abs} prior to 10 mL H₂O and loaded with the labeled peptide *via* the male side. The cartridge was washed with 8 mL PBS and eluted *via* the female side with 1 mL of a EtOH/PBS solution (7/3, v/v).

3.2.2. HYNIC-conjugated Ligands

The labeling procedure of peptides carrying a HYNIC chelator was based on the published routine for HYNIC-TOC (159). The reaction was carried out with either the aqueous labeling mixture or a freeze-dried formulation thereof. The stock solutions were prepared and used as follows:

Stock 1: 50 μL

Stock 2: 50 μL

Stock 3: 5.33 μL

Stock 4: 5.0 μL

Stock 1: Ethylenediaminediacetic acid (EDDA) was dissolved in aqueous NaOH (0.1 M) to a concentration of 10 g/L.

Stock 2: Disodiumtartrate dihydrate was dissolved in NaH₂PO₄ buffer (40 g/L) to a concentration of 40 g/L.

Stock 3: Tin(II)chloride dihydrate was dissolved in aqueous sodium ascorbate (3.0 g/L in 0.01 M HCl) to a concentration of 1.5 g/L. This mixture was freshly prepared for every labeling experiment or the preparation of freeze-dried formulations.

Stock 4: The respective HYNIC-carrying peptide was dissolved in DMSO or H₂O or a mixture thereof to a concentration of usually 1.0 mM.

For the labeling experiment, freshly eluted [^{99m}Tc]NaTcO₄-solution (0.5–8.0 mL, 50–950 MBq) was added to the aqueous mixture or freeze-dried formulation and the vial heated for 20 min at 90–95°C. The vial was removed from the heating block and left to cool for 5 minutes.

Quality control was performed by radio-TLC and radio-RP-HPLC directly from the reaction mixture as stated above.

The resulting technetium-99m-labeled compound was used without further purification when the yield was determined to be $\geq 95\%$ by both radio-RP-HPLC and TLC methods. If additional purification was needed, the procedure as depicted above was applied.

3.2.3. N4-conjugated Ligands

The labeling procedure of N4-carrying compounds with technetium-99m was adapted from published literature with some modifications (156). The reaction was carried out with either the aqueous labeling mixture or a freeze-dried formulation thereof. Such a mixture contained the following stock solutions in the respective quantities:

Stock 1: 25 μL

Stock 2: 3.0 μL

Stock 3: 5.0 μL

Stock 4: 7.5 μL

Stock 1: Na_2HPO_4 was dissolved in H_2O to yield a concentration of 0.05 M (pH = 11.5).

Stock 2: Disodiumcitrate sesquihydrate was dissolved in H_2O to a concentration of 0.1 M.

Stock 3: Tin(II)chloride dihydrate was dissolved in aqueous sodium ascorbate (3.0 g/L in 0.01 M HCl) to a concentration of 1.0 g/L. This mixture was freshly prepared for every labeling experiment or the preparation of a freeze-dried formulation.

Stock 4: The respective N4-conjugated peptide was dissolved in DMSO or H_2O or a mixture thereof to a concentration of usually 1.0 mM.

For the labeling experiment, freshly eluted $^{99\text{m}}\text{Tc}$ NaTcO₄-solution (0.5–8.0 mL, 50–950 MBq) was added and the vial heated for 10 min at 90°C. The vial was removed from the heating bath and left to cool for 5 minutes.

Quality control was performed by radio-TLC and radio-RP-HPLC directly from the reaction mixture as stated above.

The reaction mixture was used without further purification if the labeling yield was determined to be $\geq 95\%$. If additional workup was necessary, the procedure as depicted above was applied.

3.3. Lutetium-177

For ^{177}Lu -labeling of DOTA- or DOTA-GA-conjugated peptides, 0.5–2.0 nmol of the respective peptide (directly from stock, DMSO or H_2O or mixtures thereof) were mixed with 10 μL of an aqueous sodium acetate buffer (1.0 M, $\text{pH} = 5.5$). The desired amount of ^{177}Lu ($^{177}\text{LuCl}_3$ (0.04 M in HCl), usually between 5 and 80 MBq), was added and the mixture diluted with HCl (0.04 M) to a total volume of 100 μL . After 30 min at 95°C , 10 μL sodium ascorbate (0.1 M) was added to prevent radiolysis and reaction control *via* radio-RP-HPLC and radio-TLC was performed.

radio-RP-HPLC: $t_{\text{R}} (^{177}\text{LuCl}_3) = t_0 - 2$ min, $t_{\text{R}} (^{177}\text{Lu-peptide}) = > 3$ min.

Silica-coated 60 RP-18 F254s with mobile phase $\text{NH}_4\text{OAc}/\text{DMF}$ (1/1; v/v):

$R_{\text{f}} (^{177}\text{LuCl}_3) = 0$, $R_{\text{f}} (^{177}\text{Lu-colloid}) = 0$, $R_{\text{f}} (^{177}\text{Lu-peptide}) = 1$.

Cellulose ITLC-SG paper with mobile phase trisodium citrate (0.1 M):

$R_{\text{f}} (^{177}\text{LuCl}_3) = 1$, $R_{\text{f}} (^{177}\text{Lu-colloid}) = 0$, $R_{\text{f}} (^{177}\text{Lu-peptide}) = 0$.

3.4. Fluorine-18

SiFA-conjugated peptides were labeled with fluorine-18 by isotopic exchange reaction. A SAX cartridge (Sep-Pak Accell Plus QMA Carbonate light, 46 mg sorbent, *Waters*) was conditioned with 10 mL H_2O prior to passage of aqueous ^{18}F NaF. The cartridge was purged with 10 mL air, dried with 20 mL DMSO, followed by purging with another 20 mL air to remove traces of water. ^{18}F -fluoride was eluted with 500 μL of ammonium formate solution (80 mg/mL DMSO).

This mixture containing the entire eluted activity, was used for either one or several labeling experiments. The desired activity (usually 30–500 MBq) was therefore mixed with 10–25 nmol of the respective SiFA-conjugated peptide (directly from stock in DMSO) and the mixture incubated at 40°C for 5 min. The reaction solution was immediately diluted with 8 mL PBS and the enclosed peptide loaded onto a preconditioned (10 mL EtOH_{abs} , then 10 mL H_2O) Oasis HLB Plus Light cartridge (30 mg sorbent, 30 μm particle size) *via* the male side. The cartridge was purged with 10 mL PBS, followed by 10 mL air and the entire peptide eluted by passage of 500 μL of an EtOH/PBS mixture (7/3; v/v) *via* the female cartridge side. Radiochemical purities and yields were determined using radio-RP-HPLC and radio-TLC.

radio-RP-HPLC: $t_{\text{R}} (^{18}\text{F}^-) = t_0 - 2$ min, $t_{\text{R}} (^{18}\text{F-peptide}) = > 3$ min.

Silica-coated 60 RP-18 F254s with mobile phase ACN/PBS (8/2; v/v; + 10 vol% NaOAc (2.0 M in H₂O); + 1 vol% TFA):

R_f (¹⁸F-fluoride) = 0, R_f (¹⁸F-peptide) = 0.8–1.

3.5. Gallium-68

Labeling of DOTA-conjugated peptides with gallium-68 was achieved in accordance with the published procedure for the synthesis of [⁶⁸Ga]Pentixafor (113). An automated GallElut⁺ system from *Scintomics* was used. Briefly, the ⁶⁸Ge/⁶⁸Ga-generator from *IThemba LABS* was eluted with aqueous HCl (1.0 M) and a fraction (usually 1.25 mL, 500–700 MBq) was transferred into the reaction vial (*ALLTECH*, 5 mL), loaded beforehand with 2–5 nmol of the respective DOTA-conjugated peptide. The reaction mixture was heated for 5 min at 95°C before passage through a Sep-Pak C8 light cartridge (145 mg sorbent, 37–55 μm), pre-conditioned with 10 mL EtOH_{abs} followed by 10 mL H₂O. The product was eluted with 2 mL of an EtOH/H₂O mixture (1/1; v/v), the cartridge purged with 1 mL PBS and 1 mL H₂O before removal of EtOH from the combined solutions *in vacuo*. Radiochemical purities and yields were assessed by radio-TLC.

Silica-coated 60 RP-18 F254s with mobile phase NH₄OAc/DMF (1/1; v/v):

R_f (⁶⁸GaCl₃) = 0, R_f (⁶⁸Ga-colloid) = 0, R_f (⁶⁸Ga-peptide) = 1.

Cellulose ITLC-SG paper with mobile phase trisodium citrate (0.1 M):

R_f (⁶⁸GaCl₃) = 1, R_f (⁶⁸Ga-colloid) = 0, R_f (⁶⁸Ga-peptide) = 0.

3.6. Gallium-67

Labeling of DOTA-conjugated peptides with gallium-67 was carried out in analogy with a method described in literature (160). In short, [⁶⁷Ga]Ga-citrate was immobilized on a SEP-Pak Silica light cartridge (120 mg sorbent, 55–105 μm), rinsed with H₂O (10 mL), dried by purging with 10 mL air and the activity eluted with the desired volume of HCl (0.1 M). A fraction of the resulting [⁶⁷Ga]GaCl₃-solution was then diluted with HEPES to a total volume of 200 μL and given onto the DOTA carrying peptide (5 nmol, from stock in H₂O or H₂O/DMSO mixture). The mixture was then heated to 95°C for 30 min, diluted with PBS to a volume of at least 3 mL and passed through a SEP Pak C8 light cartridge (30 mg sorbent, 37–55 μm) to remove excess [⁶⁷Ga]GaCl₃. The labeled

peptide was eluted with 0.5 mL of an EtOH/PBS (1/1; v/v) mixture. Radiochemical yields and purities were assessed *via* radio-TLC.

Silica-coated 60 RP-18 F254s with mobile phase NH₄OAc/DMF (1/1; v/v):

R_f (⁶⁷GaCl₃) = 0, R_f (⁶⁷Ga-colloid) = 0, R_f (⁶⁷Ga-peptide) = 1.

Cellulose ITLC-SG paper with mobile phase trisodium citrate (0.1 M):

R_f (⁶⁷GaCl₃) = 1, R_f (⁶⁷Ga-colloid) = 0, R_f (⁶⁷Ga-peptide) = 0.

4. Cell culture, *in vitro* Experiments and Lipophilicity

4.1. Cultivation of Jurkat Lymphoma Cells

CXCR4-expressing Jurkat T lymphocyte cells were grown in *Gibco's* RPMI 1640 GlutaMAX medium supplemented with 10 vol% FBS and maintained in a 5% CO₂ atmosphere at 37°C. The cells were passaged at least twice a week and usually diluted to a factor of 5 to 20.

4.2. Cultivation of Chem-1 Cells

CXCR4-expressing Chem-1 cells were grown in DMEM-F12 medium supplemented with 10 vol% FBS, 1 vol% NEA, 1 vol% PenStrep and 1 vol% HEPES (1.0 M). Cells were maintained in a 5% CO₂ atmosphere at 37°C. The cells were passaged at least twice a week and usually diluted to a factor of 10 to 100.

4.3. IC₅₀ Determination

In preparation for the determination of IC₅₀ values, Jurkat cells were removed from their cultivation flask and counted in a hemocytometer using trypan blue as contrast agent. The cell suspension was centrifuged, and the pellet resuspended in HBSS (+1 wt% BSA) to a concentration of 2 mio cells/mL. 8x3 polystyrene tubes were loaded with 25 µL of the standard ligand ¹²⁵I-FC-131 (1.0 nM in HBSS) and 25 µL of the ligand to investigate in the respective concentration (10⁻⁴–10⁻¹⁰ M, n = 3 for each concentration). 200 µL of cell suspension (400,000 cells per tube) were added to obtain a final peptide concentration range of 10⁻⁵–10⁻¹¹ M. The tubes were cooled for 2h at 8°C to prevent internalization and the experiment then stopped by removal of the supernatant. 200 µL HBSS were added to the tubes, the resulting cell-suspension centrifuged, and the supernatant pooled with the respective initially removed fractions. This step was repeated once more before the tubes containing the supernatants and the ones containing the cell pellets were subjected to the γ-counter. IC₅₀ values were determined using the GraphPad Prism 6 software as stated above.

4.4. invIC₅₀ Determination

For the determination of inverse IC₅₀ (invIC₅₀) values, the protocol for the determination of regular IC₅₀ values was resumed with minor changes. The peptide under investigation was radioactively labeled and a stock solution in HBSS (2.0 nM) was prepared. A concentration gradient of the unlabeled standard ligand FC-131 in HBSS (10⁻⁴–10⁻¹⁰ M) was established. The cell tubes (n = 3 per concentration) were then loaded with 25 µL of the radioactive peptide solution, 25 µL of FC-131 solution with the respective concentration and 200 µL cell suspension (400,000 cells). The tubes were cooled for 2h at 8°C to prevent internalization and the experiment then stopped by removal of the supernatant. 200 µL HBSS were added to the tubes, the resulting cell-suspension centrifuged, and the supernatant pooled with the respective initially removed fractions. This step was repeated once more before the tubes containing the supernatants and the ones containing the cell pellets were subjected to the γ-counter. invIC₅₀ values were determined using the GraphPad Prism 6 software as stated above.

4.5. Internalization Studies

Prior to internalization experiments, Chem-1 cells were harvested by removal of the medium and subsequent incubation of the cells with trypsin/EDTA (0.05%/0.02%; w/v) for 30 min at 37°C. The resulting cell suspension was centrifuged, the supernatant removed, and the cell pellet resuspended in medium. The cells were then counted and seeded in 24-well plates (100,000 cell per well) 24 ± 2h prior to the experiment.

On the day of the experiment, the medium was removed, and the cells incubated in 200 µL DMEM-F12 (+5 wt% BSA) for 15 min at 37°C. Each well (n = 3 for every time point) was either treated with 25 µL DMEM-F12 (+5 wt% BSA) or 25 µL of an AMD3100 stock (1.0 mM in H₂O) for blockage of the receptors. When the experiment was carried out as a dual-tracer approach, a radio-tracer solution was prepared containing the radiolabeled standard ligand ¹²⁵I-FC-131 and the labeled peptide under investigation, each in a concentration of 2.0 nM. 25 µL of this stock was added to the wells (final ¹²⁵I-FC-131 concentration: 0.2 nM; final peptide concentration under investigation: 0.2 nM) and the cells incubated at 37°C for the respective period.

The internalization was stopped by placing the well-plate on ice and removing the supernatants. The cells were washed with 250 μL cold HBSS and both the fractions for each well combined, comprising the amount of unbound radioligand.

For the removal of cell-bound ligand, 250 μL of cold acid wash (0.02 M NaOAc in aqueous acetic acid, pH = 5) were added and the cells incubated for 15 min on ice. The supernatant was removed, the cells washed with cold HBSS and the respective fractions combined to obtain the entirety of surface-bound radioligand.

The cells were then incubated with 300 μL NaOH (1.0 M in H_2O) for at least 30 min at r.t. before the supernatant was removed. The well was washed with another 300 μL NaOH and the fractions combined that contain the amount of internalized radioligand. The different fractions were subjected to the γ -counter, measuring the activity of the radionuclide used for the labeling of the peptide under investigation first. After an adequate time, the same fractions were measured again for the activity of ^{125}I . Data was corrected for non-specific internalization and referred to the specific internalization of the standard ligand ^{125}I -FC-131.

4.6. $\log D_{7.4}$ Determination

The ligand under investigation (usually 0.5–3.0 MBq, depending on the radioisotope) was diluted in PBS (pH = 7.4) to a total volume of 0.5 mL and mixed with 0.5 mL *n*-octanol in a low-bind Eppendorf tube ($n = 6\text{--}8$). The tubes were vortexed at maximum speed for 3 min to ensure equilibrium of distribution before centrifugation at 15.000 $\times g$ for 5 min on a Biofuge 15 from *Heracus Holding GmbH* (Osterode, Germany). An aliquot of 100 μL of each fraction was measured in the γ -counter and the $\log D_{7.4}$ calculated as follows:

$$\log D_{7.4} = \text{average}(\log_{10}(\frac{\text{activity in octanol}}{\text{activity in PBS}}))$$

5. *In vivo* Experiments and Imaging

5.1. CB17-SCID Mice and Jurkat Xenograft Model

All animal experiments were conducted in accordance with general animal welfare regulations in Germany (German animal protection act, as amended on 18.05.2018, Art. 141 G v. 29.3.2017 I 626, approval no. 55.2-1-54-2532-71-13) and the institutional guidelines for the care and use of animals. To initialize tumor growth, Jurkat cells ($2\text{--}3 \times 10^7$ cells) were suspended in a mixture of *Gibco's* RPMI 1640 medium (100 μL) and Matrigel (1/1; v/v) from *BD Biosciences* (Heidelberg, Germany) and inoculated subcutaneously onto the right shoulder of 6–10 weeks old CB17-SCID mice from either *Charles River GmbH* (Sulzfeld, Germany) or the in-house mouse breeding facility. Mice were used for experiments, when tumors had grown to a diameter of 5–8 mm (4–10 weeks after inoculation).

5.2. Small Animal μSPECT Imaging

Mouse imaging experiments were conducted on a VECTor⁴ small-animal SPECT/PET/OI/CT machine from *MILabs BV*. (Utrecht, The Netherlands). The resulting data were analyzed with the associated PMOD (version 4.0) software. Mice were anaesthetized with isoflurane and the radioactively labeled compounds were injected *via* the tail vein. Mice were euthanized after the respective space of time and blood samples for later biodistribution studies were taken by cardiac puncture before image acquisition. Static images were received with 45 min acquisition time using the HE-GP-RM collimator and a stepwise multi planar bed movement. All images were reconstructed using the MILabs Rec software (version 10.02) and a pixel-based Similarity-Regulated Ordered Subsets Expectation Maximization (SROSEM) algorithm with a window-based scatter correction (20% below and 20% above the photopeak, respectively); Voxel size CT: 80 μm , voxel size SPECT/PET: 0.8 mm, 1.6 mm (FWHM) Gaussian blurring post processing filter, with calibration factor in kBq/mL and decay correction, no attenuation correction.

5.3. Biodistribution Studies

Approximately 0.5–20 MBq (0.02–0.2 nmol) of the ^{125}I -, ^{177}Lu -, $^{99\text{m}}\text{Tc}$ -, ^{18}F - or ^{68}Ga -labeled ligand were injected into the tail vein of Jurkat tumor-bearing CB-17 SCID mice and the animals sacrificed after the respective time. Selected organs were removed, weighted, and measured in a γ -counter. The resulting data were decay corrected and referred to the respective organ weight to yield %ID/g values.

In order to obtain fully comparable data sets, additional experiments prior to biodistribution studies were conducted. A serial dilution of the respective activity was prepared and the activity counts per minute of each fraction measured in the γ -counter. The resulting data was plotted against the deployed amount of radioactivity and therefore revealed the area in which the device is measuring a linear correlation between these two variables. A trendline was plotted through this area and with the help of the resulting function, a universally applicable factor derived, that correlates actual activities with measured counts from the γ -Counter. This isotope-specific factor was applied for the calculation of every %ID/g value and therefore provides comparability of values within a project.

5.4. Fluorescence Imaging

A fluorescent ligand (2.0 nmol) was injected into the tail vein of Jurkat tumor-bearing CB-17 SCID mice and the animals sacrificed after 2h. Tumor, spleen and liver were dissected and placed into the freezer for 3 days at -80°C prior to cutting into slices with 10 μm thickness. The slices were applied to microscopic slides and investigated by means of a Keyence Biorevo BZ-9000 fluorescence microscope from *KEYENCE Deutschland GmbH* (Neu-Isenburg, Germany). Images were taken under irradiation with light of a wavelength of 680 nm under 4-fold magnification. The images were edited using the Keyence BZ-II Analyzer software (Blur: 5.00, Brightness: 5.00, Reduction Rate: 0.50, Contrast: 141, Gamma: 100).

5.5. Clinical SPECT/CT Imaging

Clinical evaluation of $^{99\text{m}}\text{Tc}$]CXCR4-Tc-13 in patients was conducted under compassionate use in compliance with the German Medicinal Products Act, AMG §13

2b, and in accordance with the responsible authorities (Government of Oberbayern). First proof-of-concept studies were performed at the *Universitätsklinikum Augsburg* (Augsburg, Germany).

All subjects were examined on a Discovery MN CT 670 Pro equipped with an Optima 540 CT (GE Healthcare, Solingen, Germany). Full-body SPECT/CT scans at 5 and 60 min after tracer injection were acquired with a scanning speed of 30 cm/min, scans at 120 and 300 min were acquired with a scanning speed of 12 cm/min and scans at 21h were acquired with a scanning speed of 5 cm/min. The scans were obtained in 60 subsets using the double-head technology in matrices of 128x128 (zoom 1).

SPECT scans at 60 and 180 min after tracer injection were acquired with an exposure time of 8 sec per subset and scans at 21h were acquired with an exposure time of 16 sec per subset.

Emission data were smoothed applying a Butterworthfilter (0.48) and reconstructed iteratively by an ordered-subsets expectation maximization algorithm (2 iterations, 10 subsets).

Images were obtained after injection of 430–604 MBq of [^{99m}Tc]CXCR4-Tc-13 at 5 min to 21h p.i.

The specific and effective doses in selected organs were analyzed. For calculation of the doses, voxels of interest were defined around areas with increased uptake in full-body images. Time-activity curves for the respective organs were automatically determined and the residence time of the tracer calculated using the specific calibration of the SPECT camera and a standard activity value. The residence time was used as the input data for the Olinda/EXM software. The output of this calculation was referred to the dosimetry guideline of the *International Commission on Radiological Protection*.

5.6. Clinical PET/CT Imaging

Clinical evaluation of [¹⁸F]FDG in patients was conducted in accordance with the responsible authorities (Government of Oberbayern). The clinical studies were performed at the *Universitätsklinikum Augsburg* (Augsburg, Germany).

All subjects were examined on a Biograph mCT-S40 (Siemens Healthineers, Erlangen, Germany). Full-body PET/CT scans at 1h after injection of [¹⁸F]FDG were acquired with a scanning speed of 2 min per bed position. Emission data were reconstructed iteratively. A low-dose CT was conducted for attenuation correction and anatomical correlation.

Images were obtained after injection of 189 MBq of [¹⁸F]FDG at 1h p.i.

III. RESULTS AND DISCUSSION

1. Overview

Ligand development based on the structures of CXCL12, the endogenous agonist of CXCR4, and the horseshoe crab toxins tachyplesin and polyphemusin, has resulted in a variety of peptide scaffolds which share certain amino acids instrumental for binding to the receptor.

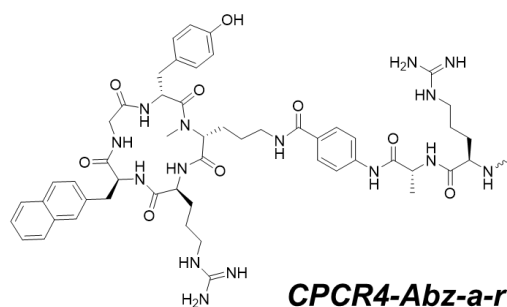
In the case of FC-131 and later *CPCR4*, the original binding sequence of polyphemusin, involving 18 amino acids was maximally downsized to a cyclic pentapeptide, of which only D-Tyr¹, Arg³ and 2-Nal⁴ are essential for high-affinity receptor binding (IC₅₀ (FC-131 (*cyclo*(D-Tyr¹-Arg²-Arg³-2-Nal⁴-Gly⁵)): 4 nM vs. [¹²⁵I]CXCL12; IC₅₀ (*CPCR4* (*cyclo*(D-Tyr¹-D-[NMe]Orn²-Arg³-2-Nal⁴-Gly⁵)): 6 nM vs. [¹²⁵I]-FC-131) (149)). For subsequent radiotracer development based on the *CPCR4* scaffold, D-ornithine (in *CPCR4*) was found to be the only residue allowing further derivatization with e.g. linkers and bifunctional chelators. However, maintaining high CXCR4 affinity still remained a major challenge during tracer design based on *CPCR4*. For example, the conjugation with -Ambz-DOTA to the ornithine sidechain and subsequent (radio)metal chelation, as in the case of [^{nat}Ga]Pentixafor and [^{nat}Lu]Pentixather, led to a reduction in CXCR4 affinity by a factor of 4.1 and 2.4, respectively (IC₅₀ (vs. [¹²⁵I]-FC-131): 24.8 ± 2.5 nM, 14.6 ± 1.0 nM, respectively). In the case of [^{nat}Bi]Pentixather, however, an IC₅₀ value of 4.4 ± 1.3 nM was observed (138). In molecular docking studies, the *CPCR4* scaffold was found to be embedded deeply insight the CXCR4 binding pocket, thus demanding additional elongation of the Pentixafor/Pentixather linker unit in order to provide ligands with higher receptor affinity and flexibility towards the attachment of sterically demanding signaling units (113,149). Recently, in her thesis at the Technical University Munich (TUM), Theresa Osl developed structural analogs of [⁶⁸Ga]Pentixafor and [¹⁷⁷Lu]Pentixather, bearing the optimized linker *Abz-a-r* (HO-4-aminobenzoic acid-D-Alanine-D-Arginine-NH₂). Both the peptides based on the *CPCR4* (Pentixafor-based) and the iodo-*CPCR4* (Pentixather-based) scaffold, respectively, displayed improved affinities (IC₅₀ (vs [¹²⁵I]-FC-131): 0.4 ± 0.1 nM, 1.7 ± 0.6 nM, [^{nat}Ga]CPCR4-Abz-a-r-DOTA and [^{nat}Lu]I-CPCR4-Abz-a-r-DOTA, respectively) and higher flexibility towards (radio)metal exchange in the DOTA chelate (147). These findings support the hypothesis that by

moving the signaling unit (e.g. the radiometal chelate) further away from the peptide core by introducing a longer linker (with a suitable interaction profile with the binding pocket), a higher tolerance towards the modification of *CPCR4*-based peptides with sterically demanding functionalities can be achieved.

Further optimization of this improved linker unit and its expansion by a variety of functionalities (chelators, fluorescent dyes, cytotoxic agents) without compromising CXCR4 affinity of the resulting imaging probes was the goal of this work. Major focus was generally directed towards identifying a “one for all” linker structure, that would accommodate any chosen labeling method and thus structurally diverse *N*-terminal linker modifications. To achieve this central objective, specific adjustments were successively and iteratively introduced during the course of the present work. The ligands originating from this iterative workflow can roughly be classified into three separate generations.

In the 1st generation (Figure 12) of compounds, the tracer backbone developed by Osl et al., from now on termed *CPCR4-Abz-a-r* ((*cyclo*(D-Tyr-D-[NMe]Orn(4-aminobenzoic acid-D-Ala-D-Arg-NH₂)-Arg-2-Nal-Gly)), was functionalized with a *mas*₃-chelator ((-D-Ser)₃-mercaptoacetic acid) (CXCR4-Tc-01) for radiolabeling with technetium-99m, a SiFA-benzoic acid (SiFA-BA) containing radiohybrid scaffold (CXCR4-SiFA-01) for labeling with fluorine-18 or a MMAE derivative (CXCR4-SiFA-01). This initial derivatization failed to result in compounds with suitable affinity and hydrophilicity. It was therefore proposed that the *CPCR4-Abz-a-r* tracer backbone required further optimization to enable the desired flexibility towards *N*-terminal modification with different signaling units.

1st generation



R₁	CXCR4-Tc-	R₂	CXCR4-SiFA-	R₃	X	CXCR4-MMAE-
/	01	/	01	/	/	01
D-Ala	02	D-His	02	/	CH ₂	02
D-Arg	03			D-His	CH ₂	03
D-Phe	04					
D-His	05					
D-Dap	06					

Figure 12: Structures of a 1st generation of novel CXCR4-targeted ligands: Compounds were based on the CPCr4-Abz-a-r scaffold developed by Osl et al. and modified with peptidic mas₃ chelators, SiFA-conjugated moieties and a MMAE derivative.

The CPCr4-Abz-a-r tracer backbone was then extended by a variety of amino acids neighboring the N-terminal D-arginine. A terminal mas₃ chelator was added to obtain structural analogs to CXCR4-Tc-01 (Figure 12). Affinities of compounds CXCR4-Tc-02 – 05 suggested a beneficial influence of a positively charged entity at this position. CXCR4-Tc-05, bearing a D-histidine between D-arginine and the mas₃-chelator displayed the highest affinity within this group, and its tracer backbone was therefore further employed in the synthesis of compounds CXCR4-SiFA-02 and CXCR4-MMAE-03 (Figure 12).

Later in this screening experiment, CXCR4-Tc-06 and -07 were prepared, containing a D-dap (D-2,3-diaminopropionic acid) moiety in exchange for D-histidine. The use of D-dap resulted in even higher affinities compared to CXCR4-Tc-05 and it was therefore integrated in the novel tracer backbone, CPCr4-Abz-a-r-dap ((cyclo(D-Tyr-D-[NMe]Orn(4-aminobenzoic acid-D-Ala-D-Arg-D-dap-NH₂)-Arg-2-Nal-Gly) (Figure 13). Compounds of the 2nd generation were then invariably based on this tracer backbone.

2nd generation

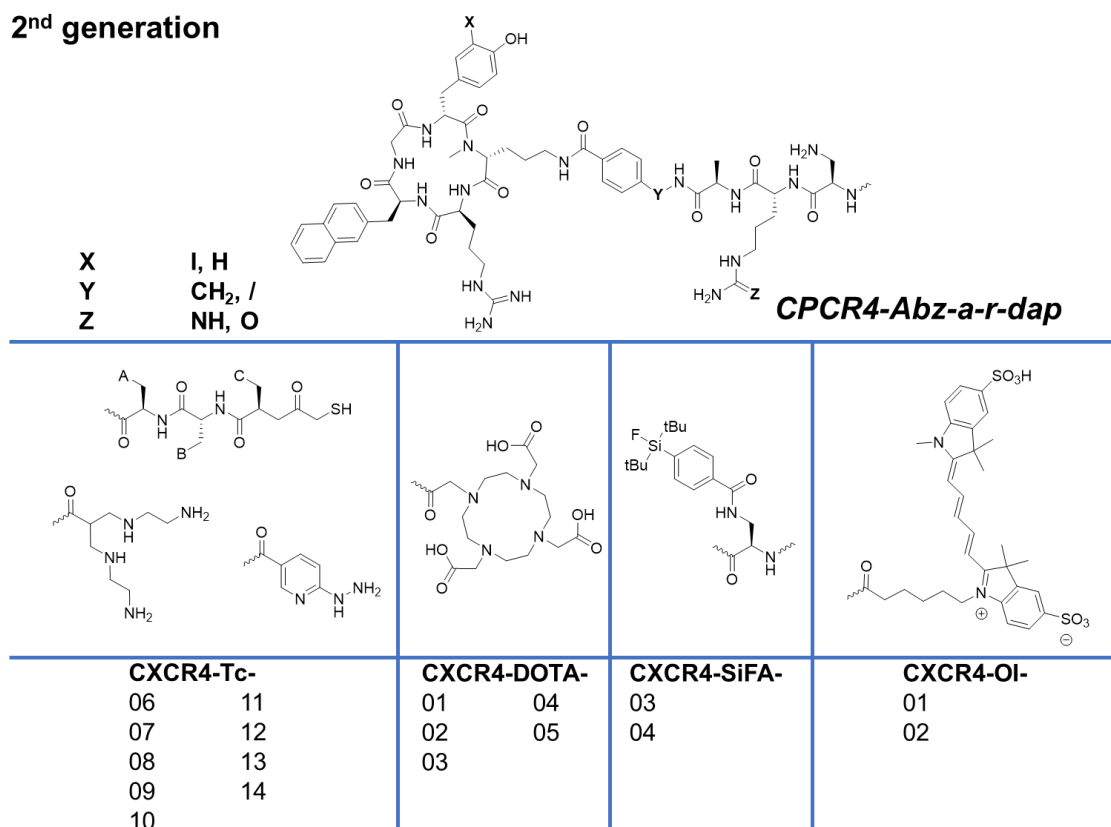
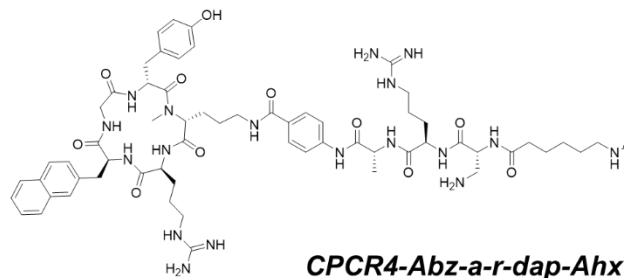


Figure 13: Structures of a 2nd generation of novel CXCR4-targeted ligands: Compounds were based on the CPCR4-Abz-a-r-dap tracer backbone developed in this work and modified with different technetium chelators, DOTA, SiFA-bearing moieties and a Cy5.5 fluorophore.

Initial results showed that the addition of sterically demanding fragments was tolerated without dramatic loss in CXCR4 affinity. As the SiFA building block needs to be shielded by *tert*-butyl groups in order to prevent hydrolysis, the modification of peptides with SiFA conveys pronounced lipophilicity (161). Compensation for the SiFA-induced increase in ligand lipophilicity was attempted by addition of charged and hydrophilic fragments. This, however, resulted in substantially decreased affinities. The compounds were then modified with an additional spacer, i.e. 6-aminohexanoic acid (Ahx), between the CPCR4 peptide scaffold and the respective charged and/or sterically demanding functional group. The CPCR4-Abz-a-r-dap tracer backbone was elongated with Ahx, creating an almost 50% greater distance (ca. 33 Å vs. ca. 23 Å, calculated by Chem3D 19.1 software) between the *N*-terminal functional group and CPCR4. This concept was broadly adopted and peptides CXCR4-Tc-15, CXCR4-SiFA-05 – 07, CXCR4-OI-03 and CXCR4-MMAE-04 were prepared.

Thus, a 3rd generation (Figure 14) of compounds was developed on the basis of the optimized *CPCR4-Abz-a-r-dap-Ahx* ((*cyclo*(D-Tyr-D-[MMe]Orn(4-aminobenzoic acid-D-Ala-D-Arg-D-dap-Ahx-NH₂)-Arg-2-Nal-Gly) tracer backbone.

3rd generation



<p>CXCR4-Tc-15</p>	<p>CXCR4-SiFA-05 06 07</p>	<p>CXCR4-MMAE-04</p>	<p>CXCR4-OI-03</p>

Figure 14: Structures of a 3rd generation of novel CXCR4-targeted ligands: Compounds were based on the extended *CPCR4-Abz-a-r-dap-Ahx* tracer backbone developed in this work and modified with a technetium chelator, SiFA-conjugated moieties, a Cy5.5 fluorophore and a MMAE toxin derivative.

The following chapter contains results of the synthesis and preclinical assessment of novel compounds as well as the discussion of the obtained data.

2. Technetium-99m Tracers

Since their introduction in the 1960s, technetium-99m tracers have been developed broadly and rapidly. Today, several radiochemical methods are implemented to obtain metal complexes in a fast and facile manner. The complexation of technetium-99m relies on the binding of the metal core in a distinct oxidation and coordination state such as $[^{99m}\text{Tc}]^{3+}$, $[\text{O}=\text{}^{99m}\text{Tc}=\text{O}]^+$ or $[^{99m}\text{Tc}=\text{O}]^{3+}$ (162). The eluate obtained from the $^{99}\text{Mo}/^{99m}\text{Tc}$ -generator contains the metal in its highest oxidation state as $[\text{}^{99m}\text{TcO}_4]^-$ pertechnetate anion, which has to be reduced in the presence of a coordinating ligand that defines the cores constitution (Figure 15) (163).

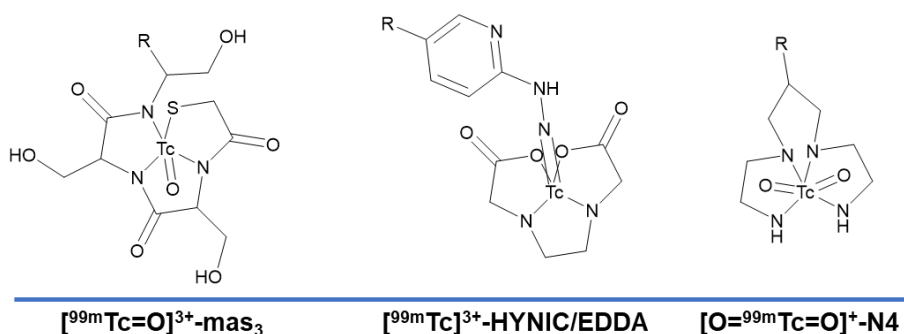


Figure 15: Structures of different technetium-99m coordination states in complex with their respective chelator: mas_3 , HYNIC/EDDA and the tetradentate N4 chelator; the coordination geometry is solely dependent on the chelators physicochemical properties and the reduction of the pertechnetate anion in their presence (163).

In the presence of a mas_3 -based chelator, a $[^{99m}\text{Tc}=\text{O}]^{3+}$ core is coordinated by free valence electrons of three amide-bond nitrogen atoms and a terminal sulfur atom. This complex possesses high stability in solution and is therefore a widely used core structure for technetium-99m-labeled radiopharmaceuticals such as prostate cancer imaging agent PSMA I&S (158). The mas_3 chelator is amino acid based and it is therefore inexpensive and available by SPPS. The chelators amino acid sidechains are not involved in binding of the radiometal and hence, any three-membered amino acid sequence terminated with a mercaptoacetic acid could serve as the chelator. More hydrophilic amino acids could be added as required without hampering the chelators labeling properties. This concept was adopted in the development of CXCR4-Tc-06 – 11 (III. 2.3.3.1).

Complexation with the chelator HYNIC results in a $^{99m}\text{Tc}^{3+}$ core that requires the coordination by an additional co-ligand such as ethylenediaminediacetic acid (EDDA) (Figure 15). HYNIC offers a facile chemical synthesis and rapid labeling and is therefore employed in a variety of clinically applied radiotracers such as sstr2 -targeted ligand

HYNIC-TOC, Bombesin analog HYNIC-[Lys³]-bombesin and the PSMA-targeted tracer HYNIC-iPSMA (164–166). We hypothesized that HYNIC would be a suitable chelator for *CPCR4*-based peptides as well and therefore prepared and evaluated the HYNIC-conjugated ligand CXCR4-Tc-12 (III. 2.3.3.2).

Maina et al. reported the synthesis of a sstr2-targeted ligand, carrying the tetradentate chelator N4 that complexes technetium-99m as a [O=^{99m}Tc=O]⁺ core (Figure 15). The tracer exhibited excellent labeling yields under mild conditions (167). Abiraj et al. revisited this idea and developed a chemical synthesis for a chelator analog that is easily integrated into tracer backbones by standard SPPS (156). On the basis of this work, new sstr2- and GRPR-(Gastrin-releasing peptide receptor)-targeted ligands were developed with improved properties compared to their HYNIC-conjugated analogs (168,169). Compounds CXCR4-Tc-13, -14 and -15, carrying such a N4 chelator will be discussed in chapters III. 2.3.3.2 and III. 2.3.4.

The detailed comparison of mas₃-conjugated, HYNIC- and N4-based CXCR4 tracers is content of the following chapter. First, synthesis of the newly developed compounds will be discussed, followed by the physicochemical properties and the performance in *in vitro* experiments. Selected compounds were evaluated in *in vivo* biodistribution and μ SPECT imaging studies, concluded by a proof-of-concept study in men.

2.1. Synthesis

2.1.1. mas₃-conjugated Ligands

Compounds of the 1st generation, CXCR4-Tc-01 – 06 are based on functionalization of the *CPCR4-Abz-a-r* tracer backbone with an adjacent amino acid and the chelator mas₃ as depicted in Figure 16.

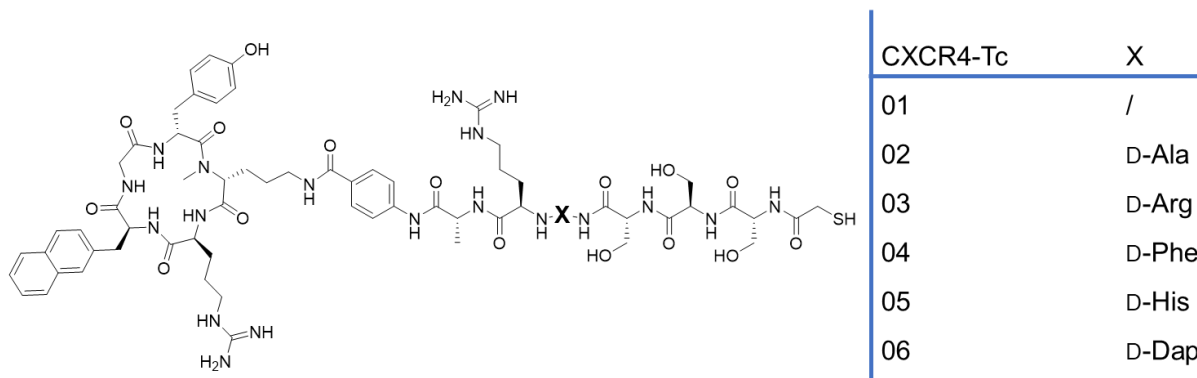


Figure 16: Summary of *mas*₃-conjugated 1st generation compounds CXCR4-Tc-01 – 06: novel structures were obtained by elongation of the *CPCR4*-Abz-a-r tracer backbone with one of 5 amino acids (X) and a terminal *mas*₃ chelator.

CXCR4-Tc-01, -03, -04 and -05 were prepared by condensation of the fully de-protected and purified *CPCR4* binding motif and a fully protected and purified linker, carrying the protected chelator. The chelator was assembled by stepwise SPPS directly at the *N*-terminal side of the resin-bound linker (resin-Abz-a-r(Pbf)-X-NH₂). Despite applying highly reactive reagents such as HATU/HOAt/TBTU/DCC, activation of the linker-chelator adducts was found to be incomplete in these types of condensations. When reaction times were stretched up to 24h, degradation of the starting materials was observed as a major obstacle for successful fragment coupling. Despite that, small portions of product could be isolated by *semi*-preparative RP-HPLC. These initial difficulties led to the conclusion that a synthesis strategy focusing on the in-solution condensation of smaller fragments up to a length of only four amino acids is to be favored. From then on, all other compounds within this study were prepared by condensation of the fully de-protected *CPCR4* with a fully protected linker moiety (HO-Abz-a-r(Pbf)-X-Fmoc). Subsequent Fmoc de-protection and purification yielded the starting material for the coupling with the separately synthesized and fully protected chelator. Removal of all protecting groups and purification *via semi*-preparative RP-HPLC afforded the desired peptides.

2.1.2. Glycosylated *mas*₃-conjugated Analogs

Sugar-conjugated D-homocysteine (HCy) in exchange for D-serine in the *mas*₃ chelator provides higher hydrophilicity of resulting radioligands. Synthesis of such building blocks was described multiple times in literature as this strategy poses a facile method for raising peptide hydrophilicity without the use of charged moieties (170–172). This concept was applied to the newly developed *CPCR4*-Abz-a-r-dap tracer backbone, to create a

spectrum of compounds with fine-tunable hydrophilicity (Figure 17). The glycosylated chelators were prepared in separate SPPS and then coupled to the scaffold.

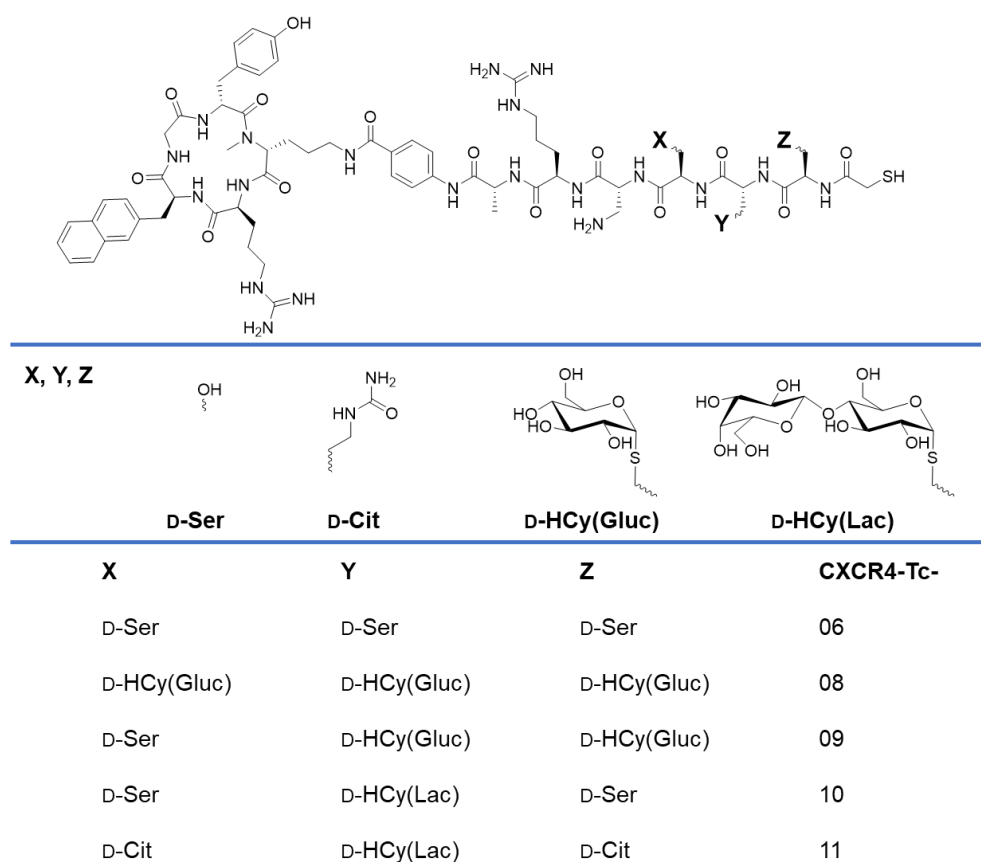


Figure 17: Summary of 2nd generation compounds CXCR4-Tc-06, 08 – 11: novel structures were obtained by elongation of the optimized CPCr4-Abz-a-r-dap tracer backbone (except for CXCR4-Tc-07 which carries a CPCr4-Ambz-a-r-dap tracer backbone). CXCR4-Tc-06 and -07 bear a terminal mas₃-chelator and CXCR4-Tc-08 – 11 bear glycosylated chelators.

As outlined in II. 2.2.4, side-chain derivatization of Fmoc-D-HCy(Trt)-OH was carried out in an one-pot reaction, utilizing the bifunctionality of SnCl₄ as both Bronsted acid for the removal of the Trityl protecting group and Lewis acid for the coordination and removal of the anomeric alpha acetate. The mechanism of this reaction is depicted in Figure 18.

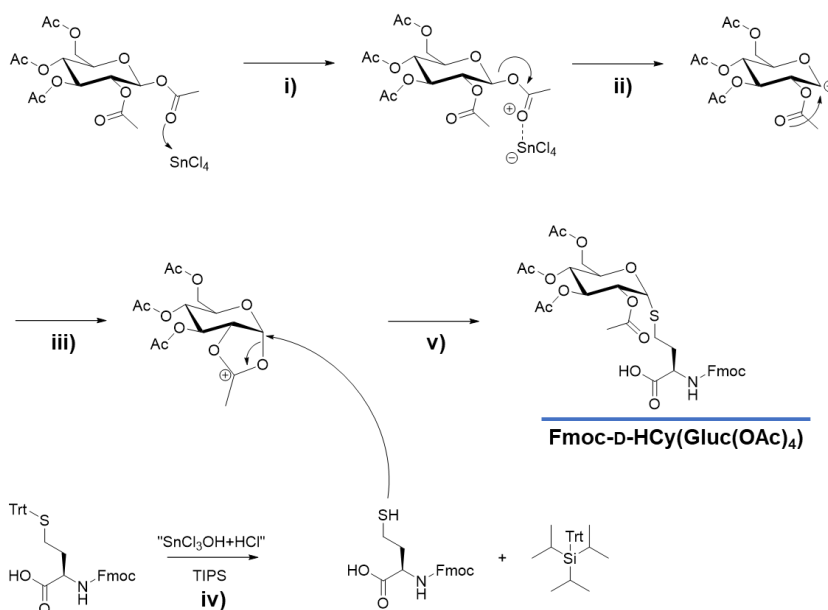


Figure 18: Mechanism of the one-pot reaction of SnCl_4 with β -D-glucosepentaacetate in presence of $\text{Fmoc-D-HCy(Trt)-OH}$ and TIPS, resulting in the side-chain-glycosylated $\text{Fmoc-D-HCy}(\beta$ -D-glucosetetraacetate)-OH synthon; **i)** SnCl_4 acts as a Lewis acid by coordinating and **ii)** removing the α -acetate protecting group of β -D-glucosepentaacetate; **iii)** the β -acetate carbonyl then forms the acetal with the neighboring carbocation and therefore facilitates **v)** the nucleophilic attack of the Fmoc-D-HCy-OH side chain to form the $\text{Fmoc-D-HCy}(\beta$ -D-glucosetetraacetate)-OH synthon; **iv)** de-protection of $\text{Fmoc-D-HCy(Trt)-OH}$ is simultaneously achieved by partial hydrolyzation of SnCl_4 in the solvent and removal of the trityl-cation by the scavenger TIPS; mechanism adapted from (173,174) .

The reaction proceeded analogously for the modification with β -D-lactoseheptaacetate. Both products of the reactions were isolated by flash-chromatography in typical yields of 30–40%.

On-resin synthesis of the glycosylated chelators CXCR4-Tc-08_F, -09_F, -10_F and -11_F (II. 2.2.7.1) was carried out by standard SPPS with the respective glycosylated homocysteine analogs. The resulting chelators were de-acetylated by incubation with KCN prior to coupling with the *CPCR4-Abz-a-r-dap* tracer backbone, with the exception of CXCR4-Tc-08_F. The latter was de-acetylated after coupling with the peptide, resulting in high losses of product due to degradation of the tracer backbone in the basic milieu.

2.1.3. HYNIC-conjugated Ligands

A detailed description of the HYNIC chelator synthesis is depicted in II. 2.2.7.2. The synthon was prepared on a gram-scale in organo-chemical synthesis and coupled Boc-protected with the *CPCR4-Abz-a-r(Pbf)-dap(Boc)-NH₂* tracer backbone or *CPCR4*.

Subsequent de-protection and RP-HPLC purification afforded the respective products (Figure 19).

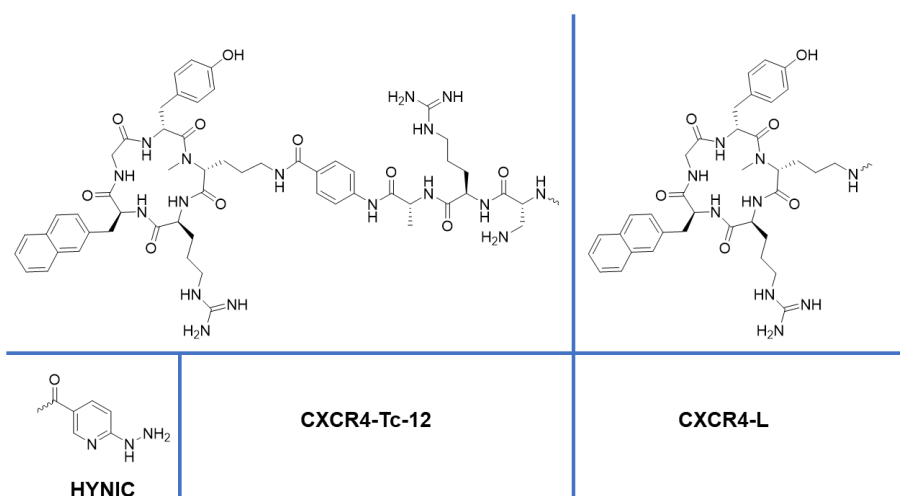


Figure 19: Summary of structures bearing the chelator HYNIC: CXCR4-Tc-12 was obtained by modification of the optimized CPCR4-Abz-a-r-dap tracer backbone and literature-known compound CXCR4-L was obtained by modification of the CPCR4 scaffold with HYNIC.

CXCR4-Tc-12 was prepared multiple times as HYNIC reacts with TFA in the final de-protection step, forming a trifluoroacetyl-HYNIC byproduct that significantly lowers yield of the synthesis and aggravates RP-HPLC purification (Figure 20) (175).

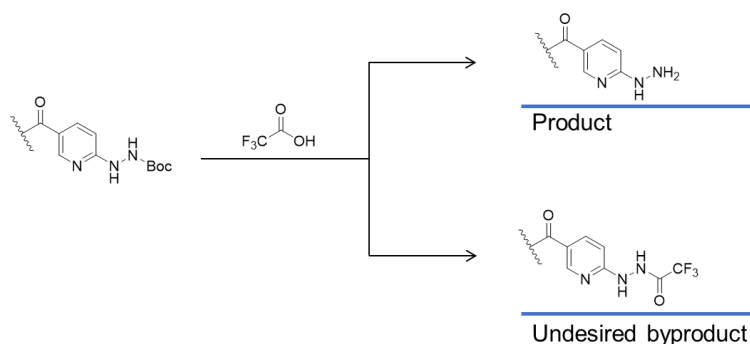


Figure 20: Formation of a trifluoroacetyl-HYNIC byproduct during the de-protection of a HYNIC(Boc)-carrying peptide using TFA (175).

The combined product fractions, however, yielded both compounds in sufficient amounts for *in vitro* and *in vivo* testing.

2.1.4. N4-conjugated Ligands

N4-conjugated ligands of the 2nd generation were prepared by fragment condensation of the CPCR4-Abz-a-r(Pbf)-dap(Boc)-NH₂ tracer backbone with the respective fully protected N4-conjugated fragment Z (CXCR4-Tc-13) or YZ (CXCR4-Tc-14). CXCR4-Tc-15 (3rd generation) was synthesized by condensation of the CPCR4-Abz-a-r(Pbf)-dap(Boc)-NH₂ tracer backbone with the *Ahx*-conjugated fragment XYZ. Ligands were obtained after global de-protection and purification *via* RP-HPLC (Figure 21).

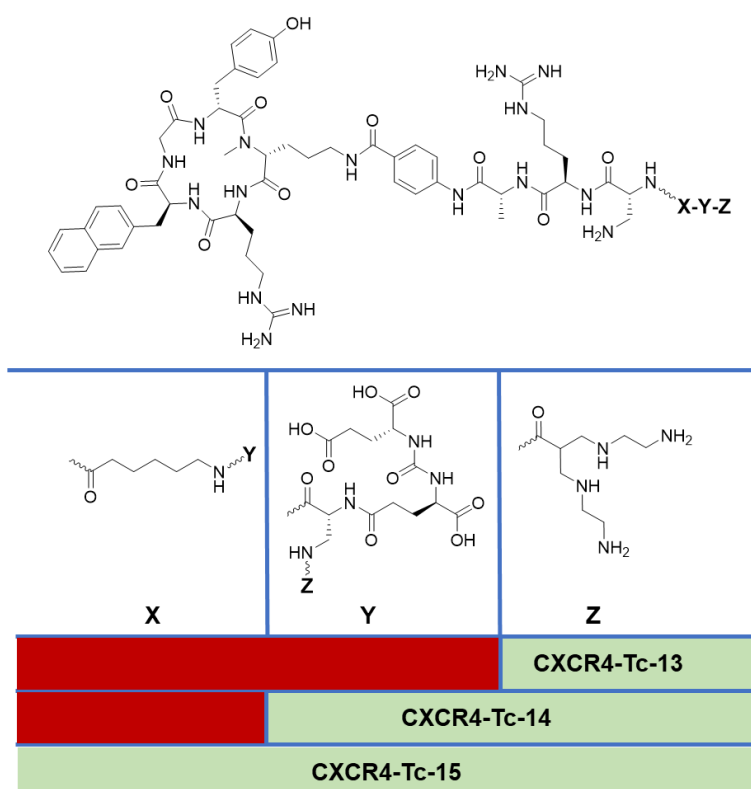


Figure 21: Summary of structures bearing the chelator N4: CXCR4-Tc-13 and -14 were obtained by elongation of the CPCR4-Abz-a-r-dap tracer backbone and CXCR4-Tc-15 was obtained by elongation of the CPCR4-Abz-a-r-dap-Ahx tracer backbone with a N4-conjugated moiety.

Synthesis of the protected chelator N4(Boc)₄ and compounds CXCR4-Tc-13, -14 and -15 carrying such chelator was complicated by the formation of an elimination byproduct (Figure 22).

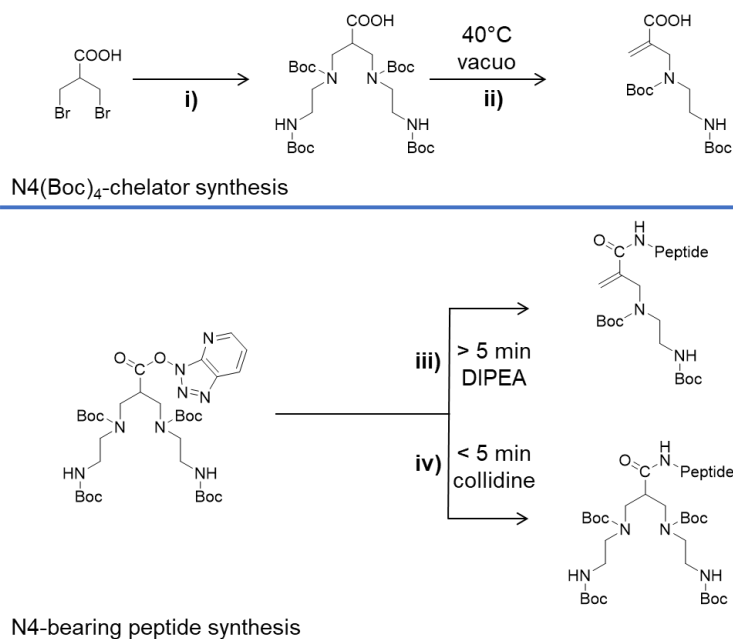


Figure 22: Formation of a heat-induced elimination byproduct during the synthesis of the N4(Boc)₄ chelator and N4(Boc)₄-conjugated ligands: **i)** reaction of 3-bromo-2-(bromomethyl)propanoic acid with tert-butyl-(2-aminoethyl)-carbamate and subsequent reaction with Boc₂O to yield the fully protected N4(Boc)₄ chelator; **ii)** heat-induced elimination of ethylenediamine(Boc)₂ forming the undesired elimination product; **iii)** elimination of ethylenediamine(Boc)₂ upon activation of the protected chelator with HOAt and incubation with DIPEA for more than 5 minutes; **iv)** successful coupling of the protected chelator onto peptides by using collidine and incubation for less than 5 minutes.

This byproduct was found as main product of the initial substitution reaction between tert-butyl-(2-aminoethyl)-carbamate and 3-bromo-2-(bromomethyl)propanoic acid, when the solvent was removed at the rotary evaporator with the heating bath set to 40°C. When the solvent was removed at ambient temperature, the formation of this byproduct was not observed. An in-detail description of the chelator synthesis is given under II. 2.2.7.3. When the fully protected and purified chelator was coupled to a tracer backbone, elimination was found to take place again (Figure 22). Pre-activation of the carboxylic acid with an HOAt/HOBt-based reagent was reduced to 2–5 minutes and 2,4,6-collidine was used as a base to circumvent this process. The resulting peptides were then fully de-protected and purified without further ado.

2.2. Radiosynthesis

2.2.1. mas₃-conjugated and Glycosylated Ligands

The radiochemical synthesis of mas₃-derived technetium-99m-labeled tracers is significantly eased due to the applicability of freeze-dried kit formulations. A detailed description of the respective kit ingredients can be found in chapter II. 3.2.1. Briefly, such a formulation contains a small amount of the respective peptide (typically between 5–25 nmol), a reducing agent such as SnCl₂ and a buffer substance. The complexation reaction is induced by the addition of fresh ⁹⁹Mo/^{99m}Tc-generator eluate and the mixture heated at 90°C for 20 minutes. Analysis of the labeling yield was undertaken by radio-TLC development and was usually found to be above 95% for any of the investigated ligands, thus making additional purification redundant. A detailed description of the quality control process after labeling with technetium-99m can be found in chapter II. 3.2.1. Decreasing radiochemical conversions were obtained when older kits (> 6 months) were used. This may be attributed to slow oxidation of the reducing agent or the chelating sulfur atom. Lower yields were generally found for the labeling of threefold glycosylated compound CXCR4-Tc-08. The sterically demanding side-chain derivatizations may hinder a correct rearrangement of these amino acids to efficiently bind the technetium-99m core.

Technetium-99m complexes based on the chelator mas₃ are well characterized entities concerning their structure. It is known that any of these complexes exists in at least two isomeric forms, the *syn*- and the *anti*-isomer (163). This isomerization was observed in every radio-RP-HPLC run with the labeled compounds. The proportion in which the isomers were formed was found to be dependent on reaction temperature and the reaction time. Figure 23 displays the outcome of radio-RP-HPLC runs during the labeling reaction of [^{99m}Tc]CXCR4-Tc-06 over the course of 120 minutes. The proportion of both isomers inverts at some point between 60 and 120 minutes and the formation of a third component can be detected.

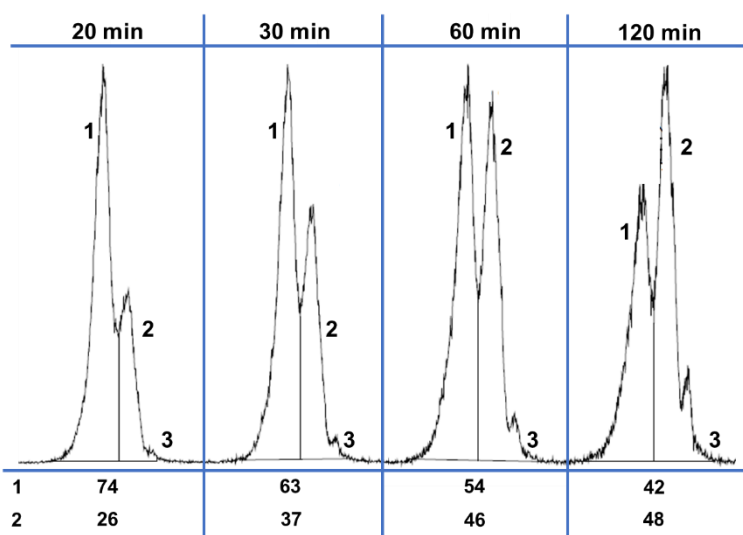


Figure 23: Sections of radio-RP-HPLC chromatograms revealing varying proportions of isomers 1 and 2 during the technetium-99m labeling reaction of $[^{99m}\text{Tc}]\text{CXCR4-Tc-06}$; samples were taken at 20, 30, 60 and 120 min reaction time and instantly subjected to qualitative RP-HPLC measurement. Chromatograms further reveal the timely formation of a third component.

The reaction time and temperature were harmonized for every ligand within this project to guarantee consistent isomer proportions and valid data. Much as any isomeric pharmakon, biodistribution profiles of the respective isomers may vary greatly, thus limiting their potential for widespread use in clinical application (163).

2.2.2. HYNIC-conjugated Ligands

Both HYNIC-carrying ligands $[^{99m}\text{Tc}]\text{CXCR4-Tc-12}$ and literature-known $[^{99m}\text{Tc}]\text{CXCR4-L}$ were either labeled in solution with the freshly prepared buffer and reducing agents or from freeze-dried kit formulations. In both cases, typically 5 nmol of peptide were used together with the reducing agent SnCl_2 and EDDA as co-ligand (II. 3.2.2). The complexation was carried out at 90°C over 20 minutes and the labeling yield was determined by radio-TLC development. Opposed to the mas_3 -conjugated compounds, no sufficient incorporation of technetium-99m was reached, thus demanding additional solid-phase extraction (SPE) cartridge purification. Radiochemical conversion for $[^{99m}\text{Tc}]\text{CXCR4-Tc-12}$ did not exceed 50% ($n = 7$) whereas up to 85% ($n = 4$) conversion (n.d.c.) was observed for $[^{99m}\text{Tc}]\text{CXCR4-L}$. This discrepancy may be linked with the peptide structures, more specifically, the terminal D-dap moiety of CXCR4-Tc-12 that may interfere with the correct complex geometry by coordinating the co-ligand used. Generally lower conversion was found for the labeling from kit formulations compared to labeling

from solution. Optimization of the labeling procedure as well as the used co-ligand may ultimately result in higher conversion. This optimization, however, is time consuming and was not part of this work.

2.2.3. N4-conjugated Ligands

Peptides carrying the N4 chelator, [^{99m}Tc]CXCR4-Tc-13, -14 and -15 were labeled from freeze-dried kit formulations containing the respective peptide in small amounts (typically 7.5 nmol), SnCl₂ and a buffer substance (details in II. 3.2.3.). Complexation was carried out at 90–95°C for 10 minutes before determination of the labeling yield. Radio-TLC development was hindered as [^{99m}Tc]CXCR4-Tc-13 is scarcely migrating while tailing on the TLC plate. The tailing effect was also visible in radio-RP-HPLC runs and hindered proper integration of radiochemical impurities. However, it was possible to alleviate this problem by using a steep gradient. Besides these analytical problems, all of the N4-conjugated compounds were labeled with consistently high yields greater 95% and radiochemical purities above 90%, superseding additional purification. Only one radioactively labeled species was observed in radio-RP-HPLC runs. This finding is in accordance with the literature, reporting only one product of this complexation (169,176,177).

2.3. *In vitro* Evaluation and Hydrophilicity

2.3.1. 1st Generation Tracers

Ligands of the 1st generation of technetium-99m-labeled tracers (Figure 16) were synthesized to evaluate, whether an additional amino acid between the *CPCR4-Abz-a-r* tracer backbone and the mas₃ chelator has a substantial impact on CXCR4 affinity. The finding of this screening was thought to be seminal for the derivatization with a variety of functional entities and answer the question whether and how tightly the *N*-terminal linker sequence is interacting with the CXCR4 binding cavity. Table 2 summarizes the outcome of IC₅₀ determinations for compounds CXCR4-Tc-01 – 06.

Table 2: IC_{50} [nM] values obtained for compounds CXCR4-Tc-01 – 06, carrying an additional amino acid between the CPCR4-Abz-a-r tracer backbone and a terminal mas_3 chelator: IC_{50} values were determined in competitive binding studies employing Jurkat cells (400,000 cells/tube; 8°C, 2h incubation) and the standard ligand ^{125}I -FC-131 (10^{-9} M, final assay-concentration). Data are expressed as mean \pm SD; experiments were conducted in triplicates or quintuplicates (*).

CXCR4-Tc-	IC_{50} [nM] (n = 3)	Amino acid
01	20.6 \pm 7.5	/
02	32.4 \pm 9.9	D-Ala
03	184 \pm 25	D-Arg
04	3490 \pm 502	D-Phe
05	11.0 \pm 1.30	D-His
06	4.97 \pm 1.34 (*)	D-Dap

CXCR4-Tc-01 (CPCR4-Abz-a-r- mas_3) is the structural analog to DOTA-conjugated ligand CPCR4-Abz-a-r-DOTA developed by Osl et al. [^{nat}Ga]CPCR4-Abz-a-r-DOTA is specified with an IC_{50} of 0.4 \pm 0.1 nM (vs. ^{125}I -FC-131) (146). Replacement of DOTA with mas_3 diminishes affinity towards CXCR4 by a factor of 26, according to our study. This drop in affinity may be caused by an elevated sterical demand of the mas_3 chelator due to the lower flexibility of its amide backbone compared to the rotational freedom within the structure of DOTA. Peptides displaying a high conformational flexibility are less prone to suffer structural repulsion with the binding cavity as a mismatch is more likely to be vanquished. Thus, higher affinity can oftentimes be achieved compared to rigid peptide counterparts (178–180).

Following the evaluation of CXCR4-Tc-01, it was proposed that the *N*-terminal domain bearing DOTA or mas_3 is located within the CXCR4 binding cavity. Hence, the respective functionality is interacting with residues in the binding pocket, resulting in positive or negative attraction. Compounds CXCR4-Tc-02 – 06 were prepared carrying an additional amino acid in the linker between the CPCR4 scaffold and the chelator to increase the distance between the core of the CXCR4 binding pocket and the ligand's signaling unit while maintaining high affinity.

CXCR4-Tc-02 bears an additional *N*-terminal D-Ala residue in its linker unit. Even though higher distance between the CPCR4 peptide scaffold and the chelator is established compared to CXCR4-Tc-01, affinity drops from 20.6 \pm 7.5 nM (CXCR4-Tc-01) to 32.4 \pm 9.9 nM. When sterically demanding amino acids such as D-Arg

(IC_{50} (CXCR4-Tc-03): 184 ± 25 nM) or D-Phe (IC_{50} (CXCR4-Tc-04): 3490 ± 502 nM) are employed, substantially decreased affinities, presumably due to elevated repulsion with the binding pocket are observed. In-depth analysis of the receptors molecular structure and co-crystallization with targeted ligands has shown that strongest interactions in the binding pocket take place between acidic moieties of CXCR4 and basic amino acid side chains of the respective ligand (105). Based on this knowledge and the results obtained from CXCR4-Tc-02 – 04, compounds CXCR4-Tc-05 and CXCR4-Tc-06, bearing basic sidechains with low sterical demand, were prepared. Introduction of D-His or D-Dap, respectively led to an increase in CXCR4 affinity when compared to CXCR4-Tc-01. The higher IC_{50} of compound CXCR4-Tc-05 (IC_{50} : 11.0 ± 1.3 nM) compared to CXCR4-Tc-06 (IC_{50} : 4.97 ± 1.34 nM) may be attributed to a higher sterical demand of the imidazolyl group compared to the dap β -amine.

CXCR4-Tc-06 emerged as the compound with the highest affinity within this series and laid the foundation for most of the synthesized ligands in this work (Figure 13). The *CPCR4-Abz-a-r-dap* tracer backbone offers high affinity and enhanced distance between the *N*-terminal signaling unit of the peptide and the *CPCR4* scaffold anchored in the CXCR4 binding pocket and therefore enables functionalization with sterically demanding moieties. A variety of technetium-99m-labeled tracers was prepared based on this tracer backbone. The in-depth analysis of these ligands demands the introduction of a method to analyze their binding properties more accurately. This method will be presented in the following chapter.

2.3.2. The Inverse IC_{50}

When ligands carrying mas_3 -based chelators are labeled with technetium-99m, a spherical structure is formed in which the components of the chelator arrange themselves around the metal core (181). This labeled compound may therefore vary greatly from its un-labeled precursor in terms of its 3D structure and with that, in its binding properties. As no stable technetium isotope exists, precursors for technetium-99m labeling are usually complexed with the chemically related and stable rhenium in order to determine the affinity towards a target. This complexation, however, requires harsh conditions or long reaction times usually followed by RP-HPLC purification, thus requiring high quantities of the respective precursor (182–184).

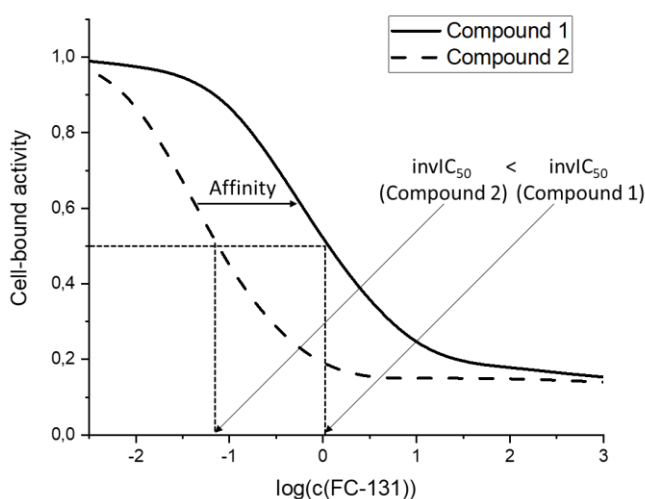


Figure 24: Hypothetical graph picturing the displacement of two differently affine radioligands (compound 1 and 2) from cells using increasing concentrations of the standard ligand FC-131: Higher concentrations of FC-131 are needed to displace half of the cell-bound compound 1 compared to less affine compound 2 and the $invIC_{50}$ value of compound 1 is therefore higher.

Hence, we introduce a novel method for the comparative study of compounds labeled with technetium-99m that utilizes the radiolabeled ligand in a constant concentration and the un-labeled reference FC-131 in decreasing concentrations, opposed to a regular IC_{50} assay that utilizes the cold ligand under investigation and a radiolabeled reference ligand. This so-termed inverse IC_{50} ($invIC_{50}$) provides higher values for more affine compounds (compound 1, Figure 24), as higher

concentrations of FC-131 are needed to replace cell-bound radioligand. The most prominent advantage of this method is the expendability of [^{nat}Re]-complexed compounds. Even though rhenium is closely related to technetium from a chemical point of view, using the intended radiometal may provide more authentic *in vitro* data. Furthermore, the amount of labeled substance per $invIC_{50}$ determination lies in the picomolar range, hence posing no waste of precious precursor. To obtain a reliable activity signal of the different assay fractions from the γ -counter, though, a certain radioactivity concentration in the probes is not to be undercut. This may limit the abundance in which $invIC_{50}$ experiments can be conducted, depending on the technetium supply of the facility. Another disadvantage is the overall higher experimental expenditure due to the fact, that testing requires freshly prepared radioligands. Furthermore, as this experimental setup is not yet established in the general context of technetium-99m-labeled tracer development, comparison to a literature-known compound is not possible unless the latter is evaluated in the same experimental setting.

2.3.3. 2nd Generation Tracers

2.3.3.1. CXCR4-Tc-06 – 11

Figure 17 gives an overview of the 2nd-generation ligands CXCR4-Tc-06 – 11. The structure of CXCR4-Tc-07 emanated from the uncertain impact of *Abz* instead of *Ambz* in the linker scaffold and served exclusively as an investigation tool for this circumstance.

Affinity and hydrophilicity

CXCR4-Tc-06 emerged as high-affinity ligand from the initial screening study of 1st-generation compounds. However, substantially lower hydrophilicity ($\log D_{7.4}$: -1.54 ± 0.02 , Table 3) of [^{99m}Tc]CXCR4-Tc-06 compared to [⁶⁸Ga]Pentixafor ($\log D_{7.4}$: -2.90 ± 0.08 , (114)) was observed which could prove detrimental in the context of an *in vivo* application. Only a limited number of measures to elevate peptide hydrophilicity are reported in literature. The introduction of a polyethylene glycol (PEG) spacer leads to an increase in hydrophilicity due to the formation of hydrogen bonds in aqueous solution. This effect, however, does not proceed in a linear fashion with increasing spacer length and may cause serious defects by shaping an amorphous “cloud” when a certain amount of PEG repetition units is reached (185). This “cloud” has been shown to hinder effective ligand-receptor interaction and compromise *in vivo* biodistribution profiles of the respective peptides (186–188). The addition of charged moieties and amino acids is synthetically facile and more effective in terms of increasing the hydrophilicity. On the other hand, however, introduction of charged residues poses a substantial change of physicochemical properties of the respective compound. As it was shown for the development of hydrophilic GRPR-targeted tracers, binding properties and *in vivo* uptake pattern may change drastically with the introduction of only one charged amino acid, potentially leading to higher off-target binding or retention of radioligand in the kidneys (189,190).

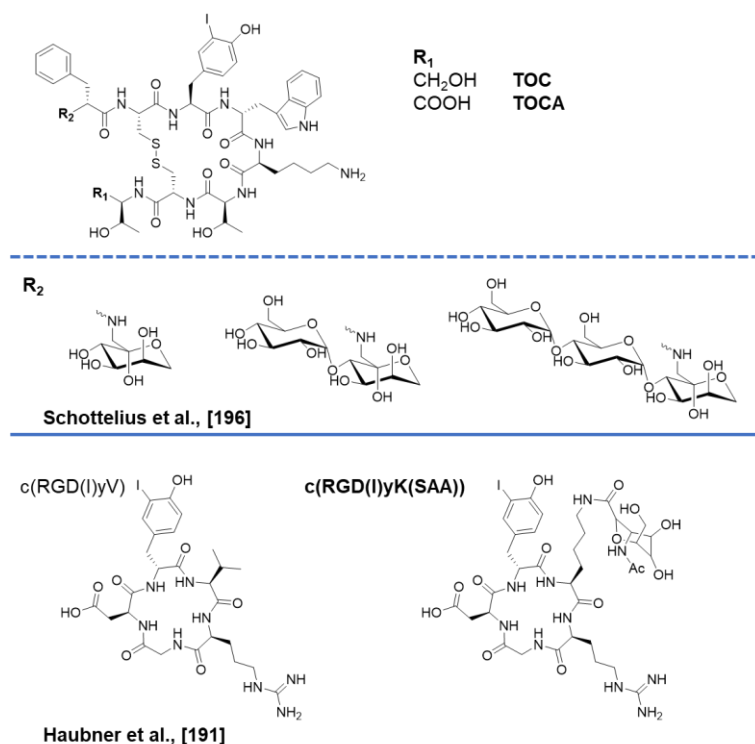


Figure 25: Summary of structures of glycosylated compounds described in literature: Amadori-reaction products glucosyl-, maltosyl- and maltotriosyl-[I]TOC and -[I]TOCA, respectively as reported by Schottelius et al.; glycosylated c(RGD(I)yK(SAA)) as reported by Haubner et al.

A combination of advantages from both presented methods, is depicted by amino acid side-chain-attached saccharides. Such glycosylated amino acids can provide substantial gains in hydrophilicity without changing the charge distribution in the peptides. Besides that, introduction of glycosylated amino acids into biologically active tracer backbones may have tremendous effects on both pharmacokinetics and bioavailability (191–194). Lower susceptibility to proteolysis and higher transport rates over cell membranes by activation of

glucose transporters has been confirmed, overall resulting in a better performance in *in vivo* experiments (195). Schottelius et al. analyzed the impact of mono-, di- and trisaccharides attached to the sstr2-targeted TOCA on its biodistribution pattern. In comparison to standard ligands [¹²⁵I]TOC and [¹²⁵I]TOCA, respective glycosylated derivatives (Figure 25) offered a faster blood clearance, lower accumulation in liver, intestines and kidneys and overall higher tumor/non-target-tissue ratios (196). Haubner et. al prepared the *N*-terminally modified derivative (c(RGD(I)yK(SAA))) of α_vβ₃-targeted peptide c(RGD(I)yV) (Figure 25) in an attempt to lower hepatobiliary accumulation. As expected, hydrophilicity was elevated by the sugar moiety and clearance *via* the renal pathway was increased, thus leading to optimized tumor/non-target-tissue ratios (191). Aim of this series of compounds, CXCR4-Tc-08 – 11, was the introduction of hydrophilic mono- and disaccharide-modified chelators to the *CPCR4-Abz-a-r-dap* tracer backbone. Table 3 summarizes the obtained logD_{7.4} and invIC₅₀ data for compounds [^{99m}Tc]CXCR4-Tc-06 – 11, [¹⁷⁷Lu]Pentixather, [⁶⁸Ga]Pentixafor and [^{99m}Tc]CXCR4-L. [⁶⁸Ga]Pentixafor was not included in invIC₅₀ determination, as required gallium-68 was not available. Reference ligand [^{99m}Tc]CXCR4-L consists of the *CPCR4* scaffold,

derivatized at its D-Orn side chain with the HYNIC chelating moiety (Figure 19) (197). This compound was tested in a first proof-of-concept study in healthy volunteers and exhibited a combined renal and hepatobiliary excretion (99).

Table 3: Summary of invIC_{50} [nM] and $\log D_{7.4}$ values for compounds $[^{99m}\text{Tc}]\text{CXCR4-Tc-06-11}$ and reference compounds $[^{177}\text{Lu}]\text{Pentixather}$, $[^{68}\text{Ga}]\text{Pentixafor}$ and $[^{99m}\text{Tc}]\text{CXCR4-L}$: invIC_{50} values were determined in competitive binding studies employing Jurkat cells (400,000 cells/tube; 8°C, 2h incubation), the standard ligand FC-131 (10^{-5} – 10^{-11} M, final assay-concentrations) and the respective radiolabeled ligands (10^{-9} M, final assay-concentration). Data are expressed as mean \pm SD; invIC_{50} data were determined as triplicates or quadruplicates (*); $\log D_{7.4}$ values were determined as octuplicates, septuplicates (**) or sextuplicates (***); (****): data adapted from literature (137).

CXCR4-Tc-	invIC₅₀ [nM] (n = 3)	logD_{7.4} (n = 8)
06	3.67 \pm 0.77	-1.54 \pm 0.02 (***)
07	3.65 \pm 1.01 (*)	-1.36 \pm 0.02
08	3.50 \pm 0.65	-2.56 \pm 0.03 (***)
09	5.13 \pm 1.81	-2.32 \pm 0.02 (**)
10	2.05 \pm 0.95	-2.94 \pm 0.02
11	4.82 \pm 1.36	-2.92 \pm 0.06
$[^{99m}\text{Tc}]\text{CXCR4-L}$	No displacement of FC-131	-1.84 \pm 0.01
$[^{177}\text{Lu}]\text{Pentixather}$	1.91 \pm 1.11	-1.76 \pm 0.03
$[^{68}\text{Ga}]\text{Pentixafor}(\text{****})$	n.d.	-2.90 \pm 0.08

$[^{99m}\text{Tc}]\text{CXCR4-L}$ is specified in literature with a K_D of 51.2 ± 8.9 nM (197). In the invIC_{50} assay, however, no displacement of the reference ligand FC-131 was observable, presumably due to insufficient receptor affinity of the technetium tracer. As outlined in III. 2.3.2, higher invIC_{50} values represent more affine ligands as more FC-131 is needed to replace cell-bound radioligand. $[^{177}\text{Lu}]\text{Pentixather}$ displays an invIC_{50} value of 1.91 ± 1.11 nM and with that, the lowest receptor affinity of compounds within this series. This outcome reinforces the underlying concept that the *CPCR4-Abz-a-r-dap* tracer backbone ensures high CXCR4 affinity even when sterically demanding functionalities are added. Highest CXCR4 affinity in this series is observed for $[^{99m}\text{Tc}]\text{CXCR4-Tc-09}$ (invIC_{50} : 5.13 ± 1.81 nM), bearing two glucosylated homocysteine residues in the chelator. Its threefold glucosylated analog $[^{99m}\text{Tc}]\text{CXCR4-Tc-08}$ (invIC_{50} : 3.50 ± 0.65 nM) displays lower receptor affinity compared to $[^{99m}\text{Tc}]\text{CXCR4-Tc-09}$ but still a value comparable to $[^{99m}\text{Tc}]\text{CXCR4-Tc-06}$. Introduction of a lactosylated homocysteine residue in the structure of $[^{99m}\text{Tc}]\text{CXCR4-Tc-10}$ led to a considerably decreased CXCR4 affinity compared to $[^{99m}\text{Tc}]\text{CXCR4-Tc-06}$. However, when the enframing serine residues were exchanged by

citrulline, the resulting ligand [^{99m}Tc]CXCR4-Tc-11 displayed even higher CXCR4 affinity than [^{99m}Tc]CXCR4-Tc-06. The use of *Ambz* in the linker of [^{99m}Tc]CXCR4-Tc-07 did not result in altered receptor affinity compared to [^{99m}Tc]CXCR4-Tc-06.

The introduction of glycosylated chelators substantially improved the hydrophilicity of the novel compounds. [^{99m}Tc]CXCR4-Tc-08 – 11 display lower logD_{7.4} values than [^{99m}Tc]CXCR4-Tc-06 and [¹⁷⁷Lu]Pentixather. Highest gain in hydrophilicity is observed for peptides containing the lactosyl-modified homocysteine, [^{99m}Tc]CXCR4-Tc-10 and -11. With a logD_{7.4} value of -2.94 ± 0.02 and -2.92 ± 0.06 , respectively, both ligands are as hydrophilic as [⁶⁸Ga]Pentixafor (logD_{7.4}: -2.90 ± 0.08) and substantially more hydrophilic compared to the glucosylated analogs [^{99m}Tc]CXCR4-Tc-08 and -09. As expected by the addition of a CH₂ group, [^{99m}Tc]CXCR4-Tc-07 shows slightly increased lipophilicity compared to [^{99m}Tc]CXCR4-Tc-06.

In literature, [¹⁷⁷Lu]Pentixather is characterized as being more affine than [⁶⁸Ga]Pentixafor. If this is indeed the case, [^{99m}Tc]CXCR4-Tc-10 and -11 are supposedly more affine than [⁶⁸Ga]Pentixafor while being as hydrophilic and should therefore be promising candidates for further evaluation as CXCR4-targeted SPECT imaging agents.

Internalization

Assessment of internalization rates of compounds [^{99m}Tc]CXCR4-Tc-06 – 11 into CXCR4-expressing Chem-1 cells was conducted in dual-tracer experiments with the internal standard ligand ¹²⁵I-FC-131. Cellular uptake values of the novel ligands are expressed as percentage values in reference to the cellular uptake of the internal standard. This proceeding guarantees coherent data unaffected by day-to-day fluctuations. The internalization efficiency describes the fraction of internalized radioligand in relation to the entire cell-bound activity and was found to be considerably increased for CXCR4 targeted agonists compared to antagonist (146).

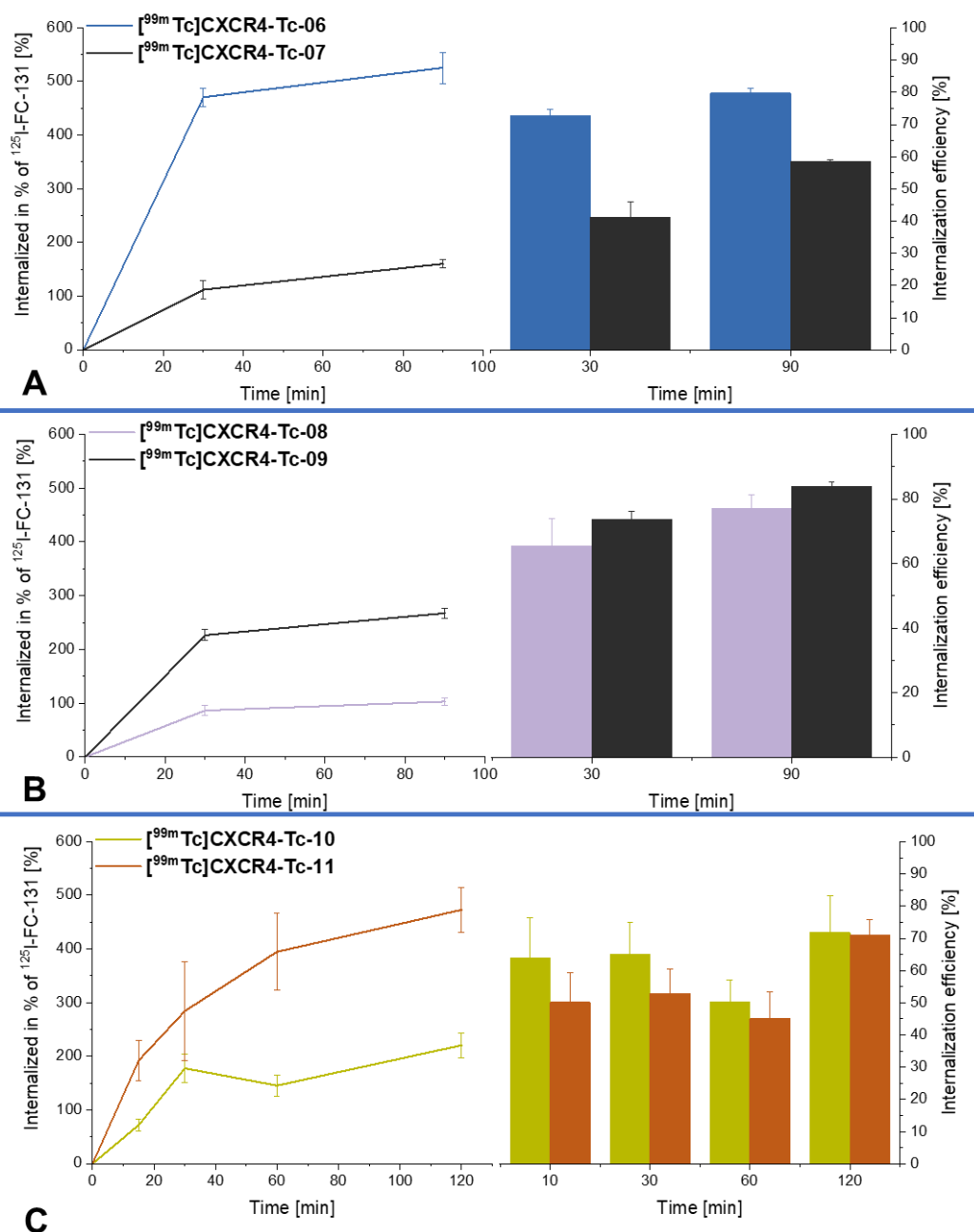


Figure 26: Dual tracer internalization of radiolabeled novel ligands and the reference compound ¹²⁵I-FC-131 (final assay concentration for each peptide 0.2 nM) into Chem-1 cells (100,000 cells per well; 37°C): **A**: [^{99m}Tc]CXCR4-Tc-06 and -07, **B**: [^{99m}Tc]CXCR4-Tc-08 and -09 and **C**: [^{99m}Tc]CXCR4-Tc-10 and -11. Data are expressed as mean ± SD; internalization at every time point was determined in triplicate and corrected for unspecific internalization; line diagrams: amount of Internalized novel ligand in relation to the amount of internalized internal standard ¹²⁵I-FC-131 in %; bar diagrams: amount of internalized novel ligand in relation to the total cell-bound novel ligand in %.

[^{99m}Tc]CXCR4-Tc-06 shows the highest cellular uptake (525 ± 29% after 90 min) within this series of tracers and a maximum internalization efficiency of 79.7 ± 1.6% (Figure 26, **A**). The structural analog [^{99m}Tc]CXCR4-Tc-07 was prepared with the intent to investigate the influence of *Ambz* versus *Abz* in the linker unit. As depicted in Table 3, affinity was

found unchanged. However, a drastic difference in internalization can be observed, as [^{99m}Tc]CXCR4-Tc-07 reaches a third ($160 \pm 8\%$ after 90 minutes) of the maximum internalized activity observed for [^{99m}Tc]CXCR4-Tc-06 (Figure 26, **A**). The internalization efficiency is found to be lowest within the series of ligands, reaching a maximum of $58.4 \pm 0.8\%$ after 90 minutes (Figure 26, **A**). Osl et al. reported a decisive gain in total cellular uptake and internalization efficiency of DOTA-conjugated CXCR4 ligands, when *Abz* was employed in the linker instead of *Ambz* (146). This finding was confirmed in our experiment and will be discussed in detail in chapter III. 3.

Affinity was not substantially compromised by insertion of hydrophilic mono- and disaccharide moieties into the chelating scaffolds of [^{99m}Tc]CXCR4-Tc-08 – 11 in comparison to [^{99m}Tc]CXCR4-Tc-06. However, major differences concerning their internalization rates can be noted. Threefold glycosylated ligand [^{99m}Tc]CXCR4-Tc-08 reaches a maximum internalization of $103 \pm 7\%$ (Figure 26, **B**). Interestingly though, almost the same internalization efficiency compared to [^{99m}Tc]CXCR4-Tc-06 is reached ($77.2 \pm 4.3\%$ vs. $79.7 \pm 1.6\%$, respectively). The twofold glycosylated compound [^{99m}Tc]CXCR4-Tc-09, being the most affine ligand in this series, reaches a maximum internalization of $267 \pm 9\%$ after 90 minutes with $83.9 \pm 1.5\%$ of its cell-bound activity internalized (Figure 26, **B**). This outcome shows that the insertion of glycosylated homocysteine residues in the chelator moiety is generally detrimental to the absolute amount of internalized radioligand. The internalization efficiency, however, is not affected by the structural changes, thus indicating that these two processes are separate mechanisms to be tested.

Both disaccharide-containing tracers [^{99m}Tc]CXCR4-Tc-10 and -11 also display lower absolute internalization values compared to [^{99m}Tc]CXCR4-Tc-06. [^{99m}Tc]CXCR4-Tc-10 reaches a maximum internalization of $221 \pm 23\%$ after 120 minutes incubation (Figure 26, **C**). This uptake is exceeded after 30 minutes incubation and increased up to $473 \pm 42\%$ in the case of [^{99m}Tc]CXCR4-Tc-11 (Figure 26, **C**), thus signaling a beneficial influence for the substitution of D-serine with D-citrulline. Both compounds, however, show no significant difference in their internalization efficiency after 120 min incubation ($71.8 \pm 11.4\%$ for [^{99m}Tc]CXCR4-Tc-10 vs. $70.9 \pm 4.9\%$ for [^{99m}Tc]CXCR4-Tc-11, Figure 26, **C**). Again, sidechain-glycosylation of the chelating moiety proves to be disadvantageous for high absolute internalization rates. Besides that, there is no clear correlation between the insertion of glycosyl- or lactosyl-derivatized building blocks and the internalization rates of the respective compounds.

Summary

In summary, the introduction of sidechain-glycosylated or -lactosylated D-homocysteine into technetium-99m chelating moieties has yielded hydrophilic and affine compounds. Although absolute internalization rates are widespread, all of the compounds assessed – with the exception of [^{99m}Tc]CXCR4-Tc-07 – exhibit comparable values for their internalization efficiency. These values lie between 71 and 84% and indicate at least partial agonistic properties of these *CPCR4-Abz-a-r-dap*-based compounds. None of the modified ligands exceeded the absolute internalization of [^{99m}Tc]CXCR4-Tc-06. [^{99m}Tc]CXCR4-Tc-11, nevertheless, reaches up to this range while offering slightly higher affinity paired with a significant increase in hydrophilicity.

2.3.3.2. CXCR4-Tc-12 – 14

Figure 19 and Figure 21 show the structures of compounds CXCR4-Tc-12 – 14. CXCR4-Tc-12 and -13 were prepared as structural analogs of mas₃-conjugated CXCR4-Tc-06, with the intention of examining the influence of the HYNIC (CXCR4-Tc-12) and N4 (CXCR4-Tc-13) chelators on the physicochemical properties of the resulting tracers. CXCR4-Tc-14 was synthesized as a reaction on the relatively low hydrophilicity of ligand CXCR4-Tc-13 (Table 4). The *eue* (glu-urea-glu) motif was chosen as a hydrophilic modifier, as it is available in large quantities by organo-chemical synthesis and easily transferable to the tracer backbone by means of SPPS.

Affinity and hydrophilicity

Table 4 summarizes the obtained $invIC_{50}$ and $logD_{7.4}$ values for compounds [^{99m}Tc]CXCR4-Tc-06 and -11 and reference compounds [^{99m}Tc]CXCR4-L, [⁶⁸Ga]Pentixafor and [¹⁷⁷Lu]Pentixather. [⁶⁸Ga]Pentixafor was not included in $invIC_{50}$ determination, as required gallium-68 was not available. [^{99m}Tc]CXCR4-Tc-11 was chosen as a comparison as it offers the most suitable compromise between hydrophilicity, affinity and internalization from the tested technetium tracers so far.

Table 4: Summary of $invIC_{50}$ [nM] and $\log D_{7.4}$ values for compounds [^{99m}Tc]CXCR4-Tc-12 – 14 in comparison with [^{99m}Tc]CXCR4-Tc-06, -11 and reference ligands [^{99m}Tc]CXCR4-L, [^{68}Ga]Pentixafor and [^{177}Lu]Pentixather: $invIC_{50}$ values were determined in competitive binding studies employing Jurkat cells (400,000 cells/tube; 8°C, 2h incubation), the standard ligand FC-131 (10^{-5} – 10^{-11} M, final assay-concentrations) and the respective radiolabeled ligands (10^{-9} M, final assay-concentration). Data are expressed as mean \pm SD; $invIC_{50}$ values were determined as triplicates; $\log D_{7.4}$ values were determined as octuplicates, pentuplicates (*) or sextuplicates (**); (***) : data adapted from literature (137).

[^{99m}Tc]CXCR4-Tc-	$invIC_{50}$ [nM] (n = 3)	$\log D_{7.4}$ (n = 8)
12 (EDDA)	4.16 \pm 1.50	-2.74 \pm 0.03 (*)
13	10.2 \pm 2.4	-1.75 \pm 0.08
14	3.69 \pm 1.32	-3.60 \pm 0.02
06	3.67 \pm 0.77	-1.54 \pm 0.02 (**)
11	4.82 \pm 1.36	-2.92 \pm 0.06
[^{99m}Tc]CXCR4-L	No displacement of FC-131	-1.84 \pm 0.01
[^{177}Lu]Pentixather	1.91 \pm 1.11	-1.76 \pm 0.03
[^{68}Ga]Pentixafor (***)	n.d.	-2.90 \pm 0.08

Highest CXCR4 affinity of all tested technetium tracers is observed for N4-conjugated ligand [^{99m}Tc]CXCR4-Tc-13. The determined $invIC_{50}$ value (10.2 \pm 2.4 nM) is more than five times higher than the $invIC_{50}$ of [^{177}Lu]Pentixather, more than twice as high as for [^{99m}Tc]CXCR4-Tc-11 or -12 and three times as high as the $invIC_{50}$ of [^{99m}Tc]CXCR4-Tc-06. Compound [^{99m}Tc]CXCR4-Tc-14 ($invIC_{50}$: 3.69 \pm 1.32 nM), bearing the hydrophilic *eue* motif and therefore a lower net charge, exhibits a loss in receptor affinity when compared to [^{99m}Tc]CXCR4-Tc-13. However, CXCR4 affinity is in the range of [^{99m}Tc]CXCR4-Tc-11, -12 and -06 and higher than that observed for [^{177}Lu]Pentixather. High affinity is also determined for HYNIC-conjugated compound [^{99m}Tc]CXCR4-Tc-12 which displays an $invIC_{50}$ of 4.16 \pm 1.50 nM. This tracer is therefore more affine than [^{177}Lu]Pentixather and [^{99m}Tc]CXCR4-Tc-06, however less potent than [^{99m}Tc]CXCR4-Tc-11 and -13.

[^{99m}Tc]CXCR4-Tc-12 ($\log D_{7.4}$: -2.74 \pm 0.03) further displays increased hydrophilicity in comparison to [^{99m}Tc]CXCR4-Tc-06 ($\log D_{7.4}$: -1.54 \pm 0.02) and only slightly lower hydrophilicity compared to [^{68}Ga]Pentixafor ($\log D_{7.4}$: -2.90 \pm 0.08 (114)). When compared to its literature-known analog [^{99m}Tc]CXCR4-L, hydrophilicity is found to be increased by the optimized *Abz-a-r-dap* linker unit. [^{99m}Tc]CXCR4-Tc-13, carrying the N4 chelator at its amine terminus, displays a $\log D_{7.4}$ value of -1.75 \pm 0.08 and with that,

exhibits considerably lower hydrophilicity than [^{99m}Tc]CXCR4-Tc-12. When compared to [^{99m}Tc]CXCR4-Tc-06, however, slightly higher hydrophilicity and comparable hydrophilicity to [¹⁷⁷Lu]Pentixather ($\log D_{7.4}$: -1.76 ± 0.03) can be attested. Introduction of the *eue* motif within compound [^{99m}Tc]CXCR4-Tc-14 elevates hydrophilicity as expected, decreasing the $\log D_{7.4}$ value for this compound to -3.60 ± 0.02 .

Internalization

The internalization rates of HYNIC- and N4-conjugated ligands was assessed using Chem-1 cells and the internal standard ¹²⁵I-FC-131. Figure 27 summarizes the obtained data.

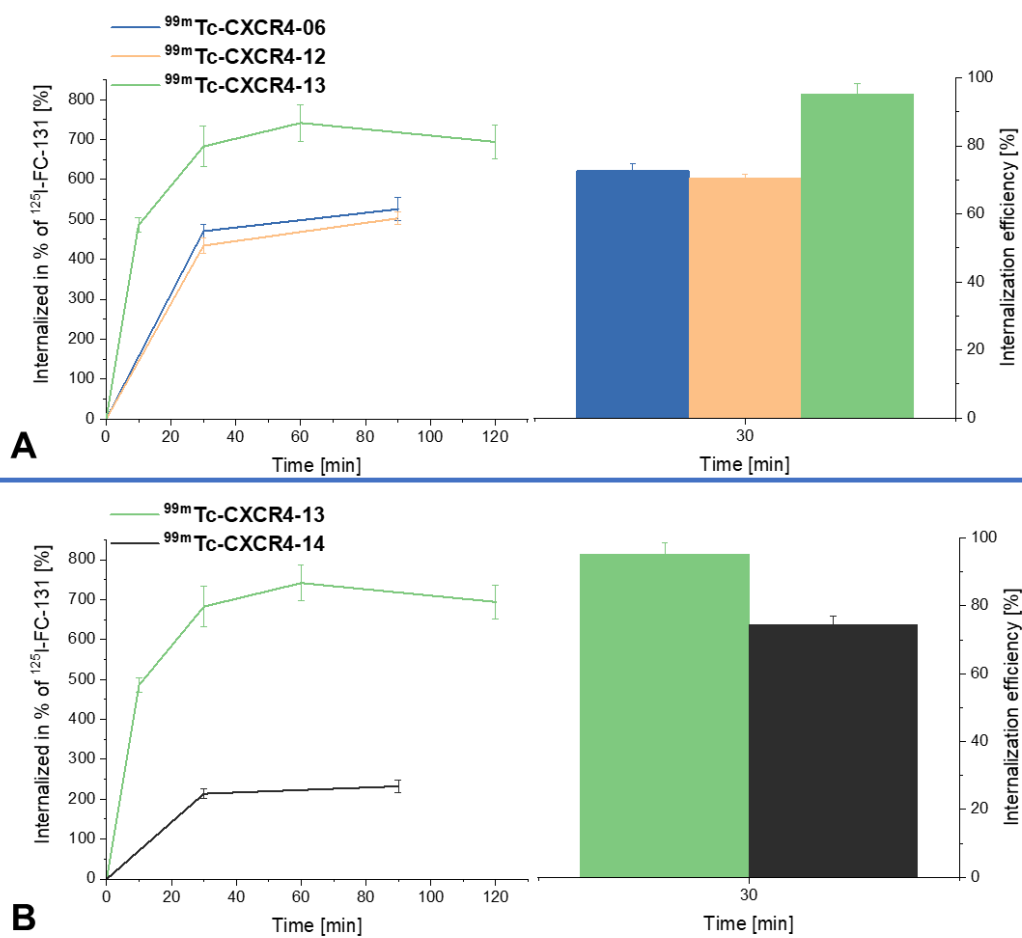


Figure 27: Dual tracer internalization of radiolabeled novel ligands and the reference compound ^{125}I -FC-131 (assay-concentration for each peptide 0.2 nM) into Chem-1 cells (100,000 cells per well; 37°C): **A**: [$^{99\text{m}}\text{Tc}$]CXCR4-Tc-06, -12 and -13, **B**: [$^{99\text{m}}\text{Tc}$]CXCR4-Tc-13 and -14. Data are expressed as mean \pm SD; internalization at every time point was determined in triplicate and corrected for unspecific internalization; line diagrams: amount of Internalized novel ligand in relation to the amount of internalized internal standard ^{125}I -FC-131 in %; bar diagrams: amount of internalized novel ligand in relation to the total cell-bound novel ligand in %.

[$^{99\text{m}}\text{Tc}$]CXCR4-Tc-13 bears the highest determined CXCR4 affinity within this series of tracers which is reflected in the highest absolute internalization and the highest internalization efficiency. A maximum internalization of $742 \pm 45\%$ relative to ^{125}I -FC-131 is reached after 60 minutes incubation and 97.6% of the cell-bound activity is internalized. Such high internalization efficiency was not even observed for [^{125}I]CXCL12 in a study by Hesselgesser et al. They noted an efficiency of 90% after 2h incubation in a similar experimental setup employing Jurkat cells (198). HYNIC-conjugated [$^{99\text{m}}\text{Tc}$]CXCR4-Tc-12 exhibits a slightly lower maximum internalization and internalization efficiency when compared to [$^{99\text{m}}\text{Tc}$]CXCR4-Tc-06 ($503 \pm 16\%$; $76.9 \pm 1.9\%$ versus $526 \pm 19\%$; $79.7 \pm 1.6\%$, respectively). Both values, however, are substantially lower compared to [$^{99\text{m}}\text{Tc}$]CXCR4-Tc-13 (Figure 27, **A**).

When *eue* is introduced into the tracer backbone of [^{99m}Tc]CXCR4-Tc-14, absolute internalization drops drastically (Figure 27, **B**). [^{99m}Tc]CXCR4-Tc-14 shows a third of internalized activity ($232 \pm 15\%$ after 90 min) in comparison to its structural analog [^{99m}Tc]CXCR4-Tc-13 and half, when compared to [^{99m}Tc]CXCR4-Tc-12. Even though its affinity is comparable to [^{99m}Tc]CXCR4-Tc-12, the decreased net charge seems to have a substantial impact on absolute internalization rates. This effect, however, is not detectable for the internalization efficiency of [^{99m}Tc]CXCR4-Tc-14, which remains on a high level of $84.0 \pm 6.9\%$ after 90 minutes incubation.

2.3.4. 3rd Generation Tracers

The high affinity and internalization observed for N4-conjugated compound CXCR4-Tc-13 were promising and we were therefore hoping to maintain these positive traits while elevating hydrophilicity. However, CXCR4-Tc-14 exhibited loss in CXCR4 affinity and internalization capability while hydrophilicity was considerably enhanced by the introduction of *eue*. We hypothesized, that additional distance between the negatively charged *eue* moiety and the *CPCR4* peptide scaffold would prove beneficial. Thus, a 3rd-generation compound was prepared carrying an *Ahx* spacer between the *CPCR4-Abz-a-r-dap* tracer backbone and *eue*. The structure of CXCR4-Tc-15 is depicted in Figure 21.

Affinity and hydrophilicity

This newly developed ligand was tested with regard to its hydrophilicity and CXCR4 affinity. Table 5 summarizes the obtained values for this tracer and the structural analogs [^{99m}Tc]CXCR4-Tc-13 and -14, together with literature-known reference compounds.

Table 5: Summary of $invIC_{50}$ [nM] and $logD_{7.4}$ values for compounds $[^{99m}Tc]CXCR4-Tc-13-15$ in comparison with reference ligands $[^{99m}Tc]CXCR4-L$, $[^{68}Ga]Pentixafor$ and $[^{177}Lu]Pentixather$: $invIC_{50}$ values were determined in competitive binding studies employing Jurkat cells (400,000 cells/tube; 8°C, 2h incubation), the standard ligand FC-131 (10^{-5} – 10^{-11} M, final assay-concentrations) and the respective radiolabeled ligands (10^{-9} M, final assay-concentration). Data are expressed as mean \pm SD; $invIC_{50}$ values were determined as triplicates; $logD_{7.4}$ values were determined as octuplates; (*): data adapted from literature (114).

$[^{99m}Tc]CXCR4-Tc-$	$invIC_{50}$ [nM] (n = 3)	$logD_{7.4}$ (n = 8)
15	6.08 ± 1.03	-2.70 ± 0.04
13	10.2 ± 2.4	-1.75 ± 0.08
14	3.69 ± 1.32	-3.60 ± 0.02
$[^{99m}Tc]CXCR4-L$	No displacement of FC-131	-1.84 ± 0.01
$[^{177}Lu]Pentixather$	1.91 ± 1.11	-1.76 ± 0.03
$[^{68}Ga]Pentixafor$ (*)	n.d.	-2.90 ± 0.08

Introduction of an additional spacer was intended to minimize repulsion with the CXCR4 binding pocket and result in increased receptor affinity. Indeed, CXCR4 affinity was elevated in comparison to $[^{99m}Tc]CXCR4-Tc-14$ ($invIC_{50}$: 6.08 ± 1.03 nM vs. 3.69 ± 1.32 nM, respectively). $[^{99m}Tc]CXCR4-Tc-15$ exhibits the highest observed $invIC_{50}$ value after $[^{99m}Tc]CXCR4-Tc-13$ within the series of technetium tracers and with that, substantially higher affinity compared to $[^{177}Lu]Pentixather$. This proves the introduction of an additional spacing to be a feasible concept for highly negatively charged moieties.

When compared to $[^{99m}Tc]CXCR4-Tc-14$, $[^{99m}Tc]CXCR4-Tc-15$ exhibits a considerably higher $logD_{7.4}$ value of -2.70 ± 0.04 . This does come expected as the introduction of the *Ahx* spacer is accompanied by its lipophilic carbohydrate chain. However, hydrophilicity is still elevated when compared to $[^{99m}Tc]CXCR4-Tc-13$ and in the range of $[^{68}Ga]Pentixafor$ ($logD_{7.4}$: -2.90 ± 0.08 , (114)).

Internalization

Despite the gain in affinity, a maximum cellular uptake of $284 \pm 10\%$ is reached for $[^{99m}Tc]CXCR4-Tc-15$ after 90 minutes incubation which is only slightly more than observed for $[^{99m}Tc]CXCR4-Tc-14$ ($232 \pm 15\%$) (Figure 28).

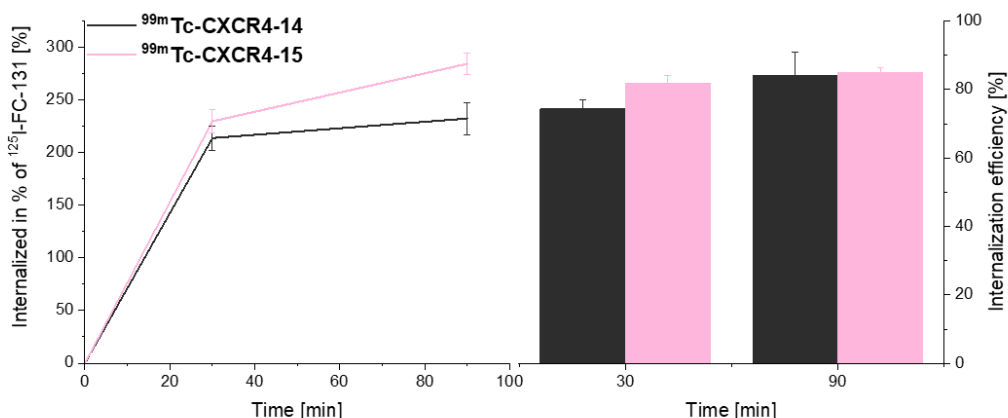


Figure 28: Dual tracer internalization of novel ligands [^{99m}Tc]CXCR4-Tc-14 and -15 and the reference compound ¹²⁵I-FC-131 (assay-concentration for each peptide 0.2 nM) into Chem-1 cells (100,000 cells per well; 37°C). Data are expressed as mean ± SD; internalization at every time point was determined in triplicate and corrected for unspecific internalization; line diagrams: amount of Internalized novel ligand in relation to the amount of internalized internal standard ¹²⁵I-FC-131 in %; bar diagrams: amount of internalized novel ligand in relation to the total cell-bound novel ligand in %.

Again, $84.9 \pm 1.4\%$ of cell-bound [^{99m}Tc]CXCR4-Tc-15 is internalized into Chem-1 cells, nearly the same fraction as observed for [^{99m}Tc]CXCR4-Tc-14. These results suggest that negatively charged moieties are generally detrimental to the internalization of CXCR4-targeted tracers. The additional distance between the *CPCR4* scaffold anchored in the binding pocket and the negative charges at the *N*-terminal site of the peptide does not change this circumstance.

2.3.5. Summary

Figure 29 gives an overview of the obtained data for [^{99m}Tc]CXCR4-Tc-06 – 15 and [¹⁷⁷Lu]Pentixather (p). Initial derivatization of the *CPCR4-Abz-a-r-dap* tracer backbone with chelators mas₃ (CXCR4-Tc-06, -07), HYNIC (CXCR4-Tc-12) and N4 (CXCR4-Tc-13) invariably led to potent technetium-99m-labeled tracers. Except for the HYNIC-conjugated compound, hydrophilicity was not found to be in the range of [⁶⁸Ga]Pentixafor. Thus, a variety of functionalizations with either glycosylated (CXCR4-Tc-08 – 11) or negatively charged moieties (CXCR4-Tc-14, -15) was conducted, to obtain compounds with higher hydrophilicity. In these cases, however, modification led to loss in receptor affinity or lower tracer internalization.

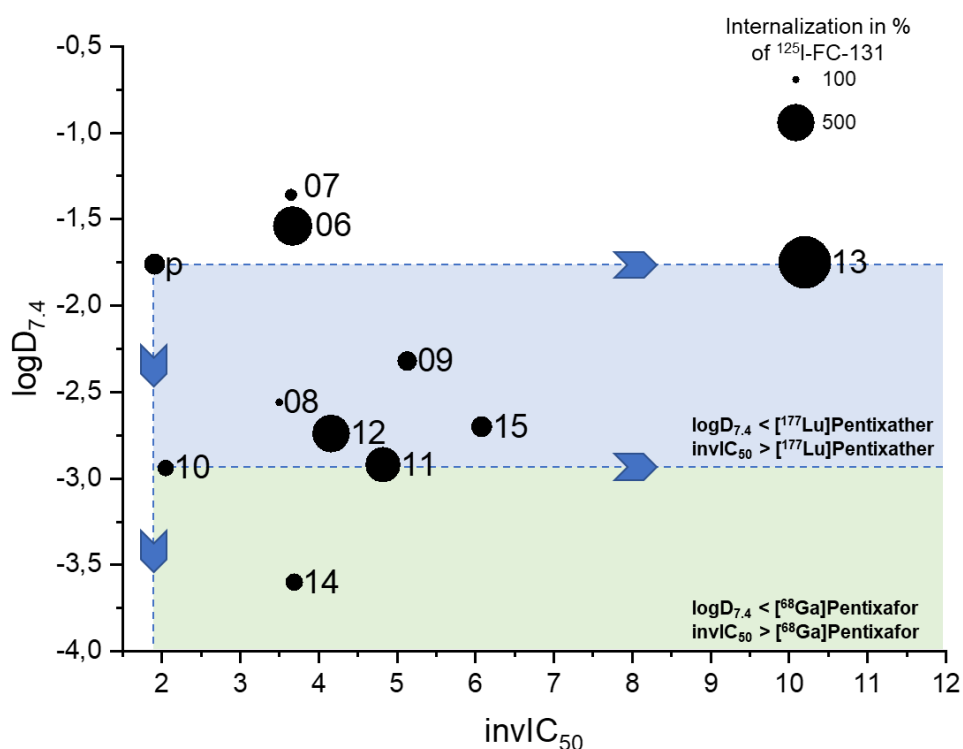


Figure 29: Summary of $\log D_{7,4}$ (y-axis), invIC_{50} (x-axis) and maximum internalization values (dot size) for [$^{99\text{m}}\text{Tc}$]CXCR4-Tc-06 – 15 as well as [^{177}Lu]Pentixather and [^{68}Ga]Pentixafor ($\log D_{7,4}$ only): Numbers next to dots represent the respective ligand within this series and the letter p represents [^{177}Lu]Pentixather; dots in the light blue area suggest compounds that are more affine and hydrophilic than [^{177}Lu]Pentixather and dots in the light green area suggest compounds that are more affine and hydrophilic than [^{68}Ga]Pentixafor.

The most promising candidates, exhibiting a higher CXCR4 affinity and hydrophilicity than [^{177}Lu]Pentixather (Figure 29, blue area) or [^{68}Ga]Pentixafor (Figure 29, green area), paired with a pronounced internalization rate were further tested in *in vivo* biodistribution studies. Those are: [$^{99\text{m}}\text{Tc}$]CXCR4-Tc-08 and -10 through -13. [$^{99\text{m}}\text{Tc}$]CXCR4-Tc-06 was chosen as a reference compound for further examination.

2.4. In vivo Biodistribution and μSPECT Imaging

The biodistribution profiles of selected technetium-99m-labeled tracers was examined in Jurkat tumor-bearing CB-17 SCID mice. Detailed description of the experimental setup can be found in chapter II. 5.

[^{68}Ga]Pentixafor exhibits high tumor/background ratios *in vivo* and rapid excretion *via* the urinary system, thus leading to low activity levels in kidneys and the bladder (114). Osl et al. reported, that the substitution of the *Ambz* linker unit within the structure of

[⁶⁸Ga]Pentixafor by *Abz-a-r*, leads to increased CXCR4 affinities and internalization rates paired with a pronounced affinity for mCXCR4. These factors were not reflected in increased tumor uptake on the one hand, but also resulted in elevated tracer uptake in mCXCR4 expressing tissues such as spleen, lung, bone marrow and liver (146). The newly developed tracers of this work are based on the *Abz-a-r-dap* linker unit and therefore presumably possess affinity to the murine CXCR4 receptor as well. Organs affiliated with the expression of mCXCR4 will be marked as CXCR4⁺ whereas background organs will be highlighted as CXCR4⁻. Within the following biodistribution experiments, values obtained for bone uptake in relation to the injected activity are not representative for mCXCR4 specific uptake, as not only bone marrow was extracted but rather the whole femur.

2.4.1. [^{99m}Tc]CXCR4-Tc-06, -08, -10 and -11

The influence of glucosyl- ([^{99m}Tc]CXCR4-Tc-08) and lactosyl-modified ([^{99m}Tc]CXCR4-Tc-10, -11) chelators on the biodistribution profile of their respective tracers was examined and compared to the mas₃-conjugated compound [^{99m}Tc]CXCR4-Tc-06. Aim of this derivatization was a series of hydrophilic and therefore rapidly clearing compounds, ultimately resulting in suitable tumor/background ratios. Compared to blood level, all of the surveyed compounds exhibit elevated uptake in tissues associated with the expression of mCXCR4 (Figure 30). This uptake and the accumulation of tracer in tumor was substantially reduced by co-administration of an excess AMD3100 as the respective μ SPECT images indicate (Supplementary 1). It is therefore proposed that tracer uptake in tumor is mainly regulated by transport processes mediated by the human CXCR4 receptor, whereas uptake in liver, lung and spleen is dependent of the murine CXCR4 receptor. Figure 30 gives a summary of the obtained biodistribution and μ SPECT imaging data.

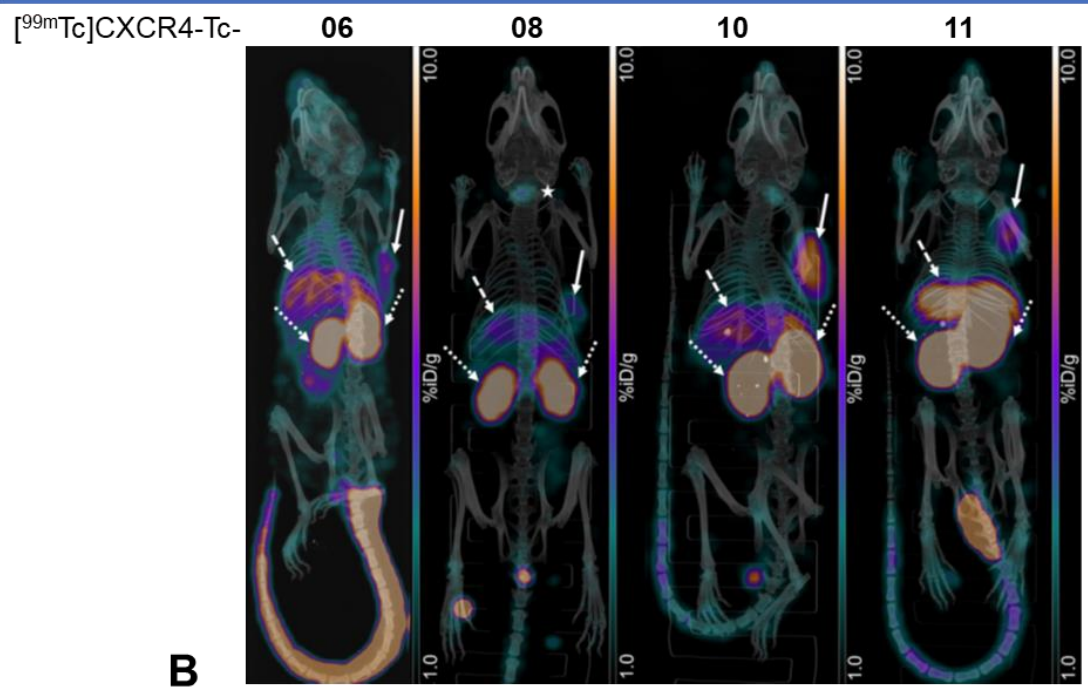
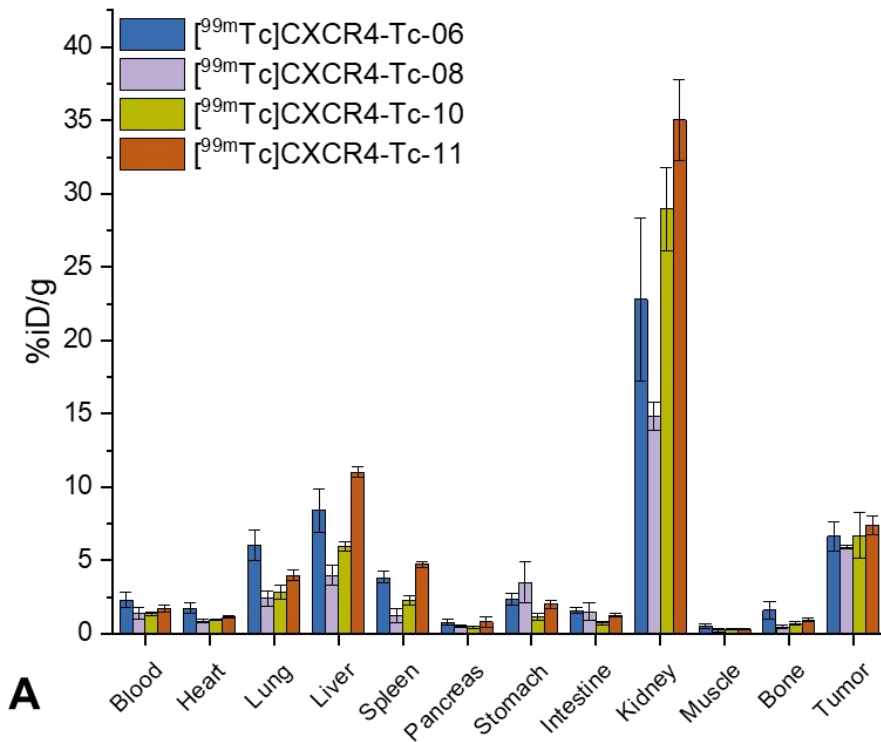


Figure 30: Results of pharmacokinetic studies 1h post injection of [^{99m}Tc]CXCR4-Tc-06, -08, -10 and -11 in Jurkat tumor-bearing female CB-17 SCID mice: **A**: Biodistribution profiles of novel ligands; data are expressed as %ID/g and are means ± SD of 5 animals per ligand; **B**: Maximum-intensity projection images obtained from static μSPECT imaging of 1 animal per ligand; arrows indicate organs of special interest: straight: tumor, dashed: liver, pointed: kidneys, star: thyroid.

The highest uptake in tumor within this series of tracers is observed for [^{99m}Tc]CXCR4-Tc-11, reaching 7.39 ± 0.64 %iD/g. This ligand displayed pronounced CXCR4 affinity and a high internalization rate in *in vitro* experiments which seem to reflect positively on the tumor uptake. On the other side, however, even though lower CXCR4 affinity was determined for [^{99m}Tc]CXCR4-Tc-10, higher uptake in tumor (6.71 ± 1.55 %iD/g) compared to [^{99m}Tc]CXCR4-Tc-06 (6.63 ± 1.02 %iD/g) and -08 (5.92 ± 0.11 %iD/g) is observed in the biodistribution experiment. As a consequence of this contrarian data, no definite link can be established between the determined CXCR4 affinity of a ligand and its tumor uptake. This finding is in accordance with the observation made by Osl et al. that the elevated CXCR4 affinity of their novel compounds did not result in increased tumor uptake compared to their reference (146).

Elevated tracer uptake in CXCR4⁺ organs is observed for any of the ligands within this series, especially pronounced for mas₃-conjugated compound [^{99m}Tc]CXCR4-Tc-06 and lactosylated citrulline-bearing ligand [^{99m}Tc]CXCR4-Tc-11, as biodistribution data and μSPECT images concordantly display (Figure 30). This circumstance may be attributed to the fact, that these compounds exhibit the respective highest and second-highest internalization rate within the series. The uptake of [^{99m}Tc]CXCR4-Tc-10 is enlisting accordingly and [^{99m}Tc]CXCR4-Tc-08, carrying three glycosylated homocysteine residues in its chelator displayed the lowest internalization value and therefore the lowest uptake in CXCR4⁺ organs. Hence, a connection can be drawn between high internalization rates and elevated uptake in CXCR4⁺ organs independently of the ligand's CXCR4 affinities or hydrophilicities. Unfortunately, it was not possible to determine mCXCR4 affinities of the compounds, which could be an additional determining factor for uptake in CXCR4⁺ organs.

High ligand uptake in lung, liver and spleen decelerates the clearance of technetium tracers. Kidney activity levels of [^{99m}Tc]CXCR4-Tc-06 (22.8 ± 5.6 %iD/g) as well as [^{99m}Tc]CXCR4-Tc-10 (29.0 ± 2.8 %iD/g) and -11 (35.0 ± 2.8 %iD/g) are found to be independent of their hydrophilicity but correlating with the retention in CXCR4⁺ organs. [^{99m}Tc]CXCR4-Tc-08 which displayed the lowest uptake in CXCR4⁺ organs concordantly shows the lowest uptake in kidney (14.8 ± 0.9 %iD/g). Moreover, this ligand exhibits lowest background activity values for heart (0.97 ± 0.13 %iD/g) and muscle (0.24 ± 0.08 %iD/g), fitting the proposal of an accelerated clearance if low uptake in CXCR4⁺ organs is present. Biodistribution and μSPECT imaging data of this compound show elevated uptake in stomach (3.51 ± 1.42 %iD/g) and thyroid glands (Figure 30, **B**)

which may be attributable to contamination with traces of technetium-99m pertechnetate, as this ion is known to accumulate in said tissues (199).

Delayed background clearance due to radioligand uptake in CXCR4⁺ organs further results in substantially reduced tumor/organ ratios. The pronounced tumor accumulation of [^{99m}Tc]CXCR4-Tc-11 is hence not reflected in overall beneficial tumor/organ ratios (Table 6), whereas [^{99m}Tc]CXCR4-Tc-10, showing a slightly lower accumulation in tumor but only moderate uptake in CXCR4⁺ organs displays favorable ratios for blood, heart, pancreas, stomach and intestine (Table 6) ultimately resulting in a promising μ SPECT image (Figure 30, **B**). This does come unexpected as the hydrophilicity of [^{99m}Tc]CXCR4-Tc-11 was determined to be as high as for [^{99m}Tc]CXCR4-Tc-10 and similar clearance kinetics could therefore be assumed. However, the elevated uptake of [^{99m}Tc]CXCR4-Tc-11 in CXCR4⁺ organs and slow ligand washout therefrom leads to a longer circulation time and an overall deferred clearance from the body. This effect is further observable in low tumor/organ ratios of [^{99m}Tc]CXCR4-Tc-06, although in this case, the elevated lipophilicity of this ligand must be considered, generally leading to a high blood activity (2.31 ± 0.53 %iD/g) level. Even though low tumor uptake is observed for [^{99m}Tc]CXCR4-Tc-08, due to its humble uptake in CXCR4⁺ organs, beneficial tumor/organ ratios are obtained especially for liver (1.49 ± 0.25) and spleen (4.77 ± 1.73).

Table 6: Tumor/organ ratios determined using data obtained from biodistribution studies 1h after injection of [^{99m}Tc]CXCR4-Tc-06, -08, -10 and -11 in Jurkat tumor-bearing female SCID mice; data are expressed as mean ± SD of 5 animals per ligand.

Tumor/Organ	[^{99m} Tc]CXCR4-Tc-			
	06	08	10	11
Blood	2.87 ± 0.80	4.18 ± 1.13	4.92 ± 1.23	4.25 ± 0.74
Heart	3.77 ± 1.00	6.84 ± 1.06	7.08 ± 1.71	6.46 ± 0.80
Pancreas	8.46 ± 2.44	12.0 ± 2.0	14.1 ± 4.0	9.24 ± 4.32
Stomach	2.82 ± 0.66	1.68 ± 0.68	5.81 ± 1.71	3.65 ± 0.59
Intestine	4.19 ± 0.86	3.95 ± 1.65	9.37 ± 2.46	5.93 ± 0.75
Muscle	12.9 ± 3.9	24.5 ± 8.5	24.0 ± 6.6	21.7 ± 2.9
Lung	1.10 ± 0.26	2.46 ± 0.50	2.35 ± 0.68	1.87 ± 0.23
Liver	0.79 ± 0.18	1.49 ± 0.25	1.13 ± 0.27	0.67 ± 0.06
Spleen	1.73 ± 0.32	4.77 ± 1.73	2.90 ± 0.78	1.57 ± 0.15
Kidneys	0.29 ± 0.08	0.10 ± 0.03	0.23 ± 0.06	0.21 ± 0.02

The obtained data reveals that increased hydrophilicity of the glycosylated tracers successfully leads to an accelerated clearance from CXCR4⁻ tissues compared to [^{99m}Tc]CXCR4-Tc-06. However, when substantial uptake in CXCR4⁺ tissues is given, this clearance is crucially slowed, deforming the classical appraisal of biodistribution data. Furthermore, this uptake is linked with the ligand's internalization capability, whereas tumor uptake is found to be dependent on both internalization and CXCR4 affinity. [^{99m}Tc]CXCR4-Tc-10 provides a suitable compromise between high accumulation in tumor and low uptake in organs, ultimately resulting in high tumor/organ ratios (Table 6) and promising μ SPECT imaging data (Figure 30, **B**).

2.4.2. [^{99m}Tc]CXCR4-Tc-12 and -13

HYNIC/EDDA ([^{99m}Tc]CXCR4-Tc-12) and N4 ([^{99m}Tc]CXCR4-Tc-13) as chelating moieties in comparison to mas₃ ([^{99m}Tc]CXCR4-Tc-06) were evaluated previously (III. 2.3.3.2) by means of invIC_{50} , internalization rate and $\log D_{7.4}$ determination. The influence of these chelators on pharmacokinetic profiles of their respective peptide tracers will be the focus of the following passage. Figure 31 gives an overview of the obtained data.

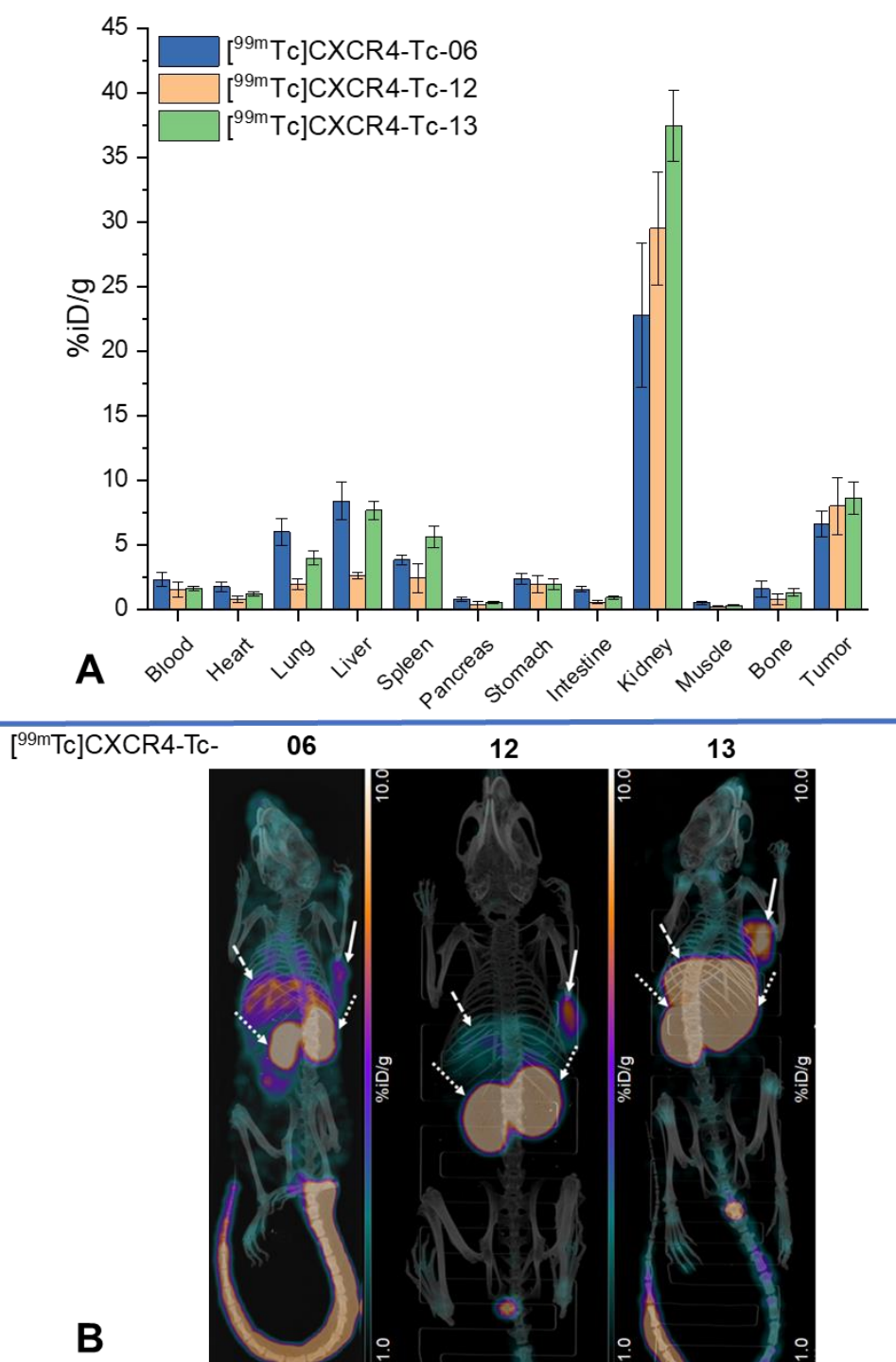


Figure 31: Results of pharmacokinetic studies 1h post injection of [^{99m}Tc]CXCR4-Tc-06, -12 and -13 in Jurkat tumor-bearing female CB-17 SCID mice: **A**: Biodistribution profiles of novel ligands; data are expressed as %iD/g and are means ± SD of 5 animals per ligand; **B**: Maximum-intensity projection images obtained from static μSPECT imaging of 1 animal per ligand; arrows indicate organs of special interest: straight: tumor, dashed: liver, pointed: kidneys.

The use of the N4 chelator resulted in the compound with the highest CXCR4 affinity and particularly highest internalization rate within the tested series, [^{99m}Tc]CXCR4-Tc-13. This

ligand accordingly exhibits the highest tumor uptake (8.63 ± 1.26 %iD/g). The HYNIC-conjugated ligand [^{99m}Tc]CXCR4-Tc-12 also shows high uptake in tumor (8.02 ± 2.21 %iD/g) compared to [^{99m}Tc]CXCR4-Tc-06 (6.63 ± 1.02 %iD/g) even though its CXCR4 affinity was found to be only slightly enhanced.

Uptake of [^{99m}Tc]CXCR4-Tc-13 in CXCR4⁺ organs such as lung (3.99 ± 0.56 %iD/g), liver (7.67 ± 0.70 %iD/g) and spleen (5.60 ± 0.82 %iD/g) is high but in the case of the former two, not exceeding the uptake of [^{99m}Tc]CXCR4-Tc-06, even though the respective μSPECT images might suggest otherwise (Figure 31, **B**). A clear delineation of CXCR4 specific and unspecific uptake, however, cannot be achieved here as [^{99m}Tc]CXCR4-Tc-06 is more lipophilic and therefore should exhibit more unspecific uptake in these organs. [^{99m}Tc]CXCR4-Tc-12, despite showing pronounced internalization, does not accumulate in CXCR4⁺ organs lung (1.94 ± 0.44 %iD/g), liver (2.62 ± 0.23 %iD/g) and spleen (2.43 ± 1.12 %iD/g). Even though the tracer backbone is left unchanged, a loss in mCXCR4 affinity must be induced by the HYNIC chelator.

In this case, however, reduced uptake in CXCR4⁺ organs is not reflected in decreased renal uptake as both compounds, [^{99m}Tc]CXCR4-Tc-12 and -13 exhibit considerably elevated retention in the kidneys compared to [^{99m}Tc]CXCR4-Tc-06 (29.5 ± 4.4 vs. 37.4 ± 2.7 vs. 22.8 ± 5.6 %iD/g, respectively). As pictured for the glycosylated ligands above, this may be a sign for deferred clearance, although the N4 and HYNIC carrying ligands are determined to be more hydrophilic than the mas₃-conjugated compound and no elevated tracer uptake in CXCR4⁺ organs is observable. An explanation could be found in the change of complexation chemistry and the accompanying differences in the ligand structures and charge distributions.

However, high hydrophilicity of the HYNIC/EDDA moiety leads to fast clearance from CXCR4⁻ tissue, resulting in low activity values for blood (1.56 ± 0.58 %iD/g), heart (0.78 ± 0.28 %iD/g), intestines (0.57 ± 0.12 %iD/g) and muscle (0.21 ± 0.05 %iD/g). These factors combined are accountable for overall high tumor to organ ratios for both CXCR4⁺ and CXCR4⁻ organs (Table 7). An apparent difference is observed when tumor/CXCR4⁻ organ ratios of [^{99m}Tc]CXCR4-Tc-06 and -12 are directly compared. Hence, tumor/heart (3.77 ± 1.00 vs. 10.2 ± 4.6 , respectively), tumor/intestine (4.19 ± 0.86 vs. 14.0 ± 4.8 , respectively) and tumor/muscle (12.9 ± 3.9 vs. 37.5 ± 13.6 , respectively) ratios are favoring the more hydrophilic HYNIC/EDDA chelator over mas₃. Also, when [^{99m}Tc]CXCR4-Tc-06 is compared to [^{99m}Tc]CXCR4-Tc-13, tumor/organ ratios are favoring the use of the N4 chelator. The difference is especially apparent for CXCR4⁻

tissues such as blood (2.87 ± 0.80 vs. 5.33 ± 0.99 , respectively), heart (3.77 ± 1.00 vs. 7.15 ± 1.53 , respectively), pancreas (8.46 ± 2.44 vs. 15.3 ± 3.6 , respectively), stomach (2.82 ± 0.66 vs. 4.38 ± 1.08 , respectively), intestines (4.19 ± 0.86 vs. 9.36 ± 1.77 , respectively) and muscle (12.9 ± 3.9 vs. 29.0 ± 6.1 , respectively).

Table 7: Tumor/organ ratios determined using data obtained from biodistribution studies 1h after injection of [^{99m}Tc]CXCR4-Tc-06, -12 and -13 in Jurkat tumor-bearing female SCID mice; data are expressed as mean \pm SD of 5 animals per ligand.

Tumor/Organ	[^{99m}Tc]CXCR4-Tc-		
	06	12	13
Blood	2.87 ± 0.80	5.13 ± 2.36	5.33 ± 0.99
Heart	3.77 ± 1.00	10.2 ± 4.6	7.15 ± 1.53
Pancreas	8.46 ± 2.44	22.5 ± 20.1	15.3 ± 3.6
Stomach	2.82 ± 0.66	4.01 ± 1.77	4.38 ± 1.08
Intestine	4.19 ± 0.86	14.0 ± 4.8	9.36 ± 1.77
Muscle	12.9 ± 3.9	37.5 ± 13.6	29.0 ± 6.1
Lung	1.10 ± 0.26	4.12 ± 1.46	2.16 ± 0.44
Liver	0.79 ± 0.18	3.06 ± 0.88	1.13 ± 0.19
Spleen	1.73 ± 0.32	3.30 ± 1.77	1.54 ± 0.32
Kidneys	0.29 ± 0.08	0.27 ± 0.08	0.23 ± 0.04

Both ligands, [^{99m}Tc]CXCR4-Tc-12 and -13 exhibit more efficient tumor targeting and overall faster clearance from background compared to [^{99m}Tc]CXCR4-Tc-06. The HYNIC-conjugated compound apparently displays substantially reduced affinity towards the murine CXCR4 receptor, leading to excellent tumor/organ ratios for lung, liver and spleen and a favorable μ SPECT image. [^{99m}Tc]CXCR4-Tc-13, on the other hand, shows the highest tumor uptake within this series of compounds and fast clearance from blood.

2.4.3. Selection of a Lead Compound

The selection of a lead compound from the *in vivo* best performing tracers [^{99m}Tc]CXCR4-Tc-10 – 13, was based on their precursor synthesis, ease of labeling, *in vitro* data and biodistribution profiles in comparison to [^{68}Ga]Pentixafor. Figure 32 gives an overview of the *in vivo* biodistribution data.

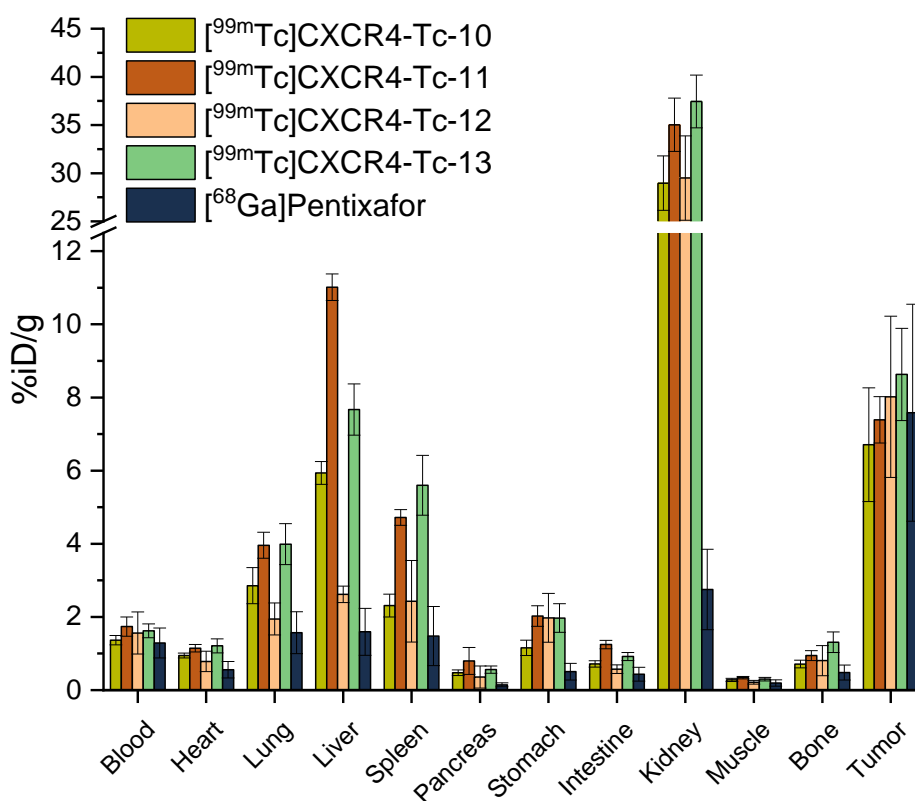


Figure 32: Biodistribution profiles of [^{99m}Tc]CXCR4-Tc-10 – 13 and [⁶⁸Ga]Pentixafor 1h post injection in Jurkat tumor-bearing female CB-17 SCID mice; data are expressed as %iD/g and are means ± SD of 5 animals per ligand.

The selection of a lead compound was hardened insofar that the mCXCR4 mediated tracer uptake into liver, lung and spleen affects the ligand's clearance kinetics. Hence, tumor/background ratios are biased and generally favoring ligands such as [^{99m}Tc]CXCR4-Tc-10 and -12 that exhibit lower uptake in CXCR4⁺ organs. At this point of the work, it remained improbable, that this uptake would be translated to an equal distribution in humans rather than being an exclusive trait in animal experiments. Opposed to [⁶⁸Ga]Pentixafor which displays no affinity towards the murine receptor, moderate affinity towards mCXCR4 is reported for [¹⁷⁷Lu]Pentixather (146). In patients, however, no detrimental effect has been reported concerning this issue.

Reflecting the obtained data in Figure 32, it is apparent that compounds [^{99m}Tc]CXCR4-Tc-11 and -13 show the highest uptakes in lung, liver and spleen within this series and signs of a delayed body clearance due to this circumstance. Elevated background activity is observed for any of the novel ligands in comparison to [⁶⁸Ga]Pentixafor even though comparable hydrophilicities are reached. However, [^{99m}Tc]CXCR4-Tc-12 and -13 excel the tumor uptake of the PET ligand and are therefore

able to challenge tumor/organ ratios of [⁶⁸Ga]Pentixafor. Unfortunately, the additional charges in the optimized linker unit lead to substantially enhanced renal retention of the novel compounds which might prove to be transmissive to an application in humans and downgrade imaging significance in the abdominal region.

Due to the distorted biodistribution data of mCXCR4-targeting ligands, [^{99m}Tc]CXCR4-Tc-12 is the only tracer presenting comparable data to [⁶⁸Ga]Pentixafor. Unfortunately, labeling of this compound was found to be awkward as radiochemical yields ranged from 19–50% (n.d.c.) with obligatory SPE purification. Furthermore, synthesis of the labeling precursor was particularly aggravated as the HYNIC chelator decomposed and underwent side reactions, thus massively diminishing the final peptide yield. The N4-conjugated compound [^{99m}Tc]CXCR4-Tc-13, on the other side, was labeled with consistently (> 20 labeling experiments) high yields (> 97%) without the need of additional purification. The precursor was obtained in relatively high yields and high purities. Most importantly, however, the tracer excelled in *in vitro* experiments and provided high uptake in tumor and fast body clearance, thus leading to overall encouraging tumor/background ratios. These positive traits have made [^{99m}Tc]CXCR4-Tc-13 the focus of a first application in men.

2.5. Proof-of-Concept Study in Men

The radiosynthesis of [^{99m}Tc]CXCR4-Tc-13 was performed manually, as described in chapter II. 3.2. Images were acquired after injection of 430–604 MBq of [^{99m}Tc]CXCR4-Tc-13 at 5 min to 21h p.i. Further details of the scanning procedure are found in the Materials and Methods section.

Due to the favorable preclinical data obtained for [^{99m}Tc]CXCR4-Tc-13, the ligand was selected for a first proof-of-concept study in patients suffering from multiple myeloma.

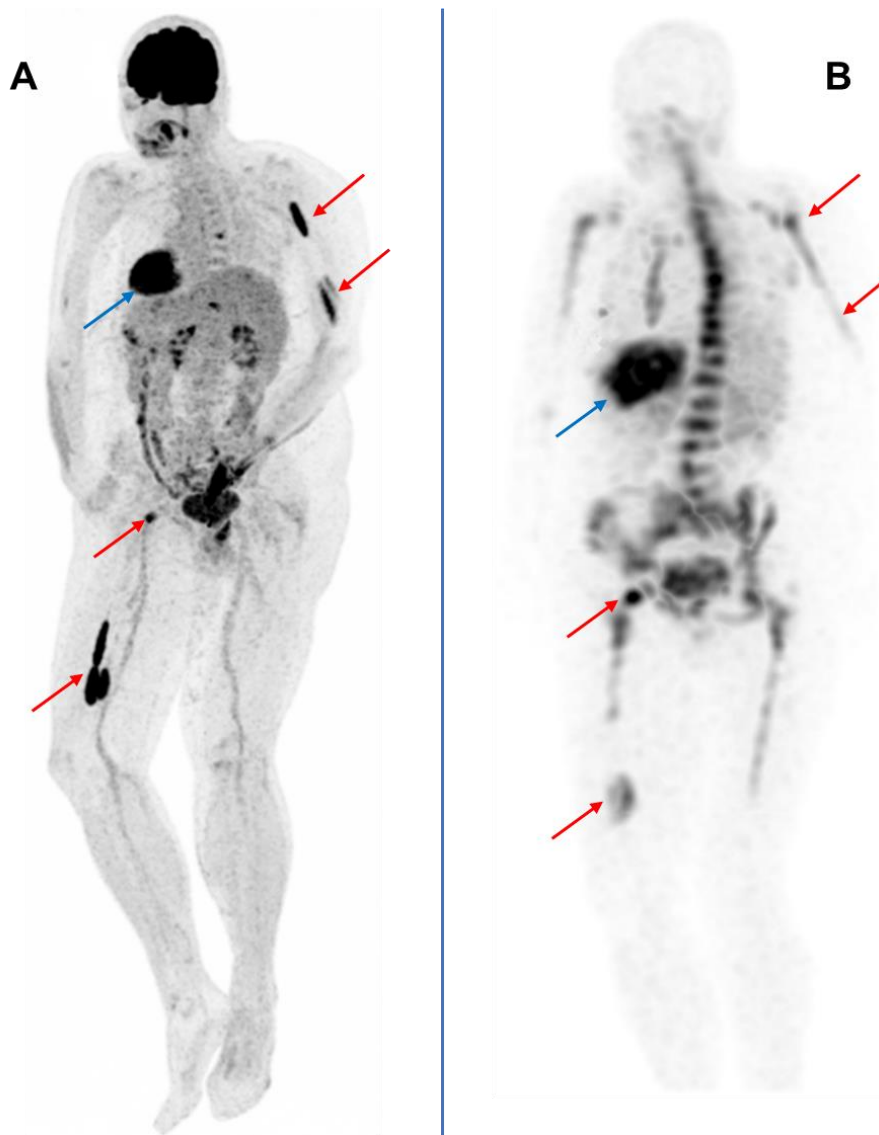


Figure 33: Maximum intensity projection (MIP) images obtained from SPECT and PET imaging of a female patient suffering from multiple myeloma; **A**) [^{18}F]FDG PET MIP (1h p.i., 189 MBq of [^{18}F]FDG), **B**) [$^{99\text{m}}\text{Tc}$]CXCR4-Tc-13 SPECT MIP (3h p.i., 604 MBq of [$^{99\text{m}}\text{Tc}$]CXCR4-Tc-13); red arrows indicate tumor lesions, blue arrows indicate physiological uptake of [^{18}F]FDG in the heart and of [$^{99\text{m}}\text{Tc}$]CXCR4-Tc-13 in the spleen.

The biodistribution of [$^{99\text{m}}\text{Tc}$]CXCR4-Tc-13 is similar to that of the established PET tracer [^{68}Ga]Pentixafor (117). In healthy organs, significant uptake is found in the kidneys. Relatively high uptake in the spleen reflects the known expression of CXCR4 and uptake of CXCR4-addressing ligands in humans. Significant uptake is also observed in liver and the bone marrow, both known to express CXCR4 under physiological but even more so under pathological conditions (116,200). The low blood pool uptake and the rapid clearance of the tracer from non-target tissues is most probably a result of the suitable hydrophilicity of [$^{99\text{m}}\text{Tc}$]CXCR4-Tc-13 ($\log D_{7.4} = -1.75$) combined with the outstanding targeting potential of the tracer determined in preclinical experiments ($\text{InvIC}_{50} = 10.2 \text{ nM}$,

Internalization (in % of ^{125}I -FC-131) = 742%). The high uptake of the tracer in the tumor lesions together with low accumulation in background tissues enables visualization of multiple metastasis in high contrast (Figure 33, **B**). The SPECT/CT image of the axial plane further acknowledges the potential of the tracer by displaying high lesion uptake and beneficial resolution of $^{99\text{m}}\text{Tc}$]CXCR4-Tc-13 in the osteolytic lesion in the pelvis in agreement with the PET/CT scan using ^{18}F]FDG (Supplementary 2). No ^{18}F]FDG-positive lesion was found negative in the CXCR4-targeted SPECT scan with $^{99\text{m}}\text{Tc}$]CXCR4-Tc-13.

Opposed to the observations made in preclinical studies with tumor-bearing mice, no substantially elevated ligand uptake was detected in human liver and lung, confirming the elevated uptake in murine liver and lung to be caused by the mCXCR4 affinity of the ligand.

Physiological uptake in the stomach and thyroids was low and comparable to other normal organs indicating the absence of $^{99\text{m}}\text{Tc}$]-pertechnetate contamination or *in vivo* loss of radiometal (201).

The following Figure 34 illustrates the biodistribution of $^{99\text{m}}\text{Tc}$]CXCR4-Tc-13 in the same patient between 5 min and 21h p.i. The specific doses were determined for $^{99\text{m}}\text{Tc}$]CXCR4-Tc-13 in different tissues and organs of interest (Figure 34, **B**).

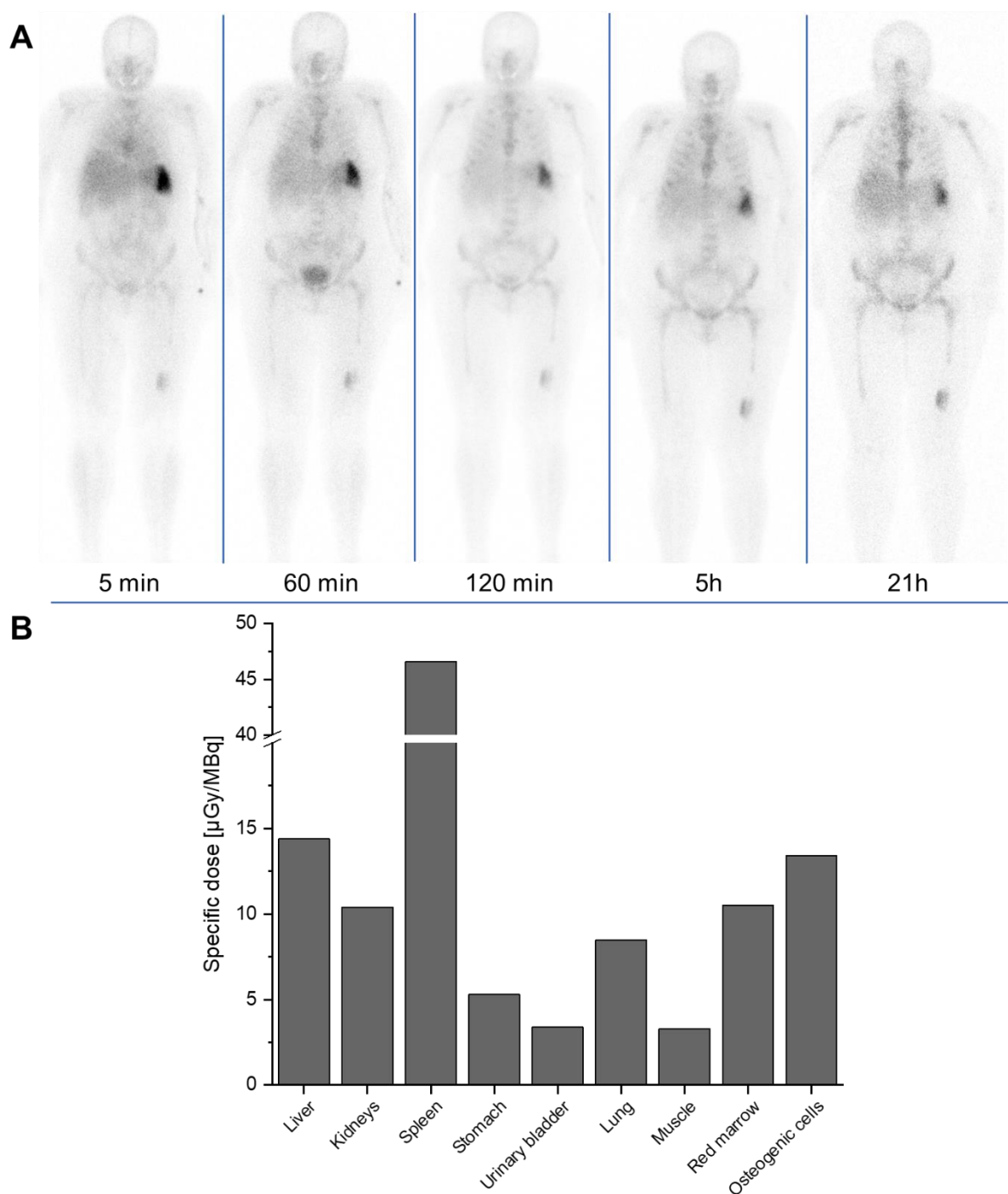


Figure 34: **A)** MIP images obtained from SPECT imaging at 5 min, 60 min, 120 min, 5h and 21h p.i. of 604 MBq $[^{99\text{m}}\text{Tc}]$ CXCR4-Tc-13 in a female patient suffering from multiple myeloma; **B)** Specific doses [$\mu\text{Gy}/\text{MBq}$] calculated for selected organs and tissues from the same patient.

The time-resolved biodistribution of $[^{99\text{m}}\text{Tc}]$ CXCR4-Tc-13 reconfirms rapid background clearance and uptake in lesions as well as the spleen and the bone marrow, even at early time points such as 5 min p.i. No delayed clearance *via* the bile can be detected at later time points, indicating clearance of the tracer *via* the kidneys. However, uptake in the kidneys as well as the urinary bladder are found to be low above the entire observation

period, suggesting prolonged retention of the ligand in CXCR4 expressing tissues (Figure 34, **B**). This might be a direct consequence of the high target affinity and the pronounced internalization into CXCR4 expressing cancer cells as determined in preclinical experiments.

The highest specific dose is determined for spleen (47 $\mu\text{Gy}/\text{MBq}$), followed by liver (14 $\mu\text{Gy}/\text{MBq}$), osteogenic cells (13 $\mu\text{Gy}/\text{MBq}$), red bone marrow (11 $\mu\text{Gy}/\text{MBq}$) and the kidneys (10 $\mu\text{Gy}/\text{MBq}$) (Figure 34, **B**). The whole-body effective dose is calculated to be 6.3 $\mu\text{Sv}/\text{MBq}$, with 604 MBq of [$^{99\text{m}}\text{Tc}$]CXCR4-Tc-13 injected, representing a delivered whole-body dose of 3.8 mSv. The specific doses delivered to organs and the whole-body effective dose is found to be similar to other technetium-99m-labeled ligands such as PSMA-targeted [$^{99\text{m}}\text{Tc}$]PSMA I&S or the CXCR4-targeted [$^{99\text{m}}\text{Tc}$]CXCR4-L (99,202). Compared to dosimetry data obtained for [^{68}Ga]Pentixafor in multiple myeloma patients, [$^{99\text{m}}\text{Tc}$]CXCR4-Tc-13 displays a higher whole-body absorbed dose but decreased specific organ doses (203).

This proof-of-concept study warrants further evaluation of [$^{99\text{m}}\text{Tc}$]CXCR4-Tc-13 in a clinical context. Furthermore, as substantial uptake of [$^{99\text{m}}\text{Tc}$]CXCR4-Tc-13 in liver and lung in preclinical studies was not equivalently seen in humans, other ligands developed within this work might possess suitable pharmacokinetics in humans as well, despite showing substantial liver/lung uptake in preclinical studies.

3. DOTA-conjugated Ligands

The following chapter includes the evaluation of CXCR4-DOTA-01 – 05 in comparison with their theranostic analogs [⁶⁸Ga]Pentixafor and [¹⁷⁷Lu]Pentixather. The theranostic concept was introduced around the turn of the last millennium and describes the use of the same or a slight variation of a labeling precursor for both nuclear imaging (in combination with a SPECT or PET isotope) and PRRT (in combination with a therapeutic isotope). Since 2011, a significant increase in publications concerning theranostic concepts arose, ultimately resulting in the establishment of a journal restricted to this topic (Ivyspring International Publisher: “Theranostics”) (204). The success of the theranostic concept is predominantly based on two advantages compared to the accustomed strategy of imaging with one compound such as [¹⁸F]FDG and PRRT with another compound. Firstly, pharmaceutical approval procedures can be significantly simplified if the only difference between therapeutic and diagnostic agent is the radioisotope used. Secondly, a theranostic approach facilitates accurate treatment planning and dosage estimation (205). Tumors and metastasis oftentimes show significant heterogeneity, thus leading to the detection of lesions with a high receptor expression and negative imaging results for such lesions with virtually lower receptor expression. If the subsequent PRRT is undertaken with the theranostic partner of this tracer, equivalent uptake patterns can be expected. This is not the case if tracer and therapeutic agent differ, for example in terms of their uptake mechanism, specificity or physicochemical properties. These advantages have led to a growing interest in the radiopharmaceutical community, and they often outweigh suboptimal therapeutic properties of a diagnostic compound or *vice versa*.

Today, several prominent examples of theranostic pairs find usage in clinical application, predominantly affiliated with the imaging and therapy of PSMA- or sstr2-overexpressing cancers (Figure 35).

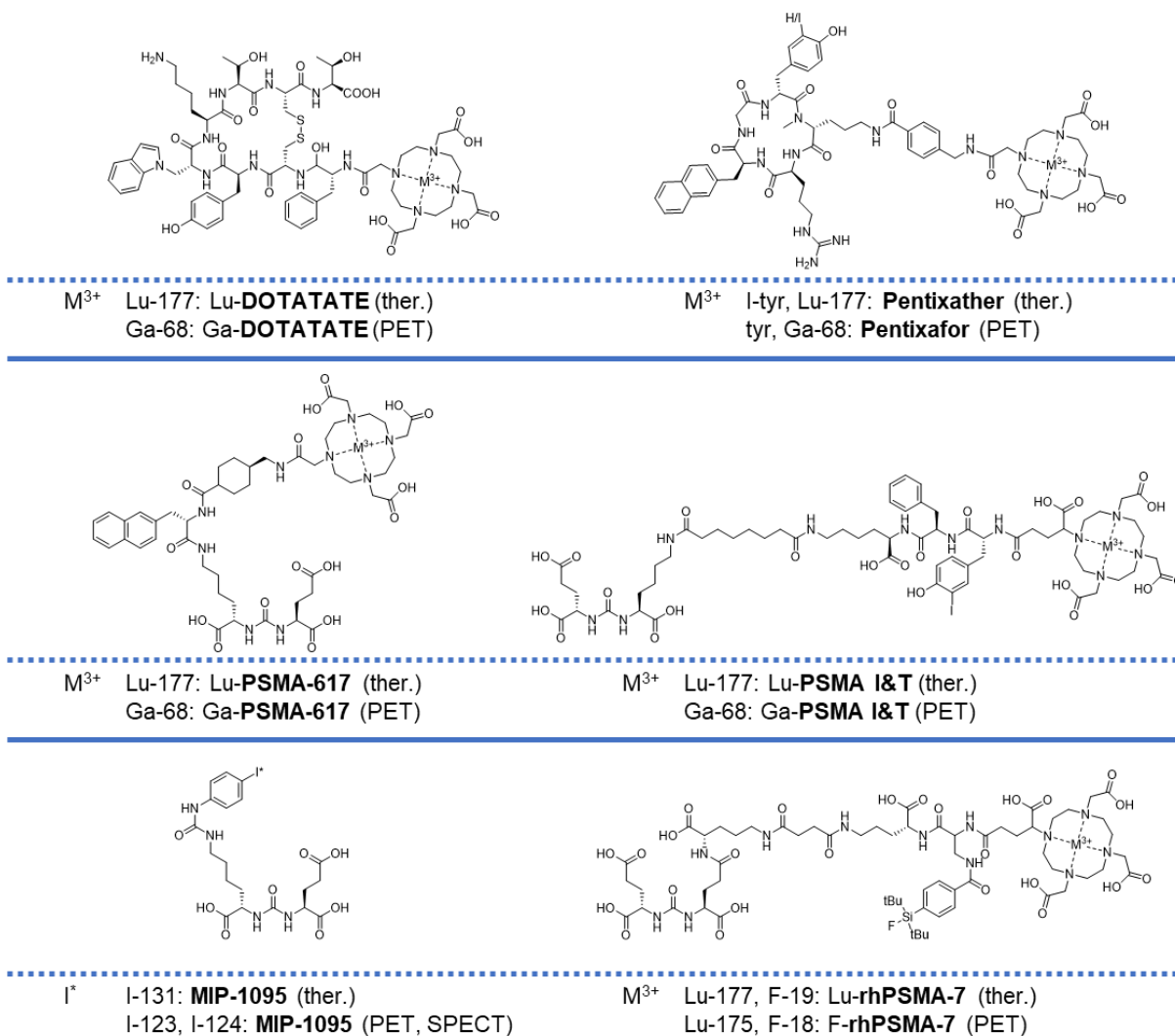


Figure 35: Structures of theranostic ligand pairs: [⁶⁸Ga/¹⁷⁷Lu]DOTATATE, [⁶⁸Ga/¹⁷⁷Lu]PSMA-617 and [⁶⁸Ga/¹⁷⁷Lu]PSMA I&T are converted into their diagnostic or therapeutic form by exchange of the radiometal only; the [⁶⁸Ga]Pentixafor scaffold is iodinated before complexation of lutetium-177 to obtain its therapeutic analog [¹⁷⁷Lu]Pentixather; [¹²³I/¹²⁴I/¹³¹I]MIP-1095 and [¹⁸F/¹⁷⁷Lu]rhPSMA-7 present the only “true” theranostic ligands as imaging and therapeutic compounds are chemically alike.

[⁶⁸Ga]DOTATATE is employed as a PET agent to confirm sstr2 expression in tumor lesions prior to treatment with its therapeutic analog [¹⁷⁷Lu]DOTATATE. When the DOTATATE scaffold is radiolabeled with lutetium-177, affinity drops 10-fold compared to the gallium-68 labeled compound. However, the prognostic value that is gained by this approach benefits the patients more than the use of a different but potentially more affine and therefore more effective therapeutic (206). Between 5 and 10% of primary prostate cancers do not show elevated PSMA levels, underlining the importance of a suitable pre-treatment imaging concept with PSMA-targeted compounds such as [⁶⁸Ga/¹⁷⁷Lu]PSMA-617 and [⁶⁸Ga/¹⁷⁷Lu]PSMA I&T (207). Exchange of the diagnostic

isotope within these ligands, however, represents a concrete structural transformation. Hence, physicochemical properties and target binding capability is oftentimes significantly influenced. A “true” theranostic approach is only then reached, when both the tracer and the therapeutic partner are chemically equal (208). This is the case for PSMA-targeted compounds [$^{123}\text{I}/^{124}\text{I}/^{131}\text{I}$]MIP-1095 and [$^{18}\text{F}, ^{\text{nat}}\text{Lu}/^{19}\text{F}, ^{177}\text{Lu}$]rhPSMA-7. MIP-1095 exhibits an interchangeable iodine residue that can be used for the application within SPECT (labeled with I-124), PET (labeled with I-123) and PRRT (labeled with I-131). This compound was the first PSMA-targeted theranostic agent to be evaluated in a patient study in 2014 (209). Recently, Wurzer et al. introduced the radiohybrid (rh) rhPSMA-7, carrying two distinct labeling sites: a SiFA moiety for labeling with fluorine-18 and a chelator for the introduction of radiometals. When labeled with fluorine-18, the cold lutetium complex is present and when labeled with lutetium-177, the SiFA moiety contains cold fluorine. Thus, a “true” theranostic pair is established (210). Radiohybrids targeting the CXCR4 receptor will be the subject of chapter III. 4. later in this work. Other compounds such as [^{68}Ga]Pentixafor for PET imaging and [^{177}Lu]Pentixather for PRRT of CXCR4 expressing tumors, are a theranostic pair in wider definition. Significant loss of affinity upon complexation of lutetium-177 instead of gallium-68 was compensated by the introduction of an I-tyr residue in the structure of [^{177}Lu]Pentixather (211).

Osl et al. reported the preparation of a second generation of ligands based on the structures of [^{68}Ga]Pentixafor and [^{177}Lu]Pentixather that display significantly elevated CXCR4 affinity and internalization rates, ultimately resulting in favorable *in vivo* data compared to [^{177}Lu]Pentixather (146). Following the development of the high-affinity tracer backbone *CPCR4-Abz-a-r-dap* (Figure 13) earlier in this work, a new generation of DOTA-conjugated theranostics (Figure 36) was prepared with the intention to obtain follow-up ligands to [^{68}Ga]Pentixafor and [^{177}Lu]Pentixather.

Chemical synthesis of the peptides and radio-complexation thereof will be the first part of the following chapter, succeeded by the presentation and discussion of obtained data in *in vitro* and *in vivo* experiments.

3.1. Synthesis

The compounds within this project were synthesized *via* fragment condensation of the separately synthesized, de-protected and purified peptide scaffold *CPCR4* or *KO-CPCR4* with the respective protected and purified linker units. Subsequent Fmoc de-protection and purification was followed by in-solution coupling with un-protected DOTA according to a procedure described in literature (157). Acidic de-protection and purification *via semi-preparative* RP-HPLC yielded the respective compounds CXCR4-DOTA-01, -03 and -05. The former two and the tyrosine-bearing precursor for KO-CXCR4-DOTA-04 were furthermore subjected to scaffold iodination using NIS (212). Subsequent purification afforded the desired ligands CXCR4-DOTA-02, -04 and KO-CXCR4-DOTA-04. Details of the synthetic procedure are noted under section II. 2.3.3. When *Abz* was used as starting material for the synthesis of linker units, lower yields compared to the *Ambz*-based linker units were obtained. Furthermore, subsequent fragment condensation with the peptide scaffold afforded higher molar excess of linker unit and coupling reagents or longer reaction times. More byproducts were found compared to the analogous synthesis of *Ambz*-based peptides, aggravating RP-HPLC purification and resulting in overall lower yields. Coupling of un-protected DOTA proceeded smoothly without virtual formation of multimers and iodination with NIS provided mono- and di-iodinated products.

3.2. Radiosynthesis

3.2.1. Lutetium-177 Labeling

The complexation of the Pentixather precursor, CXCR4-DOTA-01 – 05 and KO-CXCR4-DOTA-04 using $[^{177}\text{Lu}]\text{LuCl}_3$ was achieved with constantly high radiochemical yields and purities. Labeled substances were used for experiments when radio-TLC measurements assured yields >97% and radio-RP-HPLC chromatograms affirmed purities >90%. Typical yields ranged from 98% to 99.9% for any compound and

molar activities ranged from 5–70 MBq/nmol, depending on the deployed amount of [¹⁷⁷Lu]LuCl₃ suitable for the intended application of the labeled compound.

3.2.2. Gallium-68 Labeling

[⁶⁸Ga]Pentixafor was prepared using [⁶⁸Ga]GaCl₃ by means of an automated synthesis module. The radiochemical yields did not exceed 40%, probably due to adsorption of the labeled compound to the reaction vessel. However, radiochemical purity was found to be >95% by radio-RP-HPLC measurement and [⁶⁸Ga]GaCl₃ content was determined to be <3%. The resulting compound was then used without further purification.

3.2.3. Gallium-67 Labeling

Labeling of CXCR4-DOTA-03 and -04 with [⁶⁷Ga]GaCl₃ proceeded suboptimal. Radiochemical conversion was found to be below 30% in all cases, probably due to incomplete transformation of [⁶⁷Ga]Ga-citrate to [⁶⁷Ga]GaCl₃ in the first place. The molar activity of the resulting compounds was therefore low and not exceeding 2 MBq/nmol. However, contamination of the final products with either [⁶⁷Ga]GaCl₃ or [⁶⁷Ga]Ga-citrate was found to be <3% and the mixtures were therefore suitable for logD_{7.4} determination. The low molar activities prohibited further assessment of the ligands in internalization and biodistribution experiments.

3.3. In vitro Evaluation and Hydrophilicity

Figure 36 gives an overview of the prepared ligands within this project. As depicted above, various questions arising from the iodination of the *CPCR4* peptide scaffold and the use of the optimized *Abz-a-r-dap* linker unit were sought to be answered by the evaluation of these compounds.

Affinity and hydrophilicity

Table 8 summarizes IC₅₀ and logD_{7.4} values for DOTA-conjugated theranostic compounds within this project.

Table 8: Summary of IC_{50} [nM] and $\log D_{7.4}$ values for CXCR4-DOTA-01 – 05 and KO-CXCR4-DOTA-04 and respective gallium and lutetium complexes thereof in comparison with reference compounds [$^{nat}Lu/^{177}Lu$]Pentixather and [$^{nat}Ga/^{68}Ga$]Pentixafor: IC_{50} values were determined in competitive binding studies employing Jurkat cells (400,000 cells/tube; 8°C, 2h incubation) and the standard ligand FC-131 (10^{-9} M, final assay-concentration). Data are expressed as mean \pm SD; IC_{50} data were determined as triplicates or quadruplicates (*); $\log D_{7.4}$ values were determined as octuplicates, sextuplicates (**) or pentuplicates (***); (****): data adapted from literature (137).

CXCR4-DOTA-	[M ³⁺]	IC_{50} [nM] (n = 3)	$\log D_{7.4}$ (n = 8)
01	/	12.1 \pm 2.4	n.d.
	Ga	2.95 \pm 0.59	n.d.
	Lu	5.05 \pm 1.75 (*)	-3.41 \pm 0.05 (**)
02	/	7.03 \pm 0.59	n.d.
	Ga	3.62 \pm 1.57 (*)	n.d.
	Lu	6.47 \pm 1.75 (*)	-2.20 \pm 0.06
03	/	3.16 \pm 0.63	n.d.
	Ga	1.64 \pm 0.13	-3.35 \pm 0.08 (***)
	Lu	1.80 \pm 0.11	-3.35 \pm 0.19 (**)
04	/	4.64 \pm 0.96	n.d.
	Ga	2.73 \pm 1.45	-2.65 \pm 0.22 (**)
	Lu	3.67 \pm 1.31	-2.89 \pm 0.10 (**)
05	/	21.3 \pm 6.6	n.d.
	Ga	12.9 \pm 3.2	n.d.
	Lu	10.7 \pm 3.6	-3.58 \pm 0.08
KO-04	/	5191 \pm 943	n.d.
	Ga	1557 \pm 409	n.d.
	Lu	2168 \pm 430 (*)	-3.02 \pm 0.05
[^{177}Lu]Pentixather	Lu	19.5 \pm 2.8	-1.76 \pm 0.03
[^{68}Ga]Pentixafor (****)	Ga	24.8 \pm 2.5	-2.90 \pm 0.08

Complexation of the Pentixafor precursor with lutetium instead of gallium led to a decrease of its CXCR4 affinity by a factor of nearly two (IC_{50} : 24.8 \pm 2.5 nM [^{nat}Ga] vs. 40.9 \pm 12 nM [^{nat}Lu]). However, compared to the un-complexed precursor (IC_{50} : 102 \pm 17 nM) both metal chelates exhibited substantially improved CXCR4 affinity (137). These tendencies were observed analogously for every ligand within this series. Receptor affinity was highest when gallium was complexed with the only exception being

[^{nat}Ga]CXCR4-DOTA-05. This exceptional case, though, is probably contributable to the high standard deviation of the IC₅₀ values of both corresponding gallium and lutetium complexes. Every gallium complex in this series exhibits considerably higher CXCR4 affinity than [^{nat}Ga]Pentixafor and every lutetium complex shows substantially higher CXCR4 affinity than [^{nat}Lu]Pentixather (except for KO-CXCR4-DOTA-04), confirming the linker extension (*a-r-dap*) to be a distinct booster for CXCR4 affinity. The discrepancy is especially apparent for [^{nat}Ga/^{nat}Lu]CXCR4-DOTA-03, displaying a 15-fold and 11-fold higher CXCR4 affinity compared to [^{nat}Ga]Pentixafor and [^{nat}Lu]Pentixather, respectively. The linker extension further serves for elevated hydrophilicity of I-CPCR4-conjugated compounds [¹⁷⁷Lu]CXCR4-DOTA-02 and -04 compared to [¹⁷⁷Lu]Pentixather and CPCR4-conjugated compounds [¹⁷⁷Lu]CXCR4-DOTA-01 and -03 compared to [⁶⁸Ga]Pentixafor.

When *Abz*-bearing ligands [¹⁷⁷Lu]CXCR4-DOTA-03 and -04 are compared to their *Ambz*-bearing analogs [¹⁷⁷Lu]CXCR4-DOTA-01 and -02, higher CXCR4 affinities of the *Abz*-bearing compounds are observed. Direct arrangement of IC₅₀ values reveals a 1.8-fold ([^{nat}Ga]) and 2.8-fold ([^{nat}Lu]) elevated receptor affinity for CXCR4-DOTA-03 compared to -01 and a 1.3-fold ([^{nat}Ga]) and 1.8-fold ([^{nat}Lu]) increased affinity for CXCR4-DOTA-04 compared to -02. The interaction between the linker unit and the receptor seems to be most favorable if less rotational freedom is present in the *Abz*-based linker unit, thus “freezing” the more suitable conformation. An effect that was found to be beneficial in the initial design of the CPCR4 peptide scaffold by Demmer et al. (149).

Iodination of the CPCR4 tyrosine was initially chosen to circumvent a drop in affinity when lutetium was complexed by the Pentixafor precursor. This beneficial impact of the iodo-tyrosine residue could not be reproduced in this series of compounds. Both iodinated ligands [^{nat}Ga/^{nat}Lu]CXCR4-DOTA-02 and -04 exhibit higher IC₅₀ values compared to their respective analogs [^{nat}Ga/^{nat}Lu]CXCR4-DOTA-01 and -03. This finding follows the study by Osl et al. that suggested the expendability of peptide scaffold iodination upon the use of optimized *Abz-a-r*-based linker units. Compared to their “second-generation” analogs lacking the terminal D-dap moiety in the linker unit, CXCR4-DOTA-03 and -04 display slightly lower CXCR4 affinities (CPCR4-*Abz-a-r*-DOTA: IC₅₀: 0.4 ± 0.1 nM [^{nat}Ga], 1.5 ± 0.1 nM [^{nat}Lu]; I-CPCR4-*Abz-a-r*-DOTA: IC₅₀: 2.6 ± 1.0 nM [^{nat}Ga], 1.7 ± 0.6 nM [^{nat}Lu] (146)). The optimization of the linker unit with D-dap presented in this work seems

to be detrimental to the compound's binding capacities. This observation, however, was not consistent throughout the course of this work. Several examples were found for which the elongation of the *Abz-a-r* linker unit proved to be an essential modification in order to retain high CXCR4 affinity, especially when sterically demanding moieties were attached to the *N*-terminus. At this point, reference should be made to compounds CXCR4-Tc-01/-06 (chapter III. 2.3) and CXCR4-SiFA-01/-02 (chapter III. 4.3). Furthermore, the CXCR4 affinity determination for compounds prepared by Osl et al. was not recapitulated in our own assay and the comparison may therefore be flawed.

Even though carrying an additional charged moiety (D-dap), hydrophilicity of [⁶⁷Ga]CXCR4-DOTA-03 and -04 was determined to be lower compared to their *Abz-a-r*-conjugated counterparts. Contrary to that and more coherent, slightly lower logD_{7.4} values were observed for both the lutetium-177 labeled ligands developed by Osl (146). A reason for this different behavior might be found in the distinct labeling methods. Compounds CXCR4-DOTA-03 and -04 were labeled with gallium-67, while both "second-generation" ligands by Osl et al. were complexed with gallium-68, potentially leaving a different solvent environment that influences the logD_{7.4} determination.

CXCR4-DOTA-05 was based on the structure of CXCR4-DOTA-03 with the difference being a D-Cit instead of D-Arg in the linker unit. The underlying idea of charge reduction using a neutral amino acid with similar sterical demand while preservation of CXCR4 affinity is given, was not affirmed. IC₅₀ values of the gallium and lutetium complexes were elevated by a factor of nearly eight and six, respectively, when citrulline was employed. This outcome underlines the importance of every amino acid in its specific place within the developed linker unit, as interaction with CXCR4 is impaired by structural changes. However less affine than its analogs CXCR4-DOTA-01 – 04, CXCR4-DOTA-05 still poses an interesting alternative to [⁶⁸Ga]Pentixafor and [¹⁷⁷Lu]Pentixather due to its increased affinity ([^{nat}Ga]: 12.9 ± 3.2 nM and [^{nat}Lu]: 10.7 ± 3.6 nM), high hydrophilicity and reduced net charge.

The stereo-inversion of L-2-Nal and L-Arg in the *CPCR4* peptide scaffold of KO-CXCR4-DOTA-04 leads to sweeping loss of CXCR4 affinity. Both the gallium and lutetium complexes exhibit IC₅₀ values in the micromolar range. Compared to their potent counterpart CXCR4-DOTA-04, elevated IC₅₀ values of a factor of more than 500 are observed. Lipophilicity of the lutetium-177 labeled analog does not change greatly

(logD_{7.4}: -3.02 ± 0.05 ([¹⁷⁷Lu]KO-CXCR4-DOTA-04) vs. -2.89 ± 0.10 ([¹⁷⁷Lu]CXCR4-DOTA-04)) due to this modification which was a prerequisite for the application in a comparative biodistribution study.

Internalization

The internalization of [¹⁷⁷Lu]CXCR4-DOTA-01 – 05 into Chem-1 cells was determined and compared to [¹⁷⁷Lu]Pentixather. As previously outlined, ¹²⁵I-FC-131 was used as an internal standard and cellular uptakes related to the specific uptake of this ligand. The internalization efficiency describes the fraction of internalized ligand in relation to the entire cell-bound ligand. Figure 37 summarizes the obtained data.

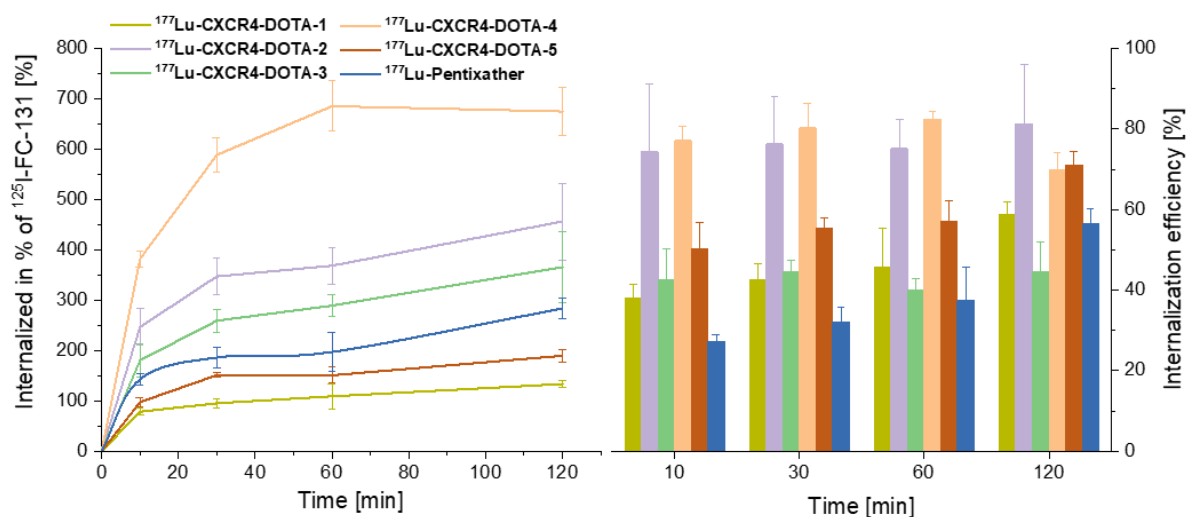


Figure 37: Dual tracer internalization of novel ligands [¹⁷⁷Lu]CXCR4-DOTA-01 – 05, [¹⁷⁷Lu]Pentixather and the reference compound ¹²⁵I-FC-131 (assay-concentration for each peptide 0.2 nM) into Chem-1 cells (100,000 cells per well; 37°C). Data are expressed as mean \pm SD; internalization at every time point was determined in triplicate and corrected for unspecific internalization; line diagram: Internalized activity of the novel ligand in relation to the internalized activity of internal standard ¹²⁵I-FC-131; bar diagram: Percentage of internalized activity of the novel ligand in relation to the total cell-bound activity.

The *Ambz*-based ligand [¹⁷⁷Lu]CXCR4-DOTA-01 shows the lowest total cellular uptake within this series, reaching a maximum of $133 \pm 7\%$ in relation to ¹²⁵I-FC-131 after 2h incubation. Even though [¹⁷⁷Lu]CXCR4-DOTA-05 displays substantially lower CXCR4 affinity, a maximum internalization of $190 \pm 13\%$ is reached by this ligand. [¹⁷⁷Lu]Pentixather was determined to be the least affine ligand within this series. However, a maximum internalization of $283 \pm 21\%$, a more than 2-fold and 1.5-fold higher value is reached compared to [¹⁷⁷Lu]CXCR4-DOTA-01 and -05, respectively. In general, no direct

correlation can be drawn between the CXCR4 affinity of a compound and its internalization rate.

When [¹⁷⁷Lu]CXCR4-DOTA-02 is compared to [¹⁷⁷Lu]Pentixather, the influence of the extended *a-r-dap* linker unit on the internalization rate can be assessed. [¹⁷⁷Lu]CXCR4-DOTA-02 reaches a maximum internalization of $456 \pm 76\%$, a 1.6-fold increased value compared to [¹⁷⁷Lu]Pentixather. This value is only outperformed by [¹⁷⁷Lu]CXCR4-DOTA-04, reaching a total cellular uptake of $675 \pm 47\%$. This data suggests that iodination of the *CPCR4* peptide scaffold induces a substantial boost in internalization. Compared to their *CPCR4*-bearing analogs [¹⁷⁷Lu]CXCR4-DOTA-01 and -03, a 3.4-fold and 1.8-fold increased internalization is noted for [¹⁷⁷Lu]CXCR4-DOTA-02 and -04, respectively. This observation was accordingly made by Osl et al. Furthermore, they justified the boost in internalization with a shift from antagonistic to partial agonistic behavior of the iodinated ligands and verified their assumption in a cAMP assay (146). A similar effect, however less pronounced, is attested when *Ambz* in the linker unit is exchanged by *Abz*. The ligand pair [¹⁷⁷Lu]CXCR4-DOTA-01 and -03 as well as [¹⁷⁷Lu]CXCR4-DOTA-02 and -04 reveal 2.7-fold and 1.5-fold higher internalization for the *Abz*-bearing ligands, respectively.

Another observation in agreement with the study by Osl et al. is that internalization efficiency of ligands is substantially enhanced upon iodination of the peptide scaffold. [¹⁷⁷Lu]CXCR4-DOTA-04 exhibits a 1.8-fold and [¹⁷⁷Lu]CXCR4-DOTA-02 a 1.4-fold elevated internalization efficiency compared to their *CPCR4*-bearing analogs [¹⁷⁷Lu]CXCR4-DOTA-03 and -01, respectively. Analogous to the ligands developed by Osl et al., a partial agonistic behavior of both iodinated compounds could be the determining factor for this notice (146). Agonistic behavior, however, seems to be induced only if both modifications, I-*CPCR4* and an optimized linker unit, are present as [¹⁷⁷Lu]Pentixather, despite bearing the I-*CPCR4* scaffold, does not exceed internalization efficiencies of $56.4 \pm 3.9\%$. When *Ambz* in the linker unit of [¹⁷⁷Lu]CXCR4-DOTA-01 and -02 is exchanged by *Abz*, no significant differences in terms of their uptake efficiency can be determined. The most distinguished ligand resulting from this internalization study is [¹⁷⁷Lu]CXCR4-DOTA-04, reaching a maximum cellular uptake of $675 \pm 47\%$ after 2h incubation and a maximum internalization efficiency of $82.4 \pm 1.9\%$.

[¹⁷⁷Lu]KO-CXCR4-DOTA-04

The discrepancy between the CXCR4 affinity of a ligand and its internalization is best illustrated using the example of [¹⁷⁷Lu]KO-CXCR4-DOTA-04, the structural analog to [¹⁷⁷Lu]CXCR4-DOTA-04. Two binding-essential amino acids in the *CXCR4* peptide scaffold were herein stereo-chemically inverted, leaving the rest of the molecule unchanged. Figure 38 illustrates the obtained internalization data for this compound.

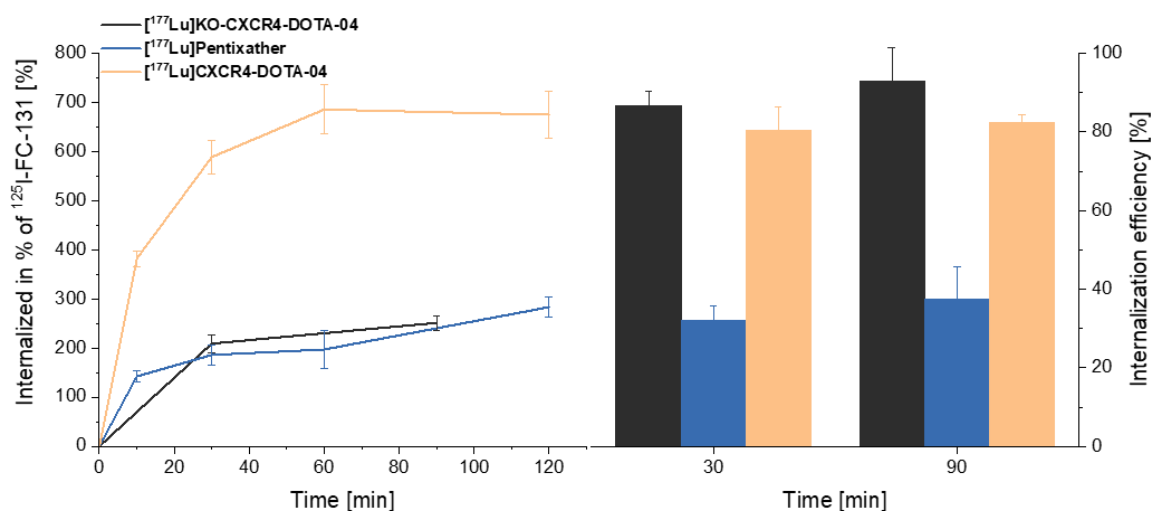


Figure 38: Dual tracer internalization of novel ligands [¹⁷⁷Lu]KO-CXCR4-DOTA-04, [¹⁷⁷Lu]CXCR4-DOTA-04, [¹⁷⁷Lu]Pentixather and the reference compound ¹²⁵I-FC-131 (assay-concentration for each peptide 0.2 nM) into Chem-1 cells (100,000 cells per well; 37°C). Data are expressed as mean ± SD; internalization at every time point was determined in triplicate and corrected for unspecific internalization; line diagram: Internalized activity of the novel ligand in relation to the internalized activity of internal standard ¹²⁵I-FC-131; bar diagram: Percentage of internalized activity of the novel ligand in relation to the total cell-bound activity.

Despite micromolar CXCR4 affinity, maximum internalization of [¹⁷⁷Lu]KO-CXCR4-DOTA-04 (251 ± 15%) is found to be equal to that of [¹⁷⁷Lu]Pentixather and even higher than that of [¹⁷⁷Lu]CXCR4-DOTA-01. More than 90% of the knock-out ligands cell-bound activity is internalized, outperforming [¹⁷⁷Lu]CXCR4-DOTA-04 to that effect. The uptake, however being unexpectedly high, still proves to be CXCR4 specific, as any ligand uptake into Chem-1 cells was blocked by co-incubation with an excess AMD3100. What is determined in IC₅₀ experiments and hence declared as a compound's CXCR4 affinity, is the capability of a ligand to replace the standard ligand ¹²⁵I-FC-131 in the CXCR4 main binding pocket. What if a novel ligand does not exclusively bind to the receptors main binding pocket but also to another region of CXCR4? The endogenous agonist CXCL12 exhibits such a two-site binding feature. A first contact is established between the ligands "12RFFESH17" motif and the extracellular loop region of CXCR4

before the agonists *N*-terminal region penetrates the receptors main binding pocket and induces signal transduction (213,214). The novel compounds within this work could be able to act in a similar way. The linker unit was elongated towards the exit of the main binding pocket to be able to add sterically demanding moieties. It was proven that the amino acids in the linker unit are capable of enhancing the affinity towards CXCR4 even though they are assumed not to be located in the main binding pocket anymore. Consequently, a two-site binding model is proposed. While the *CPCR4* peptide scaffold is located in the main binding pocket and tightly interacting with the receptor, additional contacts with the extracellular loop region are established by the elongated linker unit. If the binding in the main pocket is suppressed by AMD3100 or FC-131 challenge, interaction with CXCR4 can still take place at the extracellular site which remains untouched by both the standard ligands. In the case of [¹⁷⁷Lu]KO-CXCR4-DOTA-04, low binding affinity against ¹²⁵I-FC-131 was determined, thus proposing marginal binding in the main binding pocket of CXCR4. The interaction of the unchanged linker unit at the extracellular loop site, however, remains and could be sufficient to launch internalization of the ligand-receptor complex. Further insights into the molecular binding mechanism of these novel compounds are highly recommended. Co-crystallization of receptor and ligand may help to elucidate such processes and ultimately lead to a more targeted design of future generation compounds.

Summary

Figure 39 summarizes the experimental outcome so far: the surveyed ligands exhibit substantially higher CXCR4 affinities and hydrophilicity compared to their analogs [⁶⁸Ga]Pentixafor (light green area) and [¹⁷⁷Lu]Pentixather (light blue area).

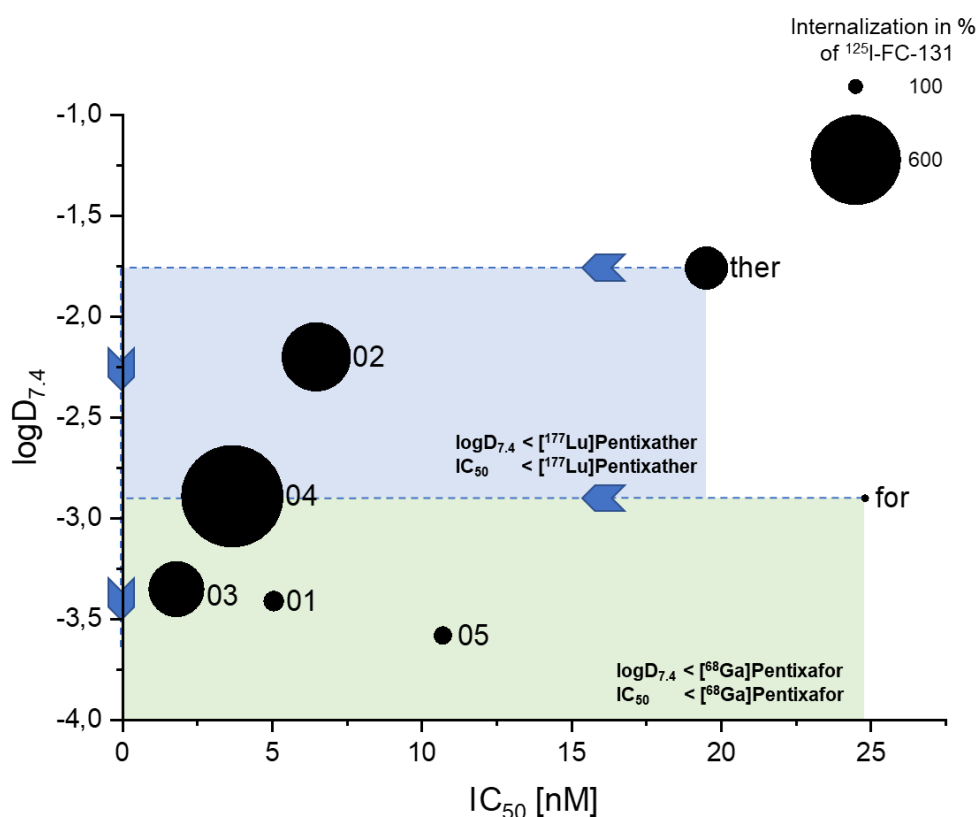


Figure 39: Summary of $\log D_{7.4}$ (y-axis), IC_{50} (x-axis) and maximum internalization values (dot size) for $[^{177}\text{Lu}]\text{CXCR4-DOTA-01} - 05$ as well as $[^{177}\text{Lu}]\text{Pentixather}$ and $[^{68}\text{Ga}]\text{Pentixafor}$ ($\log D_{7.4}$ and IC_{50} only): Numbers next to dots represent the respective ligand within this series, the letter *p* represents $[^{177}\text{Lu}]\text{Pentixather}$ and *for* represents $[^{68}\text{Ga}]\text{Pentixafor}$; dots in the light blue area suggest compounds that are more affine and hydrophilic than $[^{177}\text{Lu}]\text{Pentixather}$ and dots in the light green area suggest compounds that are more affine and hydrophilic than $[^{68}\text{Ga}]\text{Pentixafor}$.

The combination of *CPCR4* iodination and presence of the *a-r-dap* linker unit, provided $[^{177}\text{Lu}]\text{CXCR4-DOTA-02}$ and -04 , two compounds with high total cellular uptakes and internalization efficiencies. As the results described by Osl et al. suggest, a partial agonistic behavior of both these ligands can be presumed (146).

Several publications have touched the adequacy of antagonistic and agonistic peptides for their application within nuclear imaging and PRRT. A prominent example of research concerning this issue is the design of *sstr2*-targeted antagonists. A multitude of scientific papers reported higher cellular binding and accompanying higher *in vivo* uptake in tumor of antagonists such as DOTA-JR11 compared to agonists like DOTATATE and DOTATOC (206,215,216). The main reason for this enhanced binding was located within the binding mechanism of antagonists on the receptor surface. Such an interaction can take place with a variety of receptor conformations, in contrast to agonists, which require a distinct activated receptor conformation. Furthermore, upon binding of an agonist,

internalization of the receptor-ligand complex is induced, thus limiting the number of addressable receptors on the cell surface and accelerating ligand degradation and washout (217). The consideration of such effects has influenced the design of other GPCR-targeted ligands such as Demobesin-1, a GRPR-targeted antagonist which was found to be superior over the agonist Demobesin-4 in terms of cell-binding capacity and *in vivo* tumor uptake (218). These examples show that the improved *in vivo* targeting properties of antagonists are retraceable to enhanced cellular binding compared to their agonistic counterparts. Here, we present a contrarious concept that assigns higher fractions of cell-bound radioligand to potentially agonistic compounds.

The influence on the *in vivo* targeting was investigated in biodistribution studies employing [¹⁷⁷Lu]CXCR4-DOTA-01 – 04. Furthermore, the suitability of the newly developed ligands as follow-up compounds to [⁶⁸Ga]Pentixafor and [¹⁷⁷Lu]Pentixather was assessed in comparative experiments.

3.4. In vivo Biodistribution

The biodistribution profiles of [¹⁷⁷Lu]CXCR4-DOTA-01 – 04 as well as [⁶⁸Ga]Pentixafor and [¹⁷⁷Lu]Pentixather were investigated in Jurkat tumor-bearing mice. In order to spare animal lives and as [¹⁷⁷Lu]LuCl₃ for labeling was easier to obtain than [⁶⁸Ga]GaCl₃, biodistribution experiments were conducted with the lutetium-177 labeled ligands only. Because of this circumstance, special focus is set on the aptitude for an application as therapeutic analogs to [¹⁷⁷Lu]Pentixather. This ligand has been applied in the clinical treatment of CXCR4 expressing cancers and much like other candidates for PRRT, offers a variety of properties such as

- high and persistent tumor accumulation resulting in high activity doses deposited in the tumor tissue,
- rapid wash-out from non-target tissue, thus reducing full-body and organ doses to a minimum,
- high specificity for the actuated target,
- and facile radiolabeling with high molar activities (44,219–221).

The *in vitro* experiments discussed above (chapter III. 3.3.) showed higher CXCR4 affinity, cellular uptake and hydrophilicity of [¹⁷⁷Lu]CXCR4-DOTA-01 – 04 compared to [¹⁷⁷Lu]Pentixather, thus giving reason for further assessment of these compounds in *in*

vivo experiments. The four new ligands and both [⁶⁸Ga]Pentixafor and [¹⁷⁷Lu]Pentixather were examined in biodistribution and μ SPECT/CT imaging (Supplementary 3) studies 1h after injection into tumor-bearing mice. The best performing compounds, [¹⁷⁷Lu]CXCR4-DOTA-03 and -04, were further surveyed at 6 and 48h after injection, comparatively to [¹⁷⁷Lu]Pentixather. Specific uptake was determined by competition experiments employing an excess of AMD3100 (Supplementary 4). The knock-out ligand [¹⁷⁷Lu]KO-CXCR4-DOTA-04 was evaluated 24h after injection. As depicted for technetium tracers in chapter III. 2., a differentiation between organs that are affiliated with the expression of mCXCR4 (CXCR4⁺ organs), such as lung, liver and spleen and organs which are not known to express the receptor (CXCR4⁻ organs) is made.

3.4.1. One hour post Injection

Figure 40 gives an overview of the obtained data from *in vivo* biodistribution experiments 1h after injection into Jurkat tumor-bearing mice.

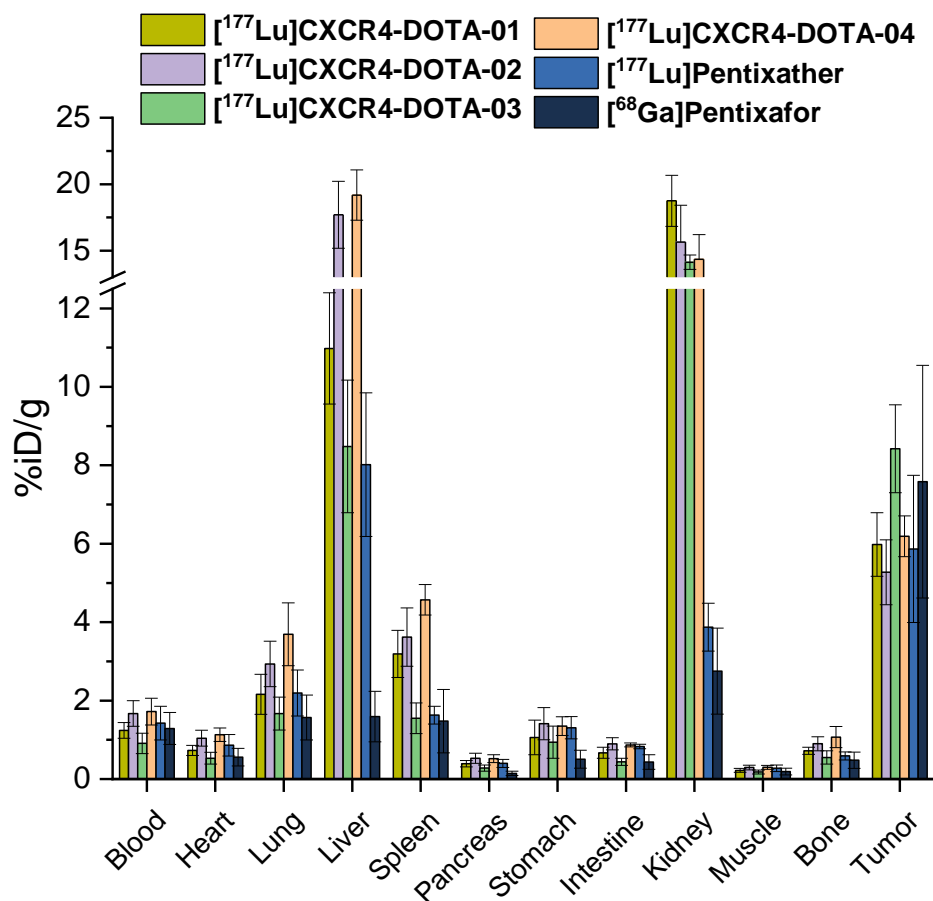


Figure 40: Biodistribution profiles of [¹⁷⁷Lu]CXCR4-DOTA-01 – 04, [¹⁷⁷Lu]Pentixather and [⁶⁸Ga]Pentixafor 1h post injection in Jurkat tumor-bearing female CB 17 SCID mice; data are expressed as %ID/g and are means ± SD of 5 animals per ligand.

[¹⁷⁷Lu]Pentixather is obtained by iodination of the Pentixafor precursor and subsequent labeling with lutetium-177 instead of gallium-68. These modifications constitute a substantially changed distribution *in vivo*. Slightly elevated blood activity levels of [¹⁷⁷Lu]Pentixather as well as higher activity values in CXCR4⁻ tissues such as heart, pancreas, kidney and muscle are observed. Its higher lipophilicity and the concomitant prolonged blood circulation time is further reflected in a 2.5-fold and 1.9-fold increased uptake in stomach and intestine, respectively. For [⁶⁸Ga]Pentixafor, 1.59 ± 0.64 %ID/g is found in liver while [¹⁷⁷Lu]Pentixather exhibits an increased uptake in liver of 8.02 ± 1.83 %ID/g. As outlined by Osl et al., moderate affinity towards mCXCR4 is suspected to be the cause of this elevated uptake in liver as well as spleen and lung

(146). As observed for technetium tracers of chapter III. 2. and further reinforced by the data from Osl et al., considerably elevated uptake in CXCR4⁺ organs is provided by the optimized tracer backbone that is the basis for each ligand within this series. μ SPECT images reveal, that this uptake is momentarily reduced upon co-injection of the respective compounds with an excess of AMD3100 (Supplementary 4). Radioligand uptake in lung, liver and spleen is therefore determined to be mCXCR4 specific. When [⁶⁸Ga]Pentixafor is compared to [¹⁷⁷Lu]CXCR4-DOTA-01, the impact of the *a-r-dap* linker elongation is reflected in a 6.9-fold and a 2.2-fold elevated uptake in liver and spleen, respectively. Similar results are obtained for the comparison of [¹⁷⁷Lu]Pentixather with its analog [¹⁷⁷Lu]CXCR4-DOTA-02. The uptake in CXCR4⁺ organs is particularly pronounced for I-CPCR4-conjugated ligands [¹⁷⁷Lu]CXCR4-DOTA-02 and -04. Compared to [¹⁷⁷Lu]Pentixather, a 2.4-fold and a 2.2-fold increased hepatic uptake is noted, respectively. Also according with the data presented in chapter III. 2. is, that highest uptake in CXCR4⁺ organs correlates with the most efficiently internalizing ligands [¹⁷⁷Lu]CXCR4-DOTA-02 and -04.

By this uptake in CXCR4⁺ organs, a reservoir of radioligand is provided, which leads to a decelerated clearance from background. Even though both compounds were determined to be substantially more hydrophilic than [⁶⁸Ga]Pentixafor, slower clearance from blood and CXCR4⁻ organs is observed for [¹⁷⁷Lu]CXCR4-DOTA-01 and -03. Equivalent results are obtained for the comparison of iodinated ligands [¹⁷⁷Lu]CXCR4-DOTA-02 and -04 with [¹⁷⁷Lu]Pentixather. Moreover, the high uptake in CXCR4⁺ organs may limit tumor uptake of the novel ligands. In comparison to [⁶⁸Ga]Pentixafor and [¹⁷⁷Lu]Pentixather, the increased hCXCR4 affinities and internalization capabilities of the novel ligands determined in *in vitro* experiments above, are not broadly reflected in enhanced tumor uptakes. This effect is already observable when tumor uptake of [⁶⁸Ga]Pentixafor is compared to that of [¹⁷⁷Lu]Pentixather and yet more obvious for [¹⁷⁷Lu]CXCR4-DOTA-01, -02 and -04 as these compounds show higher uptakes in CXCR4⁺ organs. [¹⁷⁷Lu]CXCR4-DOTA-03, on the other hand, displays comparable uptake in CXCR4⁺ organs to [¹⁷⁷Lu]Pentixather. Hence, substantially elevated targeting potential is indeed reflected in elevated tumor uptake.

As much as tumor uptake values might be flawed by the retention of radioligand in CXCR4⁺ organs, the utmost uptakes in tumor are observed for the most affine ligands [¹⁷⁷Lu]CXCR4-DOTA-03 and -04, reaching 8.42 ± 1.12 %iD/g and 6.19 ± 0.52 %iD/g, respectively. Higher tumor uptakes compared to their analogs [⁶⁸Ga]Pentixafor

(7.58 ± 2.97 %iD/g) and [^{177}Lu]Pentixafer (5.87 \pm 1.88 %iD/g) are hence obtained while [^{177}Lu]CXCR4-DOTA-01 and -02 (5.98 ± 0.82 %iD/g and 5.27 ± 0.83 %iD/g, respectively) display slightly lower uptakes in tumor, thus favoring both *Abz*-bearing ligands.

Each of the novel DOTA-conjugated ligands exhibits increased activity levels in the kidneys compared to [^{68}Ga]Pentixafer and [^{177}Lu]Pentixafer. As discussed for technetium tracers in chapter III. 2., a trapping of the positively charged radioligands is proposed due to complex formation with megalin/cubilin and subsequent reabsorption in the kidneys (222). This explanation fits well as each of the newly developed ligands carries the same number of charged amino acids and a comparable renal uptake (18.8 ± 1.9 %iD/g, 15.7 ± 2.8 %iD/g, 14.1 ± 0.5 %iD/g, 14.4 ± 1.9 %iD/g, [^{177}Lu]CXCR4-DOTA-01, -02, -03, -04, respectively) is observed that is independent of the compound's hydrophilicity.

Table 9: Tumor/organ ratios determined using data obtained from biodistribution studies 1h after injection of [¹⁷⁷Lu]CXCR4-DOTA-01 – 04, [¹⁷⁷Lu]Pentixather and [⁶⁸Ga]Pentixafor in Jurkat tumor-bearing female SCID mice; data are expressed as mean ± SD of 5 animals per ligand.

Tumor/Organ	¹⁷⁷ Lu]CXCR4-DOTA-				¹⁷⁷ Lu]Pentixather	⁶⁸ Ga]Pentixafor
	01	02	03	04		
Blood	4.82 ± 1.02	3.16 ± 0.79	9.25 ± 2.92	3.60 ± 0.77	4.12 ± 1.80	5.88 ± 2.96
Heart	8.19 ± 1.83	5.06 ± 1.27	15.9 ± 5.0	5.48 ± 0.94	6.81 ± 3.07	13.6 ± 7.6
Pancreas	15.3 ± 3.8	9.95 ± 2.90	30.1 ± 9.5	11.9 ± 2.5	14.7 ± 6.0	52.7 ± 28.5
Stomach	5.64 ± 2.46	3.74 ± 1.23	8.96 ± 4.08	4.59 ± 0.90	4.49 ± 1.74	15.0 ± 8.9
Intestine	8.93 ± 2.22	5.87 ± 1.36	19.1 ± 4.7	7.11 ± 0.72	7.06 ± 2.31	17.5 ± 10.2
Muscle	27.2 ± 7.2	17.9 ± 4.6	46.8 ± 14.4	20.6 ± 3.9	21.3 ± 9.4	39.4 ± 23.4
Lung	2.77 ± 0.75	1.80 ± 0.45	5.04 ± 1.43	1.68 ± 0.39	2.67 ± 1.12	4.83 ± 2.59
Liver	0.54 ± 0.10	0.30 ± 0.06	0.99 ± 0.24	0.32 ± 0.04	0.73 ± 0.29	4.76 ± 2.68
Spleen	1.87 ± 0.43	1.46 ± 0.38	5.43 ± 1.55	1.35 ± 0.16	3.60 ± 1.26	5.13 ± 3.45
Kidneys	0.32 ± 0.05	0.34 ± 0.08	0.60 ± 0.08	0.43 ± 0.07	1.51 ± 0.54	2.76 ± 1.54

The above-discussed uptake in CXCR4⁺ organs and the herewith connected decreased uptake in tumor and decelerated clearance from background, generally impairs tumor/organ ratios of [¹⁷⁷Lu]CXCR4-DOTA-01 – 04. Again, outstanding data is obtained for [¹⁷⁷Lu]CXCR4-DOTA-03 that displays considerably lower uptake in CXCR4⁺ organs compared to its analogs and higher tumor uptake. Compared to [¹⁷⁷Lu]Pentixather, higher ratios are obtained for the novel ligand except for the kidneys. The difference is especially pronounced for CXCR4⁻ organs such as heart, pancreas, intestine and muscle, showing 2.3-fold, 2.1-fold, 2.7-fold and 2.2-fold higher ratios, respectively, for [¹⁷⁷Lu]CXCR4-DOTA-03 (Table 9). As both compounds exhibit comparable accumulation in CXCR4⁺ organs, a distinct benefit of the structural optimization can be acknowledged. When compared to [⁶⁸Ga]Pentixafor, differences are found to be less pronounced. However, [¹⁷⁷Lu]CXCR4-DOTA-03 is able to challenge the PET ligand, showing comparable or even higher tumor/organ ratios for blood, heart, intestines, muscle, lung and spleen.

Even though the biodistribution profiles of the new ligands are biased by their uptake in mCXCR4 expressing organs, a beneficial impact of the conducted structural optimizations can be noted. [¹⁷⁷Lu]CXCR4-DOTA-03 displays higher tumor/organ ratios compared to [¹⁷⁷Lu]Pentixather and could be able to compete with [⁶⁸Ga]Pentixafor. Further experiments with the gallium-68 labeled ligand have to be conducted to verify our assumptions of a potential competitor for the established PET agent. In order to investigate biodistribution profiles over time, [¹⁷⁷Lu]CXCR4-DOTA-03 was further examined at 6 and 48h after injection and compared to its iodinated analog [¹⁷⁷Lu]CXCR4-DOTA-04 and [¹⁷⁷Lu]Pentixather, which will be the content of the following passage.

3.4.2. Six hours post Injection

Figure 41 depicts the obtained data from *in vivo* biodistribution studies 6h after injection of [¹⁷⁷Lu]Pentixather, [¹⁷⁷Lu]CXCR4-DOTA-03 and -04 in Jurkat tumor-bearing mice.

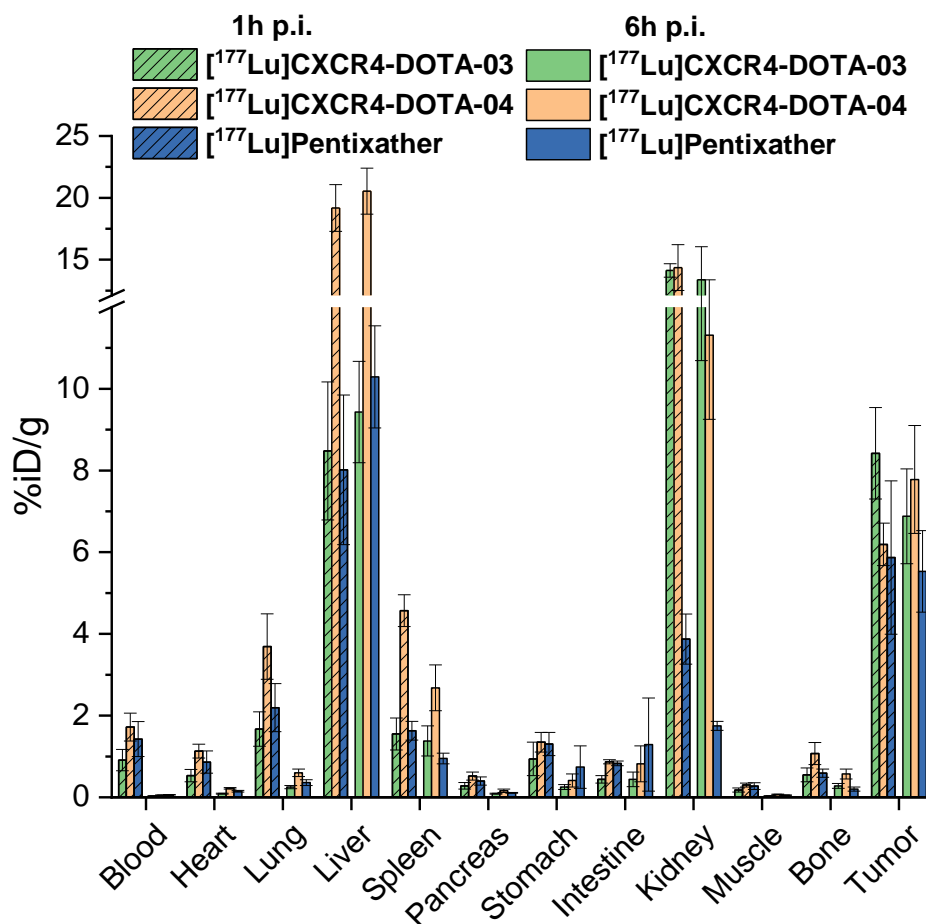


Figure 41: Biodistribution profiles of [¹⁷⁷Lu]CXCR4-DOTA-03 and -04 as well as [¹⁷⁷Lu]Pentixather 1h and 6h post injection in Jurkat tumor-bearing female CB 17 SCID mice; data are expressed as %iD/g and are means \pm SD of 5 animals per ligand.

[¹⁷⁷Lu]Pentixather experiences substantial washout from blood and CXCR4⁻ organs based on the 1h time point. Furthermore, kidney, lung and spleen activity levels are reduced 45%, 84% and 42%, respectively. Higher activity is found in liver and a more than 55% increased activity level is detected in the intestine based on the 1h time point, thus indicating a deferred clearance *via* the bile. A nearly complete retention of radioligand in the tumor (5.53 ± 1.00 %iD/g) is reached (5.87 ± 1.88 %iD/g at 1h p.i.). Similar results are obtained for [¹⁷⁷Lu]CXCR4-DOTA-03 and -04. Both ligands show efficient washout from blood and CXCR4⁻ tissues. In contrast to [¹⁷⁷Lu]Pentixather, however, the same activity levels found at 1h p.i. in the kidneys are observed at 6h p.i. as well, which is attributable to trapping of the charged ligands. Slightly elevated hepatic

uptake but no additional activity in the intestines is observed, indicating the absence of hepatobiliary excretion for both ligands. The most pronounced difference between these two compounds at 6h p.i. is their retention in the tumor. A 18% decrease to 6.88 ± 1.16 %iD/g is observed for [^{177}Lu]CXCR4-DOTA-03 whereas [^{177}Lu]CXCR4-DOTA-04 exhibits a 26% increase up to 7.78 ± 1.32 %iD/g. The high internalization of [^{177}Lu]CXCR4-DOTA-04 might be accountable for an elevated ligand trapping in the tumor cells while [^{177}Lu]CXCR4-DOTA-03 and [^{177}Lu]Pentixather are washed out more efficiently. Moreover, [^{177}Lu]CXCR4-DOTA-04 displayed the largest ligand reservoir in CXCR4⁺ organs at 1h after injection and still after 6h. Slow washout therefrom facilitates anew ligand uptake in the tumor and constitutes elevated uptake compared to the 1h time point.

Progressing full-body clearance and high tumor uptake and retention of [^{177}Lu]CXCR4-DOTA-03 and -04 are reflected in overall beneficial tumor to organ ratios compared to [^{177}Lu]Pentixather (Table 10).

Table 10: Tumor/organ ratios determined using data obtained from biodistribution studies 6h after injection of [^{177}Lu]CXCR4-DOTA-03 and -04 as well as [^{177}Lu]Pentixather in Jurkat tumor-bearing female SCID mice; data are expressed as mean \pm SD of 5 animals per ligand.

Tumor/Organ	[^{177}Lu]CXCR4-DOTA-		[^{177}Lu]Pentixather
	03	04	
Blood	223 ± 62	160 ± 43	105 ± 39
Heart	73.7 ± 14.3	34.8 ± 6.8	38.0 ± 8.8
Pancreas	76.5 ± 13.7	47.4 ± 13.1	50.3 ± 10.8
Stomach	27.8 ± 8.6	18.8 ± 8.1	7.44 ± 5.33
Intestine	15.7 ± 6.9	9.54 ± 5.45	4.30 ± 3.90
Muscle	227 ± 53	115 ± 22	113 ± 38
Lung	27.8 ± 6.2	13.1 ± 2.9	15.4 ± 4.0
Liver	0.73 ± 0.16	0.38 ± 0.07	0.54 ± 0.12
Spleen	4.97 ± 1.58	2.91 ± 0.78	5.82 ± 1.33
Kidneys	0.51 ± 0.14	0.69 ± 0.17	3.16 ± 0.60

Due to [^{177}Lu]Pentixather's lower charge, an at least 4.6-fold higher tumor/kidney ratio is observed compared to both new ligands. Enhanced hydrophilicity and fast clearance of [^{177}Lu]CXCR4-DOTA-03, is reflected in highest tumor/background ratios for blood, heart, pancreas, stomach, intestines and muscle. Compared to its I-CPCR4-bearing analog,

[¹⁷⁷Lu]CXCR4-DOTA-04, [¹⁷⁷Lu]CXCR4-DOTA-03 shows a slightly lower uptake in tumor but also an accelerated clearance from both CXCR4⁺ and CXCR4⁻ tissues and therefore substantially higher tumor/organ ratios except for the kidneys (0.51 ± 0.14 vs. 0.69 ± 0.17). Compared to [¹⁷⁷Lu]Pentixather, however, tumor/CXCR4⁻ organ ratios of [¹⁷⁷Lu]CXCR4-DOTA-04 are in the same range except for a 2.5-fold and a 2.2-fold elevated tumor/stomach and tumor/intestine ratio, respectively, which favors the novel ligand.

This biodistribution study revealed decent retention in tumor of [¹⁷⁷Lu]CXCR4-DOTA-03 and in the case of [¹⁷⁷Lu]CXCR4-DOTA-04 an increased tumor uptake compared to the 1h time point that might lead to an overall higher deposition of activity in the tumor compared to [¹⁷⁷Lu]Pentixather. However, according with the study conducted at 1h p.i., tumor/organ ratios were evidently favoring [¹⁷⁷Lu]CXCR4-DOTA-03 over both other investigated ligands. To further investigate the long-term biodistribution of these compounds, a third experiment at 48h p.i. was conducted.

3.4.3. Forty-eight hours post Injection

Figure 42 summarizes the data obtained from *in vivo* biodistribution studies at 48h p.i. of [¹⁷⁷Lu]Pentixather as well as [¹⁷⁷Lu]CXCR4-DOTA-03 and -04.

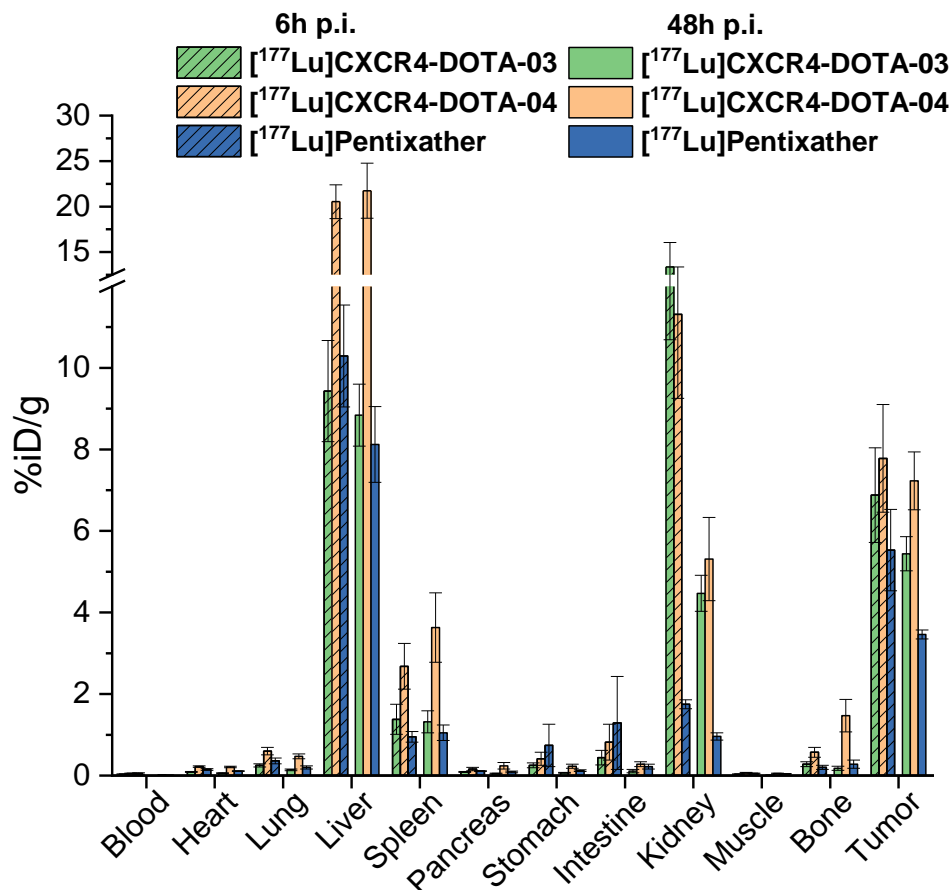


Figure 42: Biodistribution profiles of [¹⁷⁷Lu]CXCR4-DOTA-03 and -04 as well as [¹⁷⁷Lu]Pentixather 6h and 48h post injection in Jurkat tumor-bearing female CB 17 SCID mice; data are expressed as %iD/g and are means ± SD of 5 animals per ligand.

[¹⁷⁷Lu]Pentixather exhibits further washout from blood (0.010 ± 0.003 %iD/g) and CXCR4⁻ tissues as well as the kidneys (0.96 ± 0.09 %iD/g). Clearance from CXCR4⁻ tissues and subsequent uptake in CXCR4⁺ organs could be the reason for elevated uptake in spleen compared to the 6h time point and only minimal washout from the liver which shows comparable activity levels than at 1h p.i. (8.12 ± 0.93 %iD/g at 48h p.i. vs. 8.02 ± 1.83 %iD/g at 1h p.i.). This re-uptake, however, is not observed for tumor tissue as only 3.46 ± 0.11 %iD/g are found in the tumor after 48h, which represents 59% of the initially tumor-deposited activity. [¹⁷⁷Lu]CXCR4-DOTA-03 exhibits the lowest activity levels for blood (0.004 ± 0.007 %iD/g) and CXCR4⁻ tissues within this series. While renal retention is high (4.47 ± 0.44 %iD/g), 67% compared to the 6h time point is cleared.

Opposed to that, a nearly complete retention in spleen and liver is observed. In case of the latter, the uptake after 1h is even exceeded. In this case, the retention in CXCR4⁺ organs is further reflected in slow washout from tumor. With a value of 5.44 ± 0.41 %iD/g, a decent 79% and 65% retention compared to the 6h and 1h time point, respectively, is observed. [¹⁷⁷Lu]CXCR4-DOTA-04 displays the slowest clearance from blood (0.020 ± 0.002 %iD/g) and background organs. This is not surprising given the fact that uptake and retention in CXCR4⁺ organs was highest for this compound at any time point, thus decelerating full-body clearance due to the reservoir function. The retention in spleen (3.63 ± 0.85 %iD/g) and liver (21.7 ± 3.0 %iD/g) is found to be elevated compared to the 6h time point. In this case, the organ reservoir is assumed to serve for a nearly complete retention of tumor activity. After 48h, 7.23 ± 0.71 %iD/g of [¹⁷⁷Lu]CXCR4-DOTA-04 are found in the tumor, which represents a decrease of 7% and an increase of 17% compared to the 6h and 1h time point, respectively. Interpolation of time-activity-curves (using the GraphPad Interpolation tool, Supplementary 5) of all three compounds reveals that [¹⁷⁷Lu]CXCR4-DOTA-04 shows an activity maximum in the tumor at 23h p.i. while both [¹⁷⁷Lu]CXCR4-DOTA-03 and [¹⁷⁷Lu]Pentixather suffer continuous efflux from tumor after the 1h time point.

Table 11: Tumor/organ ratios determined using data obtained from biodistribution studies 48h after injection of [¹⁷⁷Lu]CXCR4-DOTA-03 and -04 as well as [¹⁷⁷Lu]Pentixather in Jurkat tumor-bearing female SCID mice; data are expressed as mean \pm SD of 5 animals per ligand.

Tumor/Organ	[¹⁷⁷Lu]CXCR4-DOTA-		[¹⁷⁷Lu]Pentixather
	03	04	
Blood	1570 \pm 335	441 \pm 74	257 \pm 60
Heart	96.3 \pm 16.4	34.3 \pm 4.9	30.2 \pm 1.9
Pancreas	105 \pm 22	30.5 \pm 10.7	36.8 \pm 7.9
Stomach	82.0 \pm 11.2	31.4 \pm 7.0	29.4 \pm 4.5
Intestine	49.0 \pm 16.5	26.2 \pm 6.5	15.6 \pm 4.5
Muscle	504 \pm 77	152 \pm 26	96.4 \pm 18.9
Lung	39.3 \pm 7.3	15.4 \pm 2.6	17.3 \pm 3.5
Liver	0.61 \pm 0.07	0.33 \pm 0.06	0.43 \pm 0.05
Spleen	4.13 \pm 0.91	1.99 \pm 0.50	3.30 \pm 0.62
Kidneys	1.22 \pm 0.15	1.36 \pm 0.30	3.60 \pm 0.35

The prolonged residence time of the new ligands in the tumor together with their elevated hydrophilicity are reflected in overall beneficial tumor to organ ratios compared to [¹⁷⁷Lu]Pentixather (Table 11). [¹⁷⁷Lu]CXCR4-DOTA-03 exhibits high ratios for blood (1570 ± 335) and CXCR4⁻ tissues such as muscle (504 ± 77) and also noticeably higher ratios for CXCR4⁺ organs lung (39.3 ± 7.3), spleen (4.13 ± 0.91) and liver (0.61 ± 0.07) among these three compounds. As already observed for the 6h time point, [¹⁷⁷Lu]CXCR4-DOTA-04, despite showing favorable tumor uptake, is substantially slower cleared and hence, lower tumor/organ ratios are observed compared to its *CPCR4*-bearing analog. Even so, enhanced ratios are found for blood (441 ± 74), heart, stomach, intestines and muscle (152 ± 26) when compared to [¹⁷⁷Lu]Pentixather (257 ± 60 for blood, 96.4 ± 18.9 for muscle). The latter excels with lower renal retention, thus showing a 2.7-fold and 3.0-fold enhanced tumor/kidney ratio compared to [¹⁷⁷Lu]CXCR4-DOTA-04 and -03, respectively.

3.4.4. Knock-out Biodistribution

The knock-out derivative of [¹⁷⁷Lu]CXCR4-DOTA-04, [¹⁷⁷Lu]KO-CXCR4-DOTA-04 was prepared by stereo-inversion of two amino acids in the *CPCR4* peptide scaffold that are detrimental for high affinity towards CXCR4. The resulting compound lost most of its CXCR4 affinity (IC₅₀: > 2 μM) while still displaying significant and specific internalization into CXCR4 expressing cells. Hence, the influence of this stereo-inversion on the biodistribution pattern was analyzed in this experiment. A biodistribution at 6 or 48h p.i. would have provided optimally comparable data. However, due to problems within the running experiment, a 24h distribution was undertaken. Figure 43 summarizes the obtained data in comparison with the 6h biodistribution study of [¹⁷⁷Lu]CXCR4-DOTA-04.

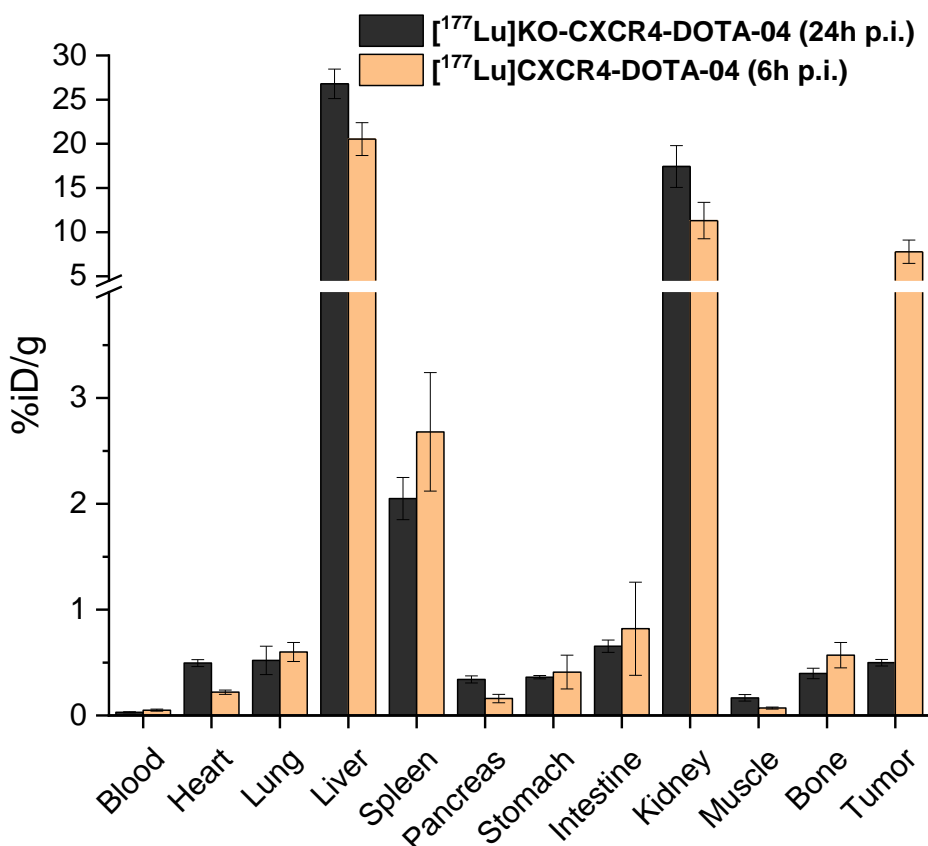


Figure 43: Biodistribution profiles of [¹⁷⁷Lu]KO-CXCR4-DOTA-04 24h post injection and of [¹⁷⁷Lu]CXCR4-DOTA-04 6h post injection in Jurkat tumor-bearing female CB-17 SCID mice; data are expressed as %iD/g and are means ± SD of 5 animals per ligand.

Due to micromolar affinity towards the human CXCR4 receptor, only slightly elevated uptake in tumor (0.50 ± 0.03 %iD/g) compared to background is observed for the knock-out ligand. This finding reconfirms the above-described connection of *in vitro* CXCR4 affinity and *in vivo* tumor uptake. Kidney activity levels (17.4 ± 2.4 %iD/g) are in the same range as observed for [¹⁷⁷Lu]CXCR4-DOTA-01 – 04, thus acknowledging the equivalent ligand trapping in the kidneys due to their positively charged characters. Clearance of the knock-out ligand from blood (0.03 ± 0.01 %iD/g) is fast and overall clearance from CXCR4⁻ tissues is comparable to its affine analog. No particularly elevated uptake into lung is observed for the knock-out peptide, whereas spleen (2.05 ± 0.20 %iD/g) and more pronounced, liver (26.8 ± 1.7 %iD/g) show comparably high values to [¹⁷⁷Lu]CXCR4-DOTA-04 (3.63 ± 0.85 %iD/g spleen, 21.7 ± 3.0 %iD/g liver). Once again, this is in accordance with the finding that the affinity towards the murine CXCR4 receptor is supposedly decoupled from the human CXCR4 receptor affinity for this type of ligands. Moreover, high internalization *in vitro* makes for substantial uptake in CXCR4⁺ organs,

independently of the determined CXCR4 affinity. In this case, however, ligand leakage from these organs does not lead to enhanced tumor retention, as only low CXCR4 affinity is described for [¹⁷⁷Lu]KO-CXCR4-DOTA-04. This study indicates that the biodistribution profiles of all novel ligands within this project are highly influenced by their interaction with the murine CXCR4 receptor. Hence, off-target ligand uptake as well as deferred background clearance and limited tumor uptakes should be interpreted with care until further insights in the molecular mechanisms of these ligands are provided.

3.5. Conclusion

Each of the developed DOTA-conjugated ligands exhibited higher CXCR4 affinity and hydrophilicity compared to [⁶⁸Ga]Pentixafor and [¹⁷⁷Lu]Pentixather. A distinct boost in total internalization and internalization efficiency was observed for the novel ligands, especially for [¹⁷⁷Lu]CXCR4-DOTA-02 and -04, which both comprise the iodinated peptide scaffold. According to literature, at least weak partial agonistic properties could be assigned to these novel ligands (146). The comparative biodistribution study of [¹⁷⁷Lu]CXCR4-DOTA-01 – 04 revealed high uptake in the mCXCR4-expressing organs lung, liver and spleen, presumably due to induced affinity towards the murine CXCR4 receptor. Moreover, uptake in CXCR4⁺ organs was found to be correlated with the ligand's internalization capability and this finding was later substantiated in the biodistribution of [¹⁷⁷Lu]KO-CXCR4-DOTA-04, which showed equivalent uptake in CXCR4⁺ organs compared to [¹⁷⁷Lu]CXCR4-DOTA-04, even though micromolar CXCR4 affinity was determined *in vitro*. High uptake in CXCR4⁺ organs served for a distorted biodistribution as gradual radioligand washout from these organs resulted in decelerated clearance and lower initial uptake in tumor at 1h p.i. After 6 and 48h, however, the organ reservoirs made for radioligand re-uptake in the tumor, especially apparent for [¹⁷⁷Lu]CXCR4-DOTA-04. However, tumor/organ ratios favored [¹⁷⁷Lu]CXCR4-DOTA-03 over any other ligand within this study, not least due to its relatively low uptake in CXCR4⁺ organs. Resembling affinities towards the murine receptor can be presumed for [¹⁷⁷Lu]CXCR4-DOTA-03 and [¹⁷⁷Lu]Pentixather, as both exhibited similar uptake in CXCR4⁺ organs. Hence, a more detailed comparison of their pharmacokinetic properties can be ventured. Figure 44 shows the temporal course of radioligand concentration in muscle, liver, spleen and tumor of these two compounds.

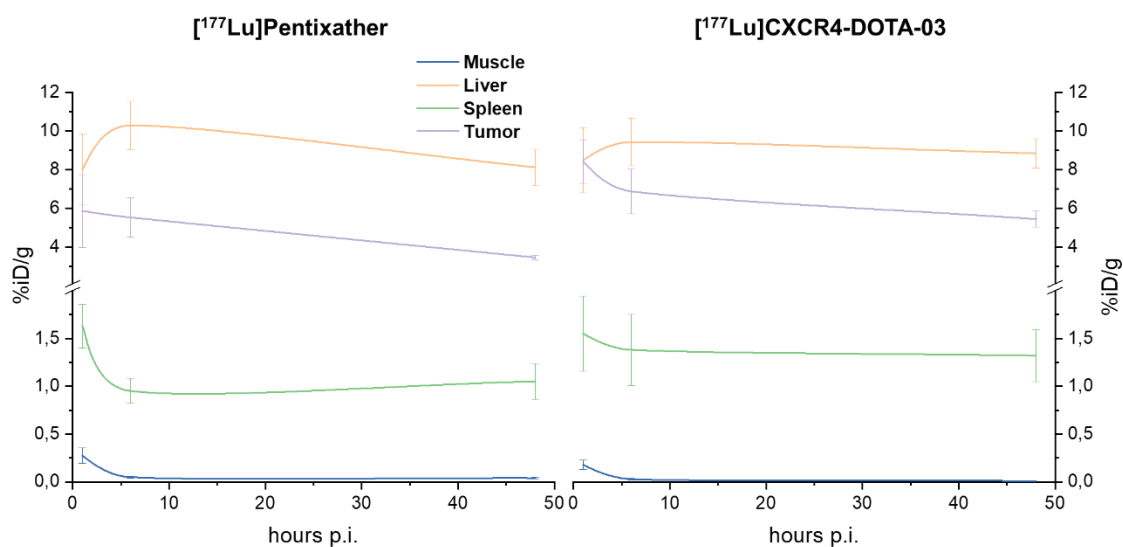


Figure 44: Time-activity curves for muscle, liver, spleen and tumor based on data obtained from biodistribution studies at 1h, 6h and 48h post injection of $[^{177}\text{Lu}]$ Pentixather and $[^{177}\text{Lu}]$ CXCR4-DOTA-03 in Jurkat tumor-bearing CB-17 SCID mice.

Area-under-the-curve (AUC) determination (calculation *via* OriginLab Integration tool) for both compounds revealed a 60% higher tumor-deposited activity for $[^{177}\text{Lu}]$ CXCR4-DOTA-03 in the period of consideration, hence justifying the structural optimization of ligands (Figure 35). Interestingly, even though $[^{177}\text{Lu}]$ CXCR4-DOTA-04 exhibited a maximum tumor uptake as late as 23h p.i., integration of its tumor time-activity-curve revealed an equivalent value compared to $[^{177}\text{Lu}]$ CXCR4-DOTA-03 (both AUC = 350, data not shown).

It is indispensable that an in-detail investigation of the interaction with the murine CXCR4 receptor is undertaken with the novel compounds. A confirmation that these distribution effects are limited to the use of mice and not translated into human application is, to our knowledge, exclusively done for $[^{177}\text{Lu}]$ Pentixather. For this ligand, mCXCR4 affinity in the high nanomolar range was determined, which resulted in elevated ligand uptake in CXCR4⁺ organs (146). In PRRT studies in men, though, no specifically elevated uptake in the liver and physiological uptake in the spleen was reported (136,139). A similar distribution is supposable for the newly developed ligands but remains to be confirmed. However, a possible problem may be caused by their increased renal uptake, although during PRRT, uptake in the kidneys of positively charged radioligands can be considerably reduced by co-infusion of basic amino acids, gelfusine or albumin fragments (223). This allows the radioligand dose escalation in order to obtain a maximum of tumor-deposited radioligand without the risk of nephrotoxicity.

Although being affected by the distorted biodistribution in mice, the collected data gives promising perspectives for four novel compounds. Elevated affinity towards the CXCR4 receptor was reflected in high tumor uptakes and prolonged retention in tumor. Among the tested ligands, [¹⁷⁷Lu]CXCR4-DOTA-03 exhibited the most promising tumor/background ratios, outperforming [¹⁷⁷Lu]Pentixather at any point of the experiments. The gallium-68 labeled derivative might be able to compete with [⁶⁸Ga]Pentixafor.

4. Fluorine-18 Tracers and Radiohybrids

Content of the following chapter will be the discussion of data obtained during the chemical and radiochemical synthesis as well as the *in vitro* and *in vivo* testing of fluorine-18 tracers and radiohybrid ligands.

The use of gallium-68 for the preparation of PET imaging agents has originated a variety of tracers such as the aforementioned [⁶⁸Ga]DOTATATE, [⁶⁸Ga]PSMA-617 and [⁶⁸Ga]Pentixafor (Figure 35). However, in recent years, reduced significance of gallium-68-labeled compounds was observed following the introduction of fluorine-18-labeled analogs. The longer half-life of fluorine-18 facilitates the central preparation of radioactive tracers and subsequent distribution, hence diminishing the costs of GMP compliant production in clinical facilities (224). Furthermore, imaging at later time points is enabled, permitting elevated circulation time for optimized tumor to organ ratios. Together with its lower particle energy and the herewith connected higher spatial resolution, various parameters are set out for an improved imaging experience (225).

While a gallium-68-labeled tracer is usually convertible into its therapeutic analog by exchange of the chelator-bound radioisotope to a β^- - or α -emitting radiometal, two distinct compounds are needed for fluorine-18 PET imaging and subsequent therapy. The lack of a theranostic approach for fluorine-18-labeled tracers was reduced when Wurzer et al. introduced the first PSMA-targeted radiohybrid tracer rhPSMA-7 (Figure 35) (210). The radiohybrid concept relies on the presence of both a SiFA moiety for the labeling with fluorine-18 by isotopic exchange and a chelator such as DOTA or DOTA-GA for complexation with radiometals (Figure 45).

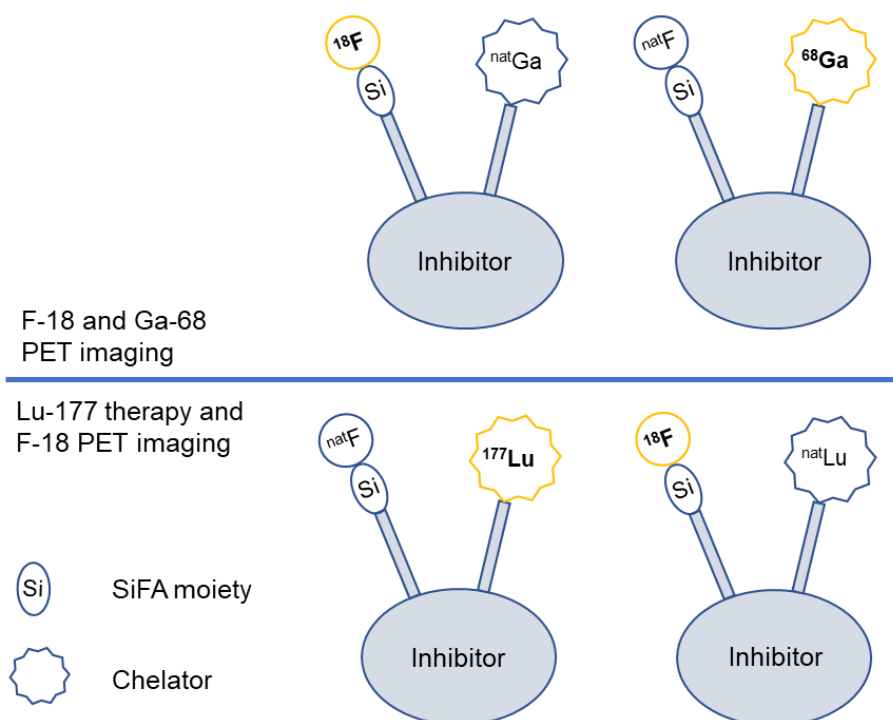


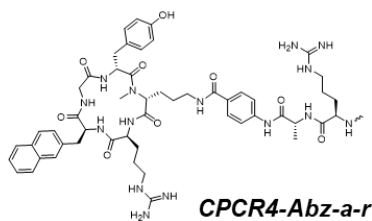
Figure 45: Conceptual structures of radiohybrid ligands: the SiFA moiety and a chelator are carrying either a stable (^{nat}F , ^{nat}Ga , ^{nat}Lu) or radioactive isotope (^{18}F , ^{68}Ga , ^{177}Lu), enabling their application within PET imaging and therapy; this concept represents a “true” theranostic approach.

One advantage of this method is a gain in diversity concerning the PET isotope used. Moreover, as both labeling moieties are always present in the molecule and always carrying either a radioactive or stable isotope, both radioactive entities ($[\text{}^{nat}\text{F}, \text{}^{68}\text{Ga}]$ and $[\text{}^{18}\text{F}, \text{}^{nat}\text{Ga}]$; $[\text{}^{nat}\text{F}, \text{}^{177}\text{Lu}]$ and $[\text{}^{18}\text{F}, \text{}^{nat}\text{Lu}]$, etc.) are chemically and therefore pharmacokinetically alike. This concept is therefore offering a “true” theranostic approach. SiFA hereby offers a fast fluorine-18 labeling chemistry paired with high radiochemical yields and hydrolytic stability *in vivo*, especially when the radiofluorine is shielded by bulky carbohydrate moieties such as *tert*-butyl groups (161,226). Yet, these bulky substituents convey a high degree of lipophilicity into the respective ligands and therefore deteriorate the pharmacokinetic profiles of the peptides. The compensation of this effect is attempted by the introduction of hydrophilic moieties such as chelators, PEG linkers or sugar moieties (227).

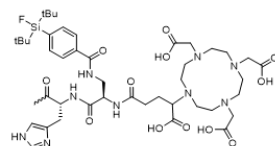
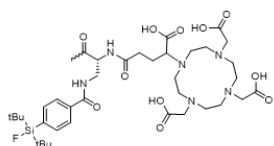
No SiFA-conjugated CXCR4-targeted ligand has been reported in literature thus far. However, several fluorine-18-labeled CXCR4-targeted ligands based on other labeling modalities were developed without successful translation into clinical routine. Most of the compounds suffered from low labeling yields and improper pharmacokinetics. Recently, Poschenrieder et al. developed NOTA-Pentixather by exchange of the DOTA chelator in the $[\text{}^{177}\text{Lu}]$ Pentixather scaffold with NOTA. This modification enabled fast and efficient

[¹⁸F]AIF labeling while the CXCR4 affinity compared to [¹⁷⁷Lu]Pentixather was left unchanged. *In vivo*, elevated lipophilicity was reflected in a delayed blood clearance and substantially reduced tumor to organ ratios compared to [⁶⁸Ga]Pentixafor (143). Kwon et al. reported the synthesis of two AMBF₃-conjugated compounds, BL08 and BL09, based on the structure of the highly affine antagonist LY2510924. Both fluorine-18-labeled ligands were tested against [⁶⁸Ga]Pentixafor and exhibited comparable CXCR4 affinity and hydrophilicity, ultimately resulting in promising biodistribution data (228). Unfortunately, the necessity for high starting activities and low labeling yields of the AMBF₃ method are yet to overcome.

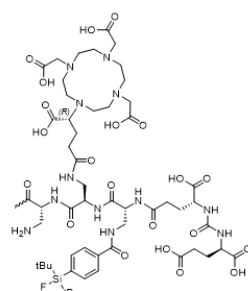
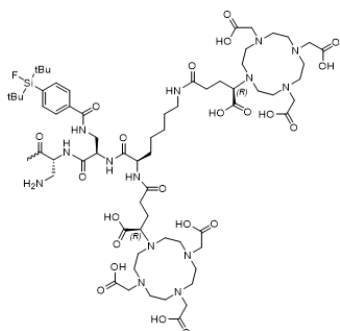
Despite the advances made in the development of CXCR4-targeted fluorine-18 PET tracers, there is still room for improvement of both labeling methodology and pharmacokinetic properties. As it is more and more observable in the cases of PSMA- and sstr2-targeted probes, advantages of fluorine-18 over gallium-68 PET imaging can lead to a benefit for the patients and manifest the need for more fluorine-18-labeled tracers. The aim of this work was the synthesis of such tracers based on the use of SiFA as a fast and high yielding labeling moiety that offers good hydrolytic stability *in vivo* (227). The chemical structures of compounds developed within this project are displayed in Figure 46.



CXCR4-SiFA-



CXCR4-SiFA-



CXCR4-SiFA-

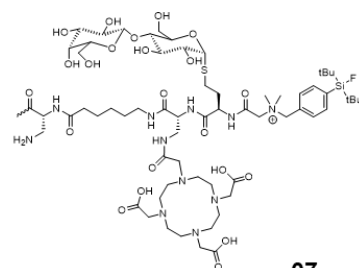
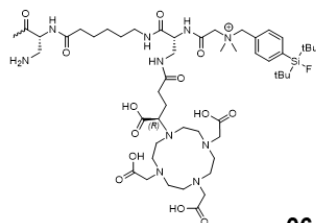
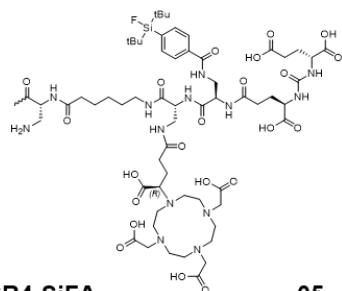


Figure 46: Summary of structures bearing a SiFA moiety: CXCR4-SiFA-01 and -02 were obtained by modification of the CPCr4-Abz-a-r tracer backbone; CXCR4-SiFA-03 and -04 were obtained by modification of the optimized CPCr4-Abz-a-r-dap tracer backbone and CXCR4-SiFA-05 – 07 were obtained by modification of the CPCr4-Abz-a-r-Ahx tracer backbone.

4.1. Synthesis

The entirety of compounds within this chapter (Figure 46) were prepared *via* condensation of separately synthesized and purified fragments. First, the HO-Abz-a-r(Pbf)-dap(Boc)-Fmoc linker unit was attached to the CPCr4 peptide scaffold, followed by Fmoc deprotection and purification, yielding the respective CPCr4-linker conjunction. The SiFA-containing part was prepared in a separate synthesis, removed from the resin under

retention of all acid-labile protecting groups, purified and coupled to the *CPCR4*-linker conjunction. Subsequent global de-protection and purification afforded the desired products CXCR4-SiFA-03 – 07. In the case of CXCR4-SiFA-01 and -02, the respective linker unit already contained the SiFA moiety before coupling to *CPCR4* was undertaken. Subsequent Fmoc de-protection and use of DOTA-GA-anhydride, global de-protection and purification provided the desired ligands. This two-fragment synthesis strategy resulted in substantially reduced yields and was changed to the higher yielding condensation of three fragments. A detailed description of building blocks used in the synthesis of these compounds can be found in II. 2.3.6. Both SiFA-containing building blocks, SiFA-BA and SiFA-Br (SiFA-bromide), the hydrophilic modifier (tBu)e(OH)ue(tBu)₂ as well as the lactosylated homocysteine moiety used in the synthesis of CXCR4-SiFA-07, were prepared in organo-chemical synthesis as depicted in II. 2.2.5, II. 2.2.6, II. 2.2.3 and II. 2.2.4, respectively.

4.2. Radiosynthesis

Due to the use of DOTA-GA anhydride in the synthesis of CXCR4-SiFA-01 and -02, two isomers, the (*S*)- and the (*R*)-enantiomers were obtained each. These enantiomers were eluted as two distinct product peaks in radio-RP-HPLC runs. The remainder of compounds in this project were synthesized enantiopure.

4.2.1. Lutetium-177 Labeling

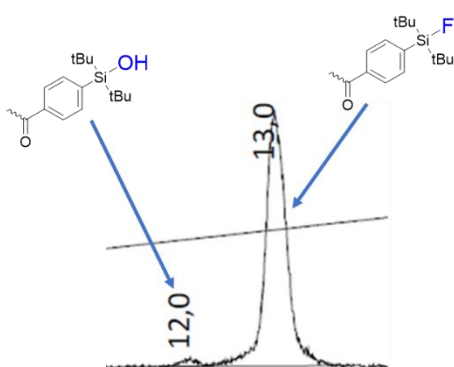


Figure 47: Cutout of a representative radio-RP-HPLC chromatogram obtained for a lutetium-177 labeled SiFA-conjugated compound ($t_r = 13.0$ min) with its respective product of hydrolysis ($t_r = 12.0$ min).

CXCR4-SiFA-01 – 07 were radiolabeled with lutetium-177, applying a standardized synthesis protocol (II. 3.3.). Radio-TLC evaluation revealed consistently high radiochemical yields greater 97%. Radio-RP-HPLC confirmed partial hydrolysis of SiFA for any compound ranging between 2% (CXCR4-SiFA-07) and 18% (CXCR4-SiFA-05) of the detected total radioactivity. The respective SiOH-carrying peptides eluted between 1.0 and 1.5 minutes before their SiFA-conjugated analogs (Figure 47). The peaks were assigned to the hydrolyzed compounds by co-injection of the labeling mixture with corresponding lutetium-177 labeled peptides that were hydrolyzed beforehand. In the future, lower temperatures or a shorter reaction time should be considered which would diminish radiochemical conversion but also limit hydrolysis to a minimum. Subsequent cartridge purification could remove unreacted $[^{177}\text{Lu}]\text{LuCl}_3$ and the resulting labeled compounds would therefore be obtained in lower radiochemical yields and concentrations but with overall higher purities.

4.2.2. Fluorine-18 Labeling

Labeling with fluorine-18 was conducted according to an unpublished procedure developed at the Technical University Munich (TUM). Briefly, $[^{18}\text{F}]\text{F}^-$ was removed from target water by trapping on a SAX cartridge prior to elution with an ammonium formate containing buffer. A part of this mixture (100–500 μL , 15–1000 MBq) was then added to the SiFA-conjugated compound (10–30 nmol) and the mixture was incubated at 40°C for 5 minutes prior to dilution with PBS and HLB cartridge purification. A detailed description of this procedure is given under II. 3.4. Elevated temperature was chosen over reaction at room temperature as radiochemical conversion was found to be improved.

Table 12 summarizes the decay-corrected radiochemical yields, the highest obtained molar activities and the minimum synthesis time in the production of $[^{18}\text{F}, ^{\text{nat}}\text{Ga}]\text{CXCR4-SiFA-01} - 07$.

Table 12: Summary of data obtained from the radio-fluorination of SiFA-conjugated compounds [^{nat}Ga]CXCR4-SiFA-01 – 07; columns comprise the decay-corrected (d.c.) radiochemical yield in %, the highest obtained molar activity *a_{mol}* at the end of synthesis (EOS) in MBq per nmol and the minimum time that was needed for the entire labeling procedure (Min. synth. Time) in minutes.

[¹⁸F,^{nat}Ga]CXCR4-SiFA-	Radiochemical yield (d.c.) in %	Max. <i>a_{mol}</i> (EOS) [MBq/nmol]	Min. synth. time [min]
01	[^{nat} Ga] 22.1 (n = 1)	0.97	13
	[^{nat} Lu] 21.3 (n = 1)	2.44	7
02	50.4 ± 6.2 (n = 2)	2.16	14
03	11.6 ± 0.6 (n = 2)	2.22	6
04	57.5 ± 4.9 (n = 2)	8.31	8
05	37.9 ± 4.7 (n = 3)	10.4	9
06	45.4 ± 3.6 (n = 3)	5.83	14
07	54.7 ± 5.9 (n = 4)	16.0	12

Over the course of the labeling experiments, inverse application of the labeling mixture *via* the male end of the HLB cartridge was found to result in substantially increased elution yields of greater 90% while standard application *via* the female end was followed by at least a 30% loss of yield. Particularly low radiochemical yields were obtained in the labeling of [^{nat}Ga]CXCR4-SiFA-03. This might be attributed to a shielding effect of the DOTA-GA chelators near the SiFA labeling moiety within this compound.

The maximum applied activity for radiolabeling of 30 nmol precursor ([^{nat}Ga]CXCR4-SiFA-07) was 1000 MBq. After 18 minutes from reaction start to final product elution, a yield of 54% (d.c.) and 481 MBq of labeled product was obtained, resulting in a molar activity of 16 MBq/nmol. In literature, common molar activities of 40–111 MBq/nmol for AMBF₃-conjugated compounds and 30–63 MBq/nmol for SiFA-conjugated ligands are reported on a laboratory scale, thus leaving room for improvements (226). Poschenrieder et al. reported a molar activity of 24.8 MBq/nmol for their [¹⁸F]AIF-NOTA-Pentixather under optimized synthesis conditions (143). According to literature, [¹⁸F]BL08 and [¹⁸F]BL09 are prepared using 100 nmol of labeling precursor and 34.6–60.2 GBq of fluorine-18 in a total volume of 100 µL, reaching molar activities of 94.2 ± 25.2 and 44.7 ± 13.9 MBq/nmol, respectively with decay-corrected yields lower than 12% (228).

This yet to be optimized labeling procedure provided the majority of CXCR4-targeted ligands within this study in decent yields and suitable molar activities. Moreover, the entire synthesis and purification process is particularly fast, yielding the desired product in less than 15 minutes.

4.3. In vitro Evaluation and Hydrophilicity

The *in vitro* binding affinity to CXCR4 of SiFA-conjugated ligands CXCR4-SiFA-01 – 07 was determined using Jurkat lymphoma cells. $\log D_{7.4}$ values were obtained after lutetium-177 complexation or fluorine-18 labeling of the [^{nat}Ga]-complexed ligands.

Affinity and hydrophilicity

Table 13 summarizes the obtained data for novel SiFA-conjugated ligands, as well as reference compounds [¹⁷⁷Lu]Pentixather, [⁶⁸Ga]Pentixafor, [¹⁸F]AIF-NOTA-Pentixather, [¹⁸F]BL08 and [¹⁸F]BL09.

Table 13: Summary of IC₅₀ [nM] and logD_{7.4} values for gallium and lutetium complexes of CXCR4-SiFA-01 – 07 as well as reference compounds [^{nat}Lu/¹⁷⁷Lu]Pentixather, [^{nat}Ga/⁶⁸Ga]Pentixafor, [^{nat}F/¹⁸F]AIF-NOTA-Pentixather, [^{nat}F/¹⁸F]BL08 and [^{nat}F/¹⁸F]BL09: IC₅₀ values were determined in competitive binding studies employing Jurkat cells (400,000 cells/tube; 8°C, 2h incubation) and the standard ligand FC-131 (10⁻⁹ M, final assay-concentration). Data are expressed as mean ± SD; IC₅₀ data were determined as triplicates or quadruplicates (*); logD_{7.4} values were determined as octuplicates, sextuplicates (**) or septuplicates (***); (I): data adapted from literature (137), (II): (143), (III): (228).

CXCR4-SiFA-	[M ³⁺]	IC ₅₀ [nM] (n = 3)	logD _{7.4} (n = 8)
01	Ga	180 ± 27 (*)	0.66 ± 0.01
	Lu	206 ± 14	1.41 ± 0.04
02	Ga	28.5 ± 2.0	0.39 ± 0.07
	Lu	39.1 ± 5.1 (*)	0.80 ± 0.04
03	Ga	23.7 ± 2.1	-1.65 ± 0.09
	Lu	50.2 ± 5.7	n.d.
04	Ga	102 ± 31	-1.92 ± 0.06
	Lu	93.4 ± 10.2	-1.71 ± 0.09
05	Ga	36.5 ± 4.5	-1.85 ± 0.07 (***)
	Lu	45.8 ± 17.4	-1.73 ± 0.05 (**)
06	Ga	5.52 ± 0.71	-1.05 ± 0.06
	Lu	8.29 ± 3.11	-0.85 ± 0.04 (**)
07	Ga	6.23 ± 1.57	-1.95 ± 0.05
	Lu	6.05 ± 1.17 (*)	-2.23 ± 0.11 (***)
[¹⁷⁷ Lu]Pentixather	Lu	19.5 ± 2.8	-1.76 ± 0.03
[⁶⁸ Ga]Pentixafor (I)	Ga	24.8 ± 2.5	-2.90 ± 0.08
NOTA-Pentixather (II)	AIF	17.9 ± 0.2	-1.4
BL08 (III)	/	11.6 ± 7.0	-3.45 ± 0.33
BL09 (III)	/	13.4 ± 2.3	-2.49 ± 0.19

The first ligand in this series, CXCR4-SiFA-01 was prepared in an early state of this work. D-Dap was used as a trifunctional unit that positions the SiFA-BA close to the peptide backbone. However, judging from the poor binding affinity of both the gallium and lutetium

complexes (>150 nM), repulsion between the sterically demanding SiFA-BA and the CXCR4 binding cavity is assumed to be significant. A similar effect was observed during the evaluation of 1st-generation technetium labeling precursors. When another sterically demanding moiety, D-phenylalanine, was attached to the *Abz-a-r* linker unit, CXCR4 affinity of the corresponding mas₃-conjugated ligand was found to be in the micromolar range. The corresponding analogs bearing less sterically demanding moieties showed >500-fold higher affinities (III. 2.3.1.).

The structure of CXCR4-SiFA-01 was then modified by the insertion of a D-histidine prior to the branched D-dap, on the one side with the intent to gain receptor affinity by removing SiFA-BA further from the *CPCR4* peptide scaffold. On the other side to strengthen the interaction with the binding cavity due to a positive reciprocation of histidine with acidic moieties of the receptor. This proposition was successfully implemented as both the gallium and lutetium complexes of CXCR4-SiFA-02 experience a more than 6- and 5-fold increased CXCR4 affinity, respectively, compared to CXCR4-SiFA-01. With an IC₅₀ of 28.5 ± 2.0 nM, [^{nat}Ga]CXCR4-SiFA-02 exhibits a comparable CXCR4 affinity to [^{nat}Ga]Pentixafor. However, further assessment of this compound was found to be dispensable as the SiFA-BA moiety conveys a high degree of lipophilicity which is not compensated by the terminal DOTA-GA chelator, resulting in a logD_{7.4} value above zero. CXCR4-SiFA-01 and -02 were prepared simultaneously with the 1st generation of technetium labeling precursors. Both compounds reinforced the search for an optimized tracer backbone that would allow the insertion of sterically demanding functionalities. Once again, such a tracer backbone was found in the structure *CPCR4-Abz-a-r-dap* (2nd generation compounds).

Following the poor hydrophilicities of CXCR4-SiFA-01 and -02, it was hypothesized that suitable hydrophilicity could be reached if further modifications were made. CXCR4-SiFA-03 bears the *CPCR4-Abz-a-r-dap* tracer backbone that was thought to provide high CXCR4 affinity and more flexibility towards attachment of moieties at the *N*-terminal site of the peptide. Hence, two DOTA-GA chelators were attached to the peptide terminus. Compared to CXCR4-SiFA-02, the resulting compound exhibits a slightly more affine gallium complex (23.7 ± 2.1 nM vs. 28.5 ± 2.0 nM) and a less affine lutetium complex (50.2 ± 5.7 nM vs. 39.1 ± 5.1 nM). As expected, hydrophilicity is substantially improved, reaching a logD_{7.4} of -1.65 ± 0.09. However, two problems concerning this compound are apparent. First, radiolabeling with gallium-68 or lutetium-177 results in two distinct labeling products, which potentially exhibit different pharmacokinetic properties.

Second, low fluorine-18-labeling yields of 12% (d.c.) are limiting further evaluation of this compound.

Consequently, one of the DOTA-GA chelators was replaced by a small and hydrophilic synthon, the urea-bridged *eue* (analogous to CXCR4-Tc-14). The SiFA-BA moiety was sandwiched between both modifiers, DOTA-GA and *eue*, to elevate hydrophilicity by creation of a hydrophilic framework. High hydrophilicity was reached, outmatching [^{nat}Ga]CXCR4-SiFA-03 and [¹⁷⁷Lu]Pentixather. Unfortunately, both metal complexes of CXCR4-SiFA-04 exhibit IC₅₀ values near 100 nM, possibly due to repulsion of the DOTA-GA carboxylates with the CXCR4 binding pocket. While the chelator was attached at the *N*-terminal site of the peptide within CXCR4-SiFA-03, a position in proximity to the *CPCR4* peptide scaffold was chosen for CXCR4-SiFA-04.

Based on this assumption, another ligand was prepared, carrying an *Ahx* spacer unit (3rd generation compound analogous to CXCR4-Tc-15). This modification offers more distance between the charged and sterically demanding moieties and the *CPCR4* peptide scaffold anchored in the binding pocket. CXCR4 affinity of the resulting ligand CXCR4-SiFA-05 is consequently improved, however not exceeding IC₅₀ values of CXCR4-SiFA-02. This outcome led to the conclusion that the identity of the hydrophilic modifiers and the herewith connected decreased net charge of the peptides plays an additional role concerning the ligand's CXCR4 affinity. Considerably improved receptor affinities should therefore be provided by peptides with a higher net charge and sterically demanding moieties further removed from the *CPCR4* peptide scaffold.

Another SiFA synthon, the SiFA*lin* building block, carries a permanent positive charge due to a quarternary amine and therefore conveys a higher hydrophilicity and net charge compared to SiFA-BA. The first CXCR4 ligand carrying a SiFA*lin* moiety, CXCR4-SiFA-06, was based on the structure of CXCR4-SiFA-05, bearing an *Ahx* spacer unit between peptide scaffold and SiFA synthon. The net charge of the resulting compound was herewith increased, and the CXCR4 affinity therefore improved to 5.52 ± 0.71 nM ([^{nat}Ga]) and 8.29 ± 3.11 nM ([^{nat}Lu]). Compared to [^{nat}Ga]Pentixafor, a more than 5-fold increased CXCR4 affinity is hence observed, outperforming [^{nat}F]AIF-NOTA-Pentixather (17.9 ± 0.2 nM) and both BL08 and BL09 (11.6 ± 7.0 nM, 13.4 ± 2.3 nM, respectively). The hydrophilicity of CXCR4-SiFA-06, however, is considerably lower compared to the reference compounds. This is not surprising given the fact that, compared to CXCR4-SiFA-05, no additional hydrophilic modifiers such as *eue* were attached.

Predicated on the results obtained by the use of a glycosylated SiFA_{lin}-conjugated TATE derivative and our own experience in the synthesis of glycosylated mas₃-conjugated technetium-99m SPECT tracers, another derivative, CXCR4-SiFA-07, was prepared (229). No additional charge was introduced but a lactosylated D-homocysteine moiety that integrates high hydrophilicity. Furthermore, DOTA-GA was exchanged by DOTA, eliminating another negatively charged carboxylate from the peptide. Compared to CXCR4-SiFA-06, CXCR4 affinity was retained, yielding a compound with an approximate affinity of 6 nM and thus a manyfold increased receptor affinity compared to the reference ligands. Moreover, the derivatization with a lactosyl moiety afforded a significant increase in hydrophilicity, reaching a logD_{7.4} value of -1.95 ± 0.05 for the gallium complex and -2.23 ± 0.11 for the lutetium complex. Both complexes are therefore more hydrophilic than [¹⁸F]AIF-NOTA-Pentixather and [¹⁷⁷Lu]Pentixather and only slightly more lipophilic compared to [¹⁸F]BL09.

Internalization

The internalization of SiFA-conjugated ligands was assessed. As depicted above, CXCR4-SiFA-01 was not tested in an internalization experiment due to its low CXCR4 affinity and molar activity just like CXCR4-SiFA-03, which did not exhibit radiochemical yields high enough for valid quantification in such experiments. The remainder of SiFA-conjugated ligands were investigated as their [^{nat}Ga]-complexes. Internalization values are corresponded to the internalized activity of the internal standard ¹²⁵I-FC-131. Figure 48 visualizes the obtained data.

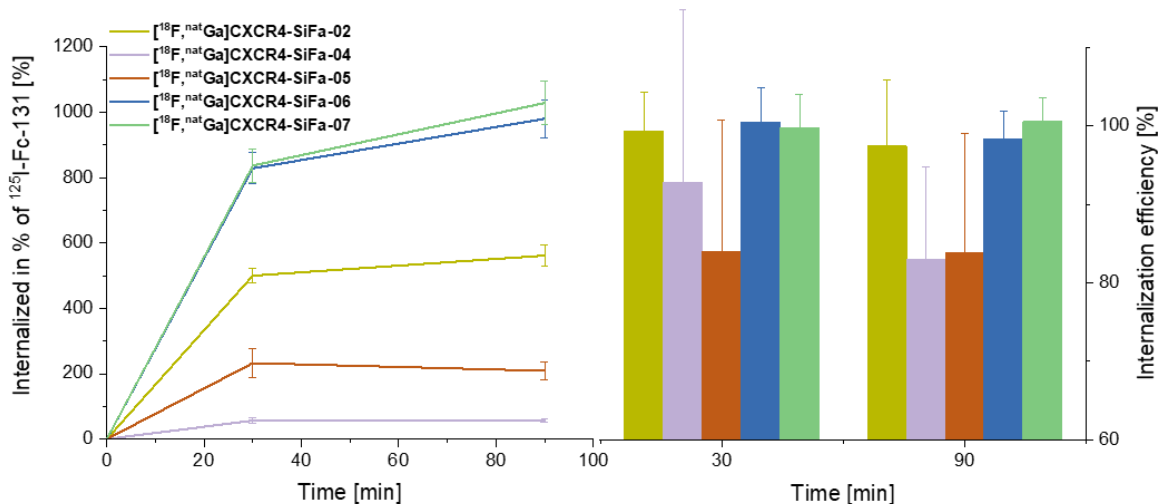


Figure 48: Dual tracer internalization of novel ligands $[^{18}\text{F},^{\text{nat}}\text{Ga}]\text{CXCR4-SiFA-02}$ and 04 – 07 and the reference compound $^{125}\text{I-FC-131}$ (assay-concentration for each peptide 0.2 nM) into Chem-1 cells (100,000 cells per well; 37°C). Data are expressed as mean \pm SD; internalization at every time point was determined in triplicate and corrected for unspecific internalization; line diagram: Internalized activity of the novel ligand in relation to the internalized activity of internal standard $^{125}\text{I-FC-131}$; bar diagram: Percentage of internalized activity of the novel ligand in relation to the total cell-bound activity.

$[^{18}\text{F},^{\text{nat}}\text{Ga}]\text{CXCR4-SiFA-02}$ exhibits high internalization into Chem-1 cells, reaching a maximum of $562 \pm 33\%$ in relation to the internal standard. Moreover, up to 99.4% of its cell-bound activity is internalized, which lies beyond what was observed for the supposedly agonistic ligand $[^{177}\text{Lu}]\text{CXCR4-DOTA-04}$ (chapter III. 3.3.). Considering the substantially lower CXCR4 affinity of CXCR4-SiFA-02 compared to $[^{177}\text{Lu}]\text{CXCR4-DOTA-04}$ (28.5 ± 2.0 nM vs. 3.67 ± 1.31 nM), the observation that internalization is detached from receptor affinity, is herewith restated. Both *eue*-conjugated compounds $[^{18}\text{F},^{\text{nat}}\text{Ga}]\text{CXCR4-SiFA-04}$ and the *Ahx*-extended $[^{18}\text{F},^{\text{nat}}\text{Ga}]\text{CXCR4-SiFA-05}$ show considerably lower internalization rates and also reduced internalization efficiencies compared to $[^{18}\text{F},^{\text{nat}}\text{Ga}]\text{CXCR4-SiFA-02}$. This finding is in accordance with the assumption that the trigger for ligand internalization is confined from ligand binding. $[^{18}\text{F},^{\text{nat}}\text{Ga}]\text{CXCR4-SiFA-04}$ and -05 both carry a negative net charge, centered at the *N*-terminal site of the peptide due to the *eue* moiety. Even though the *CPCR4* peptide scaffold is anchored in the CXCR4 binding pocket, repulsion of the ligand's *N*-terminal site may prohibit effective internalization of the receptor/ligand complex. This effect is less pronounced for $[^{18}\text{F},^{\text{nat}}\text{Ga}]\text{CXCR4-SiFA-05}$ which carries these negative charges further away from the peptide scaffold.

Both SiFAlin-conjugated compounds, [^{18}F , $^{\text{nat}}\text{Ga}$]CXCR4-SiFA-06 and -07, bear positive net charges. Hence, both ligands display increased internalization rates into Chem-1 cells reaching maxima of $980 \pm 59\%$ and $1029 \pm 67\%$, respectively, alongside with unchallenged internalization efficiencies of practically 100% at any time. Compared to the most efficiently internalizing ligands within this work, [$^{99\text{m}}\text{Tc}$]CXCR4-Tc-13 and [^{177}Lu]CXCR4-DOTA-04, a more than 30% higher internalization is observed for both SiFAlin-conjugated compounds. Again, CXCR4 affinity alone cannot be the determining factor for these values but rather a connection of high receptor affinity, elevated net charge and increased distance between sterically demanding moieties and the *CPCR4* peptide scaffold.

Summary

Figure 49 gives an overview of the obtained data in IC_{50} , $\log D_{7.4}$ and internalization experiments.

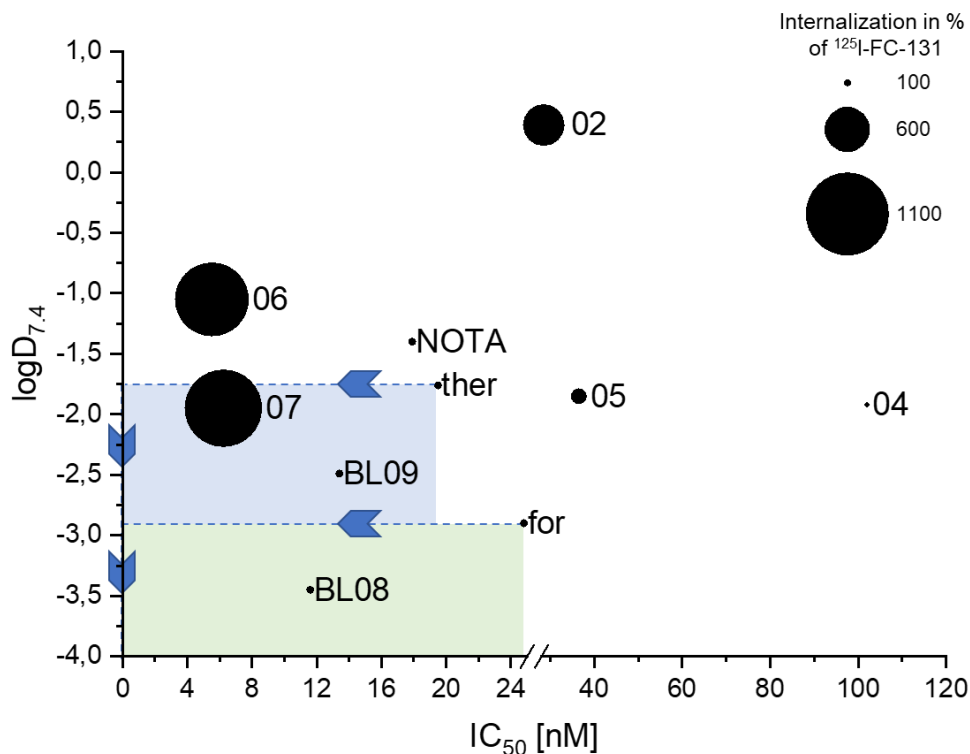


Figure 49: Summary of $\log D_{7.4}$ (y-axis), IC_{50} (x-axis) and maximum internalization values (dot size) for $[^{18}F,^{nat}Ga]CXCR4$ -SiFA-02 and -04 – 07 as well as $[^{177}Lu]$ Pentixather, $[^{68}Ga]$ Pentixafor ($\log D_{7.4}$ and IC_{50} only), $[^{18}F]$ AIF-NOTA-Pentixather ($\log D_{7.4}$ and IC_{50} only), $[^{18}F]$ BL08 ($\log D_{7.4}$ and IC_{50} only) and $[^{18}F]$ BL09 ($\log D_{7.4}$ and IC_{50} only): Numbers next to dots represent the respective ligand within this series, the letter p represents $[^{177}Lu]$ Pentixather, for represents $[^{68}Ga]$ Pentixafor and NOTA represents $[^{18}F]$ AIF-NOTA-Pentixather; dots in the light blue area suggest compounds that are more affine and hydrophilic than $[^{177}Lu]$ Pentixather and dots in the light green area suggest compounds that are more affine and hydrophilic than $[^{68}Ga]$ Pentixafor.

In terms of their CXCR4 affinity, $[^{18}F,^{nat}Ga]CXCR4$ -SiFA-06 and -07 are unchallenged compared to the remainder of compounds within this series and the selected reference compounds. $[^{18}F,^{nat}Ga]CXCR4$ -SiFA-07, however not reaching $[^{68}Ga]$ Pentixafor, $[^{18}F]$ BL08 and $[^{18}F]$ BL09, exhibits the highest hydrophilicity within this series and a substantially improved $\log D_{7.4}$ value compared to $[^{18}F]$ AIF-NOTA-Pentixather and $[^{177}Lu]$ Pentixather. A first proof-of-concept study in tumor-bearing mice was therefore ventured with $[^{18}F,^{nat}Ga]CXCR4$ -SiFA-07.

4.4. In vivo Biodistribution

The biodistribution experiments within this work showed that compounds bearing the *CPCR4-Abz-a-r-dap* tracer backbone exhibit elevated uptake in CXCR4⁺ organs lung, liver and spleen. The extent to which a radioligand is trapped in such organs is found to relate to its internalization. The organs act as a reservoir for radioligand and therefore delay full-body clearance. Moreover, due to the greater size of these organs compared to the tumor, a significant amount of radioligand can be filtered from circulation and tumor uptake correspondently decreased.

[¹⁸F,^{nat}Ga]CXCR4-SiFA-07 was tested in an *in vivo* biodistribution study in Jurkat tumor-bearing mice. The data obtained after 1h circulation are visualized in Figure 50.

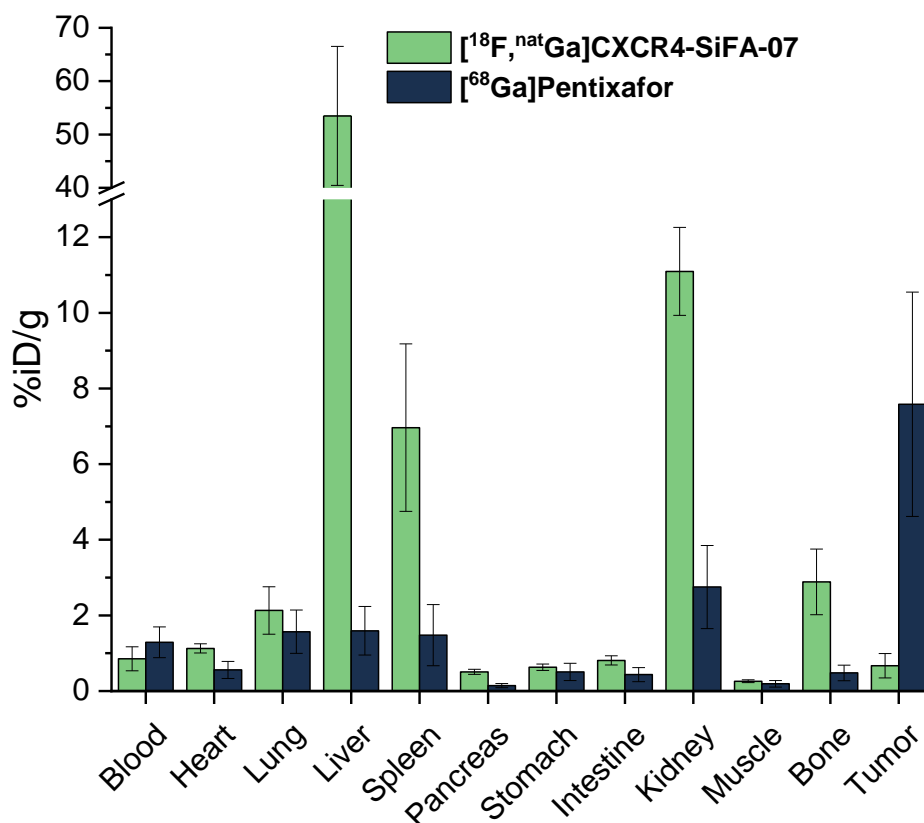


Figure 50: Biodistribution profiles of [¹⁸F,^{nat}Ga]CXCR4-SiFA-07 and [⁶⁸Ga]Pentixafor 1h post injection in Jurkat tumor-bearing female CB-17 SCID mice; data are expressed as %iD/g and are means ± SD of 5 animals per ligand.

[¹⁸F,^{nat}Ga]CXCR4-SiFA-07 is rapidly cleared from blood (0.85 ± 0.32 %iD/g) and CXCR4⁻ tissues such as pancreas (0.51 ± 0.07 %iD/g) and muscle (0.26 ± 0.04 %iD/g), giving hint to suitable hydrophilicity, especially as [⁶⁸Ga]Pentixafor exhibits a 1.5-fold higher value for blood. Moreover, no elevated uptake in stomach (0.63 ± 0.08 %iD/g) and intestine

(0.81 ± 0.12 %iD/g) can be attested for the SiFA*lin*-conjugated ligand, the latter advocating the absence of hepatobiliary excretion. As expected, kidney activity levels (11.1 ± 1.2 %iD/g) are considerably elevated compared to [^{68}Ga]Pentixafor. This finding is in accordance with biodistribution studies for the theranostic ligands and technetium-99m-labeled tracers and attributable to an increased net charge of the peptides. Elevated uptake in bone (2.89 ± 0.87 %iD/g) might either be another sign for significant mCXCR4 affinity or result of slow defluorination *in vivo*.

Extraordinarily high uptake in CXCR4⁺ organs spleen (6.96 ± 2.21 %iD/g) and liver (53.5 ± 13.0 %iD/g) is observed. These values outmatch the pronounced organ uptake of [^{177}Lu]CXCR4-DOTA-04 1.9-fold and 2.8-fold, respectively, reassuring the coherence of CXCR4⁺ organ uptake with the determined internalization. As observed for theranostic ligands above, lower uptake in tumor correlates with a higher amount of ligand trapped in CXCR4⁺ organs. In the case of [$^{18}\text{F},^{nat}\text{Ga}$]CXCR4-SiFA-07, no elevated tumor uptake (0.67 ± 0.32 %iD/g) compared to blood level is observed. Given the low injected amount of peptide and the unprecedented fraction of trapped radioligand, low tumor uptake is assumed to be a consequence of deficient amounts of radioligand in circulation.

Afterwards, two additional biodistribution studies were undertaken to review this proposition by co-injecting one and two nanomole of the cold substance, respectively. The aim of this approach was the partial and complete blockage of murine CXCR4 receptors by the cold substance.

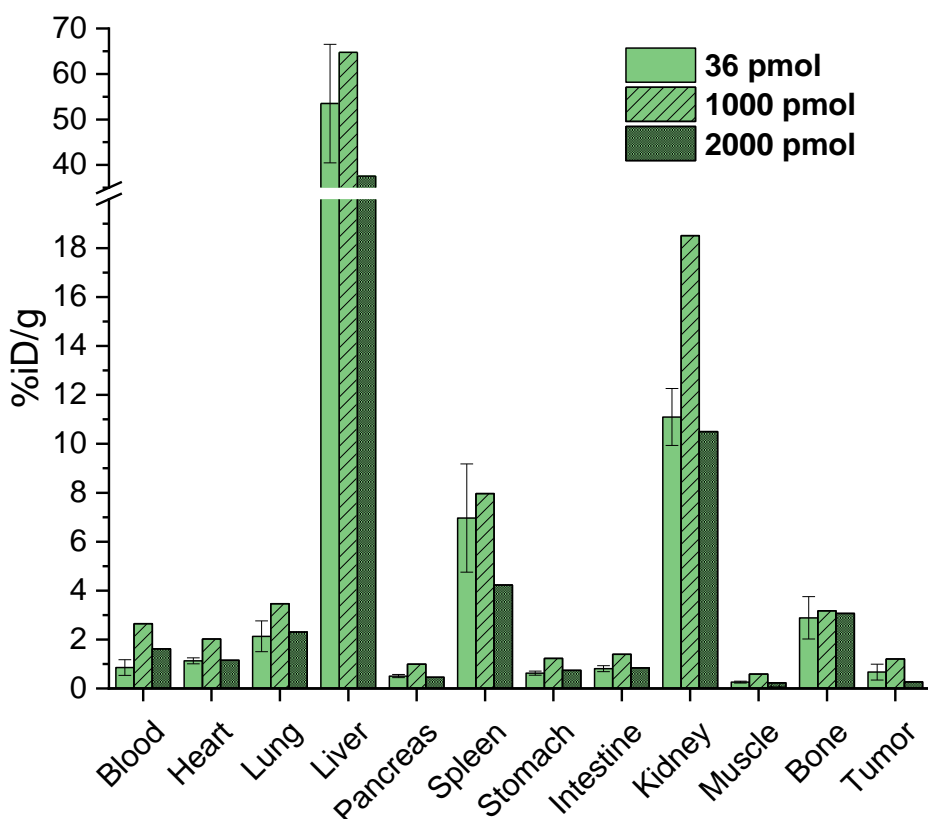


Figure 51: Biodistribution profile of $[^{18}\text{F}, \text{natGa}]$ CXCR4-SiFA-07 1h post injection in Jurkat tumor-bearing female CB-17 SCID mice; different amounts of radioligand were applied: 36 pmol, 1,000 pmol and 2,000 pmol; data are expressed as %ID/g values and are means \pm SD of 5 animals for the experiment with 36 pmol; 1 animal each was used for both other experiments.

In order to spare animal lives, additional studies were conducted using only one mouse, respectively. Data obtained in these experiments is therefore not representative. However, a certain trend can be presumed. By co-injection of 1,000 pmol cold substance, elevated levels of circulating radioligand are observed. Blood activity level is raised by 310%, leading to increased uptake in CXCR4⁻ tissues such as pancreas (196%) and muscle (226%). This extended blood circulation is particularly underrepresented in CXCR4⁺ organs liver (121%) and spleen (114%) suggesting incipient receptor saturation. With more ligand circulating, a nearly 2-fold tumor uptake (180%) compared to the un-supplemented injection is observable.

When 2,000 pmol of cold substance are co-injected, significant receptor saturation is reached. Compared to the initial biodistribution with only 36 pmol ligand, most notable changes in organ uptake are found for CXCR4⁺ organs spleen (61%) and liver (70%) and even more pronounced, the tumor (40%). These sets of data endorse the above-

described concept that uptake in tumor is dependent on the availability of mCXCR4 receptors in CXCR4⁺ organs.

4.5. Conclusion

The implementation of SiFA as a tool for fast and efficient fluorine-18 labeling of CXCR4-targeted ligands, has led to a variety of challenges concerning suitable CXCR4 affinity and hydrophilicity. Direct attachment of SiFA-BA on the *Abz-a-r* linker unit led to a substantial loss in receptor affinity that was partially restored using histidine as an additional spacer. The resulting compound, CXCR4-SiFA-02, however, exhibited pronounced lipophilicity, making it unsuitable for an *in vivo* application. A more hydrophilic compound, CXCR4-SiFA-03 bearing two DOTA-GA chelators was prepared but suffered from low labeling yields. Lipophilicity was then successfully balanced by the addition of the negatively charged *eue* moiety, which again, led to loss in CXCR4 affinity that was only partially recovered by insertion of an *Ahx* spacer unit. Decreased net charge of the resulting compounds led to repulsion with the receptor. A novel approach was chosen, implementing a permanent positive charge in close proximity to the SiFA group through introduction of the *SiFAlin* moiety. The so-designed compound CXCR4-SiFA-06 exhibited high CXCR4 affinity in the low nanomolar range but hydrophilicity in need of improvement. Hence, CXCR4-SiFA-07 was prepared, comprising *SiFAlin*, a DOTA chelator and a hydrophilic lactosyl moiety.

This ligand exhibited higher CXCR4 affinity compared to any of the CXCR4-targeted literature-known fluorine-18-labeled reference compounds, paired with exceptional internalization rates and a suitable hydrophilicity. The biodistribution data of [¹⁸F,^{nat}Ga]CXCR4-SiFA-07, however, did not reflect the promising *in vitro* data. No elevated uptake in tumor was observed presumably due to substantial ligand uptake in mCXCR4 expressing organs. However, the compound exhibited rapid clearance from CXCR4⁻ tissues. If trapping in CXCR4⁺ organs could be circumvented, efficient tumor targeting might be possible, ultimately resulting in suitable tumor to organ ratios. Further assessment of the lutetium-bearing ligand might then be of interest in order to provide a true theranostic approach comprising both imaging and therapy.

Labeling of any novel ligand with fluorine-18 was complete in less than 15 minutes, resulting in decent decay-corrected yields and molar activities. As reported for the

synthesis of SiFA-conjugated rhPSMA7 or SiFA $_{lin}$ -conjugated TATE derivatives, a high practicability of this concept is given which could result in fast and efficient translation into clinics (230,231).

5. Peptide-Drug Conjugates

Chemotherapy, as laid out in the introductory text of this work, is predicated on the elevated uptake of drugs by tumor cells due to their higher demand for nutrients compared to regular cells. In the human body, however, several types of healthy cells display rapid growth and elevated nutrient uptake as well. Hence, cells in the mucous membranes of the mouth, throat, stomach and intestines can be affected by chemotherapeutics, leading to severe toxic effects. The bone marrow, kidney and liver tissue are also oftentimes damaged and patients regularly lose their body hair due to drug uptake in the hair follicles (232). The overall poor selectivity of chemotherapeutics leads to a variety of adverse effects, graded by the WHO concerning the severity from 0–4. Common side effects such as nausea, vomiting and diarrhea substantially reduce quality of life (grade 1–2) whilst even life threatening effects such as acute nephrotoxicity and long-term damage of the neural and cardiovascular systems are prevalent (grade 3–4) (233). These side effects of conventional chemotherapy call for higher selectivity of the compounds in use.

The application of targeted peptides as vector molecules for toxic payloads bears potential for an improved selectivity and therefore less severe side effects (35). Such a concept relies on affine peptides that carry their coupled toxin onto the surface of tumor cells or mediated by receptor-induced endocytosis, into the cell lumen (Figure 52, (2)–(3)). A tailormade linker between the toxin and the peptide, such as the “val-cit-PAB” sequence can be used, that is cleaved by lysosomal enzymes such as cathepsin B (Figure 52, (3)–(4)). The released toxin then diffuses into the lumen and reaches the specific organelles that are impaired (Figure 52, (5)–(6)), eventually leading to the death of the tumor cell (234).

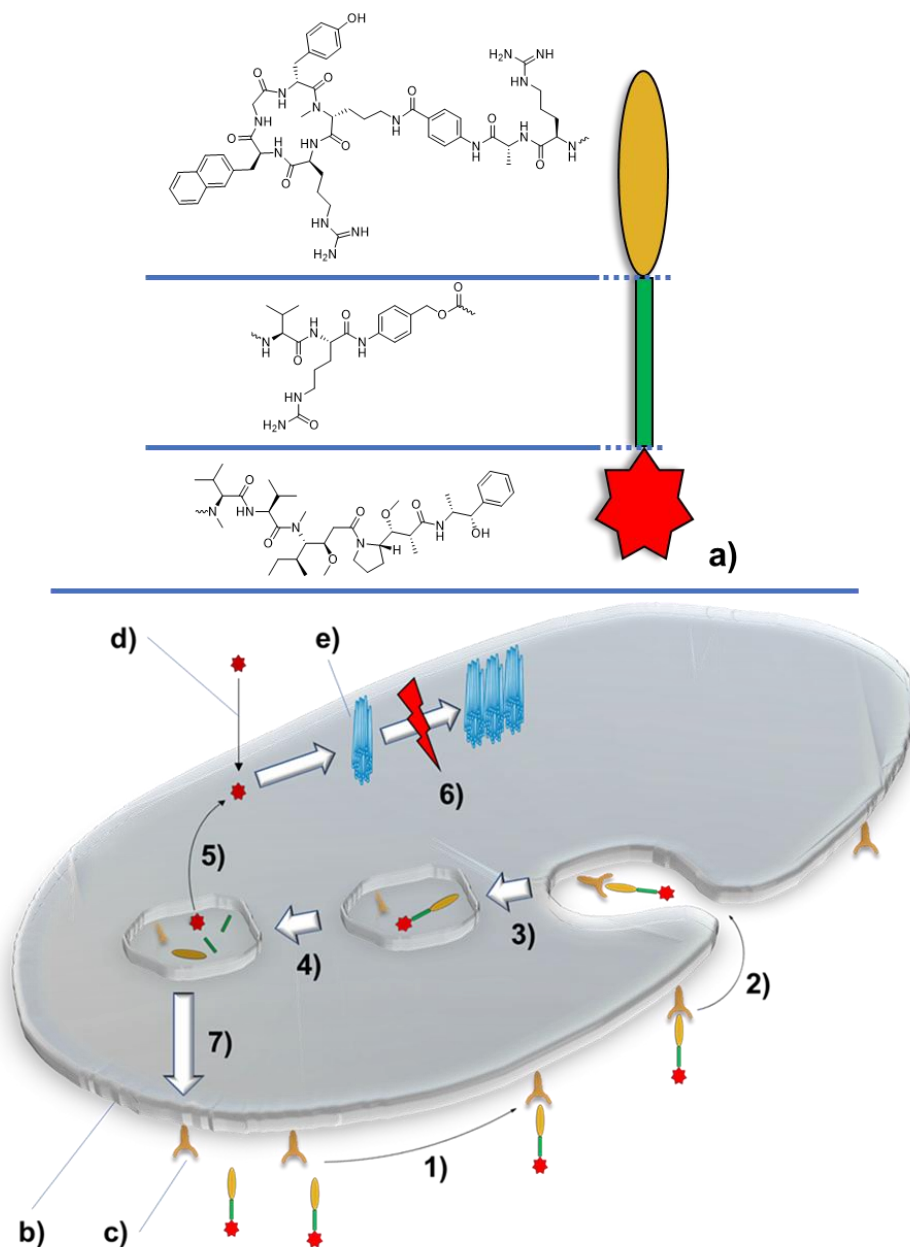


Figure 52: Concept of targeted chemotherapy as pursued within this project: a) peptide-drug conjugate consisting of the affine and internalizing transport peptide (ocher), the cleavable linker (green) and the toxin (red); b) tumor cell; c) CXCR4 receptor; d) unselective cellular uptake of toxin within conventional chemotherapy; e) microtubule; 1) specific binding of the transporter molecule onto a CXCR4 receptor at the cell surface; 2) triggered internalization of the receptor-probe complex; 3) endosomal dissociation of the receptor-probe complex; 4) cathepsin B-mediated cleavage of the linker; 5) diffusion of the released toxin into the cell lumen; 6) toxin-induced inhibition of microtubule polymerization ultimately prohibiting cell division; 7) Recycling of the CXCR4 receptor.

Numerous examples for such a vector-linked prodrug approach can be found in literature with the majority of molecules used being antibody-drug conjugates (234–236). The development of peptide-conjugated prodrugs, however, does not show equally high pace and no permission for a clinical use has been issued so far.

A variety of toxins is commercially available and chemically modified to be attachable to peptides. A class of drugs that gained exceptional attention are auristatins, which are thought to be 50–200-fold more potent compared to alkaloid drugs like Paclitaxel by binding to α -tubulin, preventing polymerization and hence, cell division (237). One monomethyl auristatin-E (MMAE) derivative, vc-PAB-MMAE is functionalized with a *val-cit-PAB* linker unit at its C-terminal site (Figure 53), facilitating specific cleavage in lysosomes by cathepsin B and therefore minimizing the amount of free toxin in the blood stream (238). Once the chemical bond following citrulline is broken, an elimination process of the *para* aminobenzyl carbamate is initiated, releasing the active toxin into the cell lumen (Figure 53).

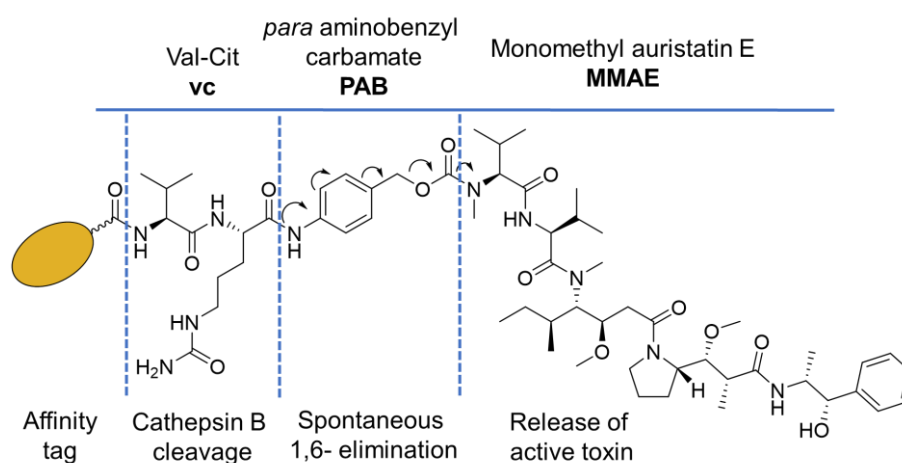


Figure 53: Structure of a peptide-vc-PAB-MMAE conjugate: Cathepsin B cleavage of the val-cit linker and subsequent spontaneous 1,6-elimination of the 4-aminobenzyl carbamate moiety facilitates the release of the active monomethyl auristatin-E toxin.

The CXCR4 targeting compounds developed within this work provide a suitable basis for the construction of such peptide-drug conjugates (PDC), as the sustainability of high receptor affinity and internalization capability upon conjugation of sterically demanding rests is a prerequisite for the successful implementation of this concept. The first three ligands in this series were prepared as a proof-of-concept, whereas CXCR4-MMAE-04 was thought to unite both PRRT and nuclear imaging with targeted chemotherapy. Figure 54 shows the chemical structures of those ligands.

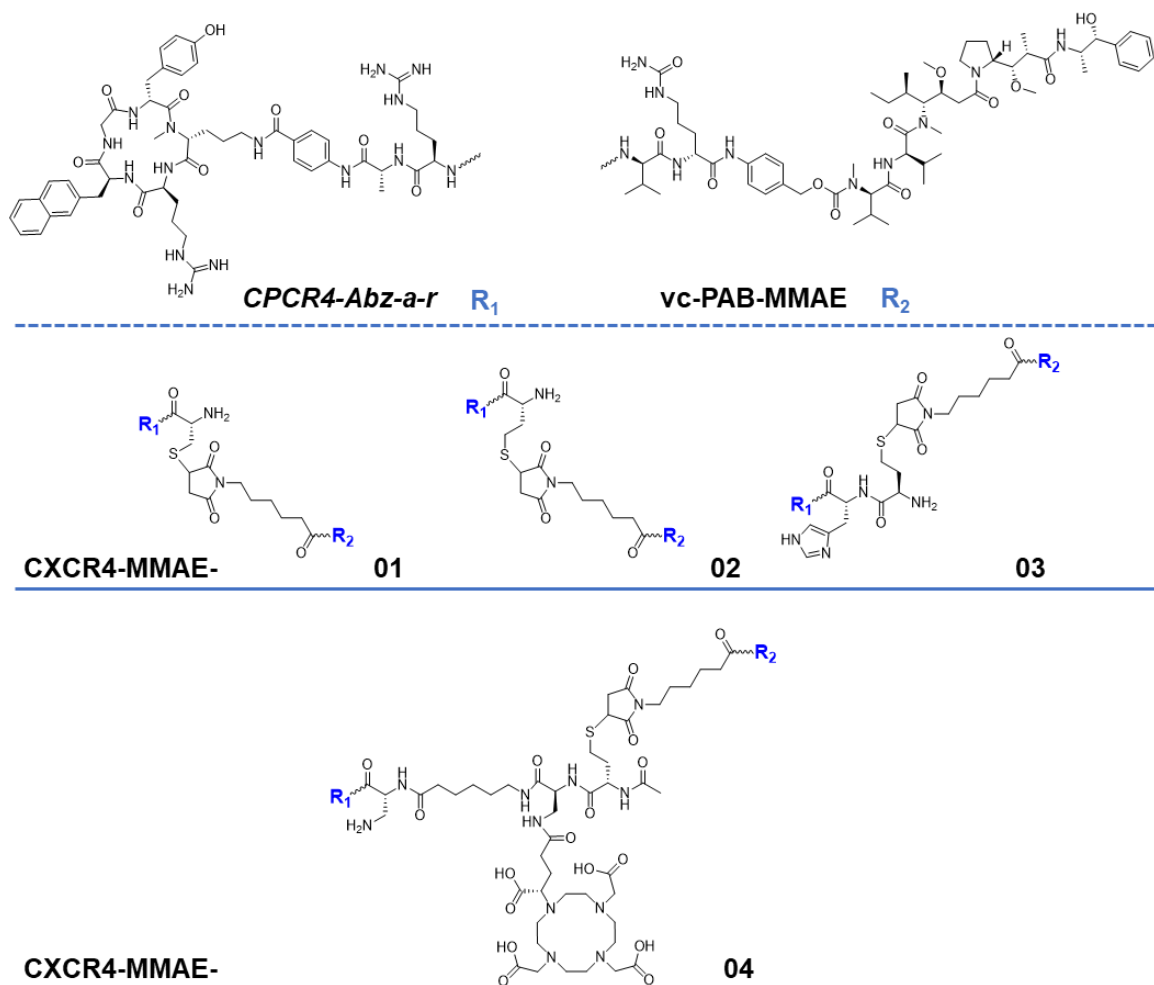


Figure 54: Summary of structures bearing the vc-PAB-MMAE moiety: CXCR4-MMAE-01 – 03 were obtained by elongation of the CPCr4-Abz-a-r tracer backbone; CXCR4-MMAE-04 was obtained by modification of the CPCr4-Abz-a-r-dap-Ahx tracer backbone.

The following chapter comprises the synthesis as well as the *in vitro* and *in vivo* evaluation of vc-PAB-MMAE-conjugated CXCR4-targeted ligands.

5.1. Synthesis

The preparation of targeted peptides prior to coupling with the toxin was based on the condensation of two separately synthesized and purified fragments. The fully de-protected and purified CPCr4 peptide scaffold was reacted with the protected linker units. The resulting conjugates were then fully de-protected and purified. The connection of the SH-bearing peptides with the maleimido-bearing vc-PAB-MMAE prodrug was then facilitated according to literature, with minor variation (239). CXCR4-MMAE-01 – 03 were hereby obtained in high yields. However, as incubation in basic medium prolonged,

advancing degradation of the compounds could be observed, thus advocating an excess maleimide in the reaction mixture alongside with truncated reaction times. A final purification by RP-HPLC yielded the desired products. During synthesis of the cysteine- and homocysteine-conjugated fragments, spontaneous elimination of Trityl protecting groups was observed, resulting in unidentified side products, and diminishing the final product yield.

In the synthesis of CXCR4-MMAE-04, an additional peptide fragment was needed, bearing the DOTA-GA chelator as well as the thiol functionality. This fragment (HO-Ahx-dap(DOTAGA(*t*Bu)₄)-HCy(Trt)-Ac) was coupled to the protected tracer backbone. Subsequent de-protection, purification and sulfhydryl-maleimido coupling in accordance with CXCR4-MMAE-01 – 03, afforded the respective ligand.

5.2. Radiosynthesis

5.2.1. Iodine-125 Labeling

As CXCR4-MMAE-01 displayed lower CXCR4 affinity compared to its analogs, labeling with Iodine-125 was not undertaken. Due to the lack of chelating moieties in the structures of CXCR4-MMAE-02 and -03, radioactive labeling had to be rendered by radio-iodination of the tyrosine residue in the *CPCR4* peptide scaffold. As it was already established in the group, the Iodogen method was used. Labeling with high yields and radiochemical purities was aggravated due to the lability of the ligands towards oxidation and the poor resolution of radio-RP-HPLC runs due to extensive formation of side products.

Table 14: Summary of data obtained from the radio-iodination of CXCR4-MMAE-02 and -03; columns comprise the used proportions of Iodogen, peptide and [¹²⁵I]NaI, as well as the obtained yields.

CXCR4-MMAE-	Iodogen eq.	Peptide eq.	[¹²⁵ I]NaI eq.	Yield in %
02	200	100	1	0
	150	75	1	25
	500	250	1	36
	300	150	1	47
03	100	50	1	0
	300	300	1	0
	300	150	1	43

According to literature, a suitable proportion between the amount of peptide, Iodogen and radio-iodine is detrimental for high radiochemical yields (240). The best results were obtained when Iodogen is used in 2-fold excess over peptide and 300-fold excess over iodine-125 (Table 14).

Extensive tailing of both compounds in preparative radio-RP-HPLC runs was partially corrected by application of a stepwise gradient. The best resolution was obtained, starting with 0% acetonitrile for two minutes to rid unreacted iodine-125 and oxidated species thereof. Subsequent increase of the acetonitrile concentration up to 35% in one minute and linear rise to 50% over the course of 15 minutes, afforded reasonable differentiation of product peaks from side products. However, repeated purification was needed to obtain [¹²⁵I]CXCR4-MMAE-02 in not more than 66% and [¹²⁵I]CXCR4-MMAE-03 in up to 81% radiochemical purity. For biodistribution experiments, acetonitrile was removed by heating of the RP-HPLC product solution in a stream of nitrogen.

5.2.2. Lutetium-177 Labeling

Labeling of DOTA-GA-conjugated CXCR4-MMAE-04 with lutetium-177 was undertaken according to a standardized labeling procedure. Determination of radiochemical conversion *via* radio-TLC measurement revealed efficient radiometal incorporation of >95% in all cases. Radiochemical purity was assessed *via* radio-RP-HPLC and confirmed

values >85%. For further experiments with the labeled substance, a fraction was taken from the reaction mixture and used without additional processing.

5.3. In vitro Evaluation and Hydrophilicity

The *in vitro* binding affinity of CXCR4-MMAE-01 – 04 was assessed using Jurkat lymphoma cells. Noteworthy, incubation of ligands was conducted at constant 8°C to avoid internalization and intracellular Cathepsin B cleavage of the PDC linker unit. logD_{7.4} values were obtained for the iodine-125 or lutetium-177 labeled substances.

Affinity and hydrophilicity

Table 15 summarizes the obtained data for the novel PDCs as well as reference ligand [¹⁷⁷Lu]Pentixather. Both logD_{7.4} values for CXCR4-MMAE-02 and -03 represent the radio-iodinated compounds.

Table 15: Summary of IC₅₀ [nM] and logD_{7.4} values for CXCR4-MMAE-01 – 03 as well as [^{nat}Lu/¹⁷⁷Lu]CXCR4-MMAE-04 and reference compound [^{nat}Lu/¹⁷⁷Lu]Pentixather: IC₅₀ values were determined in competitive binding studies employing Jurkat cells (400,000 cells/tube; 8°C, 2h incubation) and the standard ligand FC-131 (10⁻⁹ M, final assay-concentration). Data are expressed as mean ± SD; IC₅₀ data were determined as triplicates; logD_{7.4} values were determined as octuplicates, pentuplicates () or sextuplicates (**).*

CXCR4-MMAE-	[M ³⁺]	IC ₅₀ [nM] (n = 3)	logD _{7.4} (n = 8)
01	/	99.8 ± 7.6	n.d.
02	/	42.6 ± 8.3	1.11 ± 0.08 (*)
03	/	43.9 ± 6.2	0.80 ± 0.12 (**)
04	Lu	113 ± 20	-1.04 ± 0.07
[¹⁷⁷ Lu]Pentixather	Lu	19.5 ± 2.8	-1.76 ± 0.03

Compounds CXCR4-MMAE-01 and -02 were prepared simultaneously to 1st generation technetium-99m labeling precursors (chapter II. 2.3.1.) In this project, elongation of the peptide linker unit with sterically demanding amino acid moieties such as phenylalanine resulted in substantially decreased CXCR4 affinities, represented by IC₅₀ values in the micromolar range. Hence, decent receptor affinities of CXCR4-MMAE-01 and -02 were surprising, given the fact that the attached toxin is a sterically demanding moiety, outweighing the conjugated peptides. Two features of these ligands were identified to be responsible for this outcome: first, both ligands carry a vacant amino terminus which is

providing a positive charge interaction with the binding cavity. Second, high distance between the *CPCR4* peptide scaffold and the sterically demanding toxin is provided by the side-arm conjugation and more so by the hexanoic acid spacer between maleimide and the val-cit linker unit (Figure 54). Both positive features can be rediscovered in the structures of 3rd generation ligands within this work, artificially introduced using the positively charged D-dap and the *Ahx* spacer.

When histidine is introduced to the linker unit of CXCR4-MMAE-03, no additionally elevated CXCR4 affinity can be noted compared to CXCR4-MMAE-02 (IC_{50} : 43.9 ± 6.2 nM vs. 42.6 ± 8.3 nM, respectively). This outcome may seem contrary to what was observed in the synthesis of 1st generation technetium-99m labeling precursors, however, a positive charge at the location of histidine was already provided by the vacant amino terminus of CXCR4-MMAE-02 and no beneficial impact is therefore observable. A similar result is obtained for the 3rd generation ligand CXCR4-MMAE-04 (113 ± 20 nM). In this case, a decreased CXCR4 affinity compared to its analogs is displayed. Two distinct reasons could be accountable for this outcome. First, the final product of this optimization process exhibits a molar mass of more than 3000 g/mol and a multiplicity of axes of rotation. With this size, formation of secondary structures and an influence on the availability of binding sites cannot be neglected. Second, CXCR4-MMAE-04 is the only ligand within this series to display a negatively charged functional moiety, the DOTA-GA chelator. Decrease of peptide net charge proved to be detrimental for the CXCR4 affinity even when the negatively charged moiety was located at a distance from the peptide scaffold (analogous to CXCR4-SiFA-04 and -05).

$[^{125}I]$ CXCR4-MMAE-02 and -03 display low hydrophilicities above zero. $[^{177}Lu]$ CXCR4-MMAE-04 exhibits a substantially improved hydrophilicity with a $\log D_{7.4}$ value of -1.04 ± 0.07 , due to the influence of the DOTA-GA chelator and the radiometal complex. However, further experimental assessment of this compound was not undertaken due to its relatively low CXCR4 affinity.

Internalization

The internalization of $[^{125}I]$ CXCR4-MMAE-02 and -03 into Chem-1 cells was assessed and compared to data obtained for $[^{177}Lu]$ Pentixather. This time, no internal standard could be used as no differentiation in the measurement of radiation could be made. Figure 55 comprises the fraction of internalized ligand in relation to the total applied activity.

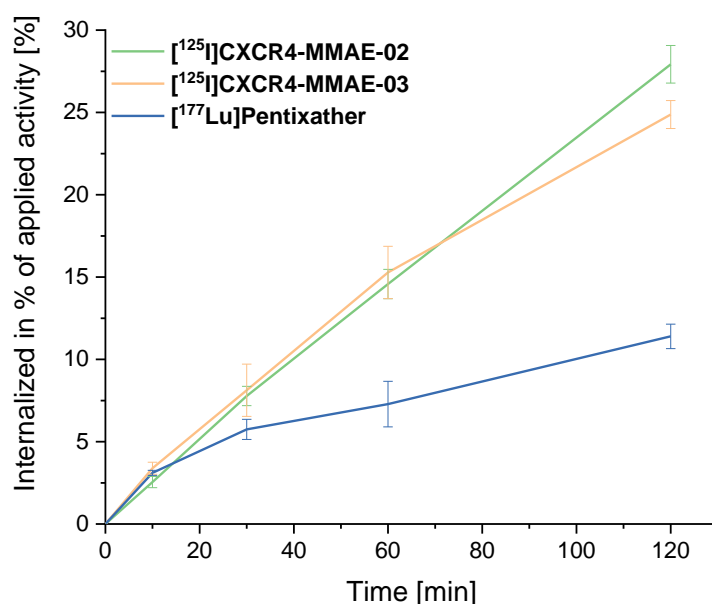


Figure 55: Internalization of novel ligands [¹²⁵I]CXCR4-MMAE-02 and -03 as well as [¹⁷⁷Lu]Pentixather (assay-concentration for each peptide 0.2 nM) into Chem-1 cells (100,000 cells per well; 37°C). Data are expressed as mean ± SD; internalization at every time point was determined in triplicate and corrected for unspecific internalization; the diagram depicts the internalized activity of a ligand in relation to the total applied activity.

In the case of the present concept, internalization of the PDC is essential for their therapeutic efficacy, as cleavage of the val-cit linker and concomitant release of the cytotoxin is limited to the proteolytic activity of intracellular Cathepsin B (238). [¹²⁵I]CXCR4-MMAE-02 and -03 exhibit comparable internalization rates. Two hours after incubation, $27.9 \pm 1.1\%$ of [¹²⁵I]CXCR4-MMAE-02 and $24.9 \pm 0.9\%$ of [¹²⁵I]CXCR4-MMAE-03 are internalized into the cells, slightly favoring the former ligand. Both compounds display a linear increase in internalized activity, suggesting a further growth beyond the 2h time point. Contrary to that, [¹⁷⁷Lu]Pentixather shows a virtually flatter curve, reaching less than half the internalized activity after 2h compared to the PDCs. These data reinforce the underlying concept that the developed ligands display efficient internalization into cancer cells despite carrying the sterically demanding toxin. Further assessment of their cytotoxic properties was therefore feasible.

5.4. Cytotoxic Effect

Evaluation of the cytotoxic efficacy was undertaken in collaboration with the group of Prof. Dr. med. Ulrich Keller, at this time leading the *Myc associated cancer biology* research at

the *Klinikum Rechts der Isar (TUM)* in Munich. The group received CXCR4-MMAE-02 for an analysis of the compound's cytotoxic capability *in vitro*.

Based on FACS quantification of their CXCR4 expression (Supplementary 6), two cell lines were selected for the respective experiments. The B-cell lymphoma cell line U2932 and the higher CXCR4 expressing lymphoblast-like Raji cell line. Both cell lines were incubated with the PDC for 24, 48, 72 and 96 hours in varying concentrations of 0 (Blank), 10, 20, 40 and 100 nM. The cell viability was then assessed using propidium iodide as a marker for deceased cells in a flow cytometry experiment (Figure 56).

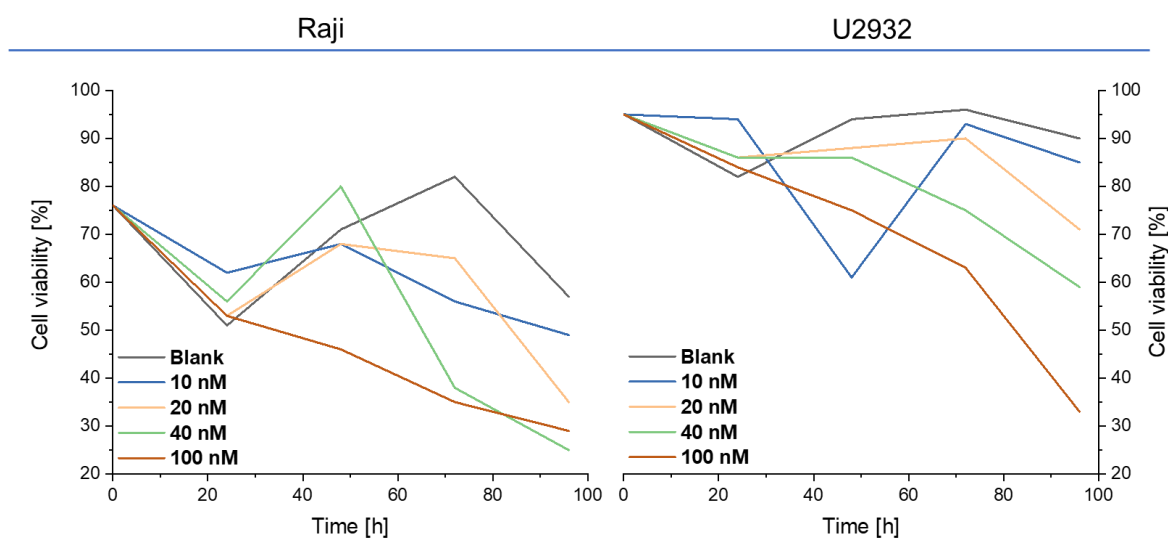


Figure 56: Flow cytometry analysis of cell viabilities using Raji (left side) and U2932 (right side) cells: the cells were incubated for 0, 24, 48, 72 and 96h with 0 (Blank), 10, 20, 40 and 100 nM of CXCR4-MMAE-02 prior to staining with propidium iodide and flow cytometry analysis; the number of vital cells related to the total number of cells represents the cell viability.

Experiments with both cell lines show decreased cell viabilities for cells incubated with increasing concentrations of PDC. Furthermore, a time-dependent effect can be observed as cell viabilities generally drop with longer incubation times. In other words, cellular death induced by incubation with CXCR4-MMAE-02 is in accordance with the amount of PDC used and the incubation period. Deviating data points can be attributed to the low sample size and therefore experimental failure. Figure 57 below visualizes the amount of deceased cancer cells upon incubation with the PDC.

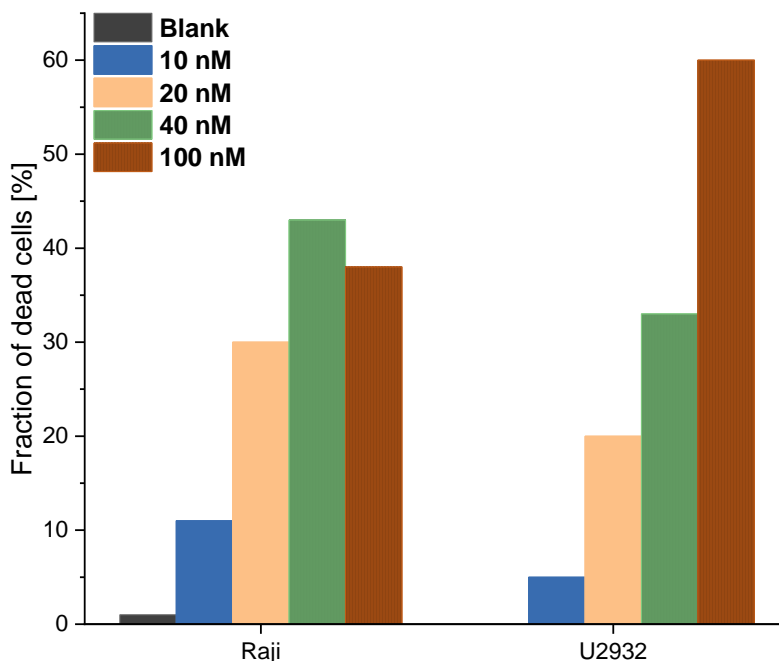


Figure 57: Flow cytometry analysis of cell viabilities using Raji and U2932 cells: the cells were incubated for 96h with 0 (Blank), 10, 20, 40 and 100 nM of CXCR4-MMAE-02 prior to staining with propidium iodide and flow cytometry analysis of dead cells.

For concentrations of 10, 20 and 40 nM, a considerably higher fraction of dead Raji cells compared to the U2932 cells can be detected. This finding is in accordance with the higher CXCR4 expression of Raji cells and the supposedly more efficient PDC uptake compared to the U2932 cells. Again, deviating outcome for the 100 nM data point might be caused by the small sample size.

A cell cycle profiling experiment of U2932 cells after 72h incubation with varying concentrations of CXCR4-MMAE-02 was performed. For that purpose, cells were fixed, permeabilized and treated with propidium iodide. The number of cells in the G0/G1-, S- and G2/M-phase was then measured with regards to the amount of PDC used.

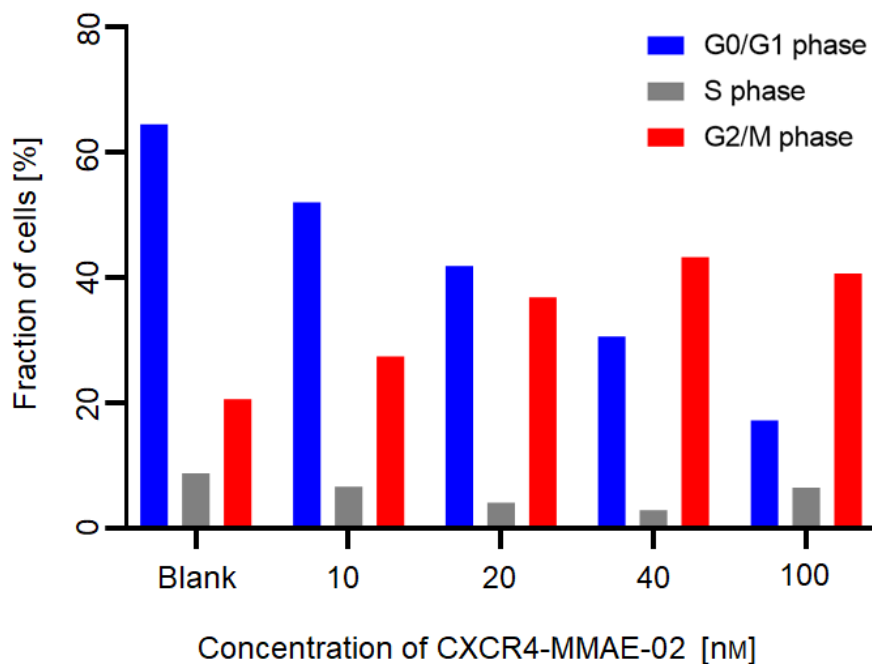


Figure 58: Cell cycle profiling experiments using U2932 cells: the cells were incubated for 72h with 0 (Blank), 10, 20, 40 and 100 nM of CXCR4-MMAE-02, fixed, permeabilized and stained with propidium iodide; the fraction of cells in the G0/G1, S or G2/M phase was determined.

Figure 58 shows a higher number of cells stuck in the G2/M-phase (Mitotic/cell dividing phase) by incubation with increasing amounts of PDC. This data suggests that MMAE is released inside the cells and prohibiting microtubule polymerization, which leads to an arrest of cells prior to their replication. This induced cell cycle arrest might then result in the activation of checkpoint sentinels such as kinases which operate the apoptosis of cancer cells.

5.5. In vivo Biodistribution

Based on the promising CXCR4 affinity of CXCR4-MMAE-02, a biodistribution of the iodine-125 labeled compound in Jurkat xenograft-bearing mice was ventured. Organs affiliated with the expression of mCXCR4, namely lung, liver and spleen will be titled as CXCR4⁺ organs, whereas CXCR4⁻ will be used for organs, which are not known to express the receptor. Figure 59 summarizes the obtained data in comparison with the biodistribution of [¹⁷⁷Lu]Pentixather.

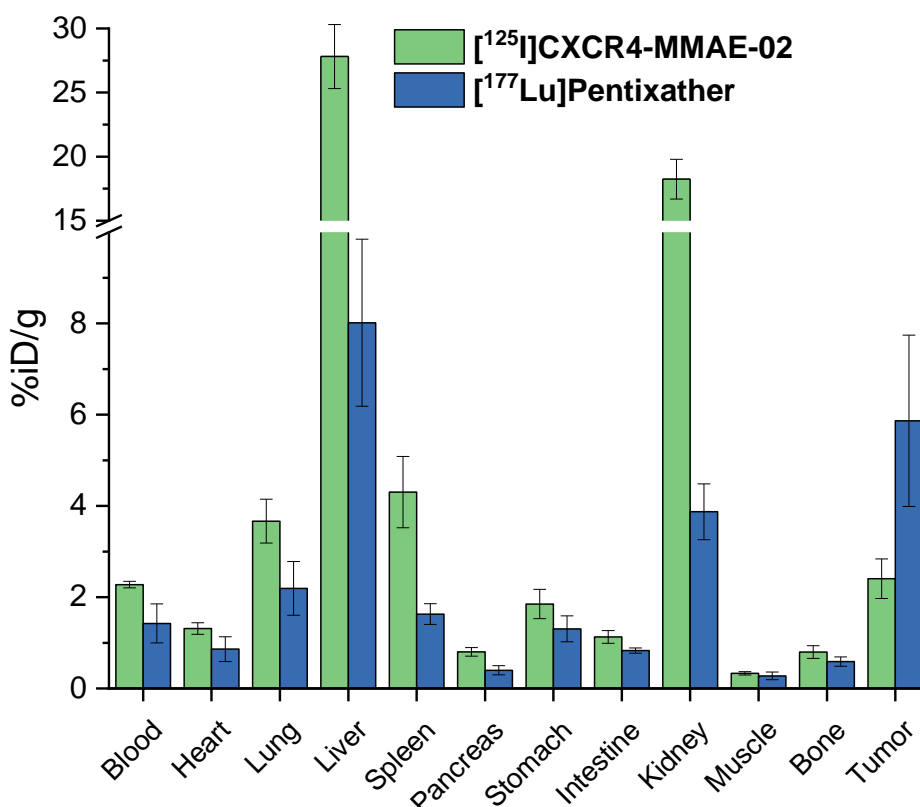


Figure 59: Biodistribution profiles of [¹²⁵I]CXCR4-MMAE-02 and [¹⁷⁷Lu]Pentixather 1h post injection in Jurkat tumor-bearing female CB-17 SCID mice; data are expressed as %iD/g and are means ± SD of 5 animals per ligand.

Compared to [¹⁷⁷Lu]Pentixather, the elevated lipophilicity of [¹²⁵I]CXCR4-MMAE-02 is reflected in slower clearance from blood (1.43 ± 0.43 vs. 2.28 ± 0.07 %iD/g) and therefore higher activity accumulation in CXCR4⁻ organs such as heart (0.86 ± 0.27 vs. 1.31 ± 0.13 %iD/g) and pancreas (0.40 ± 0.10 vs. 0.80 ± 0.09 %iD/g). High activity levels are also observed in the kidneys (18.2 ± 1.6 %iD/g). As outlined previously, this effect is attributable to an elevated net charge of the peptide that leads to renal reabsorption due to binding to the megalin/cubilin complex. No elevated activity levels are observed in the intestine (1.13 ± 0.14 %iD/g), hence no excretion *via* the bile can be confirmed at 1h p.i. Thus, the high uptake in liver (27.8 ± 2.5 %iD/g) does not suggest hepatobiliary clearance rather than being a sign for trapping of the compound. Increased activity levels are furthermore observed in both other CXCR4⁺ organs lung (3.67 ± 0.48 %iD/g) and spleen (4.31 ± 0.78 %iD/g), indicating affinity towards the murine CXCR4 receptor. This circumstance has been shown to diminish tumor uptake as the majority of radioligand is filtered from circulation and therefore prohibiting efficient tumor targeting. Indeed, that seems to be the case for [¹²⁵I]CXCR4-MMAE-02, as only a slightly elevated tumor uptake

of 2.41 ± 0.43 %iD/g can be observed. However, two more explanations are conceivable. Iodo-tyrosine, independent of its configuration, is a major starting point for peptide degradation *in vivo* (241). Even though decomposition of cyclic iodo-tyrosine-bearing peptides is slower compared to their open-chain analogs, substantial structural alterations can be observed at early time points of biodistribution studies, especially for internalizing compounds (242,243). The released [125 I]iodo-tyrosine leads to high uptake in excreting organs and trapping in the thyroids (244). Unfortunately, we were not able to dissect the thyroid properly, which could have given important insight of the *in vivo* stability. Moreover, chemical modifications at the peptide-toxin linkage can occur. Hydrolysis of the succinimidyl thioether results in the irreversible formation of two isomeric succinamic acid thioethers. This reaction can potentially cause the loss of toxin or its target specificity (245). Furthermore, in biological environment, proteins offer an excess of thiol groups that can undergo a Retro-Michael-type exchange reaction with the peptide, fixing the toxin on the respective protein (246). These types of side reactions can considerably alter the route of excretion or targeting potential of the PDC.

5.6. Conclusion

Modification of CXCR4-targeted compounds permitted the attachment of a sterically demanding toxin at the *N*-terminal site of the ligands without extensive loss of CXCR4 affinity. Hence, all ligands within this series exhibited IC_{50} values below 150 nM and CXCR4-MMAE-02 and -03 below 50 nM. Those two ligands were radiolabeled with iodine-125, subjected to internalization studies and determination of lipophilicity. Both compounds exhibited $\log D_{7.4}$ values above zero. However, internalization was found to be elevated compared to [177 Lu]Pentixather, hence, confirming the concept of intracellular delivery of the PDCs. The group of our collaborator Prof. Dr. med. Keller determined the cytotoxic activity of CXCR4-MMAE-02. In both used cell lines, viability was substantially reduced the longer the incubation with the compound and the higher the concentration of compound. They further confirmed that with increasing concentrations of PDC, a higher number of cells were stuck in the G_2/M -phase, potentially caused by inhibition of microtubule polymerization by the intracellularly released toxin. In our own lab, a biodistribution of [125 I]CXCR4-MMAE-02 in Jurkat xenograft-bearing mice revealed high off-target binding due to the lipophilicity of the compound and uptake in mCXCR4

expressing organs lung, liver and spleen, resulting in only slightly elevated uptake in the tumor.

A proof of concept was provided. However, improper pharmacokinetics and unpracticable labeling prohibited further assessment of the ligands. A dual modality approach as presented by CXCR4-MMAE-04, could help to overcome these obstacles. The compound displayed increased hydrophilicity and a facile labeling technique due to the use of a DOTA-GA chelator. Unfortunately, CXCR4 affinity was partially lost by this modification. Nevertheless, for future ligands, such a concept seems promising, as a two-headed attack on tumor tissues, using both the toxic payload and the ionizing radiation of a complexed therapeutic isotope as well as nuclear imaging in combination with a SPECT or PET isotope is feasible. Tackling the instability of the peptide-toxin thioether bond could then be of interest, using stabilized maleimides or toxin derivatives that are forming stable peptide bonds.

6. Optical Imaging Devices

Using radiation in the spectrum of visible light or the near infrared for the detection of tumor cells has been of growing interest in the molecular imaging community. While SPECT and PET imaging is capable of revealing physiological processes, both modalities are limited in terms of their resolution, high costs and lack of widespread availability of radiotracers (247). Optical imaging devices, in contrast to that, offer micrometer resolution that allows the visualization and real-time monitoring of biological processes on a cellular level while being unproblematic for both the operator and the patient (248). Furthermore, low costs and fast image acquisition make these imaging agents of special interest for their clinical application (249). The use of light for the detection of tumors *in vivo*, however, does accompany certain problems, namely low tissue penetration depth and light scattering, generally limiting the applicability of such probes to epithelium-near tumors such as breast, colon, head, neck, esophagus, lung, pancreas and stomach cancer (247). Recently, a different approach, fluorescence-guided surgery, has opened a pathway to the widespread use of optical imaging devices in the clinical context. The differentiation between healthy and malign tissue during surgery is hereby eased and proximal metastases are less likely overlooked by real-time visual imaging (250).

A number of targeted peptides has been combined with fluorescent dyes in order to obtain optical probes. Recently, efforts were focused on the combination of both, radio-imaging *via* SPECT or PET and optical imaging, resulting in one probe that contains modalities suitable for both imaging techniques (Figure 60).

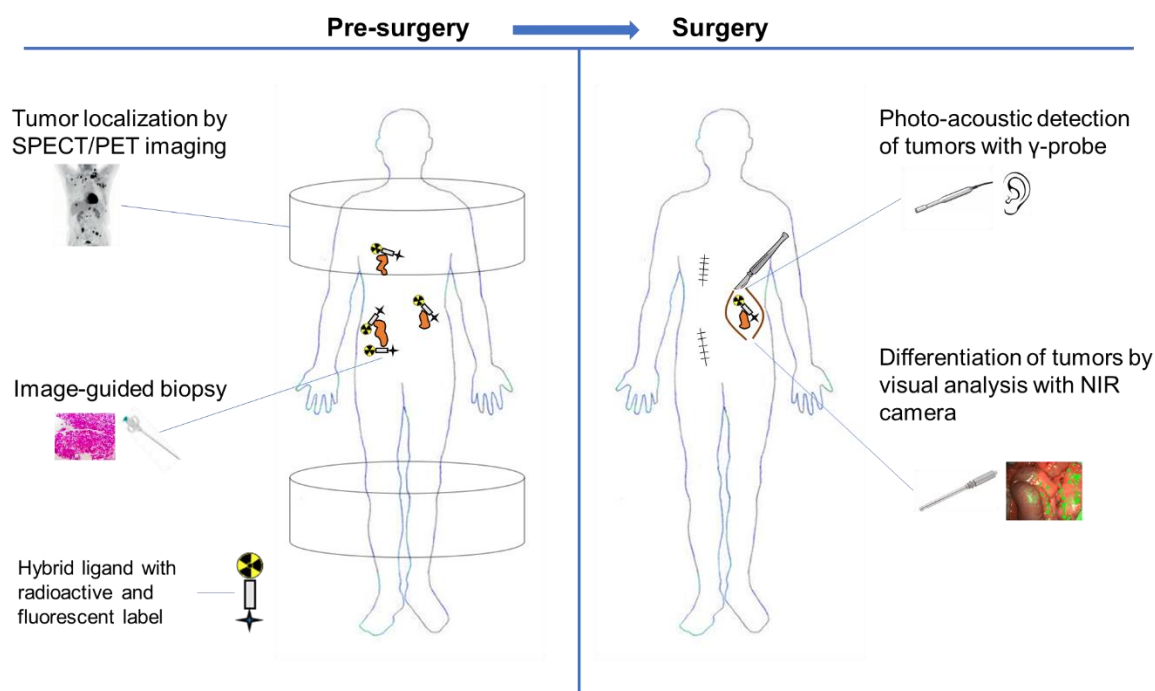


Figure 60: Concept of radio- and fluorescence-guided surgery using a hybrid ligand with both a radioactive and fluorescent label; radioactivity can be used for pre-surgical tumor localization and image-guided biopsy as well as photo-acoustic detection of tumor lesions during surgery; the fluorescent label can be used for pre-surgical *in vivo* staining of biopsy tissue and visual differentiation of malign and benign tissue during surgery.

The development of CXCR4-targeted fluorescent ligands has not yet resulted in clinically applied imaging agents. Several derivatives of Ac-TZ14011 and AMD3100 were prepared, however, most of the resulting compounds suffered from loss in CXCR4 affinity or inapt pharmacokinetic profiles (251–259). Hence, powerful tools for the *in vivo* fluorescence imaging of CXCR4 expression are still missing. The *CPCR4-Abz-a-r-dap* tracer backbone developed within this work should provide a suitable basis for the modification with a fluorescent dye as high CXCR4 affinity and flexibility towards the attachment of sterically demanding moieties is herewith provided. In a first proof of concept, the Cy5.5 dye was attached to the *N*-terminal site of the tracer backbone (CXCR4-OI-01) and the *l*-*CPCR4*-conjugated analog thereof (CXCR4-OI-02). Later, a hybrid ligand was prepared, carrying both a DOTA chelator for efficient radiolabeling and the Cy5.5 dye (CXCR4-OI-03) for fluorescence imaging. Figure 61 comprises the structures of the prepared ligands within this project.

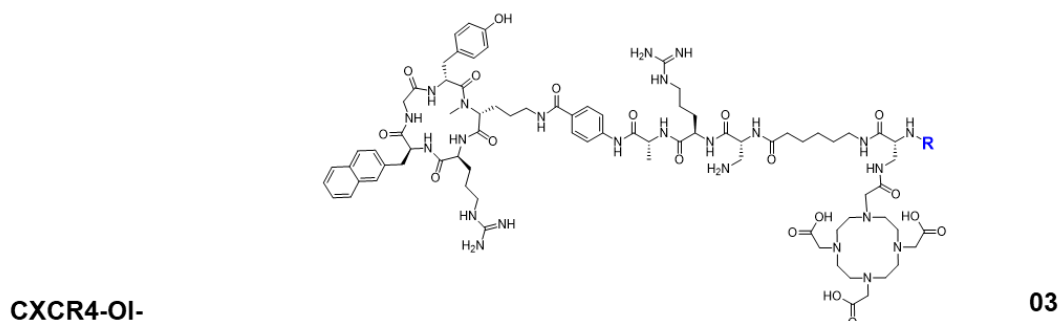
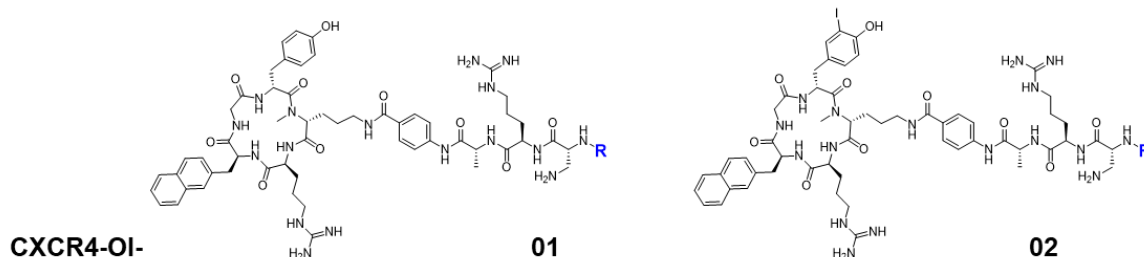
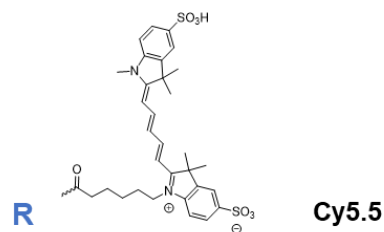


Figure 61: Summary of structures bearing a Cy5.5 fluorescent label: CXCR4-OI-01 and -02 were obtained by modification of the CPCR4-Abz-a-r-dap and the l-CPCR4-Abz-a-r-dap tracer backbone, respectively; CXCR4-OI-03 was obtained by modification of the CPCR4-Abz-a-r-dap-Ahx tracer backbone.

The following chapter comprises the synthesis as well as the *in vitro* and *in vivo* evaluation of Cy5.5-conjugated CXCR4-targeted ligands.

6.1. Synthesis

The chemical synthesis of CXCR4-OI-01 – 03 was based on condensation of separately prepared and purified peptide fragments. CXCR4-OI-01 was obtained by connection of the Cy5.5 dye with the CPCR4-Abz-a-r(Pbf)-dap(Boc)-NH₂ tracer backbone applying standard coupling conditions. The reaction resulted in significant byproduct formation potentially due to side-reactions of the dye. Subsequent acidic de-protection was kept at a timely minimum as the compound showed signs of degradation. However, after RP-HPLC purification, the desired product was obtained. Iodination of CXCR4-OI-01 to yield CXCR4-OI-02 was conducted using NIS. The resulting mixture of educt, mono- and

di-iodinated product was subjected to RP-HPLC purification and both educt and mono-iodinated product recovered.

For the synthesis of CXCR4-OI-03, an additional fragment bearing the DOTA chelator (HO-Ahx-dap(DOTA(*t*Bu)₃)-Fmoc) was prepared and coupled to the CPCR4-Abz-a-r(Pbf)-dap(Boc)-NH₂ tracer backbone. Fmoc de-protection and subsequent condensation with the dye proceeded as depicted above. Final de-protection caused major product loss due to unfinished *tert*-butyl removal from the chelator as incubation time with TFA needed to be kept at a minimum in order to prevent degradation of the dye. All three compounds were obtained in HPLC-grade purities and used as a stock solution for further experiments.

6.2. Radiosynthesis

6.2.1. Iodine-125 Labeling

Due to the lack of labeling modalities in the structure of CXCR4-OI-01, iodine-125 labeling of the tyr-bearing *CPCR4* peptide scaffold was undertaken. As depicted for CXCR4-MMAE-02 and -03, radioiodination was accompanied with byproduct formation. Best results were observed using 15 nmol of peptide with equimolar amounts of Iodogen. Labeling of CXCR4-OI-01 with 24.4 ± 1.6 MBq ($n = 5$) [¹²⁵I]NaI ultimately resulted in a radiochemical yield of $17.5 \pm 10.6\%$ ($n = 5$) after radio-RP-HPLC purification. The resolution of peaks was found to be impaired by high amounts of DMSO in the reaction mixtures, thus aggravating RP-HPLC purification. However, the product [¹²⁵I]CXCR4-OI-02 was obtained in radiochemical purities >80%. To reduce the volume of the RP-HPLC product fractions, the combined mixtures were applied to a SPE cartridge, and the product eluted with a MeOH/ACN mixture. The solvents were then evaporated in N₂-stream and the remainder dissolved in EtOH/H₂O before logD_{7.4} determination and execution of biodistribution studies.

6.2.2. Lutetium-177 Labeling

Labeling of CXCR4-OI-03 with lutetium-177 was undertaken in accordance with a standardized labeling procedure (II. 3.3.). Typically, 1.0 nmol of peptide were incubated

with 20.9 ± 4.6 MBq ($n = 4$) [^{177}Lu]LuCl₃, achieving constantly high yields of >98% as confirmed by radio-TLC measurements. Radio-RP-HPLC runs displayed signs of slow degradation, manifested in a peak that eluted earlier compared to the product peak and that grew higher, the longer the reaction time. However, consistent purities >90% were observed over all labeling experiments. The reaction mixture was therefore used without further purification for any of the respective experiments.

6.3. In vitro Evaluation and Hydrophilicity

The CXCR4 affinity of CXCR4-OI-01 – 03 was assessed using Jurkat lymphoma cells. By radioiodination of CXCR4-OI-01, [^{125}I]CXCR4-OI-02 was obtained and therefore, no logD_{7.4} value for CXCR4-OI-01 was determined. Labeling of CXCR4-OI-03 with gallium-68 was not feasible, as no [^{68}Ga]GaCl₃ was available.

Affinity and hydrophilicity

Table 16 summarizes IC₅₀ and logD_{7.4} values of the novel compounds with regard to [^{177}Lu]Pentixather and [^{68}Ga]Pentixafor.

Table 16: Summary of IC₅₀ [nM] and logD_{7.4} values for CXCR4-OI-01 and -02 as well as [$^{nat}\text{Lu}/^{177}\text{Lu}$]CXCR4-OI-03 and reference compounds [$^{nat}\text{Lu}/^{177}\text{Lu}$]Pentixather and [$^{nat}\text{Ga}/^{68}\text{Ga}$]Pentixafor: IC₅₀ values were determined in competitive binding studies employing Jurkat cells (400,000 cells/tube; 8°C, 2h incubation) and the standard ligand FC-131 (10⁻⁹ M, final assay-concentration). Data are expressed as mean ± SD; IC₅₀ data were determined as triplicates; logD_{7.4} values were determined as octuplicates; quadruplicate (), pentuplicate (**); (I): data adapted from literature (137).*

CXCR4-OI-	[M ³⁺]	IC ₅₀ [nM] (n = 3)	logD _{7.4} (n = 8)
01	/	4.43 ± 2.57(*)	n.d.
02	/	10.2 ± 4.0	-1.83 ± 0.02 (**)
03	Lu	7.34 ± 1.17	-3.38 ± 0.18
[^{177}Lu]Pentixather	Lu	19.5 ± 2.8	-1.76 ± 0.03
[^{68}Ga]Pentixafor (I)	Ga	24.8 ± 2.5	-2.90 ± 0.08

CXCR4-OI-01 displays a more than 5-fold and 4-fold higher affinity towards CXCR4 compared to [^{nat}Ga]Pentixafor and [^{nat}Lu]Pentixather, respectively. This compound proves the beneficial impact of the *CPCR4-Abz-a-r-dap* tracer backbone on the receptor affinity even when sterically demanding moieties such as the Cy5.5 dye are attached at the N-terminal site. Substantial distance between the chromophore and the *CPCR4*

peptide scaffold anchored in the CXCR4 binding pocket is provided by a carbohydrate spacer in the structure of the dye, which may contribute to the CXCR4 affinity of this ligand. CXCR4-OI-02 shows a more than 2-fold lower CXCR4 affinity compared to its analog. This detrimental effect of *CPCR4* iodination is in accordance with the data obtained for ligands CXCR4-DOTA-01 – 04. Nevertheless, CXCR4-OI-02 exhibits a more than 2-fold higher CXCR4 affinity compared to [^{nat}Ga]Pentixafor. The third peptide within this series, CXCR4-OI-03, represents a compound of the 3rd generation, carrying an additional *Ahx*-spacer between the *CPCR4-Abz-a-r-dap* tracer backbone and the signaling unit. This modification results in a more than 3-fold higher receptor affinity compared to [^{nat}Ga]Pentixafor and improved CXCR4 affinity compared to CXCR4-OI-02. Moreover, the DOTA chelator of [¹⁷⁷Lu]CXCR4-OI-03 proves to be a suitable modality to enhance hydrophilicity compared to its analog [¹²⁵I]CXCR4-OI-02 (logD_{7.4}: -3.38 ± 0.18 vs. -1.83 ± 0.02) and results in higher hydrophilicity compared to [⁶⁸Ga]Pentixafor.

Internalization

[¹⁷⁷Lu]CXCR4-OI-03 was tested in an internalization study employing Chem-1 cells and the internal standard ligand ¹²⁵I-FC-131. Data are corrected for unspecific binding and related to the internalization of the standard ligand. Figure 62 comprises the obtained data in comparison with the internalization of [¹⁷⁷Lu]Pentixather.

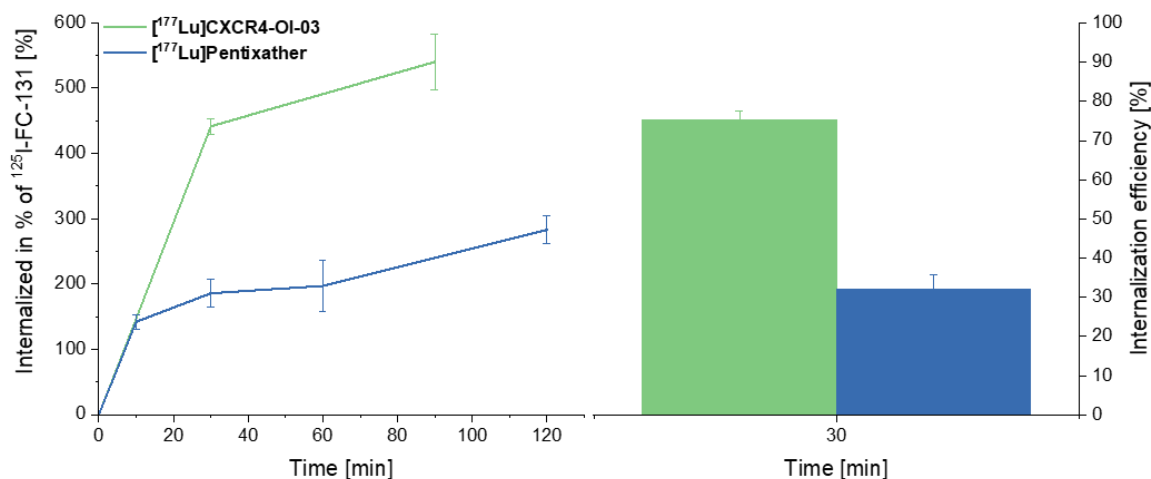


Figure 62: Dual tracer internalization of novel ligand [^{177}Lu]CXCR4-OI-03, [^{177}Lu]Pentixather and the reference compound ^{125}I -FC-131 (assay-concentration for each peptide 0.2 nM) into Chem-1 cells (100,000 cells per well; 37°C). Data are expressed as mean \pm SD; internalization at every time point was determined in triplicate and corrected for unspecific internalization; Internalized activity of the novel ligand in relation to the internalized activity of internal standard ^{125}I -FC-131; bar diagram: Percentage of internalized activity of the novel ligand in relation to the total cell-bound activity.

[^{177}Lu]CXCR4-OI-03 reaches a maximum of $540 \pm 43\%$ internalization in relation to ^{125}I -FC-131 after 1.5h incubation. Compared to [^{177}Lu]Pentixather, a nearly 2-fold maximum internalization is herewith reached. Moreover, an internalization efficiency of $82.4 \pm 4.4\%$ is observed that outgoes the internalization efficiency of [^{177}Lu]Pentixather by a factor of 1.5. Only a few ligands within this work exhibited comparable internalization characteristics that were generally reflected in considerably altered biodistribution profiles.

Based on their suitable CXCR4 affinities and hydrophilicities, [^{125}I]CXCR4-OI-02 and [^{177}Lu]CXCR4-OI-03 were further evaluated in *in vivo* biodistribution studies.

6.4. In vivo Biodistribution

Figure 63 summarizes the data obtained from biodistribution studies at 1h p.i. of [^{125}I]CXCR4-OI-02 and [^{177}Lu]CXCR4-OI-03 as well as reference compound [^{68}Ga]Pentixafor in Jurkat tumor-bearing mice. Organs affiliated with the expression of mCXCR4, namely lung, liver and spleen will be titled as CXCR4⁺ organs, whereas CXCR4⁻ will be used for organs, which are not known to express the receptor.

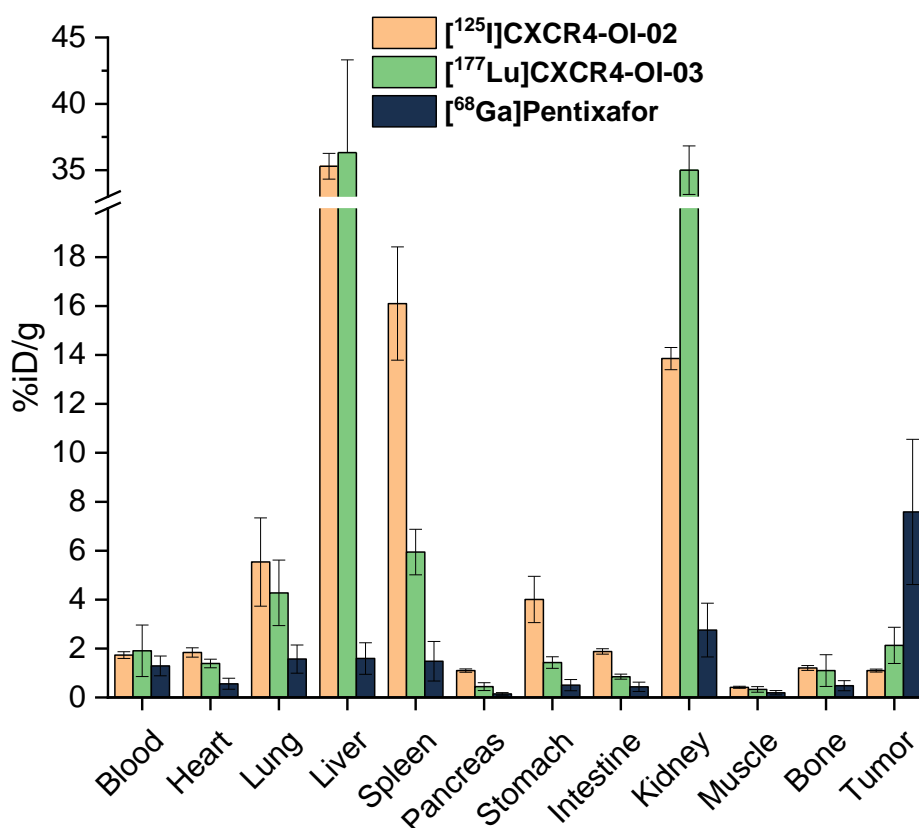


Figure 63: Biodistribution profiles of [¹²⁵I]CXCR4-OI-02, [¹⁷⁷Lu]CXCR4-OI-03 and [⁶⁸Ga]Pentixafor 1h post injection in Jurkat tumor-bearing female CB-17 SCID mice; data are expressed as %iD/g and are means ± SD of 5 animals per ligand..

Both novel ligands display slightly slower washout from blood compared to [⁶⁸Ga]Pentixafor which is generally reflected in elevated activity levels in CXCR4⁺ organs such as heart, pancreas, muscle, stomach and intestine. In the case of stomach and intestine, [¹²⁵I]CXCR4-OI-02 shows a 2.8-fold and 2.2-fold higher uptake, respectively, compared to [¹⁷⁷Lu]CXCR4-OI-03. This circumstance can be attributed to the substantially higher lipophilicity of the iodinated ligand and a partial clearance of the compound *via* the hepatobiliary pathway. Another explanation for elevated activity levels in the stomach could be the unsuccessful removal of unreacted iodine-125 from the product mixture and the interconnected uptake of the free radioisotope in the stomach wall (244). Both ligands, however, display elevated uptake in the kidneys reaching 13.9 ± 0.5 %iD/g for [¹²⁵I]CXCR4-OI-02 and 35.0 ± 1.8 %iD/g for [¹⁷⁷Lu]CXCR4-OI-03. This finding is in accordance with the other biodistribution studies presented in this work and can be backtracked to the elevated charge of the peptides and the herewith

connected reabsorption of the ligands in the kidneys due to complex formation with megalin/cubilin.

For both novel compounds, uptake in CXCR4⁺ organs is considerably elevated compared to blood level. [¹²⁵I]CXCR4-OI-02 shows higher uptake in lung (5.54 ± 1.80 %iD/g vs. 4.28 ± 1.34 %iD/g) and spleen (16.1 ± 2.3 %iD/g vs. 5.94 ± 0.93 %iD/g) and comparable uptake in liver (35.3 ± 1.0 %iD/g vs. 36.3 ± 7.0 %iD/g). As depicted for various ligands within this work, high uptake in CXCR4⁺ organs ultimately leads to decreased tumor uptake as the majority of radioligand is filtered from circulation, prohibiting efficient tumor targeting. This is again the case as [¹²⁵I]CXCR4-OI-02 displays no elevated uptake in tumor (1.10 ± 0.06 %iD/g) despite bearing nanomolar CXCR4 affinity. In the case of this ligand, another explanation for low tumor uptake could be the loss of the [¹²⁵I]-tyr in the binding scaffold due to enzymatic degradation *in vivo*. However, the thyroid glands that are known to trap I-tyr did not show elevated activity levels (1.45 ± 0.46 %iD/g, data not shown), eventually disarming this hypothesis (244). Tumor uptake of [¹⁷⁷Lu]CXCR4-OI-03 is 2-fold increased compared to its analog, reaching 2.13 ± 0.71 %iD/g. Again, excellent CXCR4 affinity is not translated into high uptake in tumor, potentially due to the elevated amount of trapped radioligand in CXCR4⁺ organs.

How a partial blockage of CXCR4⁺ organs would benefit the tumor uptake was tested in another biodistribution study, employing the radioactive ligand in low molar activity. Only one mouse was used for this study in order to spare animal lives. The obtained biodistribution is therefore not representative, however, a certain trend can be presumed. Figure 64 summarizes the experimental outcome.

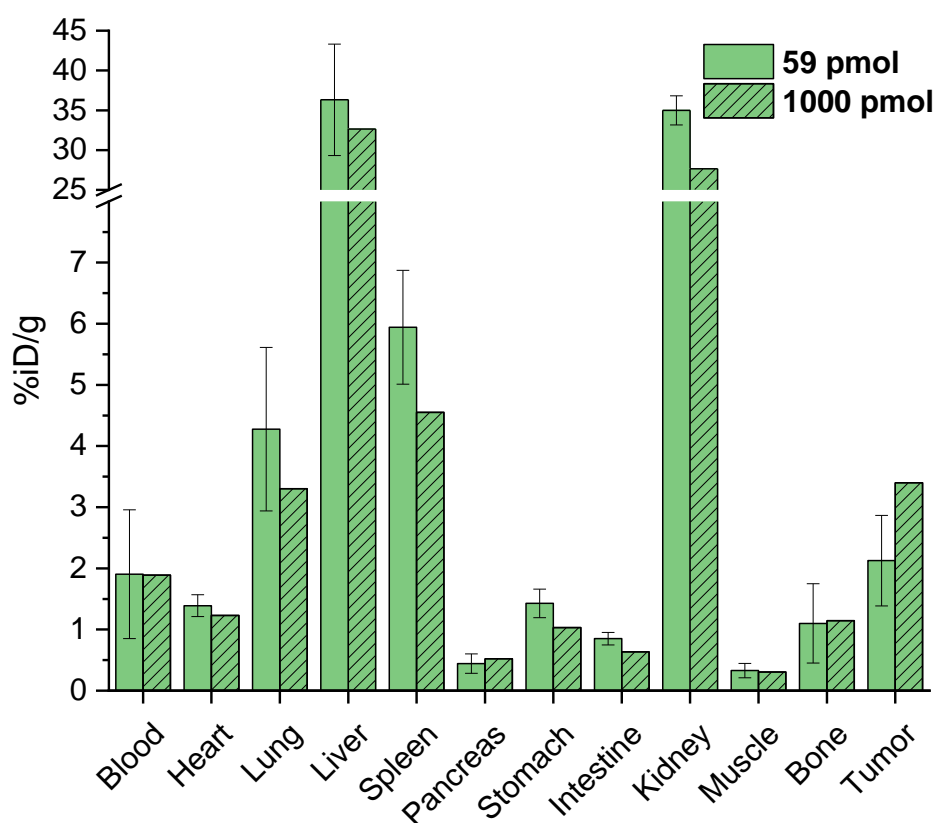


Figure 64: Biodistribution profile of [^{177}Lu]CXCR4-OI-03 1h post injection in Jurkat tumor-bearing female CB-17 SCID mice; different amounts of radioligand were applied: 59 pmol and 1,000 pmol; data are expressed as %ID/g values and are means \pm SD of 5 animals for the experiment with 59 pmol; 1 animal was used for the other experiment.

Reduced uptake in CXCR4⁺ organs lung (-23%), liver (-10%) and spleen (-23%) is observed upon injection of 1,000 pmol of cold peptide. Hence, tumor uptake is 1.6-fold increased, which indicates that the higher amount of peptide in circulation accumulates in the tumor. Low tumor uptake might therefore be attributable to the trapping of ligand in CXCR4⁺ organs and not be a result of missing targeting potential.

6.5. Fluorescence Imaging

CXCR4-OI-01 was further employed in an *in vivo* study to visualize the organ-bound fluorescent ligand. The compound was injected in a tumor-bearing mouse and the animal sacrificed after 2h. Spleen, liver and tumor tissues were collected, the samples frozen and cut into slices with 10 μm thickness. The slices were then examined using a fluorescence microscope. An equivalent experiment was conducted employing an excess

(100 nmol) of AMD3100 alongside with CXCR4-OI-01 to visualize un-specifically bound peptide. Figure 65 shows the obtained images.

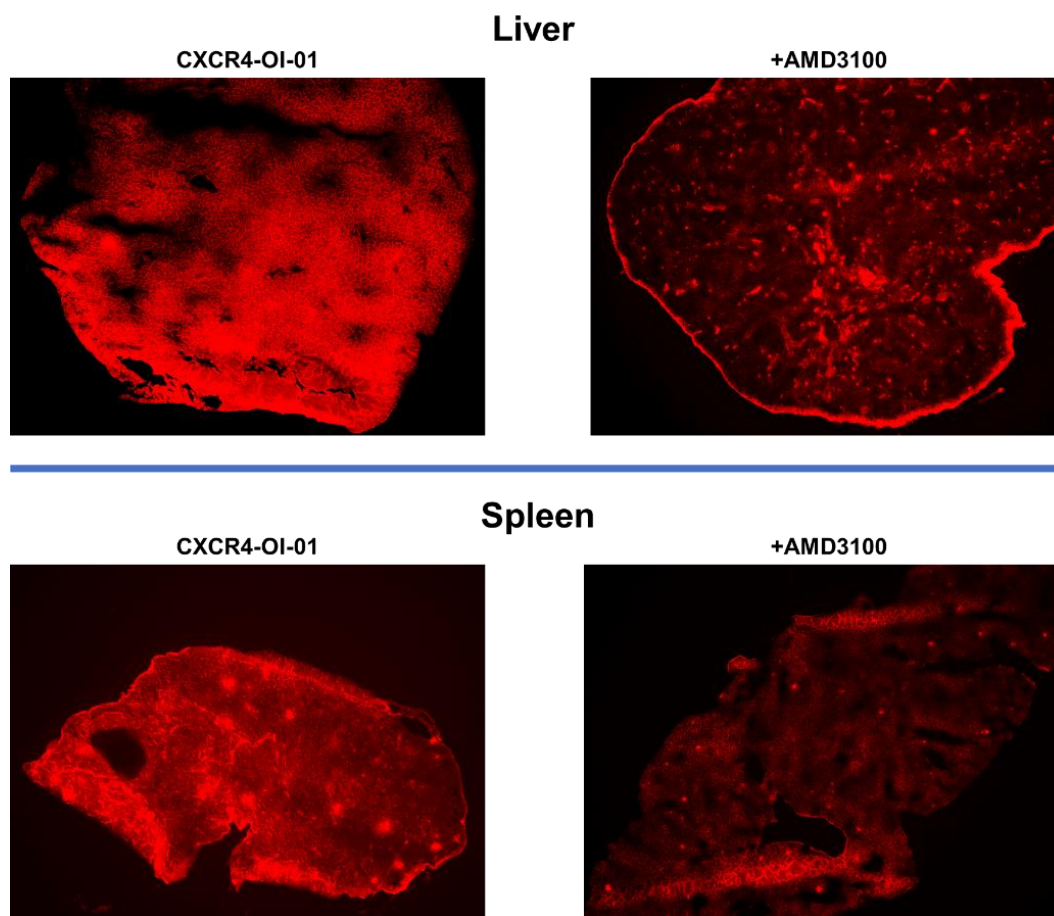


Figure 65: Fluorescence-microscopy images obtained from liver and spleen in 4-fold magnification; organs were dissected 2 hours after i.v. application of 2 nmol CXCR4-OI-01 with and without co-injection of 100 nmol AMD3100; images were obtained with 5 seconds exposure time.

CXCR4-OI-01 did not show tumor uptake high enough to obtain a reliable fluorescence signal. Liver and spleen, on the other side, exhibit a bright and homogenous signal. This observation fits the data obtained from the biodistribution study of [125 I]CXCR4-OI-02, that showed no elevated uptake in tumor but pronounced activity deposition in CXCR4⁺ organs. When CXCR4-OI-01 is co-injected with an excess of AMD3100, fluorescence in both organs is quenched. This finding provides another prove for ligand uptake mediated by the murine CXCR4 receptor expressed by spleen and liver. In the case of liver, however, bright fluorescence is still observed in the organs outer shell. Again, this outcome suits the observations made within this work as most of the blocking experiments did not result in entirely disabled liver uptake. This might have two distinct reasons: AMD3100 as a small molecule agent, exhibits a vastly different pharmacokinetic profile compared to larger peptides. Clearance of AMD3100 should be considerably faster, thus

leading to lagged peptide uptake in mCXCR4 expressing organs and not entirely blocked uptake. Moreover, a distinct trapping mechanism in the liver capsule could be present that is unaffected by an excess of AMD3100.

6.6. Conclusion

The first Cy5.5-conjugated ligand CXCR4-OI-01 exhibited high affinity towards CXCR4, reflected in an IC_{50} value in the low nanomolar range. Its l-tyr-bearing analog, CXCR4-OI-02, displayed slightly lower CXCR4 affinity, which was found to be typical for ligands bearing the iodinated binding motif. Due to the lack of chelating moieties in the structures of CXCR4-OI-01 and -02, iodine-125 labeling of CXCR4-OI-01 ultimately resulting in [^{125}I]CXCR4-OI-02, was undertaken. This compound exhibited hydrophilicity in need of improvement and thus, a third ligand, CXCR4-OI-03 was prepared, bearing both the Cy5.5 dye and a DOTA chelator for the facile labeling with radiometals. Again, a highly affine ligand was obtained with suitable hydrophilicity. The biodistribution studies of [^{125}I]CXCR4-OI-02 and [^{177}Lu]CXCR4-OI-03 showed pronounced uptake in mCXCR4 expressing organs lung, liver and spleen, ultimately resulting in low tumor uptakes. In an additional biodistribution experiment employing [^{177}Lu]CXCR4-OI-03 in low molar activity, tumor uptake was substantially enhanced by partial blockage of mCXCR4 expressing organs.

CXCR4-OI-01 was employed in *in vivo* fluorescence imaging of frozen tissue slices. Bright fluorescence signals were observed in spleen and liver tissue, thus confirming the outcome of biodistribution studies. When the ligand was administered alongside with an excess of AMD3100, signals arising from liver and spleen tissue were considerably quenched. However, the liver slices displayed remaining fluorescence signals concentrated in the livers capsule.

Taken together, the experiments within this project showed that it is possible to synthesize CXCR4-targeted fluorescence ligands that exhibit higher CXCR4 affinity and hydrophilicity compared to [^{68}Ga]Pentixafor. Moreover, bimodal ligands, carrying both the dye and a chelating moiety are feasible, easing radiolabeling and enlarging the area of application for such ligands. Unfortunately, the ligands auspicious *in vitro* data were not translated into promising biodistribution profiles so far.

IV. SUMMARY AND CONCLUSION

During the last decade, the G-protein coupled receptor CXCR4 has emerged as a valuable target for molecular imaging in cancer and in inflammatory conditions, and CXCR4-targeted PRRT has shown first promising results in hematological cancers. Amongst the broad spectrum of CXCR4-targeted imaging agents that have been evaluated preclinically, only the PET ligand [⁶⁸Ga]Pentixafor and its therapeutic analog [¹⁷⁷Lu]Pentixather - both of which have been developed at the Technical University of Munich (TUM) - have entered clinical trials to date. This is primarily due to their particularly favorable physicochemical properties and excellent CXCR4 affinities, providing high tumor-to-non-tumor ratios *in vivo* and a favorable dosimetry profile.

The only drawback associated with the ligand design of Pentixafor/Pentixather is the extremely limited flexibility of the peptide-linker-DOTA-construct towards modifications at the DOTA-chelate-position, preventing implementation of alternative radiolabeling strategies, because structural changes almost always led to loss in affinity and *in vivo* targeting potential. The work of Theresa Osl revealed an important means to circumvent some of the constraints. By introducing an extended, tailor-made linker between the *CPCR4* peptide scaffold and the signaling unit at the *N*-terminus of the linker unit, analogs with improved affinity were obtained. Of note, the need for *D*-Tyr-iodination to compensate for a loss in receptor affinity induced by changes in the signaling moiety, was obviated by the optimized linker design. Furthermore, it conveyed enhanced affinity towards the murine CXCR4 receptor as well as partially agonistic properties to the new ligands, as reflected in enhanced internalization. The design of the compounds within the present work is based on the results obtained by Theresa Osl. The objective of this work was to further exploit her initial approach of optimizing the linker unit such as to provide even greater flexibility of the *CPCR4*-linker construct towards modification with a broad spectrum of functionalities. These efforts were aimed at providing improved next-generation ligands based on the original [⁶⁸Ga]Pentixafor and [¹⁷⁷Lu]Pentixather design (CXCR4-DOTA series), ligands amenable for fluorine-18 labeling (CXCR4-SiFA series) as well as technetium-99m labeling (CXCR4-Tc series), ligands suitable for fluorescence imaging (CXCR4-OI series) and PDCs (CXCR4-MMAE series) carrying a cytotoxic payload.

In a 1st generation of ligands (CXCR4-Tc-01 – 06, CXCR4-SiFA-01, 02, CXCR4-MMAE-01 – 03), the linker developed by Osl et al. was elongated by different

single amino acid residues to evaluate the general structural requirements for optimization of the linker unit, leading to enhanced receptor affinity. While in most cases, the *N*-terminal conjugation with sterically demanding functional moieties led to considerably decreased affinities, CXCR4-Tc-06, bearing a D-dap after the three-amino acid linker, showed an affinity in the low nanomolar range. This ligand, more precisely its optimized tracer backbone *CPCR4-Abz-a-r-dap* was then used as the structural basis for the 2nd-generation compounds and was found to offer the desired flexibility towards the attachment of functional moieties. As a final optimization step, a 3rd generation of ligands was prepared in which the linker was additionally extended by an aminohexanoic acid spacer to further increase the distance between the signaling unit and the CPCR4 peptide scaffold. All ligands of this generation (CXCR4-Tc-15, CXCR4-SiFA-06, -07, CXCR4-MMAE-04, CXCR4-OI-03) exhibited suitable affinity towards CXCR4, independently from the size or charge (distribution) of the attached functionalities.

The first project within this work aimed towards the development of a suitable technetium-99m-labeled CXCR4-ligand for clinical SPECT imaging. In a first attempt, the *CPCR4-Abz-a-r-dap* tracer backbone was functionalized with a peptidic mas₃-chelator to yield [^{99m}Tc]CXCR4-Tc-06. This ligand exhibited high CXCR4 affinity but showed a comparably low hydrophilicity (logD_{7.4}: -1.54 ± 0.02). To overcome this limitation, a library of glycosylated mas₃-based chelators was prepared, including glucosyl and lactosyl residues. The resulting compounds ([^{99m}Tc]CXCR4-Tc-08 – 11) showed substantially improved hydrophilicities and overall high CXCR4 affinities (Table 3). In biodistribution and μSPECT imaging studies in Jurkat tumor-bearing mice, favorable pharmacokinetics were observed, especially for [^{99m}Tc]CXCR4-Tc-09, which showed high uptake in tumor alongside with rapid clearance from the background (Figure 30). For side-by-side comparison of the influence of different established Tc-99m-labeling approaches, analogs bearing the chelators HYNIC ([^{99m}Tc]CXCR4-Tc-12) and N4 ([^{99m}Tc]CXCR4-Tc-13 – 15) instead of the mas₃-based chelators were evaluated in parallel. While [^{99m}Tc]CXCR4-Tc-12 showed high tumor uptake and low background accumulation *in vivo*, ultimately resulting in beneficial tumor/background ratios, the obtained labeling yields using this labeling chemistry were very low, hampering easy implementation of the labeling method into clinical routine. [^{99m}Tc]CXCR4-Tc-13, however, revealed almost quantitative yields and a reliable labeling procedure, a more than 5-fold increased CXCR4 affinity compared to [⁶⁸Ga]Pentixafor and high tumor uptake *in vivo* (Figure 31). This

compound was chosen as the candidate for a first application in men. In cooperation with the *Universitätsklinikum Augsburg*, [^{99m}Tc]CXCR4-Tc-13 was employed as a SPECT agent for patients suffering from multiple myeloma, enabling high-contrast imaging of lesions due to a favorable biodistribution of the tracer (Figure 33).

Despite the promising results obtained for [^{99m}Tc]CXCR4-Tc-13, further optimization of the labeling procedure for [^{99m}Tc]CXCR4-Tc-12 could be rewarding an alternative compound for a clinical proof-of-concept study.

In the second part of this work, the chelator DOTA was attached to the optimized tracer backbones *CPCR4-Ambz-a-r-dap* and *CPCR4-Abz-a-r-dap* to obtain analogs to [⁶⁸Ga]Pentixafor. The resulting peptides CXCR4-DOTA-01 and -03 were further iodinated to yield CXCR4-DOTA-02 and -04, as direct analogs to [¹⁷⁷Lu]Pentixather. All of the newly developed ligands displayed improved receptor affinities compared to both reference compounds and enhanced hydrophilicities (Table 8). Moreover, the structural optimizations led to pronounced internalization into CXCR4 expressing cells, especially for both iodinated compounds [¹⁷⁷Lu]CXCR4-DOTA-02 and -04. Interestingly, when a knock-out derivative of CXCR4-DOTA-04 (*cyclo*(D-I-Tyr-D-[NMe]Orn(Abz-D-Ala-D-Arg-D-Dap-DOTA)-Arg-2-Nal-Gly), KO-CXCR4-DOTA-04 (*cyclo*(D-I-Tyr-D-[NMe]Orn(Abz-D-Ala-D-Arg-D-Dap-DOTA)-D-Arg-D-2-Nal-Gly) was prepared, high internalization of the ligand pursued despite an only micromolar affinity for CXCR4. A two-site binding model for the novel ligands was hence proposed in analogy to the endogenous ligand of CXCR4, CXCL12. Alongside with an altered internalization behavior, [¹⁷⁷Lu]CXCR4-DOTA-02 and -04 also displayed substantially improved affinity for mCXCR4. This was reflected by high (and blockable) tracer uptake in organs with high mCXCR4 expression such as lung, liver and spleen in biodistribution studies. Due to the fraction of radioligand trapped within these organs, leading to strongly decreased levels of circulating activity, altered overall clearance kinetics and lower tumor uptake were observed. [¹⁷⁷Lu]CXCR4-DOTA-03 and -04 were further investigated in biodistribution studies at 6 and 48h after injection. Both ligands exhibited improved retention in tumor and higher tumor/organ ratios compared to [¹⁷⁷Lu]Pentixather. A comparable in-depth investigation of the corresponding gallium-68 labeled compounds might be worthwhile, especially for CXCR4-DOTA-03. This ligand may challenge [⁶⁸Ga]Pentixafor, even though the biodistribution in mice was biased by its mCXCR4 affinity. The lutetium-177-labeled alternative might be a suitable

candidate for a first proof-of-concept study in men, as it provided a 2-fold higher deposited activity in the tumor compared to [¹⁷⁷Lu]Pentixather.

The third part of this work comprised the development of compounds, carrying a SiFA moiety for the labeling with fluorine-18 *via* isotopic exchange reaction. In order to protect the radio-synthon from hydrolysis, the SiFA building block needs to be shielded with sterically demanding *tert*-butyl groups which intrinsically convey pronounced lipophilicity to the peptides. Thus, a 1st generation of lipophilic or low-affinity ligands (CXCR4-SiFA-01, -02) and a 2nd generation of more hydrophilic but low-affinity ligands (CXCR4-SiFA-03 – 05) was obtained (Table 13). The SiFA synthon was therefore exchanged by SiFAlin, a moiety bearing a stable positive charge near the *tert*-butyl groups. The resulting ligands CXCR4-SiFA-06 and -07 displayed a strong increase in receptor affinity, reaching IC₅₀ values in the low nanomolar range. Moreover, exceptional internalization rates up to 1,000% in relation to the standard ligand and internalization efficiencies of approximately 100% were observed. [¹⁸F,^{nat}Ga]CXCR4-SiFA-07 furthermore exhibited suitable hydrophilicity (logD_{7.4}: -1.95 ± 0.05) and was therefore evaluated in a biodistribution study in tumor-bearing mice. As observed for various other compounds within this work, the high internalization rates were reflected in elevated ligand uptake in mCXCR4 expressing organs such as lung, liver and spleen. In this case, liver uptake exceeded 50 %iD/g (Figure 50), thus prohibiting efficient tumor targeting. However, further experiments showed that partial blockage of hepatic uptake eventually resulted in elevated uptake in tumor. CXCR4-SiFA-06 and -07 were designed as radiohybrid compounds, carrying a SiFA moiety alongside with a chelator for labeling with radiometals. This concept provides a “true” theranostic approach and flexibility in the radioisotope used. Even though their promising *in vitro* data were not yet reflected in favorable biodistribution profiles compared to [⁶⁸Ga]Pentixafor, the radiohybrid compounds may lay the foundation for a new class of CXCR4-targeted theranostic ligands.

The pronounced internalization of the compounds developed within this work triggered the design of PDCs. Targeted ligands were conjugated with a MMAE derivative, bearing an additional linker that is specifically cleaved by intracellular Cathepsin B. The novel compounds CXCR4-MMAE-01 – 03 exhibited CXCR4 affinities below 100 nM and improved internalization compared to [¹⁷⁷Lu]Pentixather. Our collaborators from the group

of Prof. Dr. med. Keller examined CXCR4-MMAE-02 regarding its *in vitro* potential as a targeted chemotherapeutic drug. They revealed considerably elevated fractions of dead cancer cells upon incubation with the PDC due to arrest of the cells in the G2/M-phase prior to cell division (Figure 56 and Figure 58). However, some extracellular degradation of the PDC and thus unspecific cell killing was also observed. In a next step, optimization of ligand stability, in particular of the maleimide moiety linking the cytotoxic agent to the peptide vector, is warranted (Table 15). CXCR4-MMAE-04, bearing a DOTA-GA chelator in addition to the toxin may serve as a suitable structural basis for further optimizations, since the DOTA-GA chelator substantially improves ligand hydrophilicity. Furthermore, the bimodal (“hybrid”) design of the peptide enables nuclear imaging of the pharmacokinetics of the PDC, greatly facilitating dose-finding studies.

As optical/hybrid imaging is gaining increasing significance, in particular in interventional nuclear medicine, the last project within this work focused on the development of dedicated CXCR4-targeted fluorescent probes. The prepared ligands CXCR4-OI-01 – 03, carry the far-red-dye Cy5.5 and exhibited CXCR4 affinities in the low nanomolar range alongside with favorable hydrophilicities (Table 16). *In vivo*, however, the intrinsically high affinity towards the murine receptor found for all compounds based on the optimized linker unit resulted in substantial uptake in lung, liver and spleen and therefore low uptake in the tumor (Figure 63). Fluorescence imaging of organ slices using CXCR4-OI-01 confirmed CXCR4 specific ligand uptake in spleen and liver and further provided an explanation for the incomplete blockage of hepatic uptake upon co-injection with competitor (Figure 65). The hybrid ligand, CXCR4-OI-03 additionally carries a DOTA chelator and thus enables labeling with radiometals. The application of such a bimodal ligand for CXCR4-targeted fluorescence- and radio-guided surgery is conceivable as soon as a proof of concept demonstrating suitable *in vivo* characteristics is established.

In summary, the iterative step-by-step optimization of the linker unit in Pentixafor/Pentixather-based tracers has yielded a novel scaffold that provides unprecedented flexibility towards functionalization of the targeting vector with a variety of even sterically demanding functionalities. Most of the compounds presented within this work displayed improved *in vitro* characteristics, and first *in vivo* biodistribution and imaging experiments demonstrate the great potential of the novel tracer design as a structural basis for the development of CXCR4-targeted imaging probes for diverse

applications. However, the mechanism responsible for uptake in mCXCR4 expressing organs must be further elucidated to ensure the validity and translatability of mouse biodistribution data to the human situation. As demonstrated in a first-in-man study and in clear contrast to the mouse data obtained during the preclinical evaluation, the technetium tracer [^{99m}Tc]CXCR4-Tc-13 did not show substantially elevated uptake in human liver or lung. This finding strongly encourages future clinical translation of other promising compounds obtained within the framework of this work.

V. REFERENCES

1. Sung H, Ferlay J, Siegel RL, et al. Global cancer statistics 2020: GLOBOCAN estimates of incidence and mortality worldwide for 36 cancers in 185 countries. *CA Cancer J Clin.* 2021. doi:10.3322/caac.21660.
2. Henley SJ, Ward EM, Scott S, et al. Annual report to the nation on the status of cancer, part I: National cancer statistics. *Cancer.* 2020;126:2225-2249. doi:10.1002/cncr.32802.
3. Zaorsky NG, Churilla TM, Egleston BL, et al. Causes of death among cancer patients. *Ann Oncol.* 2017;28:400-407. doi:10.1093/annonc/mdw604.
4. Weller D, Vedsted P, Rubin G, et al. The Aarhus statement: improving design and reporting of studies on early cancer diagnosis. *Br J Cancer.* 2012;106:1262-1267. doi:10.1038/bjc.2012.68.
5. Zhou Y, Abel GA, Hamilton W, et al. Diagnosis of cancer as an emergency: a critical review of current evidence. *Nat Rev Clin Oncol.* 2017;14:45-56. doi:10.1038/nrclinonc.2016.155.
6. Whitaker K. Earlier diagnosis: the importance of cancer symptoms. *The Lancet Oncology.* 2020;21:6-8. doi:10.1016/S1470-2045(19)30658-8.
7. Hayat MA. *Methods of Cancer Diagnosis, Therapy and Prognosis: Breast Carcinoma.* Dordrecht: Springer Netherlands; 2008. Methods of Cancer Diagnosis, Therapy and Prognosis; 1.
8. Haberkorn U, Schoenberg SO. Imaging of lung cancer with CT, MRT and PET. *Lung Cancer.* 2001;34:13-23. doi:10.1016/s0169-5002(01)00369-5.
9. Guo R, Lu G, Qin B, Fei B. Ultrasound Imaging Technologies for Breast Cancer Detection and Management: A Review. *Ultrasound Med Biol.* 2018;44:37-70. doi:10.1016/j.ultrasmedbio.2017.09.012.
10. Alix-Panabières C. The future of liquid biopsy. *Nature.* 2020;579:S9. doi:10.1038/d41586-020-00844-5.
11. Farwell MD, Pryma DA, Mankoff DA. PET/CT imaging in cancer: current applications and future directions. *Cancer.* 2014;120:3433-3445. doi:10.1002/cncr.28860.
12. Bertolini V, Palmieri A, Bassi MC, et al. CT protocol optimisation in PET/CT: a systematic review. *EJNMMI Phys.* 2020;7:17. doi:10.1186/s40658-020-00287-x.
13. Israel O, Pellet O, Biassoni L, et al. Two decades of SPECT/CT - the coming of age of a technology: An updated review of literature evidence. *Eur J Nucl Med Mol Imaging.* 2019;46:1990-2012. doi:10.1007/s00259-019-04404-6.
14. Rudin M. *Molecular Imaging: Basic Principles And Applications In Biomedical Research.* 3rd edition: World Scientific Europe; 2020.
15. Bailey DL, Willowson KP. An evidence-based review of quantitative SPECT imaging and potential clinical applications. *J Nucl Med.* 2013;54:83-89. doi:10.2967/jnumed.112.111476.
16. Bockisch A, Freudenberg LS, Schmidt D, Kuwert T. Hybrid imaging by SPECT/CT and PET/CT: proven outcomes in cancer imaging. *Semin Nucl Med.* 2009;39:276-289. doi:10.1053/j.semnuclmed.2009.03.003.
17. Kaufmann PA, Di Carli MF. Hybrid SPECT/CT and PET/CT imaging: the next step in noninvasive cardiac imaging. *Semin Nucl Med.* 2009;39:341-347. doi:10.1053/j.semnuclmed.2009.03.007.

18. Townsend DW. Physical principles and technology of clinical PET imaging. *Ann Acad Med Singap.* 2004;33:133-145.
19. Catana C. Principles of Simultaneous PET/MR Imaging. *Magn Reson Imaging Clin N Am.* 2017;25:231-243. doi:10.1016/j.mric.2017.01.002.
20. Disselhorst JA, Bezrukov I, Kolb A, Parl C, Pichler BJ. Principles of PET/MR Imaging. *J Nucl Med.* 2014;55:2S-10S. doi:10.2967/jnumed.113.129098.
21. Ballou B, Ernst LA, Waggoner AS. Fluorescence imaging of tumors in vivo. *Curr Med Chem.* 2005;12:795-805. doi:10.2174/0929867053507324.
22. Frangioni JV. In vivo near-infrared fluorescence imaging. *Curr Opin Chem Biol.* 2003;7:626-634. doi:10.1016/j.cbpa.2003.08.007.
23. Ntziachristos V, Bremer C, Weissleder R. Fluorescence imaging with near-infrared light: new technological advances that enable in vivo molecular imaging. *Eur Radiol.* 2003;13:195-208. doi:10.1007/s00330-002-1524-x.
24. Sevick-Muraca EM. Translation of near-infrared fluorescence imaging technologies: emerging clinical applications. *Annu Rev Med.* 2012;63:217-231. doi:10.1146/annurev-med-070910-083323.
25. Niedre M, Ntziachristos V. Elucidating Structure and Function In Vivo With Hybrid Fluorescence and Magnetic Resonance Imaging. *Proc. IEEE.* 2008;96:382-396. doi:10.1109/JPROC.2007.913498.
26. KleinJan GH, Hellingman D, van den Berg NS, et al. Hybrid Surgical Guidance: Does Hardware Integration of γ - and Fluorescence Imaging Modalities Make Sense? *J Nucl Med.* 2017;58:646-650. doi:10.2967/jnumed.116.177154.
27. Ale A, Ermolayev V, Herzog E, Cohrs C, Angelis MH de, Ntziachristos V. FMT-XCT: in vivo animal studies with hybrid fluorescence molecular tomography-X-ray computed tomography. *Nat Methods.* 2012;9:615-620. doi:10.1038/nmeth.2014.
28. van Oosterom MN, Meershoek P, Welling MM, et al. Extending the Hybrid Surgical Guidance Concept With Freehand Fluorescence Tomography. *IEEE Trans Med Imaging.* 2020;39:226-235. doi:10.1109/TMI.2019.2924254.
29. Wyld L, Audisio RA, Poston GJ. The evolution of cancer surgery and future perspectives. *Nat Rev Clin Oncol.* 2015;12:115-124. doi:10.1038/nrclinonc.2014.191.
30. Zugazagoitia J, Guedes C, Ponce S, Ferrer I, Molina-Pinelo S, Paz-Ares L. Current Challenges in Cancer Treatment. *Clin Ther.* 2016;38:1551-1566. doi:10.1016/j.clinthera.2016.03.026.
31. Nilsson S, Norlén BJ, Widmark A. A systematic overview of radiation therapy effects in prostate cancer. *Acta Oncol.* 2004;43:316-381. doi:10.1080/02841860410030661.
32. Shridhar R, Almhanna K, Meredith KL, et al. Radiation therapy and esophageal cancer. *Cancer Control.* 2013;20:97-110. doi:10.1177/107327481302000203.
33. Rutqvist LE, Rose C, Cavallin-Ståhl E. A systematic overview of radiation therapy effects in breast cancer. *Acta Oncol.* 2003;42:532-545. doi:10.1080/02841860310014444.
34. Markham MJ, Wachter K, Agarwal N, et al. Clinical Cancer Advances 2020: Annual Report on Progress Against Cancer From the American Society of Clinical Oncology. *J Clin Oncol.* 2020;38:1081. doi:10.1200/JCO.19.03141.

35. Schirmmacher V. From chemotherapy to biological therapy: A review of novel concepts to reduce the side effects of systemic cancer treatment (Review). *Int J Oncol.* 2019;54:407-419. doi:10.3892/ijo.2018.4661.
36. Wu H-C, Chang D-K, Huang C-T, Shouip H. Targeted Therapy for Cancer. 2014.
37. Qin S-Y, Cheng Y-J, Lei Q, Zhang A-Q, Zhang X-Z. Combinational strategy for high-performance cancer chemotherapy. *Biomaterials.* 2018;171:178-197. doi:10.1016/j.biomaterials.2018.04.027.
38. Joo WD, Visintin I, Mor G. Targeted cancer therapy--are the days of systemic chemotherapy numbered? *Maturitas.* 2013;76:308-314. doi:10.1016/j.maturitas.2013.09.008.
39. Tsimberidou A-M. Targeted therapy in cancer. *Cancer Chemother Pharmacol.* 2015;76:1113-1132. doi:10.1007/s00280-015-2861-1.
40. Dolgin E. Publisher Correction: Radioactive drugs emerge from the shadows to storm the market. *Nat Biotechnol.* 2019;37:193. doi:10.1038/s41587-019-0030-5.
41. Priya SR, Dravid CS, Digumarti R, Dandekar M. Targeted Therapy for Medullary Thyroid Cancer: A Review. *Front Oncol.* 2017;7:238. doi:10.3389/fonc.2017.00238.
42. Bodei L, Kidd M, Paganelli G, et al. Long-term tolerability of PRRT in 807 patients with neuroendocrine tumours: the value and limitations of clinical factors. *Eur J Nucl Med Mol Imaging.* 2015;42:5-19. doi:10.1007/s00259-014-2893-5.
43. Del Prete M, Buteau F-A, Arsenault F, et al. Personalized 177Lu-octreotate peptide receptor radionuclide therapy of neuroendocrine tumours: initial results from the P-PRRT trial. *Eur J Nucl Med Mol Imaging.* 2019;46:728-742. doi:10.1007/s00259-018-4209-7.
44. Sgouros G, Bodei L, McDevitt MR, Nedrow JR. Radiopharmaceutical therapy in cancer: clinical advances and challenges. *Nat Rev Drug Discov.* 2020;19:589-608. doi:10.1038/s41573-020-0073-9.
45. Hennrich U, Kopka K. Lutathera®: The First FDA- and EMA-Approved Radiopharmaceutical for Peptide Receptor Radionuclide Therapy. *Pharmaceuticals (Basel).* 2019;12. doi:10.3390/ph12030114.
46. Theodoropoulou M, Stalla GK. Somatostatin receptors: from signaling to clinical practice. *Front Neuroendocrinol.* 2013;34:228-252. doi:10.1016/j.yfrne.2013.07.005.
47. Barnett P. Somatostatin and Somatostatin Receptor Physiology. *ENDO.* 2003;20:255-264. doi:10.1385/ENDO:20:3:255.
48. Griffith JW, Sokol CL, Luster AD. Chemokines and chemokine receptors: positioning cells for host defense and immunity. *Annu Rev Immunol.* 2014;32:659-702. doi:10.1146/annurev-immunol-032713-120145.
49. Rossi D, Zlotnik A. The biology of chemokines and their receptors. *Annu Rev Immunol.* 2000;18:217-242. doi:10.1146/annurev.immunol.18.1.217.
50. Balestrieri ML, Balestrieri A, Mancini FP, Napoli C. Understanding the immunoangiostatic CXC chemokine network. *Cardiovasc Res.* 2008;78:250-256. doi:10.1093/cvr/cvn029.
51. Rosenbaum DM, Rasmussen SGF, Kobilka BK. The structure and function of G-protein-coupled receptors. *Nature.* 2009;459:356-363. doi:10.1038/nature08144.
52. Weis WI, Kobilka BK. The Molecular Basis of G Protein-Coupled Receptor Activation. *Annu Rev Biochem.* 2018;87:897-919. doi:10.1146/annurev-biochem-060614-033910.

53. Wootten D, Christopoulos A, Marti-Solano M, Babu MM, Sexton PM. Mechanisms of signalling and biased agonism in G protein-coupled receptors. *Nat Rev Mol Cell Biol.* 2018;19:638-653. doi:10.1038/s41580-018-0049-3.
54. Hughes CE, Nibbs RJB. A guide to chemokines and their receptors. *FEBS J.* 2018;285:2944-2971. doi:10.1111/febs.14466.
55. Teixidó J, Martínez-Moreno M, Díaz-Martínez M, Sevilla-Movilla S. The good and bad faces of the CXCR4 chemokine receptor. *Int J Biochem Cell Biol.* 2018;95:121-131. doi:10.1016/j.biocel.2017.12.018.
56. Nagasawa T. CXC chemokine ligand 12 (CXCL12) and its receptor CXCR4. *J Mol Med (Berl).* 2014;92:433-439. doi:10.1007/s00109-014-1123-8.
57. Janssens R, Struyf S, Proost P. The unique structural and functional features of CXCL12. *Cell Mol Immunol.* 2018;15:299-311. doi:10.1038/cmi.2017.107.
58. Nagasawa T, Hirota S, Tachibana K, et al. Defects of B-cell lymphopoiesis and bone-marrow myelopoiesis in mice lacking the CXC chemokine PBSF/SDF-1. *Nature.* 1996;382:635-638. doi:10.1038/382635a0.
59. Ma Q, Jones D, Borghesani PR, et al. Impaired B-lymphopoiesis, myelopoiesis, and derailed cerebellar neuron migration in CXCR4- and SDF-1-deficient mice. *Proc Natl Acad Sci U S A.* 1998;95:9448-9453. doi:10.1073/pnas.95.16.9448.
60. Smit MJ, Schlecht-Louf G, Neves M, et al. The CXCL12/CXCR4/ACKR3 Axis in the Tumor Microenvironment: Signaling, Crosstalk, and Therapeutic Targeting. *Annu Rev Pharmacol Toxicol.* 2021;61:541-563. doi:10.1146/annurev-pharmtox-010919-023340.
61. Saini V, Marchese A, Majetschak M. CXC chemokine receptor 4 is a cell surface receptor for extracellular ubiquitin. *J Biol Chem.* 2010;285:15566-15576. doi:10.1074/jbc.M110.103408.
62. Sinitski D, Kontos C, Krammer C, Asare Y, Kapurniotu A, Bernhagen J. Macrophage Migration Inhibitory Factor (MIF)-Based Therapeutic Concepts in Atherosclerosis and Inflammation. *Thromb Haemost.* 2019;119:553-566. doi:10.1055/s-0039-1677803.
63. Pawig L, Klasen C, Weber C, Bernhagen J, Noels H. Diversity and Inter-Connections in the CXCR4 Chemokine Receptor/Ligand Family: Molecular Perspectives. *Front Immunol.* 2015;6:429. doi:10.3389/fimmu.2015.00429.
64. Meyrath M, Szpakowska M, Zeiner J, et al. The atypical chemokine receptor ACKR3/CXCR7 is a broad-spectrum scavenger for opioid peptides. *Nat Commun.* 2020;11:3033. doi:10.1038/s41467-020-16664-0.
65. Sun X, Cheng G, Hao M, et al. CXCL12 / CXCR4 / CXCR7 chemokine axis and cancer progression. *Cancer Metastasis Rev.* 2010;29:709-722. doi:10.1007/s10555-010-9256-x.
66. Feng Y, Broder CC, Kennedy PE, Berger EA. HIV-1 entry cofactor: Functional cDNA cloning of a seven-transmembrane, G protein-coupled receptor. *Science.* 1996;272:872-877. doi:10.1126/science.272.5263.872.
67. García-Cuesta EM, Santiago CA, Vallejo-Díaz J, Juarranz Y, Rodríguez-Frade JM, Mellado M. The Role of the CXCL12/CXCR4/ACKR3 Axis in Autoimmune Diseases. *Front Endocrinol (Lausanne).* 2019;10:585. doi:10.3389/fendo.2019.00585.

68. Abboud D, Hanson J. Chemokine neutralization as an innovative therapeutic strategy for atopic dermatitis. *Drug Discov Today*. 2017;22:702-711. doi:10.1016/j.drudis.2016.11.023.
69. Döring Y, Pawig L, Weber C, Noels H. The CXCL12/CXCR4 chemokine ligand/receptor axis in cardiovascular disease. *Front Physiol*. 2014;5:212. doi:10.3389/fphys.2014.00212.
70. Kawaguchi N, Zhang T-T, Nakanishi T. Involvement of CXCR4 in Normal and Abnormal Development. *Cells*. 2019;8. doi:10.3390/cells8020185.
71. Dvorak HF. Tumors: wounds that do not heal. Similarities between tumor stroma generation and wound healing. *N Engl J Med*. 1986;315:1650-1659. doi:10.1056/NEJM198612253152606.
72. Sóti Z, Magill J, Dreher R. Karlsruhe Nuclide Chart – New 10th edition 2018. *EPJ Nuclear Sci. Technol*. 2019;5:6. doi:10.1051/epjn/2019004.
73. Chatterjee S, Behnam Azad B, Nimmagadda S. The intricate role of CXCR4 in cancer. *Adv Cancer Res*. 2014;124:31-82. doi:10.1016/B978-0-12-411638-2.00002-1.
74. Yazdani Z, Mousavi Z, Moradabadi A, Hassanshahi G. Significance of CXCL12/CXCR4 Ligand/Receptor Axis in Various Aspects of Acute Myeloid Leukemia. *Cancer Manag Res*. 2020;12:2155-2165. doi:10.2147/CMAR.S234883.
75. Dubrovskaya A, Elliott J, Salamone RJ, et al. CXCR4 expression in prostate cancer progenitor cells. *PLoS ONE*. 2012;7:e31226. doi:10.1371/journal.pone.0031226.
76. Liu Y, Ren C-C, Yang L, Xu Y-M, Chen Y-N. Role of CXCL12-CXCR4 axis in ovarian cancer metastasis and CXCL12-CXCR4 blockade with AMD3100 suppresses tumor cell migration and invasion in vitro. *J Cell Physiol*. 2019;234:3897-3909. doi:10.1002/jcp.27163.
77. Lombardi L, Tavano F, Morelli F, Latiano TP, Di Sebastiano P, Maiello E. Chemokine receptor CXCR4: role in gastrointestinal cancer. *Crit Rev Oncol Hematol*. 2013;88:696-705. doi:10.1016/j.critrevonc.2013.08.005.
78. Rasti A, Abolhasani M, Zanjani LS, Asgari M, Mehrazma M, Madjd Z. Reduced expression of CXCR4, a novel renal cancer stem cell marker, is associated with high-grade renal cell carcinoma. *J Cancer Res Clin Oncol*. 2017;143:95-104. doi:10.1007/s00432-016-2239-8.
79. Basile J, Thiers B, Maize J, Lathers DMR. Chemokine receptor expression in non-melanoma skin cancer. *J Cutan Pathol*. 2008;35:623-629. doi:10.1111/j.1600-0560.2007.00879.x.
80. Kim RH, Li BDL, Chu QD. The role of chemokine receptor CXCR4 in the biologic behavior of human soft tissue sarcoma. *Sarcoma*. 2011;2011:593708. doi:10.1155/2011/593708.
81. Zhao H, Guo L, Zhao H, Zhao J, Weng H, Zhao B. CXCR4 over-expression and survival in cancer: a system review and meta-analysis. *Oncotarget*. 2015;6:5022-5040. doi:10.18632/oncotarget.3217.
82. Bianchi ME, Mezzapelle R. The Chemokine Receptor CXCR4 in Cell Proliferation and Tissue Regeneration. *Front Immunol*. 2020;11:2109. doi:10.3389/fimmu.2020.02109.
83. Guo F, Wang Y, Liu J, Mok SC, Xue F, Zhang W. CXCL12/CXCR4: A symbiotic bridge linking cancer cells and their stromal neighbors in oncogenic communication networks. *Oncogene*. 2016;35:816-826. doi:10.1038/onc.2015.139.
84. Domanska UM, Kruizinga RC, Nagengast WB, et al. A review on CXCR4/CXCL12 axis in oncology: No place to hide. *Eur J Cancer*. 2013;49:219-230. doi:10.1016/j.ejca.2012.05.005.

85. Furusato B, Mohamed A, Uhlén M, Rhim JS. CXCR4 and cancer. *Pathol Int.* 2010;60:497-505. doi:10.1111/j.1440-1827.2010.02548.x.
86. Burger JA, Stewart DJ, Wald O, Peled A. Potential of CXCR4 antagonists for the treatment of metastatic lung cancer. *Expert Rev Anticancer Ther.* 2011;11:621-630. doi:10.1586/ERA.11.11.
87. Gerlach LO, Jakobsen JS, Jensen KP, et al. Metal ion enhanced binding of AMD3100 to Asp262 in the CXCR4 receptor. *Biochemistry.* 2003;42:710-717. doi:10.1021/bi0264770.
88. Jacobson O, Weiss ID, Szajek L, Farber JM, Kiesewetter DO. ⁶⁴Cu-AMD3100--a novel imaging agent for targeting chemokine receptor CXCR4. *Bioorganic & Medicinal Chemistry.* 2009;17:1486-1493. doi:10.1016/j.bmc.2009.01.014.
89. Weiss ID, Jacobson O, Kiesewetter DO, et al. Positron emission tomography imaging of tumors expressing the human chemokine receptor CXCR4 in mice with the use of ⁶⁴Cu-AMD3100. *Mol Imaging Biol.* 2012;14:106-114. doi:10.1007/s11307-010-0466-y.
90. Nimmagadda S, Pullambhatla M, Stone K, Green G, Bhujwalla ZM, Pomper MG. Molecular imaging of CXCR4 receptor expression in human cancer xenografts with ⁶⁴CuAMD3100 positron emission tomography. *Cancer Res.* 2010;70:3935-3944. doi:10.1158/0008-5472.CAN-09-4396.
91. Morimoto M, Mori H, Otake T, et al. Inhibitory effect of tachyplesin I on the proliferation of human immunodeficiency virus in vitro. *Chemotherapy.* 1991;37:206-211. doi:10.1159/000238855.
92. Tamamura H, Arakaki R, Funakoshi H, et al. Effective lowly cytotoxic analogs of an HIV-cell fusion inhibitor, T22 ([Tyr^{5,12}, Lys⁷]-polyphemusin II). *Bioorganic & Medicinal Chemistry.* 1998;6:231-238. doi:10.1016/s0968-0896(97)10037-2.
93. Tamamura H, Xu Y, Hattori T, et al. A low-molecular-weight inhibitor against the chemokine receptor CXCR4: A strong anti-HIV peptide T140. *Biochem Biophys Res Commun.* 1998;253:877-882. doi:10.1006/bbrc.1998.9871.
94. Tamamura H, Omagari A, Oishi S, et al. Pharmacophore identification of a specific CXCR4 inhibitor, T140, leads to development of effective anti-HIV agents with very high selectivity indexes. *Bioorganic & Medicinal Chemistry Letters.* 2000;10:2633-2637. doi:10.1016/s0960-894x(00)00535-7.
95. Tamamura H, Omagari A, Hiramatsu K, et al. Development of specific CXCR4 inhibitors possessing high selectivity indexes as well as complete stability in serum based on an anti-HIV peptide T140. *Bioorganic & Medicinal Chemistry Letters.* 2001;11:1897-1902. doi:10.1016/S0960-894X(01)00323-7.
96. George GPC, Stevens E, Åberg O, et al. Preclinical evaluation of a CXCR4-specific (⁶⁸Ga)-labelled TN14003 derivative for cancer PET imaging. *Bioorganic & Medicinal Chemistry.* 2014;22:796-803. doi:10.1016/j.bmc.2013.12.012.
97. Wang Z, Zhang M, Wang L, et al. Prospective Study of (⁶⁸Ga)-NOTA-NFB: Radiation Dosimetry in Healthy Volunteers and First Application in Glioma Patients. *Theranostics.* 2015;5:882-889. doi:10.7150/thno.12303.
98. Zhang M, Wang Z, Zhang M, Wang S, Yang W, Wang J. **⁶⁸Ga-NOTA-NFB PET/CT for Imaging of Chemokine Receptor 4 Expression in Breast Cancer.** *Journal of Nuclear Medicine.* 2019;60:1229.
99. Vallejo-Armenta P, Santos-Cuevas C, Soto-Andonaegui J, et al. ^{99m}Tc-CXCR4-L for Imaging of the Chemokine-4 Receptor Associated with Brain Tumor Invasiveness: Biokinetics, Radiation Dosimetry,

- and Proof of Concept in Humans. *Contrast Media Mol Imaging*. 2020;2020:2525037. doi:10.1155/2020/2525037.
100. Fujii N, Oishi S, Hiramatsu K, et al. Molecular-size reduction of a potent CXCR4-chemokine antagonist using orthogonal combination of conformation- and sequence-based libraries. *Angew Chem Int Ed Engl*. 2003;42:3251-3253. doi:10.1002/anie.200351024.
 101. Kobayashi K, Oishi S, Hayashi R, et al. Structure-activity relationship study of a CXC chemokine receptor type 4 antagonist, FC131, using a series of alkene dipeptide isosteres. *J Med Chem*. 2012;55:2746-2757. doi:10.1021/jm2016914.
 102. Tanaka T, Tsutsumi H, Nomura W, et al. Structure-activity relationship study of CXCR4 antagonists bearing the cyclic pentapeptide scaffold: identification of the new pharmacophore. *Org Biomol Chem*. 2008;6:4374-4377. doi:10.1039/b812029c.
 103. Tsutsumi H, Tanaka T, Ohashi N, et al. Therapeutic potential of the chemokine receptor CXCR4 antagonists as multifunctional agents. *Biopolymers*. 2007;88:279-289. doi:10.1002/bip.20653.
 104. Peng S-B, Zhang X, Paul D, et al. Identification of LY2510924, a novel cyclic peptide CXCR4 antagonist that exhibits antitumor activities in solid tumor and breast cancer metastatic models. *Mol Cancer Ther*. 2015;14:480-490. doi:10.1158/1535-7163.MCT-14-0850.
 105. Wu B, Chien EYT, Mol CD, et al. Structures of the CXCR4 chemokine GPCR with small-molecule and cyclic peptide antagonists. *Science*. 2010;330:1066-1071. doi:10.1126/science.1194396.
 106. Våbenø J, Nikiforovich GV, Marshall GR. Insight into the binding mode for cyclopentapeptide antagonists of the CXCR4 receptor. *Chem Biol Drug Des*. 2006;67:346-354. doi:10.1111/j.1747-0285.2006.00387.x.
 107. Kawatkar SP, Yan M, Gevariya H, et al. Computational analysis of the structural mechanism of inhibition of chemokine receptor CXCR4 by small molecule antagonists. *Exp Biol Med (Maywood)*. 2011;236:844-850. doi:10.1258/ebm.2011.010345.
 108. Yoshikawa Y, Kobayashi K, Oishi S, Fujii N, Furuya T. Molecular modeling study of cyclic pentapeptide CXCR4 antagonists: new insight into CXCR4-FC131 interactions. *Bioorganic & Medicinal Chemistry Letters*. 2012;22:2146-2150. doi:10.1016/j.bmcl.2012.01.134.
 109. Thiele S, Mungalpara J, Steen A, Rosenkilde MM, Våbenø J. Determination of the binding mode for the cyclopentapeptide CXCR4 antagonist FC131 using a dual approach of ligand modifications and receptor mutagenesis. *Br J Pharmacol*. 2014;171:5313-5329. doi:10.1111/bph.12842.
 110. Ueda S, Oishi S, Wang Z-x, et al. Structure-activity relationships of cyclic peptide-based chemokine receptor CXCR4 antagonists: Disclosing the importance of side-chain and backbone functionalities. *J Med Chem*. 2007;50:192-198. doi:10.1021/jm0607350.
 111. Tamamura H, Araki T, Ueda S, et al. Identification of novel low molecular weight CXCR4 antagonists by structural tuning of cyclic tetrapeptide scaffolds. *J Med Chem*. 2005;48:3280-3289. doi:10.1021/jm050009h.
 112. Demmer O, Dijkgraaf I, Schottelius M, Wester H-J, Kessler H. Introduction of functional groups into peptides via N-alkylation. *Org Lett*. 2008;10:2015-2018. doi:10.1021/ol800654n.
 113. Demmer O, Gourni E, Schumacher U, Kessler H, Wester H-J. PET imaging of CXCR4 receptors in cancer by a new optimized ligand. *ChemMedChem*. 2011;6:1789-1791. doi:10.1002/cmdc.201100320.

114. Gourni E, Demmer O, Schottelius M, et al. PET of CXCR4 expression by a (68)Ga-labeled highly specific targeted contrast agent. *J Nucl Med.* 2011;52:1803-1810. doi:10.2967/jnumed.111.098798.
115. Wester HJ, Keller U, Schottelius M, et al. Disclosing the CXCR4 expression in lymphoproliferative diseases by targeted molecular imaging. *Theranostics.* 2015;5:618-630. doi:10.7150/thno.11251.
116. Philipp-Abbrederis K, Herrmann K, Knop S, et al. In vivo molecular imaging of chemokine receptor CXCR4 expression in patients with advanced multiple myeloma. *EMBO Mol Med.* 2015;7:477-487. doi:10.15252/emmm.201404698.
117. Lapa C, Schreder M, Schirbel A, et al. 68GaPentixafor-PET/CT for imaging of chemokine receptor CXCR4 expression in multiple myeloma - Comparison to 18FFDG and laboratory values. *Theranostics.* 2017;7:205-212. doi:10.7150/thno.16576.
118. Herhaus P, Habringer S, Philipp-Abbrederis K, et al. Targeted positron emission tomography imaging of CXCR4 expression in patients with acute myeloid leukemia. *Haematologica.* 2016;101:932-940. doi:10.3324/haematol.2016.142976.
119. Habringer S, Lapa C, Herhaus P, et al. Dual Targeting of Acute Leukemia and Supporting Niche by CXCR4-Directed Theranostics. *Theranostics.* 2018;8:369-383. doi:10.7150/thno.21397.
120. Mayerhoefer ME, Jaeger U, Staber P, et al. 68GaGa-Pentixafor PET/MRI for CXCR4 Imaging of Chronic Lymphocytic Leukemia: Preliminary Results. *Invest Radiol.* 2018;53:403-408. doi:10.1097/RLI.0000000000000469.
121. Lapa C, Reiter T, Werner RA, et al. (68)GaPentixafor-PET/CT for Imaging of Chemokine Receptor 4 Expression After Myocardial Infarction. *JACC Cardiovasc Imaging.* 2015;8:1466-1468. doi:10.1016/j.jcmg.2015.09.007.
122. Rischpler C, Nekolla SG, Kossmann H, et al. Upregulated myocardial CXCR4-expression after myocardial infarction assessed by simultaneous GA-68 pentixafor PET/MRI. *J Nucl Cardiol.* 2016;23:131-133. doi:10.1007/s12350-015-0347-5.
123. Thackeray JT, Derlin T, Haghikia A, et al. Molecular Imaging of the Chemokine Receptor CXCR4 After Acute Myocardial Infarction. *JACC Cardiovasc Imaging.* 2015;8:1417-1426. doi:10.1016/j.jcmg.2015.09.008.
124. Reiter T, Kircher M, Schirbel A, et al. Imaging of C-X-C Motif Chemokine Receptor CXCR4 Expression After Myocardial Infarction With 68GaPentixafor-PET/CT in Correlation With Cardiac MRI. *JACC Cardiovasc Imaging.* 2018;11:1541-1543. doi:10.1016/j.jcmg.2018.01.001.
125. Koenig T, Sedding DG, Wester H-J, Derlin T. Seeing the unseen: post-infarction inflammation in an isolated right ventricular myocardial infarction visualized by combined cardiac magnetic resonance imaging and chemokine receptor CXCR4-targeted molecular imaging. *Eur Heart J.* 2018;39:966. doi:10.1093/eurheartj/ehx783.
126. Schmid JS, Schirbel A, Buck AK, Kropf S, Wester H-J, Lapa C. 68GaPentixafor-Positron Emission Tomography/Computed Tomography Detects Chemokine Receptor CXCR4 Expression After Ischemic Stroke. *Circ Cardiovasc Imaging.* 2016;9:e005217. doi:10.1161/CIRCIMAGING.116.005217.
127. Hyafil F, Pelisek J, Laitinen I, et al. Imaging the Cytokine Receptor CXCR4 in Atherosclerotic Plaques with the Radiotracer 68Ga-Pentixafor for PET. *J Nucl Med.* 2017;58:499-506. doi:10.2967/jnumed.116.179663.

128. Derlin T, Sedding DG, Dutzmann J, et al. Imaging of chemokine receptor CXCR4 expression in culprit and nonculprit coronary atherosclerotic plaque using motion-corrected 68Ga-pentixafor PET/CT. *Eur J Nucl Med Mol Imaging*. 2018;45:1934-1944. doi:10.1007/s00259-018-4076-2.
129. Li X, Heber D, Leike T, et al. 68Ga-Pentixafor-PET/MRI for the detection of Chemokine receptor 4 expression in atherosclerotic plaques. *Eur J Nucl Med Mol Imaging*. 2018;45:558-566. doi:10.1007/s00259-017-3831-0.
130. Weiberg D, Thackeray JT, Daum G, et al. Clinical Molecular Imaging of Chemokine Receptor CXCR4 Expression in Atherosclerotic Plaque Using 68Ga-Pentixafor PET: Correlation with Cardiovascular Risk Factors and Calcified Plaque Burden. *J Nucl Med*. 2018;59:266-272. doi:10.2967/jnumed.117.196485.
131. Linde P, Baues C, Wegen S, et al. Pentixafor PET/CT for imaging of chemokine receptor 4 expression in esophageal cancer - a first clinical approach. *Cancer Imaging*. 2021;21:22. doi:10.1186/s40644-021-00391-w.
132. Yusuf Menda. Gallium 68 Pentixafor in Patients With Neuroendocrine Tumors: NCT03335670. <https://clinicaltrials.gov/ct2/show/NCT03335670?term=pentixafor&draw=2&rank=1>.
133. Nantes University Hospital. Relevance of [68Ga]Ga -PentixaFor-PET for Initial Staging and Therapeutic Evaluation of Multiple Myeloma in First Line Treatment (PentiMyelo): NCT04561492. <https://clinicaltrials.gov/ct2/show/NCT04561492?term=pentixafor&draw=2&rank=2>.
134. Peking Union Medical College Hospital. Chemokine Receptor CXCR4-targeting Molecular Imaging for Metabolic Characterization of Multiple Myeloma and Lymphoma: NCT03436342. <https://clinicaltrials.gov/ct2/show/NCT03436342?term=pentixafor&draw=2&rank=3>.
135. First Affiliated Hospital of Fujian Medical University. Value of Chemokine Receptor CXCR4 Imaging for Diagnosis and Prognostic Evaluation in Lymphoproliferative Diseases: NCT04504526. <https://clinicaltrials.gov/ct2/show/NCT04504526?term=pentixafor&draw=2&rank=4>.
136. Lapa C, Herrmann K, Schirbel A, et al. CXCR4-directed endoradiotherapy induces high response rates in extramedullary relapsed Multiple Myeloma. *Theranostics*. 2017;7:1589-1597. doi:10.7150/thno.19050.
137. Poschenrieder A, Schottelius M, Schwaiger M, Kessler H, Wester H-J. The influence of different metal-chelate conjugates of pentixafor on the CXCR4 affinity. *EJNMMI Res*. 2016;6:36. doi:10.1186/s13550-016-0193-8.
138. Schottelius M, Osl T, Poschenrieder A, et al. 177Lu-pentixather: Comprehensive Preclinical Characterization of a First CXCR4-directed Endoradiotherapeutic Agent. *Theranostics*. 2017;7:2350-2362. doi:10.7150/thno.19119.
139. Herrmann K, Schottelius M, Lapa C, et al. First-in-Human Experience of CXCR4-Directed Endoradiotherapy with 177Lu- and 90Y-Labeled Pentixather in Advanced-Stage Multiple Myeloma with Extensive Intra- and Extramedullary Disease. *J Nucl Med*. 2016;57:248-251. doi:10.2967/jnumed.115.167361.
140. Lapa C, Hänscheid H, Kircher M, et al. Feasibility of CXCR4-Directed Radioligand Therapy in Advanced Diffuse Large B-Cell Lymphoma. *J Nucl Med*. 2019;60:60-64. doi:10.2967/jnumed.118.210997.

141. Lapa C, Lückcrath K, Kircher S, et al. Potential influence of concomitant chemotherapy on CXCR4 expression in receptor directed endoradiotherapy. *Br J Haematol.* 2019;184:440-443. doi:10.1111/bjh.15096.
142. Maurer S, Herhaus P, Lippenmeyer R, et al. Side Effects of CXC-Chemokine Receptor 4-Directed Endoradiotherapy with Pentixafer Before Hematopoietic Stem Cell Transplantation. *J Nucl Med.* 2019;60:1399-1405. doi:10.2967/jnumed.118.223420.
143. Poschenrieder A, Osl T, Schottelius M, et al. First 18F-Labeled Pentixafer-Based Imaging Agent for PET Imaging of CXCR4 Expression In Vivo. *Tomography.* 2016;2:85-93. doi:10.18383/j.tom.2016.00130.
144. Poschenrieder A, Schottelius M, Osl T, Schwaiger M, Wester H-J. 64CuNOTA-pentixafer enables high resolution PET imaging of CXCR4 expression in a preclinical lymphoma model. *EJNMMI Radiopharm Chem.* 2017;2:2. doi:10.1186/s41181-016-0020-6.
145. Poschenrieder A, Schottelius M, Schwaiger M, Wester H-J. Preclinical evaluation of (68)GaNOTA-pentixafer for PET imaging of CXCR4 expression in vivo - a comparison to (68)Ga-pentixafer. *EJNMMI Res.* 2016;6:70. doi:10.1186/s13550-016-0227-2.
146. Osl T, Schmidt A, Schwaiger M, Schottelius M, Wester H-J. A new class of Pentixafer- and Pentixafer-based theranostic agents with enhanced CXCR4-targeting efficiency. *Theranostics.* 2020;10:8264-8280. doi:10.7150/thno.45537.
147. Osl T, Wester H-J, Schottelius M, inventors; Technische Universität München. Therapeutic and diagnostic agents for cancer. WO2020053255A1.
148. Osl T. *Development of cyclic pentapeptide ligands for chemokine receptor targeting.* München: Universitätsbibliothek der TU München; 2017.
149. Demmer O, Frank AO, Hagn F, et al. Erhöhte CXCR4-Affinität und Anti-HIV-Aktivität eines Peptoids durch Konformationsfixierung. *Angew. Chem.* 2012;124:8234-8237. doi:10.1002/ange.201202090.
150. Chatterjee J, Gilon C, Hoffman A, Kessler H. N-methylation of peptides: A new perspective in medicinal chemistry. *Acc Chem Res.* 2008;41:1331-1342. doi:10.1021/ar8000603.
151. Weineisen M, Simecek J, Schottelius M, Schwaiger M, Wester H-J. Synthesis and preclinical evaluation of DOTAGA-conjugated PSMA ligands for functional imaging and endoradiotherapy of prostate cancer. *EJNMMI Res.* 2014;4:63. doi:10.1186/s13550-014-0063-1.
152. Iovkova L, Wängler B, Schirmacher E, et al. para-Functionalized aryl-di-tert-butylfluorosilanes as potential labeling synthons for (18)F radiopharmaceuticals. *Chemistry.* 2009;15:2140-2147. doi:10.1002/chem.200802266.
153. Kostikov AP, Iovkova L, Chin J, et al. N-(4-(di-tert-butyl[18F]fluorosilyl)benzyl)-2-hydroxy-N,N-dimethylethylammonium bromide ([18F]SiFAN+Br-): A novel lead compound for the development of hydrophilic SiFA-based prosthetic groups for 18F-labeling. *Journal of Fluorine Chemistry.* 2011;132:27-34. doi:10.1016/j.jfluchem.2010.10.008.
154. Abrams MJ, Juweid M, tenKate CI, et al. Technetium-99m-human polyclonal IgG radiolabeled via the hydrazino nicotinamide derivative for imaging focal sites of infection in rats. *J Nucl Med.* 1990;31:2022-2028.

155. Joyard Y, Bischoff L, Levacher V, Papamicael C, Vera P, Bohn P. Synthesis and Stability Evaluation of New HYNIC Derivatives as Ligands for Technetium-99m. *LOC*. 2014;11:208-214. doi:10.2174/15701786113106660087.
156. Abiraj K, Mansi R, Tamma M-L, et al. Tetraamine-derived bifunctional chelators for technetium-99m labelling: Synthesis, bioconjugation and evaluation as targeted SPECT imaging probes for GRP-receptor-positive tumours. *Chemistry*. 2010;16:2115-2124. doi:10.1002/chem.200902011.
157. Schottelius M, Schwaiger M, Wester H-J. Rapid and high-yield solution-phase synthesis of DOTA-Tyr3-octreotide and DOTA-Tyr3-octreotate using unprotected DOTA. *Tetrahedron Letters*. 2003;44:2393-2396. doi:10.1016/S0040-4039(03)00221-1.
158. Robu S, Schottelius M, Eiber M, et al. Preclinical Evaluation and First Patient Application of 99mTc-PSMA-I&S for SPECT Imaging and Radioguided Surgery in Prostate Cancer. *J Nucl Med*. 2017;58:235-242. doi:10.2967/jnumed.116.178939.
159. Kuzmanovska S, Vaskova O, Zdraveska Kocovska M. "In-house" preparation of 99mTc-EDDA/HYNIC-TOC, a specific targeting agent for somatostatin receptor scintigraphy. *Maced. Pharm. Bull.* 2011;57:65-70. doi:10.33320/maced.pharm.bull.2011.57.007.
160. Othman MFB, Mitry NR, Lewington VJ, Blower PJ, Terry SYA. Re-assessing gallium-67 as a therapeutic radionuclide. *Nucl Med Biol*. 2017;46:12-18. doi:10.1016/j.nucmedbio.2016.10.008.
161. Bernard-Gauthier V, Wängler C, Schirmacher E, et al. ¹⁸F-labeled silicon-based fluoride acceptors: potential opportunities for novel positron emitting radiopharmaceuticals. *Biomed Res Int*. 2014;2014:454503. doi:10.1155/2014/454503.
162. *Labelling of small biomolecules using novel Technetium-99m Cores*. Vienna: Internat. Atomic Energy Agency; 2007. Technical reports series; 459.
163. Liu S, Edwards DS, Barrett JA. 99mTc labeling of highly potent small peptides. *Bioconjug Chem*. 1997;8:621-636. doi:10.1021/bc970058b.
164. Decristoforo C, Mather SJ, Cholewinski W, Donnemiller E, Riccabona G, Moncayo R. 99mTc-EDDA/HYNIC-TOC: a new 99mTc-labelled radiopharmaceutical for imaging somatostatin receptor-positive tumours; first clinical results and intra-patient comparison with 111In-labelled octreotide derivatives. *Eur J Nucl Med*. 2000;27:1318-1325. doi:10.1007/s002590000289.
165. Santos-Cuevas CL, Ferro-Flores G, Arteaga de Murphy C, Pichardo-Romero PA. Targeted imaging of gastrin-releasing peptide receptors with 99mTc-EDDA/HYNIC-Lys3-bombesin: biokinetics and dosimetry in women. *Nucl Med Commun*. 2008;29:741-747. doi:10.1097/MNM.0b013e3282ffb45c.
166. Ferro-Flores G, Luna-Gutiérrez M, Ocampo-García B, et al. Clinical translation of a PSMA inhibitor for 99mTc-based SPECT. *Nucl Med Biol*. 2017;48:36-44. doi:10.1016/j.nucmedbio.2017.01.012.
167. Maina T, Stolz B, Albert R, Bruns C, Koch P, Mäcke H. Synthesis, radiochemistry and biological evaluation of a new somatostatin analogue (SDZ 219-387) labelled with technetium-99m. *Eur J Nucl Med*. 1994;21:437-444. doi:10.1007/BF00171420.
168. Abiraj K, Ursillo S, Tamma ML, et al. The tetraamine chelator outperforms HYNIC in a new technetium-99m-labelled somatostatin receptor 2 antagonist. *EJNMMI Res*. 2018;8:75. doi:10.1186/s13550-018-0428-y.

169. Nock BA, Charalambidis D, Sallegger W, et al. New Gastrin Releasing Peptide Receptor-Directed ^{99m}TcDemobesin 1 Mimics: Synthesis and Comparative Evaluation. *J Med Chem.* 2018;61:3138-3150. doi:10.1021/acs.jmedchem.8b00177.
170. Elofsson M, Walse B, Kihlberg J. Building blocks for glycopeptide synthesis: glycosylation of 3-mercaptopropionic acid and Fmoc amino acids with unprotected carboxyl groups. *Tetrahedron Letters.* 1991;32:7613-7616. doi:10.1016/0040-4039(91)80548-K.
171. Salvador LA, Elofsson M, Kihlberg J. Preparation of building blocks for glycopeptide synthesis by glycosylation of Fmoc amino acids having unprotected carboxyl groups. *Tetrahedron.* 1995;51:5643-5656. doi:10.1016/0040-4020(95)00224-V.
172. Pathak AK, El-Kattan YA, Bansal N, Maddry JA, Reynolds RC. Tin(IV) chloride mediated glycosylation in arabinofuranose, galactofuranose and rhamnopyranose. *Tetrahedron Letters.* 1998;39:1497-1500. doi:10.1016/S0040-4039(98)00051-3.
173. Oscarson S. S-Glycosylation. In: Fraser-Reid BO, Tatsuta K, Thiem J, eds. *Glycoscience.* Berlin, Heidelberg: Springer Berlin Heidelberg; 2008:661-697.
174. Benito-Alifonso D, Galan MC. Brønsted- and Lewis-Acid-Catalyzed Glycosylation. In: Bennett CS, ed. *Selective Glycosylations: Synthetic Methods and Catalysts.* Weinheim, Germany: Wiley-VCH Verlag GmbH & Co. KGaA; 2017:155-172.
175. Surfraz MB-U, King R, Mather SJ, Biagini SCG, Blower PJ. Trifluoroacetyl-HYNIC peptides: synthesis and ^{99m}Tc radiolabeling. *J Med Chem.* 2007;50:1418-1422. doi:10.1021/jm061274l.
176. Nock B, Nikolopoulou A, Chiotellis E, et al. ^{99m}TcDemobesin 1, a novel potent bombesin analogue for GRP receptor-targeted tumour imaging. *Eur J Nucl Med Mol Imaging.* 2003;30:247-258. doi:10.1007/s00259-002-1040-x.
177. Maina T, Nock B, Nikolopoulou A, et al. ^{99m}TcDemotate, a new ^{99m}Tc-based Tyr3octreotate analogue for the detection of somatostatin receptor-positive tumours: synthesis and preclinical results. *Eur J Nucl Med Mol Imaging.* 2002;29:742-753. doi:10.1007/s00259-002-0782-9.
178. Corni S. Affinity and Selectivity of Peptides for Inorganic Materials: A Thermodynamic Discussion of the Role of Conformational Flexibility. *JOM.* 2015;67:781-787. doi:10.1007/s11837-015-1334-7.
179. Zhao B, Xu P, Jiang L, et al. A cyclic peptidic serine protease inhibitor: increasing affinity by increasing peptide flexibility. *PLoS ONE.* 2014;9:e115872. doi:10.1371/journal.pone.0115872.
180. Kogot JM, Sarkes DA, Val-Addo I, Pellegrino PM, Stratis-Cullum DN. Increased affinity and solubility of peptides used for direct peptide ELISA on polystyrene surfaces through fusion with a polystyrene-binding peptide tag. *Biotechniques.* 2012;52:95-102. doi:10.2144/000113810.
181. Banerjee S, Pillai MR, Ramamoorthy N. Evolution of Tc-^{99m} in diagnostic radiopharmaceuticals. *Semin Nucl Med.* 2001;31:260-277. doi:10.1053/snuc.2001.26205.
182. Sanders VA, Iskhakov D, Abdel-Atti D, et al. Synthesis, characterization and biological studies of rhenium, technetium-^{99m} and rhenium-188 pentapeptides. *Nucl Med Biol.* 2019;68-69:1-13. doi:10.1016/j.nucmedbio.2018.11.001.
183. Banerjee SR, Foss CA, Castanares M, et al. Synthesis and evaluation of technetium-^{99m}- and rhenium-labeled inhibitors of the prostate-specific membrane antigen (PSMA). *J Med Chem.* 2008;51:4504-4517. doi:10.1021/jm800111u.

184. Pillai MRA. *Technetium-99m radiopharmaceuticals: Status and trends*. Vienna: International Atomic Energy Agency; 2009. IAEA radioisotopes and radiopharmaceuticals series; no. 1.
185. Stefanick JF, Ashley JD, Bilgicer B. Enhanced cellular uptake of peptide-targeted nanoparticles through increased peptide hydrophilicity and optimized ethylene glycol peptide-linker length. *ACS Nano*. 2013;7:8115-8127. doi:10.1021/nn4033954.
186. Däpp S, García Garayoa E, Maes V, et al. PEGylation of (99m)Tc-labeled bombesin analogues improves their pharmacokinetic properties. *Nucl Med Biol*. 2011;38:997-1009. doi:10.1016/j.nucmedbio.2011.02.014.
187. Hu K, Kuan H, Hanyu M, et al. Developing native peptide-based radiotracers for PD-L1 PET imaging and improving imaging contrast by pegylation. *Chem Commun (Camb)*. 2019;55:4162-4165. doi:10.1039/C9CC00445A.
188. Leyton J, Iddon L, Perumal M, et al. Targeting somatostatin receptors: preclinical evaluation of novel 18F-fluoroethyltriazole-Tyr3-octreotate analogs for PET. *J Nucl Med*. 2011;52:1441-1448. doi:10.2967/jnumed.111.088906.
189. García Garayoa E, Schweinsberg C, Maes V, et al. Influence of the molecular charge on the biodistribution of bombesin analogues labeled with the 99mTc(CO)₃-core. *Bioconjug Chem*. 2008;19:2409-2416. doi:10.1021/bc800262m.
190. Parry JJ, Kelly TS, Andrews R, Rogers BE. In vitro and in vivo evaluation of 64Cu-labeled DOTA-linker-bombesin(7-14) analogues containing different amino acid linker moieties. *Bioconjug Chem*. 2007;18:1110-1117. doi:10.1021/bc0603788.
191. Haubner R, Wester HJ, Burkhart F, et al. Glycosylated RGD-containing peptides: tracer for tumor targeting and angiogenesis imaging with improved biokinetics. *J Nucl Med*. 2001;42:326-336.
192. Albert R, Marbach P, Bauer W, et al. SDZ CO 611: a highly potent glycosylated analog of somatostatin with improved oral activity. *Life Sciences*. 1993;53:517-525. doi:10.1016/0024-3205(93)90703-6.
193. Kihlberg J, Ahman J, Walse B, et al. Glycosylated peptide hormones: pharmacological properties and conformational studies of analogues of 1-desamino,8-D-arginine vasopressin. *J Med Chem*. 1995;38:161-169. doi:10.1021/jm00001a021.
194. Giammei C, Balber T, Benčurová K, et al. Sorbitol as a Polar Pharmacological Modifier to Enhance the Hydrophilicity of 99mTc-Tricarbonyl-Based Radiopharmaceuticals. *Molecules*. 2020;25. doi:10.3390/molecules25112680.
195. Moradi SV, Hussein WM, Varamini P, Simerska P, Toth I. Glycosylation, an effective synthetic strategy to improve the bioavailability of therapeutic peptides. *Chem Sci*. 2016;7:2492-2500. doi:10.1039/c5sc04392a.
196. Schottelius M, Rau F, Reubi JC, Schwaiger M, Wester H-J. Modulation of pharmacokinetics of radioiodinated sugar-conjugated somatostatin analogues by variation of peptide net charge and carbohydrate chemistry. *Bioconjug Chem*. 2005;16:429-437. doi:10.1021/bc0499228.
197. Mikaeili A, Erfani M, Shafiei M, Kobarfard F, Abdi K, Sabzevari O. Development of a 99mTc-Labeled CXCR4 Antagonist Derivative as a New Tumor Radiotracer. *Cancer Biother Radiopharm*. 2018;33:17-24. doi:10.1089/cbr.2017.2226.

198. Hesselgesser J, Liang M, Hoxie J, et al. Identification and characterization of the CXCR4 chemokine receptor in human T cell lines: ligand binding, biological activity, and HIV-1 infectivity. *J Immunol.* 1998;160:877-883.
199. Mikolajków A, Chomicki OA. Scanning of the stomach with ^{99m}Tc. *Digestion.* 1970;3:357-367. doi:10.1159/000197056.
200. Vag T, Gerngross C, Herhaus P, et al. First Experience with Chemokine Receptor CXCR4-Targeted PET Imaging of Patients with Solid Cancers. *J Nucl Med.* 2016;57:741-746. doi:10.2967/jnumed.115.161034.
201. Franken PR, Guglielmi J, Vanhove C, et al. Distribution and dynamics of (^{99m}Tc)-pertechnetate uptake in the thyroid and other organs assessed by single-photon emission computed tomography in living mice. *Thyroid.* 2010;20:519-526. doi:10.1089/thy.2009.0213.
202. Urbán S, Meyer C, Dahlbom M, et al. Radiation dosimetry of Tc^{99m}-PSMA I&S: a single-center prospective study. *J Nucl Med.* 2020;jnumed.120.253476. doi:10.2967/jnumed.120.253476.
203. Herrmann K, Lapa C, Wester H-J, et al. Biodistribution and radiation dosimetry for the chemokine receptor CXCR4-targeting probe ⁶⁸Ga-pentixafor. *J Nucl Med.* 2015;56:410-416. doi:10.2967/jnumed.114.151647.
204. Wiesing U. Theranostics: is it really a revolution? Evaluating a new term in medicine. *Med Health Care Philos.* 2019;22:593-597. doi:10.1007/s11019-019-09898-3.
205. Langbein T, Weber WA, Eiber M. Future of Theranostics: An Outlook on Precision Oncology in Nuclear Medicine. *J Nucl Med.* 2019;60:13S-19S. doi:10.2967/jnumed.118.220566.
206. Fani M, Nicolas GP, Wild D. Somatostatin Receptor Antagonists for Imaging and Therapy. *J Nucl Med.* 2017;58:61S-66S. doi:10.2967/jnumed.116.186783.
207. Eiber M, Fendler WP, Rowe SP, et al. Prostate-Specific Membrane Antigen Ligands for Imaging and Therapy. *J Nucl Med.* 2017;58:67S-76S. doi:10.2967/jnumed.116.186767.
208. Notni J, Wester H-J. Re-thinking the role of radiometal isotopes: Towards a future concept for theranostic radiopharmaceuticals. *J Labelled Comp Radiopharm.* 2018:141-153. doi:10.1002/jlcr.3582.
209. Kopka K, Benešová M, Bařinka C, Haberkorn U, Babich J. Glu-Ureido-Based Inhibitors of Prostate-Specific Membrane Antigen: Lessons Learned During the Development of a Novel Class of Low-Molecular-Weight Theranostic Radiotracers. *J Nucl Med.* 2017;58:17S-26S. doi:10.2967/jnumed.116.186775.
210. Wurzer A, Di Carlo D, Schmidt A, et al. Radiohybrid Ligands: A Novel Tracer Concept Exemplified by ¹⁸F- or ⁶⁸Ga-Labeled rhPSMA Inhibitors. *J Nucl Med.* 2020:735-742. doi:10.2967/jnumed.119.234922.
211. Kircher M, Herhaus P, Schottelius M, et al. CXCR4-directed theranostics in oncology and inflammation. *Ann Nucl Med.* 2018:503-511. doi:10.1007/s12149-018-1290-8.
212. Schottelius M, Konrad M, Osl T, Poschenrieder A, Wester H-J. An optimized strategy for the mild and efficient solution phase iodination of tyrosine residues in bioactive peptides. *Tetrahedron Letters.* 2015;56:6602-6605. doi:10.1016/j.tetlet.2015.10.032.
213. Tamamis P, Floudas CA. Elucidating a key component of cancer metastasis: CXCL12 (SDF-1 α) binding to CXCR4. *J Chem Inf Model.* 2014;54:1174-1188. doi:10.1021/ci500069y.

214. Crump MP, Gong JH, Loetscher P, et al. Solution structure and basis for functional activity of stromal cell-derived factor-1; dissociation of CXCR4 activation from binding and inhibition of HIV-1. *EMBO J*. 1997;16:6996-7007. doi:10.1093/emboj/16.23.6996.
215. Dalm SU, Nonnekens J, Doeswijk GN, et al. Comparison of the Therapeutic Response to Treatment with a ¹⁷⁷Lu-Labeled Somatostatin Receptor Agonist and Antagonist in Preclinical Models. *J Nucl Med*. 2016;57:260-265. doi:10.2967/jnumed.115.167007.
216. Wild D, Fani M, Fischer R, et al. Comparison of somatostatin receptor agonist and antagonist for peptide receptor radionuclide therapy: a pilot study. *J Nucl Med*. 2014;55:1248-1252. doi:10.2967/jnumed.114.138834.
217. Ginj M, Zhang H, Waser B, et al. Radiolabeled somatostatin receptor antagonists are preferable to agonists for in vivo peptide receptor targeting of tumors. *Proc Natl Acad Sci U S A*. 2006;103:16436-16441. doi:10.1073/pnas.0607761103.
218. Cescato R, Maina T, Nock B, et al. Bombesin receptor antagonists may be preferable to agonists for tumor targeting. *J Nucl Med*. 2008;49:318-326. doi:10.2967/jnumed.107.045054.
219. Fani M, Maecke HR, Okarvi SM. Radiolabeled peptides: valuable tools for the detection and treatment of cancer. *Theranostics*. 2012;2:481-501. doi:10.7150/thno.4024.
220. Lozza C, Navarro-Teulon I, Pèlegri A, Pouget J-P, Vivès E. Peptides in receptor-mediated radiotherapy: from design to the clinical application in cancers. *Front Oncol*. 2013;3:247. doi:10.3389/fonc.2013.00247.
221. Jamous M, Haberkorn U, Mier W. Synthesis of peptide radiopharmaceuticals for the therapy and diagnosis of tumor diseases. *Molecules*. 2013;18:3379-3409. doi:10.3390/molecules18033379.
222. Gotthardt M, van Eerd-Vismale J, Oyen WJG, et al. Indication for different mechanisms of kidney uptake of radiolabeled peptides. *J Nucl Med*. 2007;48:596-601. doi:10.2967/jnumed.106.036020.
223. Rolleman EJ, Melis M, Valkema R, Boerman OC, Krenning EP, Jong M de. Kidney protection during peptide receptor radionuclide therapy with somatostatin analogues. *Eur J Nucl Med Mol Imaging*. 2010;37:1018-1031. doi:10.1007/s00259-009-1282-y.
224. Ferreira G, Iravani A, Hofman MS, Hicks RJ. Intra-individual comparison of ⁶⁸Ga-PSMA-11 and ¹⁸F-DCFPyL normal-organ biodistribution. *Cancer Imaging*. 2019;19:23. doi:10.1186/s40644-019-0211-y.
225. Werner RA, Derlin T, Lapa C, et al. ¹⁸F-Labeled, PSMA-Targeted Radiotracers: Leveraging the Advantages of Radiofluorination for Prostate Cancer Molecular Imaging. *Theranostics*. 2020;10:1-16. doi:10.7150/thno.37894.
226. Bernard-Gauthier V, Bailey JJ, Liu Z, et al. From Unorthodox to Established: The Current Status of (¹⁸F)-Trifluoroborate- and (¹⁸F)-SiFA-Based Radiopharmaceuticals in PET Nuclear Imaging. *Bioconjug Chem*. 2016;27:267-279. doi:10.1021/acs.bioconjchem.5b00560.
227. Wängler C, Niedermoser S, Chin J, et al. One-step (¹⁸F)-labeling of peptides for positron emission tomography imaging using the SiFA methodology. *Nat Protoc*. 2012;7:1946-1955. doi:10.1038/nprot.2012.109.

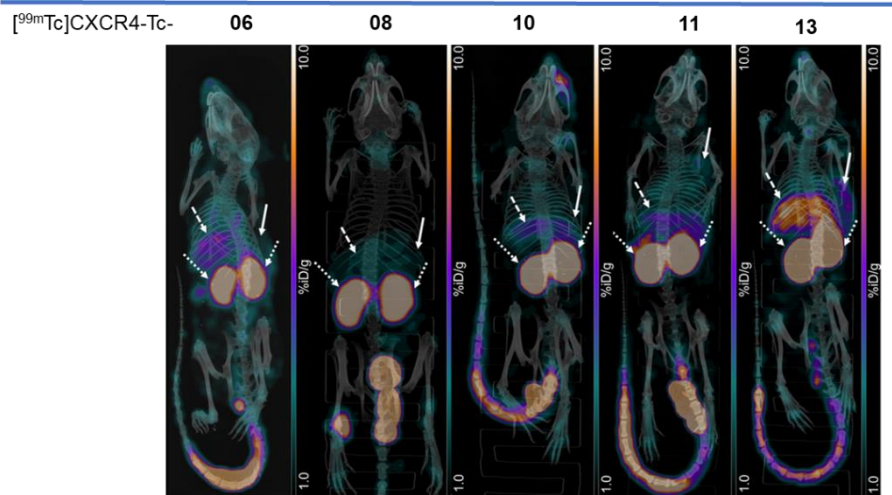
228. Kwon D, Lozada J, Zhang Z, et al. High-Contrast CXCR4-Targeted 18F-PET Imaging Using a Potent and Selective Antagonist. *Mol Pharm.* 2021;18:187-197. doi:10.1021/acs.molpharmaceut.0c00785.
229. Litau S, Niedermoser S, Vogler N, et al. Next Generation of SiFAlin-Based TATE Derivatives for PET Imaging of SSTR-Positive Tumors: Influence of Molecular Design on In Vitro SSTR Binding and In Vivo Pharmacokinetics. *Bioconjug Chem.* 2015;26:2350-2359. doi:10.1021/acs.bioconjchem.5b00510.
230. Lindner S, Simmet M, Gildehaus FJ, et al. Automated production of 18FSiTATE on a Scintomics GRP™ platform for PET/CT imaging of neuroendocrine tumors. *Nucl Med Biol.* 2020;88-89:86-95. doi:10.1016/j.nucmedbio.2020.07.008.
231. Wurzer A, Di Carlo D, Herz M, et al. Automated synthesis of 18FGa-rhPSMA-7/-7.3: results, quality control and experience from more than 200 routine productions. *EJNMMI Radiopharm Chem.* 2021;6:4. doi:10.1186/s41181-021-00120-5.
232. Oun R, Moussa YE, Wheate NJ. The side effects of platinum-based chemotherapy drugs: a review for chemists. *Dalton Trans.* 2018;47:6645-6653. doi:10.1039/c8dt00838h.
233. Nurgali K, Jagoe RT, Abalo R. Editorial: Adverse Effects of Cancer Chemotherapy: Anything New to Improve Tolerance and Reduce Sequelae? *Front Pharmacol.* 2018;9:245. doi:10.3389/fphar.2018.00245.
234. Delahousse J, Skarbek C, Paci A. Prodrugs as drug delivery system in oncology. *Cancer Chemother Pharmacol.* 2019;84:937-958. doi:10.1007/s00280-019-03906-2.
235. Ma L, Wang C, He Z, Cheng B, Zheng L, Huang K. Peptide-Drug Conjugate: A Novel Drug Design Approach. *Curr Med Chem.* 2017;24:3373-3396. doi:10.2174/0929867324666170404142840.
236. Shim H. Bispecific Antibodies and Antibody-Drug Conjugates for Cancer Therapy: Technological Considerations. *Biomolecules.* 2020;10. doi:10.3390/biom10030360.
237. Kratz F, Müller IA, Ryppa C, Warnecke A. Prodrug strategies in anticancer chemotherapy. *ChemMedChem.* 2008;3:20-53. doi:10.1002/cmdc.200700159.
238. Doronina SO, Bovee TD, Meyer DW, et al. Novel peptide linkers for highly potent antibody-auristatin conjugate. *Bioconjug Chem.* 2008;19:1960-1963. doi:10.1021/bc800289a.
239. Billiet L, Gok O, Dove AP, Sanyal A, Nguyen L-TT, Du Prez FE. Metal-Free Functionalization of Linear Polyurethanes by Thiol-Maleimide Coupling Reactions. *Macromolecules.* 2011;44:7874-7878. doi:10.1021/ma201323g.
240. Saha GB, Whitten J, Go RT. Conditions of radioiodination with iodogen as oxidizing agent. *International Journal of Radiation Applications and Instrumentation. Part B. Nuclear Medicine and Biology.* 1989;16:431-433. doi:10.1016/0883-2897(89)90112-8.
241. Koenig JA, Edwardson JM, Humphrey PP. Somatostatin receptors in Neuro2A neuroblastoma cells: ligand internalization. *Br J Pharmacol.* 1997;120:52-59. doi:10.1038/sj.bjp.0700859.
242. Koenig JA, Kaur R, Dodgeon I, Edwardson JM, Humphrey PP. Fates of endocytosed somatostatin sst2 receptors and associated agonists. *Biochem J.* 1998;336 (Pt 2):291-298. doi:10.1042/bj3360291.
243. Bunnett NW, Reeve JR, Walsh JH. Catabolism of bombesin in the interstitial fluid of the rat stomach. *Neuropeptides.* 1983;4:55-64. doi:10.1016/0143-4179(83)90009-4.

244. Kuhnast B, Bodenstein C, Haubner R, et al. Targeting of gelatinase activity with a radiolabeled cyclic HWGF peptide. *Nucl Med Biol.* 2004;31:337-344. doi:10.1016/j.nucmedbio.2003.10.011.
245. Fontaine SD, Reid R, Robinson L, Ashley GW, Santi DV. Long-term stabilization of maleimide-thiol conjugates. *Bioconjug Chem.* 2015;26:145-152. doi:10.1021/bc5005262.
246. Ravasco JMJM, Faustino H, Trindade A, Gois PMP. Bioconjugation with Maleimides: A Useful Tool for Chemical Biology. *Chemistry.* 2019;25:43-59. doi:10.1002/chem.201803174.
247. Joshi BP, Wang TD. Targeted Optical Imaging Agents in Cancer: Focus on Clinical Applications. *Contrast Media Mol Imaging.* 2018;2018:1-19. doi:10.1155/2018/2015237.
248. Melendez-Alafort L, Muzzio PC, Rosato A. Optical and multimodal peptide-based probes for in vivo molecular imaging. *Anticancer Agents Med Chem.* 2012;12:476-499. doi:10.2174/187152012800617858.
249. Aina OH, Marik J, Gandour-Edwards R, Lam KS. Near-infrared optical imaging of ovarian cancer xenografts with novel alpha 3-integrin binding peptide "OA02". *Mol Imaging.* 2005;4:439-447.
250. Staderini M, Megia-Fernandez A, Dhaliwal K, Bradley M. Peptides for optical medical imaging and steps towards therapy. *Bioorganic & Medicinal Chemistry.* 2018;26:2816-2826. doi:10.1016/j.bmc.2017.09.039.
251. Kuil J, Buckle T, Yuan H, et al. Synthesis and evaluation of a bimodal CXCR4 antagonistic peptide. *Bioconjug Chem.* 2011;22:859-864. doi:10.1021/bc2000947.
252. Nishizawa K, Nishiyama H, Oishi S, et al. Fluorescent imaging of high-grade bladder cancer using a specific antagonist for chemokine receptor CXCR4. *Int J Cancer.* 2010;127:1180-1187. doi:10.1002/ijc.25145.
253. Kuil J, Buckle T, Oldenburg J, et al. Hybrid peptide dendrimers for imaging of chemokine receptor 4 (CXCR4) expression. *Mol Pharm.* 2011;8:2444-2453. doi:10.1021/mp200401p.
254. Nayak TR, Hong H, Zhang Y, Cai W. Multimodality imaging of CXCR4 in cancer: current status towards clinical translation. *Curr Mol Med.* 2013;13:1538-1548. doi:10.2174/156652401366613111121325.
255. Sand LGL, Buckle T, van Leeuwen FWB, et al. Fluorescent CXCR4 targeting peptide as alternative for antibody staining in Ewing sarcoma. *BMC Cancer.* 2017;17:383. doi:10.1186/s12885-017-3352-z.
256. van den Berg NS, Buckle T, Kuil J, Wesseling J, van Leeuwen FWB. Immunohistochemical detection of the CXCR4 expression in tumor tissue using the fluorescent peptide antagonist Ac-TZ14011-FITC. *Transl Oncol.* 2011;4:234-240. doi:10.1593/tlo.11115.
257. Buckle T, van Berg NS, Kuil J, et al. Non-invasive longitudinal imaging of tumor progression using an (111)indium labeled CXCR4 peptide antagonist. *Am J Nucl Med Mol Imaging.* 2012;2:99-109. Published December 15, 2011.
258. Knight JC, Hallett AJ, Brancale A, Paisey SJ, Clarkson RWE, Edwards PG. Evaluation of a fluorescent derivative of AMD3100 and its interaction with the CXCR4 chemokine receptor. *Chembiochem.* 2011;12:2692-2698. doi:10.1002/cbic.201100441.
259. Khan A, Silversides JD, Madden L, Greenman J, Archibald SJ. Fluorescent CXCR4 chemokine receptor antagonists: metal activated binding. *Chem Commun (Camb).* 2007:416-418. doi:10.1039/b614557d.

VI. APPENDIX

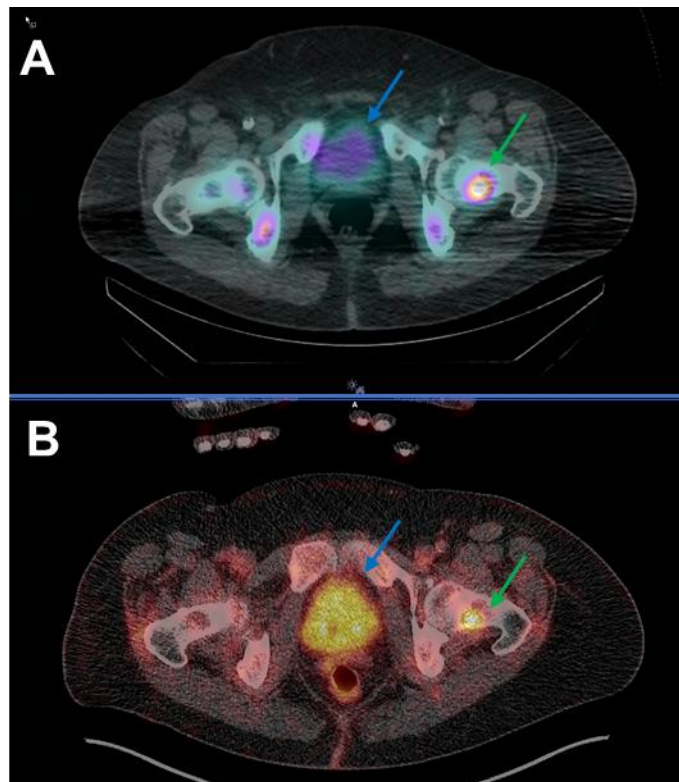
1. Additional Data

Blockage of [^{99m}Tc]CXCR4-Tc-06, -08, -10 – 13



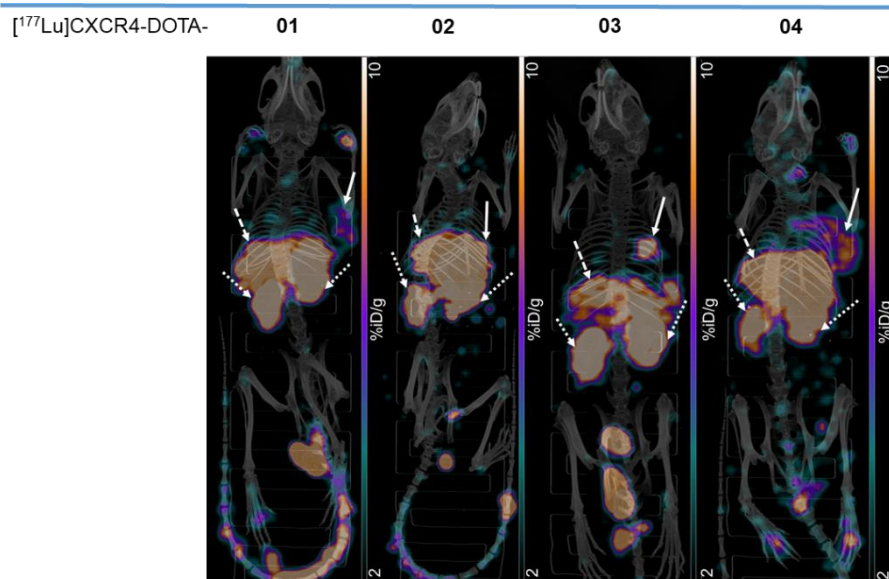
Supplementary 1: Results of SPECT/CT imaging studies 1h post injection of [^{99m}Tc]CXCR4-Tc-06, -08, -10 – 13 in presence of 100 nmol AMD3100 in Jurkat tumor-bearing female CB-17 SCID mice: Maximum-intensity projection images obtained from static SPECT imaging of 1 animal per ligand; Arrows indicate organs of special interest: straight: tumor, dashed: liver, pointed: kidneys.

SPECT/CT and PET/CT imaging in men



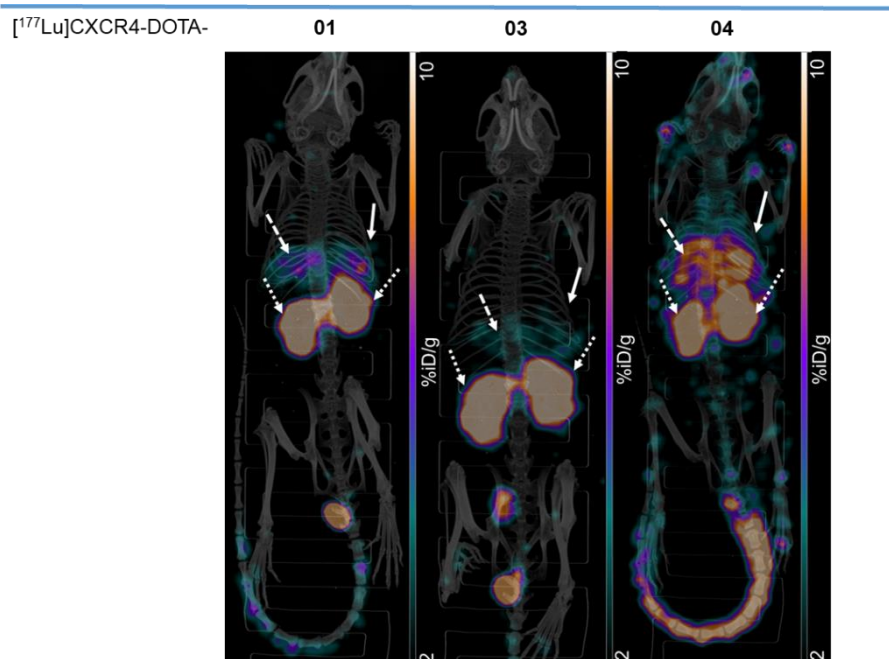
Supplementary 2: **A)** SPECT/CT image of the axial plane 3h p.i. of 604 MBq [^{99m}Tc]CXCR4-Tc-13 in a patient suffering from multiple myeloma; **B)** PET/CT image of the axial plane 1h p.i. of 189 MBq [^{18}F]FDG in the same patient: blue arrows indicate the urinary bladder, green arrows indicate osteolytic lesions.

Imaging of [¹⁷⁷Lu]CXCR4-DOTA-01 – 04



Supplementary 3: Results of SPECT/CT imaging studies 1h post injection of [¹⁷⁷Lu]CXCR4-DOTA-01 – 04 in Jurkat tumor-bearing female CB-17 SCID mice: Maximum-intensity projection images obtained from static SPECT imaging of 1 animal per ligand; Arrows indicate organs of special interest: straight: tumor, dashed: liver, pointed: kidneys.

Blockage of [¹⁷⁷Lu]CXCR4-DOTA-01 – 04



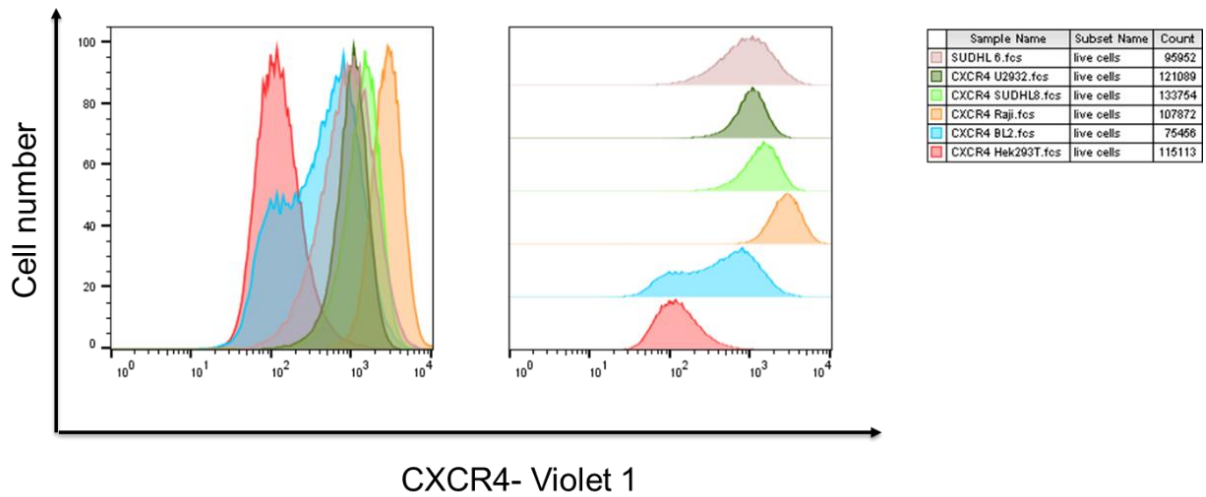
Supplementary 4: Results of SPECT/CT imaging studies 1h post injection of [¹⁷⁷Lu]CXCR4-DOTA-01 – 04 in presence of 100 nmol AMD3100 in Jurkat tumor-bearing female CB-17 SCID mice: Maximum-intensity projection images obtained from static SPECT imaging of 1 animal per ligand; Arrows indicate organs of special interest: straight: tumor, dashed: liver, pointed: kidneys.

Tumor Time-Activity-curve interpolation for [¹⁷⁷Lu]CXCR4-DOXA-03, -04 and [¹⁷⁷Lu]Pentixather

Time p.i. [h]	Tumoral activity			Time p.i. [h]	Tumoral activity		
	[¹⁷⁷ Lu]Pentixather	[¹⁷⁷ Lu]CXCR4-DOXA-03	[¹⁷⁷ Lu]CXCR4-DOXA-04		[¹⁷⁷ Lu]Pentixather	[¹⁷⁷ Lu]CXCR4-DOXA-03	[¹⁷⁷ Lu]CXCR4-DOXA-04
1	5,86707	8,42	6,19	24,73737	4,47589	4,26537	9,92029
1,47475	5,83461	8,26693	6,34926	25,21212	4,45287	4,2548	9,90716
1,94949	5,80218	8,11423	6,50806	25,68687	4,43	4,24637	9,89146
2,42424	5,76979	7,96228	6,66596	26,16162	4,40726	4,24003	9,87322
2,89899	5,73748	7,81145	6,8225	26,63636	4,38465	4,23574	9,8525
3,37374	5,70527	7,66212	6,97723	27,11111	4,36218	4,23345	9,82937
3,84848	5,67319	7,51465	7,1297	27,58586	4,33984	4,23312	9,80386
4,32323	5,64125	7,36943	7,27946	28,06061	4,31762	4,2347	9,77604
4,79798	5,60948	7,22683	7,42605	28,53535	4,29553	4,23816	9,74595
5,27273	5,57792	7,08722	7,56903	29,0101	4,27356	4,24343	9,71366
5,74747	5,54657	6,95097	7,70793	29,48485	4,25171	4,25049	9,67922
6,22222	5,51548	6,81846	7,84232	29,9596	4,22997	4,25929	9,64268
6,69697	5,48464	6,68985	7,97198	30,43434	4,20834	4,26977	9,60409
7,17172	5,45406	6,56511	8,09696	30,90909	4,18683	4,2819	9,5635
7,64646	5,42373	6,4442	8,21731	31,38384	4,16542	4,29564	9,52098
8,12121	5,39365	6,32708	8,33308	31,85859	4,14411	4,31093	9,47658
8,59596	5,36382	6,21369	8,44433	32,33333	4,1229	4,32774	9,43034
9,07071	5,33424	6,104	8,55112	32,80808	4,10179	4,34601	9,38233
9,54545	5,30489	5,99796	8,65348	33,28283	4,08078	4,36571	9,3326
10,0202	5,27579	5,89552	8,75149	33,75758	4,05985	4,38679	9,28119
10,49495	5,24692	5,79664	8,84519	34,23232	4,03902	4,4092	9,22817
10,9697	5,21828	5,70128	8,93463	34,70707	4,01827	4,43291	9,17359
11,44444	5,18988	5,6094	9,01988	35,18182	3,9976	4,45786	9,1175
11,91919	5,1617	5,52094	9,10097	35,65657	3,97701	4,48401	9,05996
12,39394	5,13374	5,43586	9,17798	36,13131	3,9565	4,51132	9,00102
12,86869	5,10601	5,35412	9,25095	36,60606	3,93606	4,53975	8,94073
13,34343	5,07849	5,27567	9,31994	37,08081	3,91569	4,56924	8,87915
13,81818	5,05119	5,20048	9,38499	37,55556	3,89539	4,59975	8,81633
14,29293	5,0241	5,12848	9,44617	38,0303	3,87516	4,63125	8,75233
14,76768	4,99723	5,05965	9,50352	38,50505	3,85499	4,66368	8,6872
15,24242	4,97055	4,99394	9,55711	38,9798	3,83487	4,697	8,62099
15,71717	4,94408	4,93129	9,60698	39,45455	3,81482	4,73116	8,55375
16,19192	4,91781	4,87167	9,65319	39,92929	3,79481	4,76613	8,48555
16,66667	4,89174	4,81504	9,69579	40,40404	3,77486	4,80185	8,41643
17,14141	4,86587	4,76134	9,73484	40,87879	3,75495	4,83828	8,34645
17,61616	4,84018	4,71053	9,77039	41,35354	3,73509	4,87539	8,27567
18,09091	4,81469	4,66258	9,8025	41,82828	3,71527	4,91311	8,20413
18,56566	4,78937	4,61742	9,83121	42,30303	3,69548	4,95142	8,13188
19,0404	4,76425	4,57503	9,85658	42,77778	3,67574	4,99025	8,059
19,51515	4,7393	4,53535	9,87867	43,25253	3,65602	5,02958	7,98552
19,9899	4,71453	4,49835	9,89753	43,72727	3,63633	5,06936	7,9115
20,46465	4,68993	4,46397	9,91321	44,20202	3,61667	5,10953	7,837
20,93939	4,6655	4,43217	9,92577	44,67677	3,59704	5,15006	7,76207
21,41414	4,64125	4,40291	9,93526	45,15152	3,57742	5,1909	7,68676
21,88889	4,61715	4,37614	9,94174	45,62626	3,55783	5,23201	7,61112
22,36364	4,59322	4,35181	9,94525	46,10101	3,53824	5,27334	7,53522
22,83838	4,56945	4,3299	9,94586	46,57576	3,51867	5,31485	7,45911
23,31313	4,54583	4,31034	9,94361	47,05051	3,49911	5,35649	7,38283
23,78788	4,52237	4,29309	9,93856	47,52525	3,47955	5,39822	7,30644
24,26263	4,49906	4,27812	9,93077	48	3,46	5,44	7,23

Supplementary 5: Time-activity-curve interpolation of tumor activity of [¹⁷⁷Lu]CXCR4-DOXA-03 and -04 as well as [¹⁷⁷Lu]Pentixather; Start and end values were taken from 1h and 48h biodistribution experiments with the respective ligands.

FACS for CXCR4 expression levels



Supplementary 6: FACS of different cell types to determine their CXCR4 expression levels; higher CXCR4 expression is observed for higher values of CXCR4-Violet 1.

2. List of Abbreviations

2-CTC	2-Chlorotrityl chloride	FBS	Fetal bovine serum
Abz	Para-aminobenzoic acid	FDG	Fluorodeoxyglucose
ACKR3	Atypical chemokine receptor 3	GMP	Good manufacturing practice
ACN	Acetonitrile	GP	General procedure
Ahx	6-Aminohexanoic acid	GPCR	G-protein-coupled receptor
Ambz	Para-aminomethylbenzoic acid	GRPR	Gastrin-releasing peptide receptor
AUC	Area-under-the-curve	HATU	[O-(7-Azabenzotriazol-1-yl)-N,N,N',N'-tetramethyluronium-hexafluorophosphat]
Boc	Tert-butyl oxycarbonyl	HBSS	Hank's buffered salt solution
BSA	Bovine serum albumin	HEPES	4-(2-Hydroxyethyl)-1-piperazineethanesulfonic acid
CAF	Cancer-associated fibroblasts	HFIP	1,1,1,3,3,3-Hexafluoro-2-propanol
cAMP	Cyclic adenosine monophosphate	HI	Human immunodeficiency
CDI	Carbonyldiimidazole	HIV	Human immunodeficiency virus
CT	Computed tomography	HLB	Hydrophilic-lipophilic balance
d.c.	Decay-corrected	HOAt	1-Hydroxy-7-azabenzotriazol
dap	2,3-Diamino propionic acid	HOBt	1-Hydroxybenzotriazole
DBU	1,8-Diazabicyclo[5.4.0]undec-7-en	HYNIC	Hydrazinonicotinic acid
DCE	Dichloroethane	i.v.	Intravenous
DCM	Dichloromethane	iD	Injected dose
Dde	N-(1-(4,4-Dimethyl-2,6-dioxocyclohexylidene)ethyl)	ITLC-SG	Instant thin-layer chromatography-silica gel
DIAD	Diisopropyl azodicarboxylate	KO	Knock-out
DIPEA	N,N-Diisopropylethylamine	MIF	Macrophage migration inhibitory factor
DMAP	4-(dimethylamino)pyridine	MMAE	Monomethyl auristatin-E
DMEM	Dulbecco's modified Eagle's medium	MRT	Magnetic resonance tomography
DMF	N,N-Dimethylformamide	n.d.c.	non-decay corrected
DMSO	Dimethylsulfoxide	N4	3-((2-Aminoethyl)amino)-2-(((2-aminoethyl)amino)methyl)propanoic acid
DOTA	2,2',2'',2'''-(1,4,7,10-Tetraazacyclododecane-1,4,7,10-tetrayl)tetraacetic acid	NEA	Non-essential amino acid
DOTA-GA	5-(tert-butoxy)-5-oxo-4-(4,7,10-tris(2-(tert-butoxy)-2-oxoethyl)-1,4,7,10-tetraazacyclododecan-1-yl)pentanoic acid	NIR	Near-infrared
DPPA	Diphenylphosphorylazide	NIS	N-iodosuccinimid
ECL	Extracellular loop	NMP	N-Methyl-2-pyrrolidon
ECR	Extracellular region	NOTA	2,2',2''-(1,4,7-Triazacyclononane-1,4,7-triyl)triacetic acid
EDDA	Ethylenediaminediacetic acid	OI	Optical imaging
EDTA	Ethylendiaminetetraacetic acid	O-NBS-Cl	2-Nitrobenzene sulfonylchloride
EGF	Epidermal growth factor	p.i.	Post injection
EOS	End of synthesis	Pbf	2,2,4,6,7-Pentamethyldihydrobenzofuran-5-sulfonyl
Et ₂ O	Diethylether	PBS	Phosphate-buffered saline
EtOAc	Ethylacetate	PCC	Pyridinium chlorochromate
EtOH	Ethanol		
FACS	Fluorescence-activated cell sorting		

PDC *Peptide-drug conjugate*
 PEG *Polyethylene glycol*
 PET *Positron emission tomography, Positron emission tomography*
 PRRT *Peptide-receptor radionuclide therapy*
 PSA *Prostate-specific antigen*
 PSMA *Prostate-specific membrane antigen*
 r.t. *Room temperature*
 R_f *Retarding front*
 rh *Radiohybrid*
 RP-HPLC *Reversed-phase high pressure liquid chromatography*
 RPMI *Rosewell park memorial institute*
 sat. *Saturated*
 SAX *Strong anion exchange*
 SD *Standard deviation*
 SDF-1 *Stromal cell-derived factor-1*
 SiFA *Silicon-fluoride acceptor*
 SiFA-BA *SiFA-benzoic acid*
 SiFA-Br *SiFA-bromide*
 SPE *Solid phase extraction*
 SPECT *Single-photon emission computed tomography*
 SPPS *Solid-phase peptide synthesis*
 sst *Somatostatin*
 sstr *Somatostatin receptor*
 TBDMSCl *Tert-butyldimethylsilyl chloride*
 TBTU *2-(1H-Benzotriazole-1-yl)-1,1,3,3-tetramethylaminium tetrafluoroborate*
 tBu *Tert-butyl*
 TEA *Triethylamine*
 TFA *Trifluoroacetic acid*
 THF *Tetrahydrofuran*
 TIPS *Triisopropylsilane*
 TLC *Thin-layer chromatography*
 TM *Trans-membrane region*
 TMA *Trimethylamine*
 t_R *Retention time*
 TRIS *Tris(hydroxymethyl)amino methane*
 Trt *Trityl*
 US *Ultrasound*
 USA *United States of America*
 UV *Ultraviolet*
 VEGF *Vascular endothelial growth factor*
 WHO *World health organization*

3. Figure Index

FIGURE 1: RANKING OF CANCER-ASSOCIATED PREMATURE MORTALITY WORLDWIDE; FIGURE ADAPTED FROM LITERATURE (1).	1
FIGURE 2: THE PRINCIPLES OF PET AND SPECT IMAGING: A : SCHEMATIC REPRESENTATION OF I.V. PET TRACER APPLICATION AND Γ -PHOTON COINCIDENCE DETECTION BY A Γ -DETECTOR RING; POSITRON EMISSION AND ANNIHILATION BY COLLISION WITH AN ELECTRON UNDER EMISSION OF TWO Γ -PHOTONS IN OPPOSITE DIRECTION (ENCIRCLED), B : SCHEMATIC REPRESENTATION OF I.V. SPECT TRACER APPLICATION AND Γ -PHOTON DETECTION BY A ROTATING Γ -CAMERA; RELAXATION OF AN EXCITED RADIONUCLIDE UNDER EMISSION OF A Γ -PHOTON (ENCIRCLED).	2
FIGURE 3: SCHEMATIC REPRESENTATION OF LOCAL CANCER THERAPY BY RADIATION BEAM EXPOSURE AND SURGERY (LEFT SIDE); SYSTEMIC CHEMOTHERAPY USING AN UNSELECTIVE APPROACH (DOTTED ARROW) DAMAGING BOTH MALIGN AND BENIGN TISSUE AND TARGETED THERAPY (RED ARROW) THAT IDEALLY DAMAGES ONLY MALIGN TISSUE (RIGHT SIDE).	4
FIGURE 4: DOWNSTREAM SIGNALING PATHWAYS INITIATED BY CXCL12 BINDING ONTO CXCR4 AND THE SUBSEQUENT RELEASE OF INTRACELLULARLY ATTACHED HETEROTRIMERIC G-PROTEINS; THE ACTIVITY OF THE RECEPTOR IS THEN REGULATED BY RECRUITMENT OF B-ARRESTIN AND THE CONCOMITANT INTERNALIZATION OF THE CXCL12/CXCR4 COMPLEX; FIGURE ADAPTED FROM LITERATURE (55).	7
FIGURE 5: THE ROLE OF THE CXCR4/CXCL12/ACKR3 AXIS IN TUMOR PROLIFERATION AND METASTASIS: CROSSTALK OF CXCR4 EXPRESSING CANCER CELLS IN THE PRIMARY LESION WITH THE MICROENVIRONMENT SUCH AS CANCER-ASSOCIATED FIBROBLASTS (CAF) REGULATES TUMOR GROWTH AND SURVIVAL UNTIL A MISMATCH OCCURS THAT DRIVES THE TARGETED METASTASIS INTO CXCL12 EXPRESSING NICHES SUCH AS LUNG, LIVER, LYMPH NODES AND BONE MARROW; THE ROLE OF ACKR3 DURING TUMOR METASTASIS REMAINS UNCERTAIN; FIGURE ADAPTED FROM LITERATURE (60).	10
FIGURE 6: BINDING MODE OF FC-131 IN COMPLEX WITH THE CXCR4 RECEPTOR; CYCLIC PENTAPEPTIDES ARE LOCATED WITHIN THE MAJOR BINDING POCKET, SANDWICHED BETWEEN TRANSMEMBRANE (TM) REGIONS 3 AND 5 AND EXTRACELLULAR LOOP (ECL) 2; TYROSINE IS POINTING TOWARDS THE EXTRACELLULAR REGION (ECR). FIGURES WERE ADAPTED FROM (109) AND MODIFIED.	13
FIGURE 7: STRUCTURES OF PET IMAGING AGENT [⁶⁸ Ga]PENTIXAFOR AND ITS THERAPEUTIC ANALOG [⁹⁰ Y/ ¹⁷⁷ Lu]PENTIXATHER.	15
FIGURE 8: PET IMAGING OF A PATIENT SUFFERING FROM MULTIPLE MYELOMA PRE AND POST [¹⁷⁷ Lu]PENTIXATHER TREATMENT: A : PRE-TREATMENT MAXIMUM-INTENSITY PROJECTIONS (MIP) OF [¹⁸ F]FDG (LEFT) AND [⁶⁸ Ga]PENTIXAFOR (RIGHT) PET IMAGES; B : SCINTIGRAPHY IMAGES OF THE SAME PATIENT 7 DAYS AFTER INJECTION OF 7.8 GBq [¹⁷⁷ Lu]PENTIXATHER; C : POST-TREATMENT MIP OF [⁶⁸ Ga]PENTIXAFOR PET IMAGES OF THE SAME PATIENT; FIGURE ADAPTED FROM (136).	16
FIGURE 9: STRUCTURES (AND CORRESPONDING ARTISTIC 3D MODELS) OF THE CPCR4 BINDING SCAFFOLD (BLUE SPHERE) AND ITS IODINE CARRYING ANALOG I-CPCR4, PENTIXAFOR AND PENTIXATHER WITH THEIR AMBZ LINKER HIGHLIGHTED IN ORANGE (ORANGE CYLINDER) AND THE ABZ-A-R ANALOG WITH ITS IMPROVED LINKER HIGHLIGHTED IN BLUE (BLUE CYLINDER); INTERACTION SITES WITH THE CXCR4 BINDING CAVITY ARE HIGHLIGHTED IN GREEN (GREEN SPHERES) AND DOTA CHELATORS REPRESENTED BY YELLOW SPHERES.	18
FIGURE 10: MAXIMUM-INTENSITY-PROJECTION (MIP) IMAGES OF DAUDI XENOGRAFT-BEARING CB-17 SCID MICE INJECTED WITH [⁶⁸ Ga]PENTIXAFOR (LEFT), [⁶⁸ Ga]CPCR4-ABZ-A-R-DOTA (MIDDLE) AND [⁶⁸ Ga]I-CPCR4-ABZ-A-R-DOTA (RIGHT); STATIC PET IMAGES WERE ACQUIRED ONE HOUR AFTER INJECTION OF THE RESPECTIVE TRACER; FIGURES ADAPTED FROM (146).	19
FIGURE 11: THE SCOPE OF THIS WORK: DEVELOPMENT OF A NOVEL TRACER BACKBONE BASED ON CXCR4 LIGANDS CARRYING THE CPCR4 PEPTIDE SCAFFOLD (BLUE SPHERE) AND AN OPTIMIZED LINKER (BLUE CYLINDER) AS REPORTED BY OSL ET AL.:	

ENHANCEMENT OF THE LINKER-BINDING POCKET INTERACTION (GREEN SPHERES) BY ELONGATION WITH AN ADDITIONAL OPTIMIZED LINKER (GREEN CYLINDER) WHICH FACILITATES THE REMOVAL OF THE FUNCTIONAL MOIETY (YELLOW SPHERE) FROM THE BINDING CAVITY TO MINIMIZE REPULSION (RED SPHERE). THIS MODIFICATION ENABLES THE APPLICATION OF THIS TRACER BACKBONE IN PET, SPECT AND FLUORESCENCE IMAGING, PRRT AND TARGETED CHEMOTHERAPY.....	20
FIGURE 12: STRUCTURES OF A 1 ST GENERATION OF NOVEL CXCR4-TARGETED LIGANDS: COMPOUNDS WERE BASED ON THE CPCR4-ABZ-A-R SCAFFOLD DEVELOPED BY OSL ET AL. AND MODIFIED WITH PEPTIDIC MAS ₃ CHELATORS, SIFA-CONJUGATED MOIETIES AND A MMAE DERIVATIVE.	101
FIGURE 13: STRUCTURES OF A 2 ND GENERATION OF NOVEL CXCR4-TARGETED LIGANDS: COMPOUNDS WERE BASED ON THE CPCR4-ABZ-A-R-DAP TRACER BACKBONE DEVELOPED IN THIS WORK AND MODIFIED WITH DIFFERENT TECHNETIUM CHELATORS, DOTA, SIFA-BEARING MOIETIES AND A Cy5.5 FLUOROPHORE.	102
FIGURE 14: STRUCTURES OF A 3 RD GENERATION OF NOVEL CXCR4-TARGETED LIGANDS: COMPOUNDS WERE BASED ON THE EXTENDED CPCR4-ABZ-A-R-DAP-AHX TRACER BACKBONE DEVELOPED IN THIS WORK AND MODIFIED WITH A TECHNETIUM CHELATOR, SIFA-CONJUGATED MOIETIES, A Cy5.5 FLUOROPHORE AND A MMAE TOXIN DERIVATIVE.....	103
FIGURE 15: STRUCTURES OF DIFFERENT TECHNETIUM-99M COORDINATION STATES IN COMPLEX WITH THEIR RESPECTIVE CHELATOR: MAS ₃ , HYNIC/EDDA AND THE TETRADENTATE N4 CHELATOR; THE COORDINATION GEOMETRY IS SOLELY DEPENDENT ON THE CHELATORS PHYSICO-CHEMICAL PROPERTIES AND THE REDUCTION OF THE PERTECHNETATE ANION IN THEIR PRESENCE (163).	104
FIGURE 16: SUMMARY OF MAS ₃ -CONJUGATED 1 ST GENERATION COMPOUNDS CXCR4-Tc-01 – 06: NOVEL STRUCTURES WERE OBTAINED BY ELONGATION OF THE CPCR4-ABZ-A-R TRACER BACKBONE WITH ONE OF 5 AMINO ACIDS (X) AND A TERMINAL MAS ₃ CHELATOR.	106
FIGURE 17: SUMMARY OF 2 ND GENERATION COMPOUNDS CXCR4-Tc-06, 08 – 11: NOVEL STRUCTURES WERE OBTAINED BY ELONGATION OF THE OPTIMIZED CPCR4-ABZ-A-R-DAP TRACER BACKBONE (EXCEPT FOR CXCR4-Tc-07 WHICH CARRIES A CPCR4-AMBZ-A-R-DAP TRACER BACKBONE). CXCR4-Tc-06 AND -07 BEAR A TERMINAL MAS ₃ -CHELATOR AND CXCR4-Tc-08 – 11 BEAR GLYCOSYLATED CHELATORS.	107
FIGURE 18: MECHANISM OF THE ONE-POT REACTION OF SnCl ₄ WITH B-D-GLUCOSEPENTAACETATE IN PRESENCE OF FMOC-D-HCY(Trt)-OH AND TIPS, RESULTING IN THE SIDE-CHAIN-GLYCOSYLATED FMOC-D-HCY(B-D-GLUCOSE-TETRAACETATE)-OH SYNTHON; i) SnCl ₄ ACTS AS A LEWIS ACID BY COORDINATING AND ii) REMOVING THE A-ACETATE PROTECTING GROUP OF B-D-GLUCOSEPENTAACETATE; iii) THE B-ACETATE CARBONYL THEN FORMS THE ACETAL WITH THE NEIGHBORING CARBOCATION AND THEREFORE FACILITATES v) THE NUCLEOPHILIC ATTACK OF THE FMOC-D-HCY-OH SIDE CHAIN TO FORM THE FMOC-D-HCY(B-D-GLUCOSE-TETRAACETATE)-OH SYNTHON; iv) DE-PROTECTION OF FMOC-D-HCY(Trt)-OH IS SIMULTANEOUSLY ACHIEVED BY PARTIAL HYDROLYZATION OF SnCl ₄ IN THE SOLVENT AND REMOVAL OF THE TRITYL-CATION BY THE SCAVENGER TIPS; MECHANISM ADAPTED FROM (173,174)	108
FIGURE 19: SUMMARY OF STRUCTURES BEARING THE CHELATOR HYNIC: CXCR4-Tc-12 WAS OBTAINED BY MODIFICATION OF THE OPTIMIZED CPCR4-ABZ-A-R-DAP TRACER BACKBONE AND LITERATURE-KNOWN COMPOUND CXCR4-L WAS OBTAINED BY MODIFICATION OF THE CPCR4 SCAFFOLD WITH HYNIC.	109
FIGURE 20: FORMATION OF A TRIFLUOROACETYL-HYNIC BYPRODUCT DURING THE DE-PROTECTION OF A HYNIC(Boc)-CARRYING PEPTIDE USING TFA (175).	109
FIGURE 21: SUMMARY OF STRUCTURES BEARING THE CHELATOR N4: CXCR4-Tc-13 AND -14 WERE OBTAINED BY ELONGATION OF THE CPCR4-ABZ-A-R-DAP TRACER BACKBONE AND CXCR4-Tc-15 WAS OBTAINED BY ELONGATION OF THE CPCR4-ABZ-A-R-DAP-AHX TRACER BACKBONE WITH A N4-CONJUGATED MOIETY.....	110

FIGURE 22: FORMATION OF A HEAT-INDUCED ELIMINATION BYPRODUCT DURING THE SYNTHESIS OF THE N4(BOC)₄ CHELATOR AND N4(BOC)₄-CONJUGATED LIGANDS: **i**) REACTION OF 3-BROMO-2-(BROMOMETHYL)PROPANOIC ACID WITH TERT-BUTYL-(2-AMINOETHYL)-CARBAMATE AND SUBSEQUENT REACTION WITH BOC₂O TO YIELD THE FULLY PROTECTED N4(BOC)₄ CHELATOR; **ii**) HEAT-INDUCED ELIMINATION OF ETHYLENEDIAMINE(BOC)₂ FORMING THE UNDESIRED ELIMINATION PRODUCT; **iii**) ELIMINATION OF ETHYLENEDIAMINE(BOC)₂ UPON ACTIVATION OF THE PROTECTED CHELATOR WITH HOAt AND INCUBATION WITH DIPEA FOR MORE THAN 5 MINUTES; **iv**) SUCCESSFUL COUPLING OF THE PROTECTED CHELATOR ONTO PEPTIDES BY USING COLLIDINE AND INCUBATION FOR LESS THAN 5 MINUTES. 111

FIGURE 23: SECTIONS OF RADIO-RP-HPLC CHROMATOGRAMS REVEALING VARYING PROPORTIONS OF ISOMERS 1 AND 2 DURING THE TECHNETIUM-99M LABELING REACTION OF [^{99m}Tc]CXCR4-Tc-06; SAMPLES WERE TAKEN AT 20, 30, 60 AND 120 MIN REACTION TIME AND INSTANTLY SUBJECTED TO QUALITATIVE RP-HPLC MEASUREMENT. CHROMATOGRAMS FURTHER REVEAL THE TIMELY FORMATION OF A THIRD COMPONENT. 113

FIGURE 24: HYPOTHETICAL GRAPH PICTURING THE DISPLACEMENT OF TWO DIFFERENTLY AFFINE RADIOLIGANDS (COMPOUND 1 AND 2) FROM CELLS USING INCREASING CONCENTRATIONS OF THE STANDARD LIGAND FC-131: HIGHER CONCENTRATIONS OF FC-131 ARE NEEDED TO DISPLACE HALF OF THE CELL-BOUND COMPOUND 1 COMPARED TO LESS AFFINE COMPOUND 2 AND THE INVIC50 VALUE OF COMPOUND 1 IS THEREFORE HIGHER. 117

FIGURE 25: SUMMARY OF STRUCTURES OF GLYCOSYLATED COMPOUNDS DESCRIBED IN LITERATURE: AMADORI-REACTION PRODUCTS GLUCOSYL-, MALTOsyl- AND MALTOTRIOSYL-[I]TOC AND -[I]TOCA, RESPECTIVELY AS REPORTED BY SCHOTTELIUS ET AL.; GLYCOSYLATED C(RGD(I)YK(SAA)) AS REPORTED BY HAUBNER ET AL. 119

FIGURE 26: DUAL TRACER INTERNALIZATION OF RADIOLABELED NOVEL LIGANDS AND THE REFERENCE COMPOUND ¹²⁵I-FC-131 (FINAL ASSAY CONCENTRATION FOR EACH PEPTIDE 0.2 nM) INTO CHEM-1 CELLS (100,000 CELLS PER WELL; 37°C): **A**: [^{99m}Tc]CXCR4-Tc-06 AND -07, **B**: [^{99m}Tc]CXCR4-Tc-08 AND -09 AND **C**: [^{99m}Tc]CXCR4-Tc-10 AND -11. DATA ARE EXPRESSED AS MEAN ± SD; INTERNALIZATION AT EVERY TIME POINT WAS DETERMINED IN TRIPLICATE AND CORRECTED FOR UNSPECIFIC INTERNALIZATION; LINE DIAGRAMS: AMOUNT OF INTERNALIZED NOVEL LIGAND IN RELATION TO THE AMOUNT OF INTERNALIZED INTERNAL STANDARD ¹²⁵I-FC-131 IN %; BAR DIAGRAMS: AMOUNT OF INTERNALIZED NOVEL LIGAND IN RELATION TO THE TOTAL CELL-BOUND NOVEL LIGAND IN %. 122

FIGURE 27: DUAL TRACER INTERNALIZATION OF RADIOLABELED NOVEL LIGANDS AND THE REFERENCE COMPOUND ¹²⁵I-FC-131 (ASSAY-CONCENTRATION FOR EACH PEPTIDE 0.2 nM) INTO CHEM-1 CELLS (100,000 CELLS PER WELL; 37°C): **A**: [^{99m}Tc]CXCR4-Tc-06, -12 AND -13, **B**: [^{99m}Tc]CXCR4-Tc-13 AND -14. DATA ARE EXPRESSED AS MEAN ± SD; INTERNALIZATION AT EVERY TIME POINT WAS DETERMINED IN TRIPLICATE AND CORRECTED FOR UNSPECIFIC INTERNALIZATION; LINE DIAGRAMS: AMOUNT OF INTERNALIZED NOVEL LIGAND IN RELATION TO THE AMOUNT OF INTERNALIZED INTERNAL STANDARD ¹²⁵I-FC-131 IN %; BAR DIAGRAMS: AMOUNT OF INTERNALIZED NOVEL LIGAND IN RELATION TO THE TOTAL CELL-BOUND NOVEL LIGAND IN %. 127

FIGURE 28: DUAL TRACER INTERNALIZATION OF NOVEL LIGANDS [^{99m}Tc]CXCR4-Tc-14 AND -15 AND THE REFERENCE COMPOUND ¹²⁵I-FC-131 (ASSAY-CONCENTRATION FOR EACH PEPTIDE 0.2 nM) INTO CHEM-1 CELLS (100,000 CELLS PER WELL; 37°C). DATA ARE EXPRESSED AS MEAN ± SD; INTERNALIZATION AT EVERY TIME POINT WAS DETERMINED IN TRIPLICATE AND CORRECTED FOR UNSPECIFIC INTERNALIZATION; LINE DIAGRAMS: AMOUNT OF INTERNALIZED NOVEL LIGAND IN RELATION TO THE AMOUNT OF INTERNALIZED INTERNAL STANDARD ¹²⁵I-FC-131 IN %; BAR DIAGRAMS: AMOUNT OF INTERNALIZED NOVEL LIGAND IN RELATION TO THE TOTAL CELL-BOUND NOVEL LIGAND IN %. 130

FIGURE 29: SUMMARY OF LOGD_{7.4} (Y-AXIS), INVIC₅₀ (X-AXIS) AND MAXIMUM INTERNALIZATION VALUES (DOT SIZE) FOR [^{99m}Tc]CXCR4-Tc-06 – 15 AS WELL AS [¹⁷⁷Lu]PENTIXATHER AND [⁶⁸Ga]PENTIXAFOR (LOGD_{7.4} ONLY): NUMBERS NEXT TO DOTS REPRESENT THE RESPECTIVE LIGAND WITHIN THIS SERIES AND THE LETTER P REPRESENTS [¹⁷⁷Lu]PENTIXATHER; DOTS IN THE LIGHT BLUE AREA SUGGEST COMPOUNDS THAT ARE MORE AFFINE AND HYDROPHILIC THAN [¹⁷⁷Lu]PENTIXATHER AND DOTS IN THE LIGHT GREEN AREA SUGGEST COMPOUNDS THAT ARE MORE AFFINE AND HYDROPHILIC THAN [⁶⁸Ga]PENTIXAFOR. 131

FIGURE 30: RESULTS OF PHARMACOKINETIC STUDIES 1H POST INJECTION OF [^{99m}Tc]CXCR4-Tc-06, -08, -10 AND -11 IN JURKAT TUMOR-BEARING FEMALE CB-17 SCID MICE: **A:** BIODISTRIBUTION PROFILES OF NOVEL LIGANDS; DATA ARE EXPRESSED AS %iD/G AND ARE MEANS ± SD OF 5 ANIMALS PER LIGAND; **B:** MAXIMUM-INTENSITY PROJECTION IMAGES OBTAINED FROM STATIC μSPECT IMAGING OF 1 ANIMAL PER LIGAND; ARROWS INDICATE ORGANS OF SPECIAL INTEREST: STRAIGHT: TUMOR, DASHED: LIVER, POINTED: KIDNEYS, STAR: THYROID. 133

FIGURE 31: RESULTS OF PHARMACOKINETIC STUDIES 1H POST INJECTION OF [^{99m}Tc]CXCR4-Tc-06, -12 AND -13 IN JURKAT TUMOR-BEARING FEMALE CB-17 SCID MICE: **A:** BIODISTRIBUTION PROFILES OF NOVEL LIGANDS; DATA ARE EXPRESSED AS %iD/G AND ARE MEANS ± SD OF 5 ANIMALS PER LIGAND; **B:** MAXIMUM-INTENSITY PROJECTION IMAGES OBTAINED FROM STATIC μSPECT IMAGING OF 1 ANIMAL PER LIGAND; ARROWS INDICATE ORGANS OF SPECIAL INTEREST: STRAIGHT: TUMOR, DASHED: LIVER, POINTED: KIDNEYS. 137

FIGURE 32: BIODISTRIBUTION PROFILES OF [^{99m}Tc]CXCR4-Tc-10 – 13 AND [⁶⁸Ga]PENTIXAFOR 1H POST INJECTION IN JURKAT TUMOR-BEARING FEMALE CB-17 SCID MICE; DATA ARE EXPRESSED AS %iD/G AND ARE MEANS ± SD OF 5 ANIMALS PER LIGAND. 140

FIGURE 33: MAXIMUM INTENSITY PROJECTION (MIP) IMAGES OBTAINED FROM SPECT AND PET IMAGING OF A FEMALE PATIENT SUFFERING FROM MULTIPLE MYELOMA; **A)** [¹⁸F]FDG PET MIP (1H P.I., 189 MBQ OF [¹⁸F]FDG), **B)** [^{99m}Tc]CXCR4-Tc-13 SPECT MIP (3H P.I., 604 MBQ OF [^{99m}Tc]CXCR4-Tc-13); RED ARROWS INDICATE TUMOR LESIONS, BLUE ARROWS INDICATE PHYSIOLOGICAL UPTAKE OF [¹⁸F]FDG IN THE HEART AND OF [^{99m}Tc]CXCR4-Tc-13 IN THE SPLEEN. 142

FIGURE 34: **A)** MIP IMAGES OBTAINED FROM SPECT IMAGING AT 5 MIN, 60 MIN, 120 MIN, 5H AND 21H P.I. OF 604 MBQ [^{99m}Tc]CXCR4-Tc-13 IN A FEMALE PATIENT SUFFERING FROM MULTIPLE MYELOMA; **B)** SPECIFIC DOSES [μGy/MBQ] CALCULATED FOR SELECTED ORGANS AND TISSUES FROM THE SAME PATIENT. 144

FIGURE 35: STRUCTURES OF THERANOSTIC LIGAND PAIRS: [⁶⁸Ga/¹⁷⁷Lu]DOTATATE, [⁶⁸Ga/¹⁷⁷Lu]PSMA-617 AND [⁶⁸Ga/¹⁷⁷Lu]PSMA I&T ARE CONVERTED INTO THEIR DIAGNOSTIC OR THERAPEUTIC FORM BY EXCHANGE OF THE RADIOMETAL ONLY; THE [⁶⁸Ga]PENTIXAFOR SCAFFOLD IS IODINATED BEFORE COMPLEXATION OF LUTETIUM-177 TO OBTAIN ITS THERAPEUTIC ANALOG [¹⁷⁷Lu]PENTIXATHER; [¹²³I/¹²⁴I/¹³¹I]MIP-1095 AND [¹⁸F/¹⁷⁷Lu]RHPSMA-7 PRESENT THE ONLY “TRUE” THERANOSTIC LIGANDS AS IMAGING AND THERAPEUTIC COMPOUNDS ARE CHEMICALLY ALIKE. 147

FIGURE 36: STRUCTURES OF DOTA-CONJUGATED THERANOSTIC COMPOUNDS CXCR4-DOTA-01 – 05 AND KO-CXCR4-DOTA-04 DEVELOPED WITHIN THIS WORK: ENCIRCLED RESTS HIGHLIGHT THE SPECIAL FEATURE OF THE RESPECTIVE COMPOUND THAT WILL BE ACCENTUATED DURING THE DISCUSSION OF DATA. 149

FIGURE 37: DUAL TRACER INTERNALIZATION OF NOVEL LIGANDS [¹⁷⁷Lu]CXCR4-DOTA-01 – 05, [¹⁷⁷Lu]PENTIXATHER AND THE REFERENCE COMPOUND ¹²⁵I-FC-131 (ASSAY-CONCENTRATION FOR EACH PEPTIDE 0.2 nM) INTO CHEM-1 CELLS (100,000 CELLS PER WELL; 37°C). DATA ARE EXPRESSED AS MEAN ± SD; INTERNALIZATION AT EVERY TIME POINT WAS DETERMINED IN TRIPPLICATE AND CORRECTED FOR UNSPECIFIC INTERNALIZATION; LINE DIAGRAM: INTERNALIZED ACTIVITY OF THE NOVEL LIGAND IN RELATION TO THE INTERNALIZED ACTIVITY OF INTERNAL STANDARD ¹²⁵I-FC-131; BAR DIAGRAM: PERCENTAGE OF INTERNALIZED ACTIVITY OF THE NOVEL LIGAND IN RELATION TO THE TOTAL CELL-BOUND ACTIVITY. 155

FIGURE 38: DUAL TRACER INTERNALIZATION OF NOVEL LIGANDS [¹⁷⁷Lu]KO-CXCR4-DOTA-04, [¹⁷⁷Lu]CXCR4-DOTA-04, [¹⁷⁷Lu]PENTIXATHER AND THE REFERENCE COMPOUND ¹²⁵I-FC-131 (ASSAY-CONCENTRATION FOR EACH PEPTIDE 0.2 NM) INTO CHEM-1 CELLS (100,000 CELLS PER WELL; 37°C). DATA ARE EXPRESSED AS MEAN ± SD; INTERNALIZATION AT EVERY TIME POINT WAS DETERMINED IN TRIPLICATE AND CORRECTED FOR UNSPECIFIC INTERNALIZATION; LINE DIAGRAM: INTERNALIZED ACTIVITY OF THE NOVEL LIGAND IN RELATION TO THE INTERNALIZED ACTIVITY OF INTERNAL STANDARD ¹²⁵I-FC-131; BAR DIAGRAM: PERCENTAGE OF INTERNALIZED ACTIVITY OF THE NOVEL LIGAND IN RELATION TO THE TOTAL CELL-BOUND ACTIVITY. 157

FIGURE 39: SUMMARY OF LOGD_{7.4} (Y-AXIS), IC₅₀ (X-AXIS) AND MAXIMUM INTERNALIZATION VALUES (DOT SIZE) FOR [¹⁷⁷Lu]CXCR4-DOTA-01 – 05 AS WELL AS [¹⁷⁷Lu]PENTIXATHER AND [⁶⁸Ga]PENTIXAFOR (LOGD_{7.4} AND IC₅₀ ONLY): NUMBERS NEXT TO DOTS REPRESENT THE RESPECTIVE LIGAND WITHIN THIS SERIES, THE LETTER P REPRESENTS [¹⁷⁷Lu]PENTIXATHER AND FOR REPRESENTS [⁶⁸Ga]PENTIXAFOR; DOTS IN THE LIGHT BLUE AREA SUGGEST COMPOUNDS THAT ARE MORE AFFINE AND HYDROPHILIC THAN [¹⁷⁷Lu]PENTIXATHER AND DOTS IN THE LIGHT GREEN AREA SUGGEST COMPOUNDS THAT ARE MORE AFFINE AND HYDROPHILIC THAN [⁶⁸Ga]PENTIXAFOR..... 159

FIGURE 40: BIODISTRIBUTION PROFILES OF [¹⁷⁷Lu]CXCR4-DOTA-01 – 04, [¹⁷⁷Lu]PENTIXATHER AND [⁶⁸Ga]PENTIXAFOR 1H POST INJECTION IN JURKAT TUMOR-BEARING FEMALE CB 17 SCID MICE; DATA ARE EXPRESSED AS %ID/G AND ARE MEANS ± SD OF 5 ANIMALS PER LIGAND..... 162

FIGURE 41: BIODISTRIBUTION PROFILES OF [¹⁷⁷Lu]CXCR4-DOTA-03 AND -04 AS WELL AS [¹⁷⁷Lu]PENTIXATHER 1H AND 6H POST INJECTION IN JURKAT TUMOR-BEARING FEMALE CB 17 SCID MICE; DATA ARE EXPRESSED AS %ID/G AND ARE MEANS ± SD OF 5 ANIMALS PER LIGAND..... 167

FIGURE 42: BIODISTRIBUTION PROFILES OF [¹⁷⁷Lu]CXCR4-DOTA-03 AND -04 AS WELL AS [¹⁷⁷Lu]PENTIXATHER 6H AND 48H POST INJECTION IN JURKAT TUMOR-BEARING FEMALE CB 17 SCID MICE; DATA ARE EXPRESSED AS %ID/G AND ARE MEANS ± SD OF 5 ANIMALS PER LIGAND..... 170

FIGURE 43: BIODISTRIBUTION PROFILES OF [¹⁷⁷Lu]KO-CXCR4-DOTA-04 24H POST INJECTION AND OF [¹⁷⁷Lu]CXCR4-DOTA-04 6H POST INJECTION IN JURKAT TUMOR-BEARING FEMALE CB-17 SCID MICE; DATA ARE EXPRESSED AS %ID/G AND ARE MEANS ± SD OF 5 ANIMALS PER LIGAND. 173

FIGURE 44: TIME-ACTIVITY CURVES FOR MUSCLE, LIVER, SPLEEN AND TUMOR BASED ON DATA OBTAINED FROM BIODISTRIBUTION STUDIES AT 1H, 6H AND 48H POST INJECTION OF [¹⁷⁷Lu]PENTIXATHER AND [¹⁷⁷Lu]CXCR4-DOTA-03 IN JURKAT TUMOR-BEARING CB-17 SCID MICE. 175

FIGURE 45: CONCEPTUAL STRUCTURES OF RADIOHYBRID LIGANDS: THE SIFA MOIETY AND A CHELATOR ARE CARRYING EITHER A STABLE (^{NAT}F, ^{NAT}GA, ^{NAT}LU) OR RADIOACTIVE ISOTOPE (¹⁸F, ⁶⁸GA, ¹⁷⁷LU), ENABLING THEIR APPLICATION WITHIN PET IMAGING AND THERAPY; THIS CONCEPT REPRESENTS A “TRUE” THERANOSTIC APPROACH. 178

FIGURE 46: SUMMARY OF STRUCTURES BEARING A SIFA MOIETY: CXCR4-SIFA-01 AND -02 WERE OBTAINED BY MODIFICATION OF THE CPCR4-ABZ-A-R TRACER BACKBONE; CXCR4-SIFA-03 AND -04 WERE OBTAINED BY MODIFICATION OF THE OPTIMIZED CPCR4-ABZ-A-R-DAP TRACER BACKBONE AND CXCR4-SIFA-05 – 07 WERE OBTAINED BY MODIFICATION OF THE CPCR4-ABZ-A-R-AHX TRACER BACKBONE. 180

FIGURE 47: CUTOUT OF A REPRESENTATIVE RADIO-RP-HPLC CHROMATOGRAM OBTAINED FOR A LUTETIUM-177 LABELED SIFA-CONJUGATED COMPOUND (R_T = 13.0 MIN) WITH ITS RESPECTIVE PRODUCT OF HYDROLYSIS (R_T = 12.0 MIN)..... 182

FIGURE 48: DUAL TRACER INTERNALIZATION OF NOVEL LIGANDS [¹⁸F,^{NAT}GA]CXCR4-SIFA-02 AND 04 – 07 AND THE REFERENCE COMPOUND ¹²⁵I-FC-131 (ASSAY-CONCENTRATION FOR EACH PEPTIDE 0.2 NM) INTO CHEM-1 CELLS (100,000 CELLS PER

WELL; 37°C). DATA ARE EXPRESSED AS MEAN ± SD; INTERNALIZATION AT EVERY TIME POINT WAS DETERMINED IN TRIPLICATE AND CORRECTED FOR UNSPECIFIC INTERNALIZATION; LINE DIAGRAM: INTERNALIZED ACTIVITY OF THE NOVEL LIGAND IN RELATION TO THE INTERNALIZED ACTIVITY OF INTERNAL STANDARD ¹²⁵ I-FC-131; BAR DIAGRAM: PERCENTAGE OF INTERNALIZED ACTIVITY OF THE NOVEL LIGAND IN RELATION TO THE TOTAL CELL-BOUND ACTIVITY.....	189
FIGURE 49: SUMMARY OF LOGD _{7.4} (Y-AXIS), IC ₅₀ (X-AXIS) AND MAXIMUM INTERNALIZATION VALUES (DOT SIZE) FOR [¹⁸ F, ^{NAT} GA]CXCR4-SiFA-02 AND -04 – 07 AS WELL AS [¹⁷⁷ Lu]PENTIXATHER, [⁶⁸ GA]PENTIXAFOR (LOGD _{7.4} AND IC ₅₀ ONLY), [¹⁸ F]ALF-NOTA-PENTIXATHER (LOGD _{7.4} AND IC ₅₀ ONLY), [¹⁸ F]BL08 (LOGD _{7.4} AND IC ₅₀ ONLY) AND [¹⁸ F]BL09 (LOGD _{7.4} AND IC ₅₀ ONLY): NUMBERS NEXT TO DOTS REPRESENT THE RESPECTIVE LIGAND WITHIN THIS SERIES, THE LETTER P REPRESENTS [¹⁷⁷ Lu]PENTIXATHER, FOR REPRESENTS [⁶⁸ GA]PENTIXAFOR AND NOTA REPRESENTS [¹⁸ F]ALF-NOTA-PENTIXATHER; DOTS IN THE LIGHT BLUE AREA SUGGEST COMPOUNDS THAT ARE MORE AFFINE AND HYDROPHILIC THAN [¹⁷⁷ Lu]PENTIXATHER AND DOTS IN THE LIGHT GREEN AREA SUGGEST COMPOUNDS THAT ARE MORE AFFINE AND HYDROPHILIC THAN [⁶⁸ GA]PENTIXAFOR.	191
FIGURE 50: BIODISTRIBUTION PROFILES OF [¹⁸ F, ^{NAT} GA]CXCR4-SiFA-07 AND [⁶⁸ GA]PENTIXAFOR 1H POST INJECTION IN JURKAT TUMOR-BEARING FEMALE CB-17 SCID MICE; DATA ARE EXPRESSED AS %ID/G AND ARE MEANS ± SD OF 5 ANIMALS PER LIGAND.	192
FIGURE 51: BIODISTRIBUTION PROFILE OF [¹⁸ F, ^{NAT} GA]CXCR4-SiFA-07 1H POST INJECTION IN JURKAT TUMOR-BEARING FEMALE CB-17 SCID MICE; DIFFERENT AMOUNTS OF RADIOLIGAND WERE APPLIED: 36 PMOL, 1,000 PMOL AND 2,000 PMOL; DATA ARE EXPRESSED AS %ID/G VALUES AND ARE MEANS ± SD OF 5 ANIMALS FOR THE EXPERIMENT WITH 36 PMOL; 1 ANIMAL EACH WAS USED FOR BOTH OTHER EXPERIMENTS.	194
FIGURE 52: CONCEPT OF TARGETED CHEMOTHERAPY AS PURSUED WITHIN THIS PROJECT: A) PEPTIDE-DRUG CONJUGATE CONSISTING OF THE AFFINE AND INTERNALIZING TRANSPORT PEPTIDE (OCHER), THE CLEAVABLE LINKER (GREEN) AND THE TOXIN (RED); B) TUMOR CELL; C) CXCR4 RECEPTOR; D) UNSELECTIVE CELLULAR UPTAKE OF TOXIN WITHIN CONVENTIONAL CHEMOTHERAPY; E) MICROTUBULE; 1) SPECIFIC BINDING OF THE TRANSPORTER MOLECULE ONTO A CXCR4 RECEPTOR AT THE CELL SURFACE; 2) TRIGGERED INTERNALIZATION OF THE RECEPTOR-PROBE COMPLEX; 3) ENDOSOMAL DISSOCIATION OF THE RECEPTOR-PROBE COMPLEX; 4) CATHEPSIN B-MEDIATED CLEAVAGE OF THE LINKER; 5) DIFFUSION OF THE RELEASED TOXIN INTO THE CELL LUMEN; 6) TOXIN-INDUCED INHIBITION OF MICROTUBULE POLYMERIZATION ULTIMATELY PROHIBITING CELL DIVISION; 7) RECYCLING OF THE CXCR4 RECEPTOR.	198
FIGURE 53: STRUCTURE OF A PEPTIDE-VC-PAB-MMAE CONJUGATE: CATHEPSIN B CLEAVAGE OF THE VAL-CIT LINKER AND SUBSEQUENT SPONTANEOUS 1,6-ELIMINATION OF THE 4-AMINO BENZYL CARBAMATE MOIETY FACILITATES THE RELEASE OF THE ACTIVE MONOMETHYL AURISTATIN-E TOXIN.	199
FIGURE 54: SUMMARY OF STRUCTURES BEARING THE VC-PAB-MMAE MOIETY: CXCR4-MMAE-01 – 03 WERE OBTAINED BY ELONGATION OF THE CPCR4-ABZ-A-R TRACER BACKBONE; CXCR4-MMAE-04 WAS OBTAINED BY MODIFICATION OF THE CPCR4-ABZ-A-R-DAP-AHX TRACER BACKBONE.	200
FIGURE 55: INTERNALIZATION OF NOVEL LIGANDS [¹²⁵ I]CXCR4-MMAE-02 AND -03 AS WELL AS [¹⁷⁷ Lu]PENTIXATHER (ASSAY-CONCENTRATION FOR EACH PEPTIDE 0.2 NM) INTO CHEM-1 CELLS (100,000 CELLS PER WELL; 37°C). DATA ARE EXPRESSED AS MEAN ± SD; INTERNALIZATION AT EVERY TIME POINT WAS DETERMINED IN TRIPLICATE AND CORRECTED FOR UNSPECIFIC INTERNALIZATION; THE DIAGRAM DEPICTS THE INTERNALIZED ACTIVITY OF A LIGAND IN RELATION TO THE TOTAL APPLIED ACTIVITY.	205
FIGURE 56: FLOW CYTOMETRY ANALYSIS OF CELL VIABILITIES USING RAJI (LEFT SIDE) AND U2932 (RIGHT SIDE) CELLS: THE CELLS WERE INCUBATED FOR 0, 24, 48, 72 AND 96H WITH 0 (BLANK), 10, 20, 40 AND 100 NM OF CXCR4-MMAE-02 PRIOR TO	

STAINING WITH PROPIDIUM IODIDE AND FLOW CYTOMETRY ANALYSIS; THE NUMBER OF VITAL CELLS RELATED TO THE TOTAL NUMBER OF CELLS REPRESENTS THE CELL VIABILITY.	206
FIGURE 57: FLOW CYTOMETRY ANALYSIS OF CELL VIABILITIES USING RAJI AND U2932 CELLS: THE CELLS WERE INCUBATED FOR 96H WITH 0 (BLANK), 10, 20, 40 AND 100 NM OF CXCR4-MMAE-02 PRIOR TO STAINING WITH PROPIDIUM IODIDE AND FLOW CYTOMETRY ANALYSIS OF DEAD CELLS.	207
FIGURE 58: CELL CYCLE PROFILING EXPERIMENTS USING U2932 CELLS: THE CELLS WERE INCUBATED FOR 72H WITH 0 (BLANK), 10, 20, 40 AND 100 NM OF CXCR4-MMAE-02, FIXED, PERMEABILIZED AND STAINED WITH PROPIDIUM IODIDE; THE FRACTION OF CELLS IN THE G0/G1, S OR G2/M PHASE WAS DETERMINED.....	208
FIGURE 59: BIODISTRIBUTION PROFILES OF [¹²⁵ I]CXCR4-MMAE-02 AND [¹⁷⁷ Lu]PENTIXATHER 1H POST INJECTION IN JURKAT TUMOR-BEARING FEMALE CB-17 SCID MICE; DATA ARE EXPRESSED AS %ID/G AND ARE MEANS ± SD OF 5 ANIMALS PER LIGAND.	209
FIGURE 60: CONCEPT OF RADIO- AND FLUORESCENCE-GUIDED SURGERY USING A HYBRID LIGAND WITH BOTH A RADIOACTIVE AND FLUORESCENT LABEL; RADIOACTIVITY CAN BE USED FOR PRE-SURGICAL TUMOR LOCALIZATION AND IMAGE-GUIDED BIOPSY AS WELL AS PHOTO-ACOUSTIC DETECTION OF TUMOR LESIONS DURING SURGERY; THE FLUORESCENT LABEL CAN BE USED FOR PRE-SURGICAL IN VIVO STAINING OF BIOPSY TISSUE AND VISUAL DIFFERENTIATION OF MALIGN AND BENIGN TISSUE DURING SURGERY.	213
FIGURE 61: SUMMARY OF STRUCTURES BEARING A Cy5.5 FLUORESCENT LABEL: CXCR4-OI-01 AND -02 WERE OBTAINED BY MODIFICATION OF THE CPCR4-ABZ-A-R-DAP AND THE I-CPCR4-ABZ-A-R-DAP TRACER BACKBONE, RESPECTIVELY; CXCR4-OI-03 WAS OBTAINED BY MODIFICATION OF THE CPCR4-ABZ-A-R-DAP-AHX TRACER BACKBONE.	214
FIGURE 62: DUAL TRACER INTERNALIZATION OF NOVEL LIGAND [¹⁷⁷ Lu]CXCR4-OI-03, [¹⁷⁷ Lu]PENTIXATHER AND THE REFERENCE COMPOUND ¹²⁵ I-FC-131 (ASSAY-CONCENTRATION FOR EACH PEPTIDE 0.2 NM) INTO CHEM-1 CELLS (100,000 CELLS PER WELL; 37°C). DATA ARE EXPRESSED AS MEAN ± SD; INTERNALIZATION AT EVERY TIME POINT WAS DETERMINED IN TRIPLICATE AND CORRECTED FOR UNSPECIFIC INTERNALIZATION; INTERNALIZED ACTIVITY OF THE NOVEL LIGAND IN RELATION TO THE INTERNALIZED ACTIVITY OF INTERNAL STANDARD ¹²⁵ I-FC-131; BAR DIAGRAM: PERCENTAGE OF INTERNALIZED ACTIVITY OF THE NOVEL LIGAND IN RELATION TO THE TOTAL CELL-BOUND ACTIVITY.	218
FIGURE 63: BIODISTRIBUTION PROFILES OF [¹²⁵ I]CXCR4-OI-02, [¹⁷⁷ Lu]CXCR4-OI-03 AND [⁶⁸ Ga]PENTIXAFOR 1H POST INJECTION IN JURKAT TUMOR-BEARING FEMALE CB-17 SCID MICE; DATA ARE EXPRESSED AS %ID/G AND ARE MEANS ± SD OF 5 ANIMALS PER LIGAND..	219
FIGURE 64: BIODISTRIBUTION PROFILE OF [¹⁷⁷ Lu]CXCR4-OI-03 1H POST INJECTION IN JURKAT TUMOR-BEARING FEMALE CB-17 SCID MICE; DIFFERENT AMOUNTS OF RADIOLIGAND WERE APPLIED: 59 PMOL AND 1,000 PMOL; DATA ARE EXPRESSED AS %ID/G VALUES AND ARE MEANS ± SD OF 5 ANIMALS FOR THE EXPERIMENT WITH 59 PMOL; 1 ANIMAL WAS USED FOR THE OTHER EXPERIMENT.....	221
FIGURE 65: FLUORESCENCE-MICROSCOPY IMAGES OBTAINED FROM LIVER AND SPLEEN IN 4-FOLD MAGNIFICATION; ORGANS WERE DISSECTED 2 HOURS AFTER I.V. APPLICATION OF 2 NMOL CXCR4-OI-01 WITH AND WITHOUT CO-INJECTION OF 100 NMOL AMD3100; IMAGES WERE OBTAINED WITH 5 SECONDS EXPOSURE TIME.....	222

4. Table Index

TABLE 1: CANCER TYPES ARISING FROM CELLS OF THE HEMATOPOIETIC SYSTEM, BRAIN, GASTROINTESTINAL SYSTEM AND MISCELLANEOUS TISSUES THAT REPORTEDLY OVEREXPRESS THE CXCR4 RECEPTOR; TABLE WAS ADAPTED FROM LITERATURE (81) AND MODIFIED.	9
TABLE 2: IC ₅₀ [NM] VALUES OBTAINED FOR COMPOUNDS CXCR4-Tc-01 – 06, CARRYING AN ADDITIONAL AMINO ACID BETWEEN THE CPCr4-Abz-A-R TRACER BACKBONE AND A TERMINAL MAS ₃ CHELATOR: IC ₅₀ VALUES WERE DETERMINED IN COMPETITIVE BINDING STUDIES EMPLOYING JURKAT CELLS (400,000 CELLS/TUBE; 8°C, 2H INCUBATION) AND THE STANDARD LIGAND ¹²⁵ I-FC-131 (10 ⁻⁹ M, FINAL ASSAY-CONCENTRATION). DATA ARE EXPRESSED AS MEAN ± SD; EXPERIMENTS WERE CONDUCTED IN TRIPLICATES OR QUINTUPLICATES (*).	115
TABLE 3: SUMMARY OF INVIC ₅₀ [NM] AND LOGD _{7.4} VALUES FOR COMPOUNDS [^{99m} Tc]CXCR4-Tc-06 – 11 AND REFERENCE COMPOUNDS [¹⁷⁷ Lu]PENTIXATHER, [⁶⁸ Ga]PENTIXAFOR AND [^{99m} Tc]CXCR4-L: INVIC ₅₀ VALUES WERE DETERMINED IN COMPETITIVE BINDING STUDIES EMPLOYING JURKAT CELLS (400,000 CELLS/TUBE; 8°C, 2H INCUBATION), THE STANDARD LIGAND FC-131 (10 ⁻⁵ -10 ⁻¹¹ M, FINAL ASSAY-CONCENTRATIONS) AND THE RESPECTIVE RADIOLABELED LIGANDS (10 ⁻⁹ M, FINAL ASSAY-CONCENTRATION). DATA ARE EXPRESSED AS MEAN ± SD; INVIC ₅₀ DATA WERE DETERMINED AS TRIPLICATES OR QUADRUPPLICATES (*); LOGD _{7.4} VALUES WERE DETERMINED AS OCTUPLICATES, SEPTUPLICATES (**) OR SEXTUPLICATES (***) (****); DATA ADAPTED FROM LITERATURE (137).	120
TABLE 4: SUMMARY OF INVIC ₅₀ [NM] AND LOGD _{7.4} VALUES FOR COMPOUNDS [^{99m} Tc]CXCR4-Tc-12 – 14 IN COMPARISON WITH [^{99m} Tc]CXCR4-Tc-06, -11 AND REFERENCE LIGANDS [^{99m} Tc]CXCR4-L, [⁶⁸ Ga]PENTIXAFOR AND [¹⁷⁷ Lu]PENTIXATHER: INVIC ₅₀ VALUES WERE DETERMINED IN COMPETITIVE BINDING STUDIES EMPLOYING JURKAT CELLS (400,000 CELLS/TUBE; 8°C, 2H INCUBATION), THE STANDARD LIGAND FC-131 (10 ⁻⁵ -10 ⁻¹¹ M, FINAL ASSAY-CONCENTRATIONS) AND THE RESPECTIVE RADIOLABELED LIGANDS (10 ⁻⁹ M, FINAL ASSAY-CONCENTRATION). DATA ARE EXPRESSED AS MEAN ± SD; INVIC ₅₀ VALUES WERE DETERMINED AS TRIPLICATES; LOGD _{7.4} VALUES WERE DETERMINED AS OCTUPLICATES, PENTUPLICATES (*) OR SEXTUPLICATES (**); (***): DATA ADAPTED FROM LITERATURE (137).	125
TABLE 5: SUMMARY OF INVIC ₅₀ [NM] AND LOGD _{7.4} VALUES FOR COMPOUNDS [^{99m} Tc]CXCR4-Tc-13 – 15 IN COMPARISON WITH REFERENCE LIGANDS [^{99m} Tc]CXCR4-L, [⁶⁸ Ga]PENTIXAFOR AND [¹⁷⁷ Lu]PENTIXATHER: INVIC ₅₀ VALUES WERE DETERMINED IN COMPETITIVE BINDING STUDIES EMPLOYING JURKAT CELLS (400,000 CELLS/TUBE; 8°C, 2H INCUBATION), THE STANDARD LIGAND FC-131 (10 ⁻⁵ -10 ⁻¹¹ M, FINAL ASSAY-CONCENTRATIONS) AND THE RESPECTIVE RADIOLABELED LIGANDS (10 ⁻⁹ M, FINAL ASSAY-CONCENTRATION). DATA ARE EXPRESSED AS MEAN ± SD; INVIC ₅₀ VALUES WERE DETERMINED AS TRIPLICATES; LOGD _{7.4} VALUES WERE DETERMINED AS OCTUPLICATES; (*): DATA ADAPTED FROM LITERATURE (114).	129
TABLE 6: TUMOR/ORGAN RATIOS DETERMINED USING DATA OBTAINED FROM BIODISTRIBUTION STUDIES 1H AFTER INJECTION OF [^{99m} Tc]CXCR4-Tc-06, -08, -10 AND -11 IN JURKAT TUMOR-BEARING FEMALE SCID MICE; DATA ARE EXPRESSED AS MEAN ± SD OF 5 ANIMALS PER LIGAND.	136
TABLE 7: TUMOR/ORGAN RATIOS DETERMINED USING DATA OBTAINED FROM BIODISTRIBUTION STUDIES 1H AFTER INJECTION OF [^{99m} Tc]CXCR4-Tc-06, -12 AND -13 IN JURKAT TUMOR-BEARING FEMALE SCID MICE; DATA ARE EXPRESSED AS MEAN ± SD OF 5 ANIMALS PER LIGAND.	139
TABLE 8: SUMMARY OF IC ₅₀ [NM] AND LOGD _{7.4} VALUES FOR CXCR4-DOTA-01 – 05 AND KO-CXCR4-DOTA-04 AND RESPECTIVE GALLIUM AND LUTETIUM COMPLEXES THEREOF IN COMPARISON WITH REFERENCE COMPOUNDS [^{NAT} Lu/ ¹⁷⁷ Lu]PENTIXATHER AND [^{NAT} Ga/ ⁶⁸ Ga]PENTIXAFOR: IC ₅₀ VALUES WERE DETERMINED IN COMPETITIVE BINDING STUDIES EMPLOYING JURKAT CELLS	

(400,000 CELLS/TUBE; 8°C, 2H INCUBATION) AND THE STANDARD LIGAND FC-131 (10^{-9} M, FINAL ASSAY-CONCENTRATION). DATA ARE EXPRESSED AS MEAN \pm SD; IC₅₀ DATA WERE DETERMINED AS TRIPPLICATES OR QUADRUPPLICATES (*); LOGD_{7.4} VALUES WERE DETERMINED AS OCTUPLICATES, SEXTUPLICATES (**) OR PENTUPLICATES (***) (****): DATA ADAPTED FROM LITERATURE (137). 152

TABLE 9: TUMOR/ORGAN RATIOS DETERMINED USING DATA OBTAINED FROM BIODISTRIBUTION STUDIES 1H AFTER INJECTION OF [¹⁷⁷Lu]CXCR4-DOTA-01 – 04, [¹⁷⁷Lu]PENTIXATHER AND [⁶⁸Ga]PENTIXAFOR IN JURKAT TUMOR-BEARING FEMALE SCID MICE; DATA ARE EXPRESSED AS MEAN \pm SD OF 5 ANIMALS PER LIGAND. 165

TABLE 10: TUMOR/ORGAN RATIOS DETERMINED USING DATA OBTAINED FROM BIODISTRIBUTION STUDIES 6H AFTER INJECTION OF [¹⁷⁷Lu]CXCR4-DOTA-03 AND -04 AS WELL AS [¹⁷⁷Lu]PENTIXATHER IN JURKAT TUMOR-BEARING FEMALE SCID MICE; DATA ARE EXPRESSED AS MEAN \pm SD OF 5 ANIMALS PER LIGAND..... 168

TABLE 11: TUMOR/ORGAN RATIOS DETERMINED USING DATA OBTAINED FROM BIODISTRIBUTION STUDIES 48H AFTER INJECTION OF [¹⁷⁷Lu]CXCR4-DOTA-03 AND -04 AS WELL AS [¹⁷⁷Lu]PENTIXATHER IN JURKAT TUMOR-BEARING FEMALE SCID MICE; DATA ARE EXPRESSED AS MEAN \pm SD OF 5 ANIMALS PER LIGAND..... 171

TABLE 12: SUMMARY OF DATA OBTAINED FROM THE RADIO-FLUORINATION OF SIFA-CONJUGATED COMPOUNDS [^{NAT}Ga]CXCR4-SIFA-01 – 07; COLUMNS COMPRISE THE DECAY-CORRECTED (D.C.) RADIOCHEMICAL YIELD IN %, THE HIGHEST OBTAINED MOLAR ACTIVITY A_{MOL} AT THE END OF SYNTHESIS (EOS) IN MBQ PER NMOL AND THE MINIMUM TIME THAT WAS NEEDED FOR THE ENTIRE LABELING PROCEDURE (MIN. SYNTH. TIME) IN MINUTES..... 183

TABLE 13: SUMMARY OF IC₅₀ [NM] AND LOGD_{7.4} VALUES FOR GALLIUM AND LUTETIUM COMPLEXES OF CXCR4-SIFA-01 – 07 AS WELL AS REFERENCE COMPOUNDS [^{NAT}Lu/¹⁷⁷Lu]PENTIXATHER, [^{NAT}Ga/⁶⁸Ga]PENTIXAFOR, [^{NAT}F/¹⁸F]ALF-NOTA-PENTIXATHER, [^{NAT}F/¹⁸F]BL08 AND [^{NAT}F/¹⁸F]BL09: IC₅₀ VALUES WERE DETERMINED IN COMPETITIVE BINDING STUDIES EMPLOYING JURKAT CELLS (400,000 CELLS/TUBE; 8°C, 2H INCUBATION) AND THE STANDARD LIGAND FC-131 (10^{-9} M, FINAL ASSAY-CONCENTRATION). DATA ARE EXPRESSED AS MEAN \pm SD; IC₅₀ DATA WERE DETERMINED AS TRIPPLICATES OR QUADRUPPLICATES (*); LOGD_{7.4} VALUES WERE DETERMINED AS OCTUPLICATES, SEXTUPLICATES (**) OR SEPTUPLICATES (***); (I): DATA ADAPTED FROM LITERATURE (137), (II): (143), (III): (228). 185

TABLE 14: SUMMARY OF DATA OBTAINED FROM THE RADIO-IODINATION OF CXCR4-MMAE-02 AND -03; COLUMNS COMPRISE THE USED PROPORTIONS OF IODOGEN, PEPTIDE AND [¹²⁵I]NAI, AS WELL AS THE OBTAINED YIELDS. 202

TABLE 15: SUMMARY OF IC₅₀ [NM] AND LOGD_{7.4} VALUES FOR CXCR4-MMAE-01 – 03 AS WELL AS [^{NAT}Lu/¹⁷⁷Lu]CXCR4-MMAE-04 AND REFERENCE COMPOUND [^{NAT}Lu/¹⁷⁷Lu]PENTIXATHER: IC₅₀ VALUES WERE DETERMINED IN COMPETITIVE BINDING STUDIES EMPLOYING JURKAT CELLS (400,000 CELLS/TUBE; 8°C, 2H INCUBATION) AND THE STANDARD LIGAND FC-131 (10^{-9} M, FINAL ASSAY-CONCENTRATION). DATA ARE EXPRESSED AS MEAN \pm SD; IC₅₀ DATA WERE DETERMINED AS TRIPPLICATES; LOGD_{7.4} VALUES WERE DETERMINED AS OCTUPLICATES, PENTUPLICATES (*) OR SEXTUPLICATES (**). 203

TABLE 16: SUMMARY OF IC₅₀ [NM] AND LOGD_{7.4} VALUES FOR CXCR4-OI-01 AND -02 AS WELL AS [^{NAT}Lu/¹⁷⁷Lu]CXCR4-OI-03 AND REFERENCE COMPOUNDS [^{NAT}Lu/¹⁷⁷Lu]PENTIXATHER AND [^{NAT}Ga/⁶⁸Ga]PENTIXAFOR: IC₅₀ VALUES WERE DETERMINED IN COMPETITIVE BINDING STUDIES EMPLOYING JURKAT CELLS (400,000 CELLS/TUBE; 8°C, 2H INCUBATION) AND THE STANDARD LIGAND FC-131 (10^{-9} M, FINAL ASSAY-CONCENTRATION). DATA ARE EXPRESSED AS MEAN \pm SD; IC₅₀ DATA WERE DETERMINED AS TRIPPLICATES; LOGD_{7.4} VALUES WERE DETERMINED AS OCTUPLICATES; QUADRUPPLICATE (*), PENTUPLICATE (**); (I): DATA ADAPTED FROM LITERATURE (137). 216

5. Scheme Index

SCHEME 1: SYNTHESIS OF CPCr4: z) 20% PIPERIDINE IN DMF (v/v); A) FMOC-L-2-NAL-OH (1.5 EQ.), HOAT (1.5 EQ.), TBTU (1.5 EQ.), DIPEA (3.0 EQ.); B) FMOC-L-ARG(PBF)-OH (1.5 EQ.), HOAT (1.5 EQ.), TBTU (1.5 EQ.), DIPEA (3.0 EQ.); C) FMOC-D-ORN(BOC)-OH (1.5 EQ.), HOAT (1.5 EQ.), TBTU (1.5 EQ.), DIPEA (3.0 EQ.); D) COLLIDINE (10 EQ.), O-NBS-CL (4.0 EQ.); E) PH ₃ P (5.0 EQ.), ME ₂ SO ₄ (10 EQ.), DBU (3.0 EQ.); F) ME ₂ SO ₄ (10 EQ.), DBU (3.0 EQ.); G) DBU (5.0 EQ.), MERCAPTOETHANOL (10 EQ.), H) FMOC-D-TYR(TBU)-OH (3.0 EQ.), HOAT (3.0 EQ.), HATU (3.0 EQ.), DIPEA (5.0 EQ.); I) 20% HFIP IN DCM (v/v); J) DPPA (3.0 EQ.), NAHCO ₃ (5.0 EQ.); K) TFA.	30
SCHEME 2: SYNTHESIS OF (TBU)E(OH)UE(TBU) ₂ : A) TEA (2.5 EQ.), DMAP (0.04 EQ.), CDI (1.1 EQ.); 0°C-R.T., O.N.; B) TEA (2.0 EQ.), D-GLU(OBN)-OTBU (1.0 EQ.); 0°C-R.T., 40°C, O.N.; C) Pd/C (10%); R.T., O.N.....	32
SCHEME 3: REACTION OF FMOC-D-HCY(TRT)-OH WITH PERACETYLATED B-D-GLUCOSE OR B-D-LACTOSE EMPLOYING SNCL ₄ AND TIPS IN A ONE-POT REACTION.....	33
SCHEME 4: SYNTHESIS OF SIFA-BA: A) TBDMSCL, IMIDAZOLE (DMF); R.T., O.N.; B) TBU ₂ LI, DI-TERT-BUTYLDIFLUOROSILANE (THF); -78°C-R.T., O.N.; C) HCL (MEOH); R.T., O.N.; D) PYRIDINIUM CHLOROCHROMATE (DCM); 0°C, 2.5H; E) KMNO ₄ (DCM, TBUOH, NAH ₂ PO ₄ BUFFER); R.T.-5°C.	34
SCHEME 5: SYNTHESIS OF SIFA-BR: A) CBR ₄ , PPH ₃ ; 0°C-R.T.....	36
SCHEME 6: SYNTHESIS OF MAX ₃ -BASED CHELATORS ACCORDING TO FMOC-PEPTIDE SYNTHESIS STRATEGY.....	37
SCHEME 7: BOC PROTECTION OF 6-HYDRAZINONICOTINIC ACID: A) BOC ₂ O (1.0 EQ.), NET ₃ (1.3 EQ.).....	38
SCHEME 8: SYNTHESIS OF THE PROTECTED N ₄ CHELATOR: A) TERT-BUTYL-(2-AMINOETHYL)-CARBAMATE (4.0 EQ.); B) NET ₃ (3.0 EQ.), BOC ₂ O (4.0 EQ.).....	38
SCHEME 9: PRINCIPLE OF CPCr4-LINKER CONJUNCTION SYNTHESIS; SPPS OF THE CPCr4 PEPTIDE SCAFFOLD, A UNIVERSAL LINKER UNIT CXCR4-X _L AND THE FINAL PRODUCT OF A CONDENSATION BETWEEN BOTH FRAGMENTS CXCR4-X _{CLC}	40
SCHEME 10: STRUCTURE OF THE CPCr4-LINKER CONJUNCTION CXCR4-Tc-06 _{CLC} , PARAPHRASED AS OPTIMIZED TRACER BACKBONE CPCr4-ABZ-A-R-DAP.	41
SCHEME 11: SYNTHESIS OF THE N ₄ -CHELATOR-CONJUGATED MOIETY CXCR4-Tc-14 _F : A) IMIDAZOLE (0.46 G), [NH ₃ OH]CL (0.63 G); B) HO-N ₄ (BOC) ₄ (1.5 EQ.), HOAT (1.5 EQ.), TBTU (1.5 EQ.), 2,4,6-COLLIDINE (3.0 EQ.); z) 20% PIPERIDINE IN DMF (v/v); C) (TBU)E(OH)UE(TBU) ₂ (1.5 EQ.), HOAT (1.5 EQ.), TBTU (1.5 EQ.), DIPEA (3.0 EQ.); K) 20% HFIP IN DCM (v/v).....	54
SCHEME 12: SYNTHESIS OF THE N ₄ -CHELATOR-CONJUGATED MOIETY CXCR4-Tc-15 _F : A) IMIDAZOLE (0.46 G), [NH ₃ OH]CL (0.63 G); B) HO-N ₄ (BOC) ₄ (1.5 EQ.), HOAT (1.5 EQ.), TBTU (1.5 EQ.), 2,4,6-COLLIDINE (3.0 EQ.); z) 20% PIPERIDINE IN DMF (v/v); C) (TBU)E(OH)UE(TBU) ₂ (1.5 EQ.), HOAT (1.5 EQ.), TBTU (1.5 EQ.), DIPEA (3.0 EQ.); K) 20% HFIP IN DCM (v/v).....	55
SCHEME 13: SYNTHESIS OF CXCR4-SIFA-01 _L VIA SPPS: z) 20% PIPERIDINE IN DMF (v/v); A) FMOC-D-ALA-OH (2.0 EQ.), HOAT (2.0 EQ.), HATU (2.0 EQ.), DIPEA (5.0 EQ.); B) FMOC-D-ARG(PBF)-OH (1.5 EQ.), HOAT (1.5 EQ.), TBTU (1.5 EQ.), DIPEA (3.0 EQ.); C) FMOC-D-DAP(DDE)-OH (1.5 EQ.), HOAT (1.5 EQ.), TBTU (1.5 EQ.), 2,4,6-COLLIDINE (3.0 EQ.); D) IMIDAZOLE (0.46 G), [NH ₂ OH]CL (0.63 G); E) SIFA-BA-OH (1.5 EQ.), HOAT (1.5 EQ.), TBTU (1.5 EQ.), DIPEA (3.0 EQ.); K) 20% HFIP IN DCM (v/v).....	63

SCHEME 14: SYNTHESIS OF THE SIFA-CONJUGATED FRAGMENT CXCR4-SIFA-03_F: A) IMIDAZOLE (0.43 G), [NH ₂ OH]Cl (0.63 G); B) SIFA-BA-OH (1.5 EQ.), HOAT (1.5 EQ.), TBTU (1.5 EQ.), DIPEA (3.0 EQ.); Z) 20% PIPERIDINE IN DMF (V/V); C) FMOC-K(DDE)-OH (1.5 EQ.), HOAT (1.5 EQ.), TBTU (1.5 EQ.), DIPEA (3.0 EQ.); D) 2% HYDRAZINE IN DMF (V/V); E) (R)-DOTA-GA(TBU) ₄ -OH (3.0 EQ.), HOAT (3.0 EQ.), HATU (3.0 EQ.), DIPEA (6.0 EQ.); K) 20% HFIP IN DCM (V/V).	67
SCHEME 15: SYNTHESIS OF THE SIFA-CONJUGATED FRAGMENT CXCR4-SIFA-04_F: A) IMIDAZOLE (0.43 G), [NH ₂ OH]Cl (0.63 G); B) (R)-DOTA-GA(TBU) ₄ -OH (1.5 EQ.), HOAT (1.5 EQ.), TBTU (1.5 EQ.), DIPEA (3.0 EQ.); Z) 20% PIPERIDINE IN DMF (V/V); C) FMOC-D-DAP(DDE)-OH (1.5 EQ.), HOAT (1.5 EQ.), TBTU (1.5 EQ.), 2,4,6-COLLIDINE (3.0 EQ.); D) SIFA-BA-OH (1.5 EQ.), HOAT (1.5 EQ.), TBTU (1.5 EQ.), DIPEA (3.0 EQ.); E) (TBU)E(OH)UE(TBU) ₂ , HOAT (1.5 EQ.), TBTU (1.5 EQ.), DIPEA (3.0 EQ.); K) 20% HFIP IN DCM (V/V).....	69
SCHEME 16: SYNTHESIS OF THE SIFA-CONJUGATED FRAGMENT CXCR4-SIFA-05_F: Z) 20% PIPERIDINE IN DMF (V/V); A) FMOC-D-DAP(DDE)-OH (1.5 EQ.), HOAT (1.5 EQ.), TBTU (1.5 EQ.), 2,4,6-COLLIDINE (3.0 EQ.); B) IMIDAZOLE (0.43 G), [NH ₂ OH]Cl (0.63 G); C) (R)-DOTA-GA(TBU) ₄ -OH (1.5 EQ.), HOAT (1.5 EQ.), TBTU (1.5 EQ.), DIPEA (3.0 EQ.); D) FMOC-D-DAP(DDE)-OH (1.5 EQ.), HOAT (1.5 EQ.), TBTU (1.5 EQ.), 2,4,6-COLLIDINE (3.0 EQ.); E) SIFA-BA-OH (1.5 EQ.), HOAT (1.5 EQ.), TBTU (1.5 EQ.), DIPEA (3.0 EQ.); F) (TBU)E(OH)UE(TBU) ₂ , HOAT (1.5 EQ.), TBTU (1.5 EQ.), DIPEA (3.0 EQ.); K) 20% HFIP IN DCM (V/V).....	71
SCHEME 17: SYNTHESIS OF THE SIFA-CONJUGATED FRAGMENT CXCR4-SIFA-06_F: Z) 20% PIPERIDINE IN DMF (V/V); A) FMOC-D-DAP(DDE)-OH (1.5 EQ.), HOAT (1.5 EQ.), TBTU (1.5 EQ.), 2,4,6-COLLIDINE (3.0 EQ.); B) IMIDAZOLE (0.43 G), [NH ₂ OH]Cl (0.63 G); C) (R)-DOTA-GA(TBU) ₄ -OH (1.5 EQ.), HOAT (1.5 EQ.), TBTU (1.5 EQ.), DIPEA (3.0 EQ.); D) DMG-OH (1.5 EQ.), HOAT (1.5 EQ.), TBTU (1.5 EQ.), 2,4,6-COLLIDINE (3.0 EQ.); E) SIFA-BR (3.0 EQ.), DIPEA (3.0 EQ.); K) 20% HFIP IN DCM (V/V).....	73
SCHEME 18: SYNTHESIS OF THE SIFA-CONJUGATED FRAGMENT CXCR4-SIFA-07_F: Z) 20% PIPERIDINE IN DMF (V/V); A) FMOC-D-DAP(DDE)-OH (1.5 EQ.), HOAT (1.5 EQ.), TBTU (1.5 EQ.), 2,4,6-COLLIDINE (3.0 EQ.); B) IMIDAZOLE (0.43 G), [NH ₂ OH]Cl (0.63 G); C) DOTA(TBU) ₃ -OH (1.5 EQ.), HOAT (1.5 EQ.), TBTU (1.5 EQ.), DIPEA (3.0 EQ.); D) FMOC-D-HCY(B-D-LACTOSYL)-OH (1.5 EQ.), HOAT (1.5 EQ.), HATU (1.5 EQ.), DIPEA (3.0 EQ.); E) DMG-OH (1.5 EQ.), HOAT (1.5 EQ.), TBTU (1.5 EQ.), 2,4,6-COLLIDINE (3.0 EQ.); F) SIFA-BR (3.0 EQ.), DIPEA (3.0 EQ.); K) 20% HFIP IN DCM (V/V).....	75
SCHEME 19: SYNTHESIS OF THE (R)-DOTA-GA(TBU) ₄ -CONJUGATED FRAGMENT CXCR4-MMAE-04_F: Z) 20% PIPERIDINE IN DMF (V/V); A) FMOC-D-DAP(DDE)-OH (1.5 EQ.), HOAT (1.5 EQ.), TBTU (1.5 EQ.), 2,4,6-COLLIDINE (3.0 EQ.); B) IMIDAZOLE (0.43 G), [NH ₂ OH]Cl (0.63 G); C) (R)-DOTA-GA(TBU) ₄ -OH (1.5 EQ.), HOAT (1.5 EQ.), TBTU (1.5 EQ.), DIPEA (3.0 EQ.); D) FMOC-D-HCY(TRT)-OH (1.5 EQ.), HOAT (1.5 EQ.), HATU (1.5 EQ.), DIPEA (3.0 EQ.); E) DIPEA (5.0 EQ.), Ac ₂ O (5.0 EQ.) K) TFA/TIPS/H ₂ O (95/2.5/2.5; V/V/V).....	80
SCHEME 20: SYNTHESIS OF THE DOTA-CONJUGATED FRAGMENT CXCR4-OI-03_F: Z) 20% PIPERIDINE IN DMF (V/V); A) FMOC-D-DAP(DDE)-OH (1.5 EQ.), HOAT (1.5 EQ.), TBTU (1.5 EQ.), 2,4,6-COLLIDINE (3.0 EQ.); B) IMIDAZOLE (0.43 G), [NH ₂ OH]Cl (0.63 G); C) DOTA(TBU) ₃ -OH (1.5 EQ.), HOAT (1.5 EQ.), TBTU (1.5 EQ.), DIPEA (3.0 EQ.); K) 20% HFIP IN DCM (V/V).....	83

6. Supplementary Index

SUPPLEMENTARY 1: RESULTS OF SPECT/CT IMAGING STUDIES 1H POST INJECTION OF [^{99m} Tc]CXCR4-Tc-06, -08, -10 – 13 IN PRESENCE OF 100 NMOL AMD3100 IN JURKAT TUMOR-BEARING FEMALE CB-17 SCID MICE: MAXIMUM-INTENSITY PROJECTION IMAGES OBTAINED FROM STATIC SPECT IMAGING OF 1 ANIMAL PER LIGAND; ARROWS INDICATE ORGANS OF SPECIAL INTEREST: STRAIGHT: TUMOR, DASHED: LIVER, POINTED: KIDNEYS.....	249
SUPPLEMENTARY 2: A) SPECT/CT IMAGE OF THE AXIAL PLANE 3H P.I. OF 604 MBQ [^{99m} Tc]CXCR4-Tc-13 IN A PATIENT SUFFERING FROM MULTIPLE MYELOMA; B) PET/CT IMAGE OF THE AXIAL PLANE 1H P.I. OF 189 MBQ [¹⁸ F]FDG IN THE SAME PATIENT: BLUE ARROWS INDICATE THE URINARY BLADDER, GREEN ARROWS INDICATE OSTEOLYTIC LESIONS.	250
SUPPLEMENTARY 3: RESULTS OF SPECT/CT IMAGING STUDIES 1H POST INJECTION OF [¹⁷⁷ Lu]CXCR4-DOTA-01 – 04 IN JURKAT TUMOR-BEARING FEMALE CB-17 SCID MICE: MAXIMUM-INTENSITY PROJECTION IMAGES OBTAINED FROM STATIC SPECT IMAGING OF 1 ANIMAL PER LIGAND; ARROWS INDICATE ORGANS OF SPECIAL INTEREST: STRAIGHT: TUMOR, DASHED: LIVER, POINTED: KIDNEYS.	251
SUPPLEMENTARY 4: RESULTS OF SPECT/CT IMAGING STUDIES 1H POST INJECTION OF [¹⁷⁷ Lu]CXCR4-DOTA-01 – 04 IN PRESENCE OF 100 NMOL AMD3100 IN JURKAT TUMOR-BEARING FEMALE CB-17 SCID MICE: MAXIMUM-INTENSITY PROJECTION IMAGES OBTAINED FROM STATIC SPECT IMAGING OF 1 ANIMAL PER LIGAND; ARROWS INDICATE ORGANS OF SPECIAL INTEREST: STRAIGHT: TUMOR, DASHED: LIVER, POINTED: KIDNEYS.....	251
SUPPLEMENTARY 5: TIME-ACTIVITY-CURVE INTERPOLATION OF TUMOR ACTIVITY OF [¹⁷⁷ Lu]CXCR4-DOTA-03 AND -04 AS WELL AS [¹⁷⁷ Lu]PENTIXATHER; START AND END VALUES WERE TAKEN FROM 1H AND 48H BIODISTRIBUTION EXPERIMENTS WITH THE RESPECTIVE LIGANDS.	252
SUPPLEMENTARY 6: FACS OF DIFFERENT CELL TYPES TO DETERMINE THEIR CXCR4 EXPRESSION LEVELS; HIGHER CXCR4 EXPRESSION IS OBSERVED FOR HIGHER VALUES OF CXCR4-VIOLET 1.....	253